



HAL
open science

Development of lipid-based nanoparticles for chemo-attraction and targeting of *Helicobacter pylori*

Van Hung Nguyen

► **To cite this version:**

Van Hung Nguyen. Development of lipid-based nanoparticles for chemo-attraction and targeting of *Helicobacter pylori*. Galenic pharmacology. Université Paris-Saclay, 2022. English. NNT : 2022UP-ASQ048 . tel-04839404

HAL Id: tel-04839404

<https://theses.hal.science/tel-04839404v1>

Submitted on 16 Dec 2024

HAL is a multi-disciplinary open access archive for the deposit and dissemination of scientific research documents, whether they are published or not. The documents may come from teaching and research institutions in France or abroad, or from public or private research centers.

L'archive ouverte pluridisciplinaire **HAL**, est destinée au dépôt et à la diffusion de documents scientifiques de niveau recherche, publiés ou non, émanant des établissements d'enseignement et de recherche français ou étrangers, des laboratoires publics ou privés.

Development of lipid-based nanoparticles
for chemo-attraction and targeting of
Helicobacter pylori

*Développement de nanoparticules lipidiques pour la chimio-attraction et
le ciblage d'Helicobacter pylori*

Thèse de doctorat de l'université Paris-Saclay

École doctorale n°569 innovation thérapeutique : du fondamental à l'appliqué (ITFA)
Spécialité de doctorat : pharmacotechnie et biopharmacie
Graduate School : Santé et médicaments. Référent : Faculté de pharmacie

Thèse préparée dans l'unité de recherche **Université Paris-Saclay, CNRS, Institut
Galien Paris-Saclay, 92296, Châtenay-Malabry, France**, sous la direction de
Vincent FAIVRE, Professeur

Thèse soutenue à Paris-Saclay, le 12 décembre 2022, par

Van Hung NGUYEN

Composition du Jury

Gilles PONCHEL Professeur, Université Paris-Saclay	Président
Imogen FOUBERT Professeure, KU Leuven	Rapporteur & Examinatrice
Giovanna LOLLO Maîtresse de conférences, HDR, Université Claude Bernard Lyon 1	Rapporteur & Examinatrice
Christophe BURUCOA Professeur, Université de Poitiers	Examineur
Susanne FLORIN MUSCHERT Maîtresse de conférences, HDR, Université de Lille	Examinatrice
Vincent FAIVRE Professeur, HDR, Université Paris- Saclay	Directeur de thèse

Titre : Développement de nanoparticules lipidiques pour la chimio-attraction et le ciblage d'*Helicobacter pylori*

Mots clés : Nanoparticules lipidiques, *Helicobacter pylori*, Chimiotactisme, Ciblage

Résumé : *Helicobacter pylori* (*H. pylori*) est une bactérie qui vit à l'intérieur de l'estomac humain. Elle infecte plus de 50 % de la population mondiale. L'infection par *H. pylori* peut entraîner des ulcères gastriques et duodénaux, des gastrites, et dans certains cas des cancers gastriques. Lorsqu'il se trouve dans l'estomac, *H. pylori* fuit le gradient d'acide et suit le gradient d'urée pour trouver l'épithélium gastrique. Il crée alors des niches dans les glandes gastriques, sous la couche de mucus, où le pH est neutre. Le traitement de *H. pylori* est difficile en raison de la faible activité des antibiotiques dans un environnement acide.

Dans cette thèse de doctorat, pour tenter d'améliorer l'activité des antibiotiques et améliorer l'efficacité du traitement contre *H. pylori*, nous avons préparé des nanoparticules lipidiques qui co-encapsulent l'érythromycine, un antibiotique hydrophobe, et l'urée, un chimioattractant hydrophile pour *H. pylori*. Ces nanoparticules lipidiques ont été conçues pour cibler les facteurs de survie de la bactérie dans l'estomac. L'utilisation de nanoparticules facilite la pénétration de la formulation dans la couche de mucus, où se trouvent les bactéries. L'urée crée un gradient pour attirer *H. pylori* vers les nanoparticules et faciliter la rencontre entre les nanoparticules et les bactéries. L'érythromycine est libérée dans l'environnement tamponné autour de la bactérie. La formulation contient un revêtement de chitosane, qui adhère à la couche de mucus gastrique, favorisant la rétention de la formulation dans l'estomac. En outre, le chitosane adhère également à la bactérie, servant ainsi de stratégie de ciblage actif.

Pour encapsuler l'érythromycine et l'urée, qui ont des solubilités opposées, nous solubilisons l'érythromycine dans la matrice lipidique et stabilisons la solution d'urée dans le lipide en utilisant un tensioactif lipophile. Les nanoparticules lipidiques contenant les deux molécules sont stabilisées dans

l'eau à l'aide d'un tensioactif hydrophile. Après le processus de sélection des matériaux, nous avons trouvé que le mélange de beurre de cacao, agissant comme le compartiment lipidique, et de monostéarate de sorbitane, agissant comme le tensioactif lipophile, est adapté à notre objectif. Il est intéressant de noter que le monostéarate de sorbitane a une structure α -gel, qui est une structure lamellaire solide. Nous avons observé que la solution d'urée peut être stabilisée à l'intérieur de la structure lamellaire. Le monostéarate de sorbitane est monomorphe, ce qui confère à la structure lamellaire hydratée une grande stabilité dans le temps.

Les nanoparticules lipidiques sont stabilisées dans l'eau par le dodécylsulfate de sodium (SDS), qui est un agent de surface hydrophile chargé négativement. Le SDS s'intègre bien dans le lipide et ne modifie pas la structure cristalline lipidique lyotrope des nanoparticules lipidiques. Le SDS interagit de manière électrostatique avec le chitosane, qui a des charges positives en acide. L'interaction électrostatique assure la stabilité du revêtement en milieu acide.

Les nanoparticules lipidiques sont fabriquées par la méthode d'homogénéisation à chaud et à haute pression. La fabrication est simple et évolutive. Après avoir éliminé le médicament non encapsulé par ultra-centrifugation, le chitosane est ajouté et mélangé aux nanoparticules lipidiques pour les enrober. La suspension est ensuite lyophilisée pour obtenir une poudre destinée à la voie d'administration orale.

La formulation finale présente une activité antibactérienne *in vitro* due à l'érythromycine encapsulée. La libération de l'érythromycine et de l'urée à partir de la poudre lyophilisée est durable pendant 3-4 heures, indiquant un potentiel pour notre application.

Title : Development of lipid-based nanoparticles for chemo-attraction and targeting of *Helicobacter pylori*

Keywords : Lipid nanoparticles, *Helicobacter pylori*, Chemotactism, Targeting

Abstract : *Helicobacter pylori* (*H. pylori*) is a bacterium that lives inside the human stomach. It infects more than 50% of the world's population. The infection of *H. pylori* may lead to peptic, gastritis, duodenal ulcers, and eventually gastric cancer. While living in the stomach, *H. pylori* cannot live in acids. It runs away from the acid gradient and follows the urea gradient to find gastric epithelium. It then makes niches in the gastric glands, below the mucus layer, where the pH is neutral. The treatment of *H. pylori* is difficult due to the low activity of antibiotics in gastric acid.

In this doctoral thesis, to facilitate the activity of antibiotics and improve the *H. pylori* treatment efficiency, we fabricated lipid nanoparticles that co-encapsulate erythromycin, a hydrophobic antibiotic, and urea, a hydrophilic chemoattractant for *H. pylori*. We apply the lipid nanoparticles to target survival factors of *H. pylori* in the stomach. The use of nanoparticles facilitates the penetration of the formulation into the mucus layer, where the bacteria locate. The urea creates a urea gradient to attract *H. pylori* towards the nanoparticles and facilitate the meeting between the nanoparticles and the bacteria. Erythromycin is released around the buffered environment around the bacteria. The formulation contains a chitosan coating, which adheres to the gastric mucus layer, promoting the retention of the formulation in the stomach. In addition, the chitosan also adheres to the bacteria, serving as an active targeting strategy.

To encapsulate both erythromycin and urea, which have opposite solubilities, we solubilize erythromycin in the lipid matrix and stabilize the urea solution in the lipid by using a lipophilic surfactant. The lipid nanoparticles containing both molecules are

stabilized in water using a hydrophilic surfactant. After the material screening process, we found the mixture of cocoa butter, acting as the lipid compartment, and sorbitan monostearate, acting as the lipophilic surfactant, is suitable for our purpose. Interestingly, sorbitan monostearate has an α -gel structure, which is a solid lamellar structure. We found that urea solution can be stabilized inside the lamellar structure. Sorbitan monostearate is monomorphic, giving the hydrated lamellar high stability over a long period of time.

The lipid nanoparticles are stabilized in water by sodium dodecyl sulfate (SDS), which is a negatively charged hydrophilic surfactant. SDS can integrate well in the lipid and does not change the lyotropic lipid crystalline structure of lipid nanoparticles. SDS interacts electrostatically with chitosan, which has positive charges in acid. The electrostatic interaction ensures the coating stability in acid media.

The lipid nanoparticles are fabricated by the hot high-pressure homogenization method. The fabrication is simple and scalable. After removing the non-encapsulated drug by ultra-centrifugation, chitosan is added and mixed with the lipid nanoparticles for coating. The suspension is then lyophilized to obtain a powder for the oral administration route.

The final formulation has antibacterial activity *in vitro* from encapsulated erythromycin. The release of erythromycin and urea from the lyophilized powder is sustainable for 3-4 hours, indicating a potential for our application.

ACKNOWLEDGMENT

My doctoral study has been a long journey for me, during which I have developed myself not only in scientific knowledge but also in several other facets of life. This 3-year work could not be finished without the help of many people below, to whom I am always grateful. Due to several reasons, it is very hard to express fully my gratitude [1], especially for me who has blunt words and sentences. In addition, I may forget to include some people. So, this list below is not exhaustive. If you are not in it, it does not mean you are not important. It means my mind is not perfect when I am writing this section and I am very sorry for the mistakes. However, I am sure you all who were involved with me in my doctoral period, whether on the list or not, will always be in my deep memory. I and my thesis would be different without the contribution of all of you.

The relationship, both personally and academically, between the supervisor and the student is one of the important factors of the PhD project success rate [2]. Therefore, I would like to express my gratitude to my thesis supervisor, my teacher, my colleague, and my friend, Vincent FAIVRE. He is an excellent and respectable teacher-researcher. In research, his scientific ideas and methods are exceptionally excellent. He is very honest about his works, does not rush to publish, and always aims for high-quality research. As a supervisor, he accompanies me in every step of my work. While he always gives me freedom in my research and in the realization of my ideas, he also follows closely and gives me advice. He always tries to get the best things for his students, although it is difficult sometimes due to the research's financial situation. I may not have the most modern equipment or expensive materials, but I have a top-quality supervisor. In scientific discussions, he always respects my opinions and explains to me well his thoughts. It is obvious that our ideas and opinions are not always aligned, but I am grateful that he always shows me another way of thinking and the other faces of the problem. Other than science, I also learned a lot from his calm, nice and cheerful personality. He told me several times that he is not good at communication, but I do not think so. I am not qualified to judge if his communication method is good or bad, but I can say his way of communication is what makes him unique and likable. As a team leader, he is always supportive to everyone and treats everyone fairly. Being one of his students, I never have more privilege than other team members. I am very happy that I have had a chance to work with him and learn from him. Although I am very excited to finish my thesis, I regret that I have to stop working with him. I hope I will have a chance to collaborate, to work with him and his team again in the future.

I would like to thank Giovanna LOLLO and Imogen FOUBERT for accepting to be the reporters for my thesis. Their contribution and evaluation are very valuable for the thesis. I would like to express my gratitude to Gilles PONCHEL, Susanne FLORIN

MUSCHERT, and Christophe BURUCOA for accepting to be the examiners for the thesis. Their comments are also very helpful for the project.

My thesis project would not be realized without the funding from LabEx LERMIT organization. This project has received Labex LERMIT financial support from « Investissements d'avenir » program (ANR-10-LABX-33). LabEX LERMIT also gives me an extension of 3 months to compensate for the 1st confinement period in 2020 due to COVID-19. In addition, I received from them also a mobility fund, which covers my living expense in Poitiers for the biological experiments. I am very grateful to the funding organization and to all people behind it.

The antimicrobial activity of the formulation *in vitro* is very important to my project. Without them, all the formulation results do not have any significant meaning. I would like to thank Christophe BURUCOA and his team in CHU Poitiers for their support in the *in vitro* experiment on *H. pylori*. During my time in Poitiers, Christophe was very welcoming and friendly. He taught me how to work with bacteria and answered all my questions. I learned a lot from his passion for *H. pylori* research. I am very grateful to all the technicians in the laboratory, especially in the medium preparation (Catherine BONNEAU and Dominique DUHAUT) and laundry/sterilization/packaging service (Marie Noelle FOUCAULT and Nadine MET). Their roles were highly essential. They prepared everything for my experiments, taught me how to work correctly in the lab and showed me how they work daily. I would like to thank Julie CREMNITER who helped me to read the experiment results and Maxime PICHON who showed me where to buy lunch in the hospital.

The concept of the project would not be demonstrated without the help of Manuel R. AMIEVA and his team at Stanford Medicine. I am very grateful to have a discussion with him in Paris. I admire his enthusiasm for research. The video-microscopy results that he prepared for us are very important to demonstrate the movement of bacteria. I hope the collaboration between the 2 teams will be further tightened in the future with more exciting experiments.

I would like to thank Bastien PROST and Audrey SOLGADI from Service d'Analyse des Médicaments et Métabolites (SAMM) for their help with the LC-MS experiments. They are very nice and friendly. They helped me to set up the experiment and showed me the method to treat data. They also gave us LC-MS grade isopropanol for our experiments, which is essential in LC-MS experiments. The data from the LC-MS experiment are valuable and changed the way I interpret our input materials.

I am grateful to Heinz AMENITSCH for his support in the X-ray scattering experiments at Elettra Synchrotron Trieste. The SAXS and WAXS data are very valuable to us in understanding better our materials.

I express my gratitude to Lucia MANCINI et Elena LONGO at Elettra Synchrotron Trieste for their help with the X-ray tomography experiments. Observing the interior of the samples is truly exciting for me.

I would like to thank Eric LARQUET for his help with the Cryo-TEM experiment. It is very interesting and essential to see nanoparticles in the dispersion state.

My thesis work was conducted at the Institute Galien Paris-Saclay (UMR CNRS 8612). I would like to thank the administration team, Sylvie ZEMMOUR for her help with my administration and financial documents like working contracts, convention d'accueil etc, Patricia LIVET for her help with the consumable products and Fatiha HAMZA for her help with the procedure of my missions. Without the help of the whole administration team, I could not get through the struggle with documents and visa procedures. In scientific experiments, I am truly grateful for the help of many engineers. I would like to thank Sylvie LIU for her instruction and support with HPLC. She is always there when the machines have problems. She is also a very cheerful and friendly person, and I wish her all the best in her new adventure. I am very grateful to David CHAPRON for his help with the DSC and surface tension experiments. He is a very kind and meticulous person, and I learned many things from his personality. He also helps me with the internet connection and the institute's intranet access, which I know nothing about. I express my sincere gratitude to Jean-Jacques VACHON for his help with the Microcalix machine and various mechanical problems. I always borrow his trolley to carry consumable products for our team. He is a very funny and helpful person. I always feel comfortable when working with him. Although sometimes I do not understand him and I feel he does not understand me due to the language barrier, we always can find a way to work it out.

The research environment and the research team determine the success of PhD projects and the future of PhD students [3,4]. The success at the early stage of a researcher highly influences the career after [3,5]. I was a member of the team Chemistry and Physic of multiphase systems, which became a part of the large team MULTIPHASE (MULTIscale physical chemistry for PHArmaceutical SciencEs) in January 2022. I would like to thank everybody of the large new team. The not-so-high number of PhD students in the team during my period created an interactive, friendly environment, a powerful "training ground" for me [4]. Besides science, from the interaction between team members, I learned a lot about the way of collaboration and communication. For example, the current situation of equipment reservation in the team reminds me of the infinite prisoner's dilemma in game theory. However, it is not in the Nash equilibrium point, meaning that the collaboration between members still can be further improved. This fact was also stated in the Institute's evaluation report in 2014 (not much information in the 2019 public version report) [6]. However, it has been years since 2014, everything is changing positively now. Humans are not always logical, and the real situation is much more complicated than a scenario of game theory. Or

maybe the team is in its own equilibrium, I do not know, but I wish all the best for the whole team in the future.

I am very lucky that I have been surrounded by many talented researchers. I am happy that I had a chance to meet Claudie BOURGAUX (she retired shortly after I entered the team). Although I do not talk too much with her, she always gives me a peaceful feeling. I can definitely say she has a friendly and nice personality. Her smile and her vibe always make me comfortable. I hope her retirement is full of happiness. I am very grateful to Gillian BARRATT, who retired in June 2022. Although I do not work directly with her, I can see her work through the thesis of her student, also my friend, Antonio LIPA CASTRO. I can say she is a wonderful researcher and a very friendly colleague. Her recommendations for my work presentation are very valuable. She also taught me to use the ultra-centrifuge machine. I believe that her retirement is a loss of expertise in biology for the team. I wish her retirement is full of joy, and hope that the team will have someone to fill in this loss of expertise. I am very grateful for the help of Sylviane LESIEUR in my work. Her scientific comments and questions during my work presentations are always helpful and directly to the point. She is an expert in my field of research. She is also very friendly; she gave me advice about housing when I recently arrived in the Ile-de-France area. I would like to express my gratitude to Angéline ANGELOVA. As her students are in the same office with me, I meet her quite often. She is very nice and smiling. In science, she is an impactful researcher, and I always appreciate her comments on my work. I also appreciate the quality of the works of her and her students (Miora RAKOTOARISOA and Yu WU). Through their works, I realized and learned about different perspectives, ways of thinking, and problem approaches in research. I would like to thank François-Xavier LEGRAND for his help with some experiments like X-ray diffraction or Cryo-TEM. He is very active in the lab with many students. His students are also very hard-working. They (notably Paul and Luc AUGIS) usually stay late to work in the lab, probably too late in my opinion. I believe that he will become a big researcher/professor in the future. But I also strongly believe that the work-life balance should be the achievement that we need to aim at. I would like to thank Jean-Philippe MICHEL, Ali MAKKY, Véronique ROSILIO, who were from the old team 1, for their scientific comments on my presentation during the team meeting.

My research environment would not be so interesting and fun without other interns and PhD students. I would like to thank Antonio, Matis, Louis, Miora, and Islam, who started their work before me and were very helpful and welcoming when I came to the lab. Antonio helped me a lot in the lab. He showed me the place of everything, protocols for the biological media, and how to get the consumable products. He is also very hard-working, and I admire his determination. I am very lucky that I have a chance to be friends with Yu WU, Yaowei LU, Jesse (Fang-Ching CHAO), Paul (NGUYỄN Cảnh Hưng), Claire DELMAS, and Luc AUGIS - PhD students in my team who started at the same time or after me. I will always remember the over-positivity of Yu and the over-negativity of Jesse. They are like the yin and yang and remind me of the balance that we all need in

life. I thank Jesse for all the discussion, which gave me many ideas, and thank Yu for her friendliness. International experience in our lab is extremely valuable for me. I realized that Claire and Luc have a totally different style compared to Yu and Jesse. I would like to express my gratitude to Claire for her effort in trying to socialize me. Although it is not always effective, effort and determination are more important than results. Luc helps her sometimes, and I also thank Luc for his kindness. I would like to thank Yaowei for all his help in the office. He reminds me of myself when I was younger. If he can keep his hard-working nature, he will be successful in his project. I am grateful that I have met Paul, the other Hung, the other Mr. Nguyen and the other Vietnamese student in the team. I will always miss our discussions together. Without him, I would have forgotten my mother tongue at work. I would like to also thank all interns that have been in our team (Lucas, Cécile, Lou, Thelma, and Sarra). Although their time in the lab is short, the impacts that they have left on me and my project are huge.

The family is the foundation of any success. The income of a household highly influences the development, academic performance, and hence the future of children [7,8]. All my achievements now would not be possible without the support of my parents. While growing up in a small city in a developing country, my living conditions have always been perfect. My parents always provide their best for their children. I am and will be forever grateful for their support and their love since I was born. I also learned a lot from my mother, who is very hard-working and caring. My academic background now is partially constructed by my older brother, who gave me advice in the most important times, for example, my 8th grade and university entrance. I am very grateful for his constant support.

Last but not least, I would like to express my gratitude to my own small family (my wife Giang, my furry son Béton and my calico daughter Méline). They are my motivation to move forward, my place to rest after work, and the infinite source of love. My wife has always been by my side and goes with me through all difficulties. I am fortunate that I have her in my life. I am grateful that I have the chance to adopt Méline and Béton. Their love helps me to go through hard times. They have taught me many aspects of life, given me other views of the world, and influenced my thinking and reasoning. Probably because they have their own philosophy, which is a bit different from human's [9].

References

- [1] A. Kumar, N. Epley, Undervaluing Gratitude: Expressers Misunderstand the Consequences of Showing Appreciation, *Psychol. Sci.* 29 (2018) 095679761877250. <https://doi.org/10.1177/0956797618772506>.
- [2] E. van Rooij, M. Fokkens-Bruinsma, E. Jansen, Factors that influence PhD candidates' success: the importance of PhD project characteristics, *Stud. Contin. Educ.* 43 (2021) 48–67. <https://doi.org/10.1080/0158037X.2019.1652158>.

- [3] D.L. Belavy, P.J. Owen, P.M. Livingston, Do successful PhD outcomes reflect the research environment rather than academic ability?, *PLoS ONE*. 15 (2020) e0236327. <https://doi.org/10.1371/journal.pone.0236327>.
- [4] A. Broström, Academic breeding grounds: Home department conditions and early career performance of academic researchers, *Res. Policy*. 48 (2019) 1647–1665. <https://doi.org/10.1016/j.respol.2019.03.009>.
- [5] V. Sekara, P. Deville, S.E. Ahnert, A.-L. Barabási, R. Sinatra, S. Lehmann, The chaperone effect in scientific publishing, *Proc. Natl. Acad. Sci. U. S. A.* 115 (2018) 12603–12607. <https://doi.org/10.1073/pnas.1800471115>.
- [6] IGPS - Institut galien Paris Sud, Hcéres. (n.d.). <https://www.hceres.fr/fr/rechercher-une-publication/igps-institut-galien-paris-sud-0> (accessed June 16, 2022).
- [7] K. Cooper, K. Stewart, Does Household Income Affect children’s Outcomes? A Systematic Review of the Evidence, *Child Indic. Res.* 14 (2021) 981–1005. <https://doi.org/10.1007/s12187-020-09782-0>.
- [8] Z. Li, Z. Qiu, How does family background affect children’s educational achievement? Evidence from Contemporary China, *J. Chin. Sociol.* 5 (2018) 13. <https://doi.org/10.1186/s40711-018-0083-8>.
- [9] J. Gray, *Feline Philosophy: Cats and the Meaning of Life*, Farrar Straus & Giroux, New York, 2020.

TABLE OF CONTENTS

ACKNOWLEDGMENT	4
LIST OF FIGURES	14
LIST OF TABLES	20
LIST OF ABBREVIATIONS	21
I. GENERAL INTRODUCTION	26
II. BIBLIOGRAPHIC PART	29
Chapter 1. <i>Helicobacter pylori</i> survival factors and treatment	30
1. <i>Helicobacter pylori</i> survival factors in the stomach	30
1.1. Acid neutralization to survive in the acid environment	31
1.2. Chemotactic behavior to colonize in the mucosa layer	31
1.3. Adhesin for attachment and persistent infection	33
2. Treatment of <i>Helicobacter pylori</i>	35
2.1. Current clinical treatments of <i>H. pylori</i> infection	35
2.2. Current drug delivery strategies for <i>H. pylori</i> treatment in research	36
3. Conclusion	39
References	40
Chapter 2. Targeted drug delivery therapies inspired by natural taxes	47
Abstract	47
1. Introduction	48
1.1. Physical stimulus responsive taxis.....	49
1.2. Chemical stimulus responsive taxis.....	51
2. Targeted drug delivery therapies inspired by natural taxes.....	51
2.1. Guiding carriers to a target.....	51
2.2. Attracting targets to a desired location	67
3. Future prospects and conclusion	73
References	76
Chapter 3. Lyotropic lipid particles formulation for co-encapsulation of both hydrophilic and lipophilic drugs	99
1. Introduction	99

2. Lyotropic crystals	100
2.1. Lamellar mesophase	100
2.2. Columnar mesophase	101
2.3. Globular mesophases	102
2.4. Bicontinuous mesophases.....	103
2.5. Sponge-disordered bicontinuous mesophase.....	104
3. Water-containing drug delivery systems from lyotropic lipid structures	105
3.1. Multiple emulsion	106
3.2. Liposome and α -gel particle	109
3.3. Hexosome, cubosome and sponge particle.....	114
4. Conclusion	117
References	118
III. EXPERIMENTAL PART	123
Chapter 4. Excipients screening, pre-formulation and process parameters optimization	124
Abstract	124
1. Introduction	124
2. Materials and methods.....	125
2.1. Materials.....	125
2.2. Taguchi's design of experiment for excipients screening.....	125
2.3. DSC measurement of w/o emulsions	127
2.4. Sample morphology characterization by polarized light microscopy	127
2.5. Lipid structure characterization	128
2.6. Fabrication of lipid nanoparticles.....	128
2.7. Particles' size and zeta potential measurement.....	129
2.8. Solution surface tension measurement	129
2.9. Finding the solubility of erythromycin in SDS solution	129
3. Results and discussion.....	130
3.1. Input materials screening using DoE.....	130
3.2. Optimization of Montane 60 and cocoa butter ratio	133
3.3. Optimization of nanoparticles fabrication parameters	136

3.4. The incorporation of charge into lipid particles	138
3.5. Characterization of the SDS, erythromycin, and urea.....	140
4. Conclusion	143
References	144
Chapter 5. Sorbitan stearate: from the hydration behavior to the preparation of α-gel based particles	147
Abstract	147
1. Introduction	147
2. Materials and methods.....	148
2.1. Materials	148
2.2. Montane 60 chemical composition analysis method	149
2.3. Sorbitan stearate spontaneous hydration method	150
2.4. Acquisition of the synchrotron radiation computed microtomography (SR μ CT) dataset	150
2.5. Montane 60 hot hydration method	150
2.6. α -gel particles fabrication process	151
2.7. Lipid crystal structure determination method.....	151
2.8. Particles' size and zeta potential measurement	152
3. Results and discussion.....	152
3.1. Chemical composition analysis of Montane 60	152
3.2. Spontaneous hydration of Montane 60 and Span 65	156
3.3. Crystal structure and lyotropic behavior of Montane 60 studied by hot hydration method	158
3.4. Formation of Montane 60 α -gel suspension.....	169
4. Conclusion	177
References	178
Chapter 6. Solid lipid particles - chitosan nanocomposite for chemoattraction and elimination of <i>Helicobacter pylori</i>	182
Abstract	182
1. Introduction	182
2. Materials and methods.....	183

2.1. Materials	183
2.2. Fabrication of lipid nanoparticles suspension	184
2.3. Physico-chemical characterization of LNP suspension.....	184
2.4. Fabrication process of lipid nanoparticles – chitosan (LNP-C) nanocomposite	186
2.5. Physico-chemical characterization of LNP-C nanocomposite	187
2.6. <i>In vitro</i> release studies of LNP-C nanocomposite	188
2.7. Antimicrobial and chemoattraction property studies of LNP-C nanocomposite	189
3. Results and discussion.....	189
3.1. Physico-chemical properties and structure of lipid nanoparticles suspension (LNP) and lipid nanoparticles – chitosan nanocomposite (LNP-C).....	189
3.2. Drugs and particles release profile of LNP-C nanocomposite <i>in vitro</i>	196
3.3. Antimicrobial and chemoattraction properties of LNP-C	200
4. Conclusion	203
References	203
IV. GENERAL DISCUSSION AND CONCLUSION	207
1. About the formulation	207
2. About the <i>in vitro</i> drug delivery and anti-microbial activity tests	210
3. About <i>in vitro</i> chemotactic experiments	211
3.1. Video-microscope experiment	211
3.2. Gradient soft agar swim plate assay.....	213
4. Perspective.....	217
References	217
V. CURRICULUM VITAE.....	219

LIST OF FIGURES

Figure I.1. Schematic of <i>H. pylori</i> structure and its virulence factors; the figure is adapted from ref. [8].	26
Figure 1.1. The morphology of <i>H. pylori</i> is shown under scanning electron microscopy (SEM). The scale bar represents 0.5 μm [7].....	30
Figure 1.2. <i>H. pylori</i> swims toward the urea gradient thanks to the TlpB receptor, figure adapted from ref. [16].....	33
Figure 1.3. Mice's gastric glands were co-infected with 2 different labelled (green fluorescence protein – GFP and tdTomato – tdT) <i>H. pylori</i> strains. Images showed that different <i>H. pylori</i> strains compete for niches in gastric glands. The scale bar represents 10 μm . [26]	35
Figure 1.4. <i>H. pylori</i> (green) adheres to a chitosan bead (red), photo taken under confocal microscopy, figure adapted from ref. [48].....	37
Figure 1.5. 3D reconstruction confocal laser scanning microscopy images of adenocarcinoma epithelial (AGS) cells infected by <i>H. pylori</i> incubated with (a) uncoated liposome and (b) pectin-coated liposome. AGS cell's DNA is blue, <i>H. pylori</i> is green, liposome is red. The overlap of green and red in figure b shows the interaction between pectin-coated liposome and <i>H. pylori</i> . The figure is adapted from ref. [54].	39
Figure 2.1. Summary of taxes-inspired targeted drug delivery therapies	49
Figure 2.2. (A) Illustrative, fluorescence and TEM images of magnetically guided micro-swimmer show the screw shape and the success in p-DNA loading, marked with green fluorescence. (B) The wobbling moving behavior of a screw-shaped swimmer and its moving speed are dependent on the magnetic field frequency and the helix angle. (C) The ciprofloxacin release rate from drug-loaded silica microtubes and the photo of magnetotactic bacteria carrying those microtubules; drug-carrying magnetotactic bacteria can be guided to an <i>E. coli</i> biofilm using a magnetic field.....	56
Figure 2.3. (A) Structure and moving mechanism of Mg micro-motor in acidic environments; (B) The application of clarithromycin-loaded micromotors in <i>H. pylori</i> treatment in mice shows comparable performance to the combination of clarithromycin and proton pump inhibitor. Reproduced with open-access permission from ref. [122]	61
Figure 2.4. Images of <i>Salmonella Typhimurium</i> carrying paclitaxel-loaded liposomes; The drug release rate of liposomes and of bacteria carrying liposomes are almost identical,	

while the moving speed of the bacteria-liposome system is higher than single liposomes. Reproduced with permission from ref. [144].....	64
Figure 2.5. (A) EM@MSNs (top-left) and MSNs (bottom-left) uptake percentage by neutrophils characterized by flow cytometry. The release rate of loaded DOX inside each system in different pH shows that the <i>E. coli</i> membrane coating reduces the leakage of drug. (B) Trajectories of 10 neutrophils carrying drugs over 8 minutes in the absence or the presence of an <i>E. coli</i> gel. Reproduced with permission from ref. [159]	66
Figure 2.6. (A) The release rate of GM-CSF and CpG from the scaffold; GM-CSF-loaded scaffold recruits more neutrophils and DCs, but fewer macrophages than the blank scaffold. (B) The implantation of the vaccine scaffold improves the production of anti-cancer antibody; the location of implantation (near or far from the draining inguinal lymph nodes) influences the kinetics of antibody response, resulting in the difference in survival rates after 150 days. Reproduced with permission from ref. [209]	72
Figure 3.1. Morphology of amphiphilic molecules in water and oil mixture: (a) type 1 - w/o, (b) lamellar phase, (c) type 2 - o/w. The shaded area represents water. The image adapted from ref. [1]	100
Figure 3.2. Illustration of lyotropic lamellar mesophase, adapted from ref. [1]	101
Figure 3.3. Illustration of (a) hexagonal mesophase type 2 (H_2) side view and top view with lattice parameter α ; (b) ribbon mesophase type 2, centered configuration, with lattice parameters α and β . The figure is adapted from ref. [1].	102
Figure 3.4. Globular body-centered cubic (bcc) mesophase in an exploded view, each cell contains a micelle. The figure is adapted from ref. [1].	102
Figure 3.5. Morphology of type 2 cubic bicontinuous mesophases, the figure is adapted from ref. [3].	103
Figure 3.6. Morphology of mesh bicontinuous mesophases in tetragonal geometry, with the lattice parameters α and c . The figure is adapted from ref. [1].	104
Figure 3.7. Illustration of a sponge having folded continuous lipid bilayer, creating connected aqueous channels. The figure is adapted from ref. [5].....	104
Figure 3.8. Lyotropic lipid structures and examples of their particulate forms, only water-containing lipid particles are presented. Lipid lyotropic structure illustrations are adapted from ref. [11]. From left to right, cryo-EM images of a sponge particle [6], cubosome [7], α -gel emulsion [8], liposome [12], hexosome [9], and multiple emulsion [10] are adapted from the corresponding references.....	106

Figure 3.9. Janus lipid nanoparticles under Cryo-EM, figure adapted from ref. [13]..	107
Figure 3.10. α -gel based emulsion under Cryo-EM, the arrow points to the α -gel region, the star indicates the oil droplet, the figure is adapted from ref. [8].....	110
Figure 3.11. The main components of liposome (a) glycerolphospholipid, R1 and R2 are fatty acids, such as decanoic acid, lauric acid, palmitic acid, oleic acid, myristic acid, stearic acid, and erucic acid, R3 can be phosphatidylcholine (PC), phosphatidyl ethanolamine (PE), phosphatidyl serine (PS), phosphatidyl inositol (PI), phosphatidic acid (PA), phosphatidylglycerol (PG), and cardiolipin. (b) sphingomyelin and (c) cholesterol. The figure is adapted from ref. [22].....	111
Figure 3.12. The molecular structure of glycerol monooleate (GMO) and phytantriol (PHYT).....	115
Figure 4.1. Summary of responses (enthalpy ratio) from main effects	131
Figure 4.2. (a) DSC freezing and melting peaks of eutectic urea solution, (b) DSC freezing and melting peaks of urea solution in the sample (15 wt% Montane 60, 10% hydration rate, cocoa butter as lipid) which only had small urea solution droplet.....	131
Figure 4.3. w/o emulsion (10% hydration rate) made from mixture of cocoa butter, Montane 60 (15 wt%) and urea solution at (a) 80°C, (b) 45°C and (c) 25°C.....	132
Figure 4.4. S-WAXS spectra of cocoa butter, Montane 60, and 30% hydrated Montane 60.....	133
Figure 4.5. (a) S-WAXS spectra and (b) DSC signal in heating step of w/o emulsions made of cocoa butter (CB), Montane 60 (M60) and urea solution, each thermogram is an emulsion with different ratio of CB/M60. The hydration rate of M60 in all samples is the same (at 30%). In figure a, the sample CB/M60 = 1/0 contained only CB and was not hydrated. The dash arrow in figure b is only for eyes guidance.....	135
Figure 4.6. Structure of particles population found in nanoparticles fabricated in different conditions (a) CB/M60 = 1/0, T = 40°C – using as reference, (b) CB/M60 = 6/4, T = 40°C, (c) CB/M60 = 2/8, T = 85°C.....	138
Figure 4.7. S-WAXS spectra at different temperatures of ODA-containing emulsion (20 wt% Montane 60, 2 wt% ODA, and 78 wt% water). The emulsion was heated from 17°C to 71.8°C at 2°C/min (red curves), kept at 71.8°C for 5 minutes (orange curves) and cooled down to 25°C at 5°C/min (blue curves). Red dots indicate the peaks position.	140
Figure 4.8. The surface tension of SDS solution at different concentrations, error bars present the standard deviation calculated from 3 measurements.....	141

Figure 4.9. The saturated concentration of erythromycin in SDS solution, error bars present the standard deviation from 3 measurements.	142
Figure 4.10. Jellification of saturated erythromycin in 0.1 wt% SDS solution	142
Figure 5.1. Mass spectra of (a) Montane 60 and (b) Span 65	154
Figure 5.2. The retention time of different sorbitan esters detected in Montane 60.	155
Figure 5.3. The estimated composition of Montane 60 and Span 65 calculated from LC-MS peaks' area	156
Figure 5.4. Spontaneous hydration experiment shows (a) hydration rate of M60 grain over time (the error bars of hydration rate are from 0.5% - 1%, which is too small to be seen in the graph), (b) the photo of M60 grain in DI water after 3 days (left) and anhydrous M60 grain (right), (c) the SR μ CT photo of anhydrous M60 grain, (d) the SR μ CT photo of hydrated M60 grain, (e) the SR μ CT photo of lipid microsphere containing water domains as a comparison reference. The width of each view of SR μ CT photos is 1843 μ m	157
Figure 5.5. Structure of a fully hydrated M60 grain in comparison with an anhydrous M60 grain, the arrow shows the hydrated structure peak.....	158
Figure 5.6. SAXS spectrum of 20% hydrated Montane 60 as an example of peak identification	159
Figure 5.7. (a) S- and WAXS spectra at room temperature of anhydrous and Montane 60 hydrated by hot hydration method in DI water, (b) the evolution of the lamellar distance of Montane 60 with the hydration rate in DI water and in buffer pH5, (c) 80% hydrated M60 sample after ultra-centrifugation.	160
Figure 5.8. (a) SAXS spectra at different temperature of 20% hydrated Montane 60 as an example of the visualization, and S-WAXS spectra at different temperature of anhydrous and hydrated Montane 60 (b) H = 0%, (c) H = 20%, (d) H = 40%, (e) H = 60%, (f) H = 80%	164
Figure 5.9. (a) Lamellar distance of hydrated Montane 60 as the function of temperature and (b) the lamellar distance of hydrated Montane 60 at room temperature, before melted in comparison with the theoretical case, in which Montane 60 contains only hydrophilic structure. The lamellar distance of the theoretical case is the maximum lamellar distance that Montane 60 may have due to the hydration effect (i.e. the expansion due to water getting into the lamellar structure). Note: In figure b, the fit relation between the lamellar distance at room temperature (orange point) and the curve in theory (blue) is purely coincidental.	166

Figure 5.10. Illustration of Montane 60 structure	169
Figure 5.11. Size distribution and zeta potential of M60 microparticles (MPs) and nanoparticles (NPs), the sample dilution for DLS and zeta potential measurement reduces the SDS concentration to below its critical micelle concentration (CMC) point.	170
Figure 5.12. The S-WAXS spectra of (a) M60 MPs and (b) M60 NPs	171
Figure 5.13. (a) The change in the lamellar distances with different concentrations of SDS in M60 MPs and M60 NPs in different media; (b) the lamellar distance of 80% hydrated M60 in NaCl solution in comparison with the lamellar distance of M60 MPs in water. Note: the percentage of M60 is 20 wt% of the formulation.	173
Figure 5.14. Structure of M60 MPs stabilized by (a) 0.1% SDS, (b) 0.5% SDS, (c) 2% SDS at different temperatures	175
Figure 5.15. The increase in the lamellar distance versus temperature of M60 MPs stabilized by different SDS concentration	176
Figure 5.16. S-WAXS spectra of (a) M60 α -gel MPs stabilized by P90G at different concentrations, and (b) the structure of M60-2% P90G α -gel MPs at different temperatures.	177
Figure 6.1. The change in the structure of LNP during the fabrication process examined by S-WAXS.....	190
Figure 6.2. Cryo-TEM image of LNP-E1% in dilution condition. The nanoparticles do not contain chitosan.....	191
Figure 6.3. LNP loaded with erythromycin under a dark field optical microscope, the percentage of erythromycin in the formulation is (a) 0.5 wt%, (b) 1 wt%, (c) 2 wt% and (d) 4 wt%. The percentage of lipid in the formulation is 20%, the samples were not diluted. The large particles in figures a and b are dust.	192
Figure 6.4. Equilibrium of (a) SDS and (b) erythromycin in lipid particle suspension during the fabrication, when lipid mixture is in liquid form.....	194
Figure 6.5. S-WAXS spectra of lyophilized powder of solid lipid particles - chitosan nanocomposite containing both erythromycin and urea (PEU-C5).....	195
Figure 6.6. The SR μ CT images of LNP-C powder show the high porosity with different pore sizes.....	196
Figure 6.7. The release of particles from lipid nanoparticles - chitosan nanocomposite PEU-C5 in SGF pH5	197

Figure 6.8. (a) Cryo-TEM image of nanoparticles released from nanocomposite without chitosan (PEU-C0) after 30 minutes in SGF pH5 and (b) the internal structure of an aggregation of nanoparticles.....	198
Figure 6.9. The hydration behavior of PEU-C0 in SGF pH5.....	199
Figure 6.10. The release of erythromycin and urea from lipid particles - chitosan nanocomposite PEU-C5 in SGF pH5.....	200
Figure IV.1. Freeze-fracture transmission electron microscopy image of the α -gel structure of distilled saturated monoglycerides in water (25 : 75); figure adapted from ref. [3].....	208
Figure IV.2. (a) S-WAXS spectra of M60 hydrated with eutectic urea solution and (b) the lamellar distance in comparison with M60 hydrated with water	209
Figure IV.3. SR μ CT photo of solid lipid microsphere fabricated from Precirol and Montane 60 by the prilling method. The width of the view is 1843 μ m.....	210
Figure IV.4. (a) Configuration of the video-microscopy experiment, (b) the view of the microscope, the yellow arrow indicates the pipette tip, black spots are <i>H. pylori</i> , and (c) the image treatment method for quantification, figure adapted from ref. [5]	212
Figure IV.5. Photo from video-microscopy of <i>H. pylori</i> in interaction with the formulation containing only urea (PU-C0), (a) phase-contrast image at t=0, (b) the trace of bacteria in the view from 0 to 2s, (c) trace of bacteria in the view from 8 to 10s. The orange stars indicate the position of lipid particles.	213
Figure IV.6. Gradient soft agar swim plate assay configuration, oval shape colony indicates the response of bacteria to the plug, while round shape indicates that the bacteria are not sensitive to the chemoattractant.....	214
Figure IV.7. Chemotactic swarming experiments of <i>H. pylori</i> on agar gel, induced by (a) a blank gel plug button acting as a reference, (b) PB-C0 button, (c) PB-C5 button, (d) PU-C0 button, (e) PU-C5 button, (f) PEU-C0 button and (g) PEU-C5 button.	216

LIST OF TABLES

Table 4.1. Summary of the factors and their levels in the design of experiment	126
Table 4.2. Results summary of nanoparticles fabricated in different conditions	136
Table 4.3. Solubility of erythromycin in Montane 60 and cocoa butter at 85°C.....	143
Table 5.1. Composition of M60 particles	151
Table 6.1. Size and zeta potential of LNP in suspension (having 1 wt% erythromycin, in comparison to blank particles having 0 wt% erythromycin)	190
Table 6.2. Dosage of erythromycin inside and outside lipid particles, drug loading and encapsulation efficiency of LNP-E1% (LNP suspension having 1 wt% of erythromycin) before and after HPH, the errors are the standard deviation of measurements from 3 samples.....	194
Table 6.3. <i>H. pylori</i> strains description with data from Poitiers University Hospital ...	202
Table 6.4. MIC value of erythromycin in different nanocomposite formulations tested on 9 <i>H. pylori</i> strains	202
Table IV.1. Sample description of formulations used in chemotactic swarming experiments	215
Table IV.2. <i>H. pylori</i> strains used for chemotactic swarming experiments with data from Poitiers University Hospital	215

LIST OF ABBREVIATIONS

5-FU	5-fluorouracil
ACN	Acetonitrile
ADC	Antibody-drug conjugates
AGS cell	Adenocarcinoma epithelial cell
AHA	Acetohydroxamic acid
AMO	Amoxicillin
API	Active pharmaceutical ingredient
BabA / BabB	Blood group antigen-binding adhesin
BC	B-carotene
bcc	Body-centered cubic
BJO	<i>Brucea javanica</i> oil
CB	Cocoa butter
Chol	Cholesterol
CLA	Clarithromycin
CMC	Critical micelle concentration
CpG-ODN	Cytosine guanosine oligonucleotide
CPP	Critical packing parameter
Cryo-EM	Cryogenic electron microscopy
Cryo-SEM	Cryogenic scanning electron microscopy
Cryo-TEM	Cryogenic transmission electron microscopy
DCs	Dendritic cells
DNFB	Dinitrofluorobenzene
DoE	Design of experiment

DOX	Doxorubicin
DSC	Differential scanning calorimetry
DS ⁻	Dodecyl sulfate anion
<i>E. coli</i>	<i>Escherichia coli</i>
EE	Encapsulation efficiency
ESI	Electrospray ionization
EGCG	Epigallocatechin-3-gallate
EM	<i>E. coli</i> membrane
ERY	Erythromycin
EtOH	Ethanol
fcc	Face-centered cubic
GC	Gas chromatography
GFP	Green fluorescence protein
GM-CSF	Granulocyte-macrophage colony-stimulating factor
GMO	Glycerol monooleate
GP	Glycerolphospholipid
<i>H. pylori</i>	<i>Helicobacter pylori</i>
H _{corr}	Corrected hydration rate
HLB	Hydrophilic-lipophilic balance
HPH	High-pressure homogenization
HPLC	High-performance liquid chromatography
Hsp60	Heat shock protein 60
H-α	Hexagonal alpha
IARC	International Agency for Research on Cancer

ID50	50% infectious dose
IPA	Isopropanol
LC-MS	Liquid chromatography-mass spectrometry
LNP	Lipid nanoparticles
LNP-C	Lipid nanoparticle–chitosan
LOD	Limit of detection
LOQ	Limit of quantification
M60	Montane 60
MET	Metronidazole
MIC	Minimum inhibitory concentration
MIP	Macrophage inflammatory protein
MPs	Microparticles
MRI	Magnetic resonance imaging
MS	Mass spectrometry
MSN	Mesoporous silica nanoparticles
NAP	Neutrophil activating protein
NPs	Nanoparticles
o/w	Oil-in-water
ODA	1-octadecylamine
OXA	Oxaliplatin
P90G	Lecithin phospholipon 90g
PA	Phosphatidic acid
PC	Phosphatidylcholine
PDI	Polydispersity index

PE	Phosphatidyl ethanolamine
PEG	Polyethylene glycol
PG	Phosphatidylglycerol
PHYT	Phytantriol
PI	Phosphatidyl inositol
PLGA	Poly(lactic-co-glycolic acid)
PPI	Proton-pump inhibitor
PS	Phosphatidyl serine
sabA / sabB	Sialic acid binding protein
SAXS	Small-angle X-ray scattering
SDS	Sodium dodecyl sulfate
SEM	Scanning electron microscopy
SGF	Simulated gastric fluid
SLN	Solid lipid nanoparticles
SM	Sphingomyelin
SR μ CT	Synchrotron radiation computed microtomography
STP	Syrmep tomo project
S-WAXS	Small- and wide-angle X-ray scattering
tdT	Tdtomato
TET	Tetracycline
THF	Tetrahydrofuran
TIN	Tinidazole
TRAIL	Tumor necrosis factor-related apoptosis-inducing ligand
VEGF	Vascular endothelial growth factor

LIST OF ABBREVIATIONS

w/o	Water-in-oil
w/o/w	Water-in-oil-in-water
WAXS	Wide-angle X-ray scattering
WHO	World Health Organization

I. GENERAL INTRODUCTION

Helicobacter pylori (*H. pylori*) is a bacterium that lives inside the human stomach. 50% of the world's population is infected with *H. pylori* [1]. A small percentage of infected patients develop duodenal and gastric ulcers, ultimately leading to gastric cancer. *H. pylori* has been classified as carcinogen class 1 since 1994 by International Agency for Research on Cancer (IARC), and in the World Health Organization (WHO) list of high priority for the R&D of antibiotics in 2017 [2,3]. However, the eradication rate of *H. pylori* nowadays is only 70%-75%, despite the use of a high dose of antibiotics [4,5]. Therefore, urgent research about the treatment of *H. pylori* is necessary.

The difficulty in *H. pylori* treatment is due to the location of the bacteria and its survival capacity. For example, because the site of action of antibiotics is in the stomach, the use of a proton pump inhibitor to reduce the pH in the stomach is necessary to enable the activity of antibiotics [6]. *H. pylori* evolved to well adapt to the gastric acid environment. To survive in acid media, *H. pylori* has a high quantity of urease, which is an enzyme that degrades urea to create CO₂ and NH₃ to create a buffer environment around its body [7]. It has chemotaxis behavior away from acid and toward urea, meaning that it can detect acid and urea, and run away from the acid gradient and move toward the urea gradient [7]. The detection of urea also helps it to localize gastric epithelium. After the localization of gastric epithelium, *H. pylori* attaches to gastric cells via the action of adhesins and colonizes gastric glands [7]. The virulence factors of *H. pylori* are illustrated in Figure I.1.

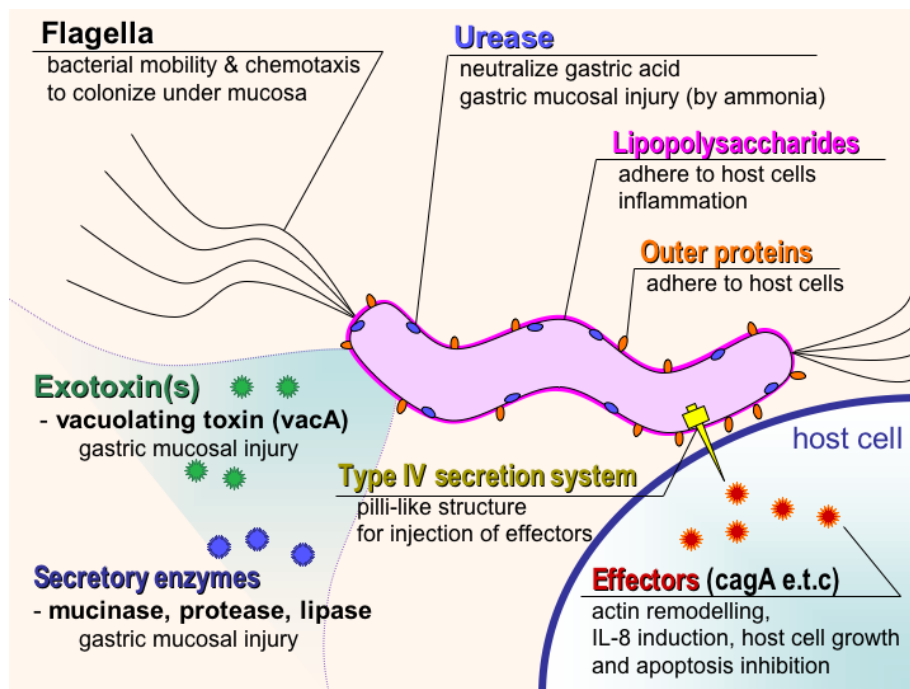


Figure I.1. Schematic of *H. pylori* structure and its virulence factors; the figure is adapted from ref. [8].

To facilitate the activity of antibiotics and improve the *H. pylori* treatment efficiency, we fabricate an innovative lipid nanoparticle formulation that targets the survival factors of *H. pylori* in the stomach. The nanoparticles contain erythromycin, a hydrophobic antibiotic, and urea, a hydrophilic molecule. The use of nanoparticles facilitates the penetration of the formulation into the mucus layer, where the bacteria locate. The urea creates a urea gradient to attract *H. pylori* towards the nanoparticles and facilitate the meeting between the nanoparticles and the bacteria. Erythromycin is released around the buffered environment around the bacteria. The formulation contains a chitosan coating, which adheres to the gastric mucus layer, promoting the retention of the formulation in the stomach. In addition, the chitosan also adheres to the bacteria, serving as an active targeting strategy.

In this doctoral thesis, we have 2 parts: the bibliographic and the experimental parts. In the bibliographic part, we will analyze the survival factors of *H. pylori* and address *H. pylori* treatment formulations in the literature that target those factors. Then, as a base for our chemotaxis-based formulation, we will analyze targeted therapies that mimic or use the natural taxes of microorganisms. Finally, we explore methods and existing formulations that co-encapsulate both hydrophilic and hydrophobic compounds in lipid particles. In the experimental part, using the literature review information in the bibliography part, we present the fabrication of lipid particle formulation from the pre-formulation step to *in vitro* test of the final products. We will first discuss the choice of materials and formulation strategy. Then we present the analysis of the main materials to understand the mechanism of drug loading. In the last chapter, we report the fabrication of the formulation and investigate its antimicrobial activity *in vitro*.

References

- [1] J. Calam, J.H. Baron, ABC of the upper gastrointestinal tract: Pathophysiology of duodenal and gastric ulcer and gastric cancer, *BMJ*. 323 (2001) 980–982. <https://doi.org/10.1136/bmj.323.7319.980>.
- [2] WHO publishes list of bacteria for which new antibiotics are urgently needed, (n.d.). <https://www.who.int/news/item/27-02-2017-who-publishes-list-of-bacteria-for-which-new-antibiotics-are-urgently-needed> (accessed September 30, 2022).
- [3] I.F.N. Hung, B.C.Y. Wong, Assessing the risks and benefits of treating *Helicobacter pylori* infection, *Ther. Adv. Gastroenterol.* 2 (2009) 141–147. <https://doi.org/10.1177/1756283X08100279>.
- [4] Y. Tang, G. Tang, L. Pan, H. Zhu, S. Zhou, Z. Wei, Clinical factors associated with initial *Helicobacter pylori* eradication therapy: a retrospective study in China, *Sci. Rep.* 10 (2020) 15403. <https://doi.org/10.1038/s41598-020-72400-0>.

- [5] E.A. Argueta, S.F. Moss, How We Approach Difficult to Eradicate *Helicobacter pylori*, *Gastroenterology*. 162 (2022) 32–37. <https://doi.org/10.1053/j.gastro.2021.10.048>.
- [6] S. Suzuki, C. Kusano, T. Horii, R. Ichijima, H. Ikehara, The Ideal *Helicobacter pylori* Treatment for the Present and the Future, *Digestion*. 103 (2022) 62–68. <https://doi.org/10.1159/000519413>.
- [7] C.-Y. Kao, B.-S. Sheu, J.-J. Wu, *Helicobacter pylori* infection: An overview of bacterial virulence factors and pathogenesis, *Biomed. J.* 39 (2016) 14–23. <https://doi.org/10.1016/j.bj.2015.06.002>.
- [8] File:H pylori virulence factors en.png - Wikimedia Foundation Governance Wiki, (n.d.). https://commons.wikimedia.org/wiki/File:H_pylori_virulence_factors_en.png (accessed October 12, 2022).

II. BIBLIOGRAPHIC PART

Chapter 1. <i>Helicobacter pylori</i> survival factors and treatment.....	30
Chapter 2. Targeted drug delivery therapies inspired by natural taxes.....	47
Chapter 3. Lyotropic lipid particles formulation for co-encapsulation of both hydrophilic and lipophilic drugs.....	99

Chapter 1. *Helicobacter pylori* survival factors and treatment

Hung V. Nguyen, Vincent Faivre

Université Paris-Saclay, CNRS, Institut Galien Paris-Saclay, 5 rue JB Clément, 92296 Châtenay-Malabry, France.

1. *Helicobacter pylori* survival factors in the stomach

Helicobacter pylori (*H. pylori*) is a spiral-shaped, gram-negative bacterium colonizing in human stomach (Figure 1.1). More than 50% of the human population is infected with *H. pylori* [1]. In detail, the regions having the highest *H. pylori* prevalence are Africa (70.1%), South America (69.4%) and Western Asia (66.6%) [2]. The lowest prevalence regions are Oceania (24.4%), Western Europe (34.3%), and Northern America (37.1%) [2]. The high prevalence is generally related to the low hygienic living condition, explaining the high prevalence in developing regions [2]. The main route for *H. pylori* spreading is intrafamilial transmission [2]. *H. pylori* is responsible for about 89% of gastric cancer cases worldwide, and since 1994, International Agency for Research on Cancer (IARC) has categorized *H. pylori* as carcinogen class 1 [2,3]. Besides, it is also a casual cause of peptic, gastritis, duodenal ulcers, and mucosal-associated lymphoid tissue lymphoma [4,5]. If the eradication treatment is not completed, *H. pylori* stays in the human stomach forever by lying around a few hundred microns away from the low pH lumen and making niches in the stomach mucosa [6].



Figure 1.1. The morphology of *H. pylori* is shown under scanning electron microscopy (SEM). The scale bar represents 0.5 μm [7].

1.1. Acid neutralization to survive in the acid environment

To survive in the human stomach, *H. pylori* has mechanisms to neutralize the high acidity of the stomach and to escape to neutral pH regions. *H. pylori* adapts to the highly acidic environment in the stomach by regulating the activity of urease, which is an enzyme that catalyzes the degradation of urea into NH_3 and CO_2 [4]. Because of the activity of urease, a buffer environment having lower acidity than the stomach lumen is created in the cytoplasm and periplasm of the bacterium. The urease of *H. pylori* can be found on the surface (extracellular) or inside (intracellular) of the bacterium. Intracellular urease increases the acid resistance of *H. pylori* and is regulated by the activity of the proton-gated urea channel Urel, which is situated in the inner membrane [4]. Urel channel controls the diffusion of urea and is fully open at pH 5 and close at pH 7, preventing the death of *H. pylori* during neutral pH periods due to the alkalization [8]. In highly acidic conditions, Urel is fully open, letting urea to penetrate into the bacterium. Then, under the activity of urease, *H. pylori* produces NH_3 and/or NH_4^+ , which are both extruded via the Urel channel to neutralize H^+ in the periplasm [8]. Extracellular urease of *H. pylori* also breaks down urea to CO_2 and NH_3 , creating a neutral micro-environment around the bacterium, helping it to swim through the gastric juice. Interestingly, besides the role of acid neutralization, urease also controls the interaction of *H. pylori* and macrophages via the regulation of the pH of phagosome and megasome formation, which are important for the survival of *H. pylori* inside macrophages.

1.2. Chemotactic behavior to colonize in the mucosa layer

H. pylori high mobility is originated from its flagella and chemosensor system, which are essential for the ability of colonization in gastric mucosa, where the pH is around 7 [9]. The bacterial density is higher in patients infected with higher motility *H. pylori* strain, leading to a higher inflammatory response [10]. In addition, in the non-chemotactic mutant *H. pylori* strain, whose chemotactic signal regulator proteins CheW, CheA or CheY are deactivated, the 50% infectious dose (ID_{50}) is approximately 200 times higher than the ID_{50} of the wild strain [11]. Some groups even found that the non-chemotactic mutant *H. pylori* strain did not infect the host's stomach [11,12]. However, over a long period, at a high dose, the non-chemotactic mutant strain was able to colonize and survive in host's stomach for up to 6 months like the wild strain [11]. The chemosensor system includes the chemoreceptors TlpA, TlpB, TlpC and TlpD, and the signal regulator protein CheA kinase, which is coupled by the CheW coupling protein, and CheY response regulator [12]. The CheW protein acts as a scaffold protein that connects the chemoreceptors with CheA to control the kinase activity. The rotation direction of the flagella is controlled by the state of phosphorylation of CheY, which is influenced by the activity of CheA kinase [12]. For example, in the presence of a chemoattractant, the activity of CheA is quenched. Hence, the amount of non-phosphorylated CheY dominates the amount of phosphorylated CheY (CheY-P). In this situation, CheY cannot

bind to the flagella switch, leading to the counterclockwise rotation of bacteria flagella, pushing the bacteria toward the source of the signal. Meanwhile, in the absence of chemoattractants, CheY is phosphorylated by CheA to become CheY-P, which binds to the flagella switch, turning the flagella clockwise for the bacteria to change the moving direction.

Among 4 chemoreceptors of *H. pylori*, TlpA, TlpB, TlpC are integral membrane proteins, while TlpD is a soluble receptor. TlpA contributes to the positive chemotaxis toward arginine and bicarbonate, and to the negative chemotaxis toward H⁺ [13–15]. Since bicarbonate is secreted from gastric epithelial cells in a process related to local pH neutralization, the positive chemotactic movement of *H. pylori* toward the bicarbonate source helps it to find and to colonize the gastric mucus [13]. On the other hand, arginine is an essential amino acid that *H. pylori* cannot synthesize itself [13]. In addition, arginine is also a substrate for the urea cycle, which plays a vital role in acid neutralization via the production of urea – the substrate of urease, creating a buffer environment for *H. pylori* [14]. Both TlpA and TlpD are acid sensors; however, they work independently and can maintain the ability to avoid acid in case one of them is inactivated [15]. Besides inducing negative chemotaxis toward H⁺, TlpD is also responsible for the positive chemotaxis toward the basic pH environment [15]. While TlpA is an integral membrane protein, TlpD is a cytoplasmic protein; thus, it senses the external pH gradient indirectly. Interestingly, Huang et al. have shown that the sensitivity of detecting HCl of TlpD is higher than that of TlpA [15]. In addition to running away from acidic regions, *H. pylori* also breaks down urea to neutralize the acid around its body. Hence, they have the ability to sense urea and then to swim to high urea concentration regions, thanks to the presence of TlpB receptor (Figure 1.2) [16]. *H. pylori* simultaneously senses and destroys urea, helping it to neutralize acid while finding its way to the urea source, which is the gastric epithelial layer [16]. Lastly, TlpC has been shown to be responsible for sensing lactate as a chemoattractant [17]. Lactate promotes the growth of *H. pylori*, and serves as a carbon or energy source [18,19].

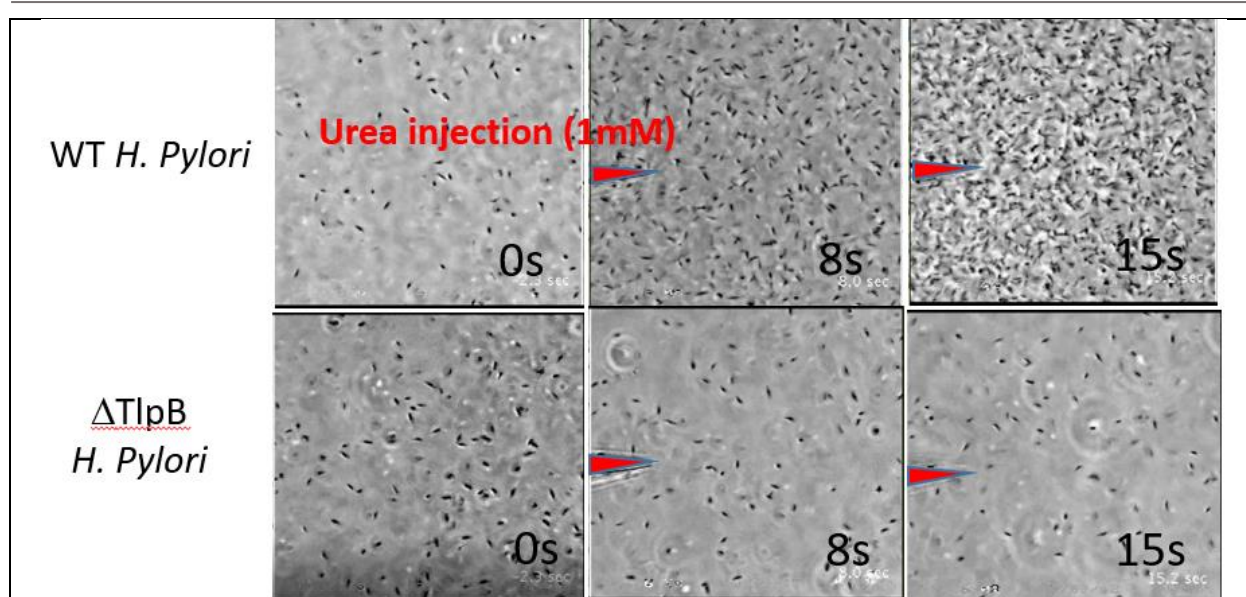


Figure 1.2. *H. pylori* swims toward the urea gradient thanks to the TlpB receptor, figure adapted from ref. [16].

The flagella of *H. pylori* are made of the hook-basal structure and extracellular filament [12]. The hook-basal structure contains several proteins to control the rotation of the flagellum, such as FlhG, FlhM and FlhN. FlhG is the rotor component, which turns the direction of rotation (clockwise or counterclockwise) of the flagellum, depending on the chemotaxis signal [12]. Meanwhile, FlhM and FlhN bind to the chemotaxis response regulator phosphorylated-CheY (CheY-P), which decides the direction of rotation of the flagellum [12]. The hook-basal structure also provides energy for the rotation via the protein MotA and MotB. These 2 proteins create the stator component and a proton channel, which link the flow of proton and generation of torque for flagellum rotation [12]. Because the motor is powered by proton motive force, *H. pylori* swimming speed is optimal at low pH, helping it to escape from highly acidic regions [14]. The filament is important for the mobility of bacteria. It is created from the major flagellin FlaA and the minor flagellin FlaB [12].

1.3. Adhesin for attachment and persistent infection

After reaching the mucosal layer of the stomach, *H. pylori* interacts with epithelial cells using adhesin on its surface. This interaction anchors *H. pylori* to the epithelial layer, protecting it from the fluctuation of the stomach contraction force [4]. *H. pylori* possesses blood group antigen-binding adhesin (BabA and BabB). BabA binds to fucosylated Lewis B (Le^b) blood group antigen expressed on host gastric epithelial cells [20]. The BabA-Le^b interaction is stable and persistent in chronic human infection cases [4]. The density of *H. pylori* is largely dependent on the density of Le^b on the gastric epithelial lining [21]. Interestingly, BabA increases the risk of peptic ulcer and gastric cancer in Western countries; however, it is not associated with gastric-related diseases in Asian countries [4]. While the role of BabB is not clear, its expression correlates with the increase in gastric lesions in patients [4]. Another protein that helps *H. pylori* in the

colonization and adhesion to the epithelial cells is sialic acid binding protein (sabA and sabB) [4]. The function of sabB remains unclear, while sabA has been identified to bind with sialyl-Lewis x glycosphingolipid (sLe^x) antigen on epithelial cell surface [4]. While all babA-genopositive *H. pylori* express BabA, only 80% of them are sabA-genopositive and 31% of them express sabA [21]. Though the interaction between BabA-Le^b is the major factor that influences the colonization of *H. pylori*, the sabA-sLe^x interaction is compulsory to keep high *H. pylori* density in patients with low Le^b expression [21]. However, once the Le^b expression is strong, the sabA-sLe^x interaction has little impact on the *H. pylori* density [21].

Adhesion of *H. pylori* triggers the host's immune response and causes inflammation in the host's stomach. Neutrophil activating protein (NAP) of *H. pylori* stimulates oxygen radical production of neutrophils and promotes the adhesion of neutrophils to stomach epithelial cells, damaging local tissues [22]. Moreover, NAP also makes neutrophils to release IL-8 and macrophage inflammatory protein (MIP), causing inflammation [4]. The major receptor that interacts and binds with NAP of *H. pylori* is the glycosphingolipids expressed on the surface of neutrophils [23]. Besides the adhesion application, NAP also defends *H. pylori* DNA from damage, because of NAP ability to bind to DNA, preventing the attack of free radicals [4]. Another *H. pylori* protein provoking immune response is the heat shock protein 60 (Hsp60). Hsp60 induces the production of IL-6, IL-8, tumor necrosis factor from gastric epithelial cells [24]. Moreover, the antibody of Hsp60 is frequently detected in *H. pylori*-infected gastric cancer patients, associating Hsp60 with gastric carcinogenesis [25].

To live and stay persistently in the stomach, *H. pylori* uses the gastric gland as a micro-niche to hide and get protection from gastric acid (Figure 1.3) [26]. The shredding and ascending of gastric gland cells help bringing bacteria-associated cells to the epithelium surface, spreading the bacteria to other glands throughout the stomach. The bacteria staying inside the gland continue to grow and replenish the micro-niche to compensate for the number of bacteria attaching to gastric gland cells to the epithelium surface [26]. This continuous process expands the bacteria's territory. The gland-associated bacteria do not want to mix with the free-swimming bacteria in the mucus layer. They compete for space in the gland and prevent newcomers from entering their established niches (Figure 1.3). The ability to colonize gastric glands is essential for the persistent infection. While they are in the gland, they are affected by the activity of host T-cells. T-cells' response may reduce the bacterial density inside gastric glands. In chronic infections, *H. pylori* may induce the suppression of T-cell response to promote the infection persistence in the gland.

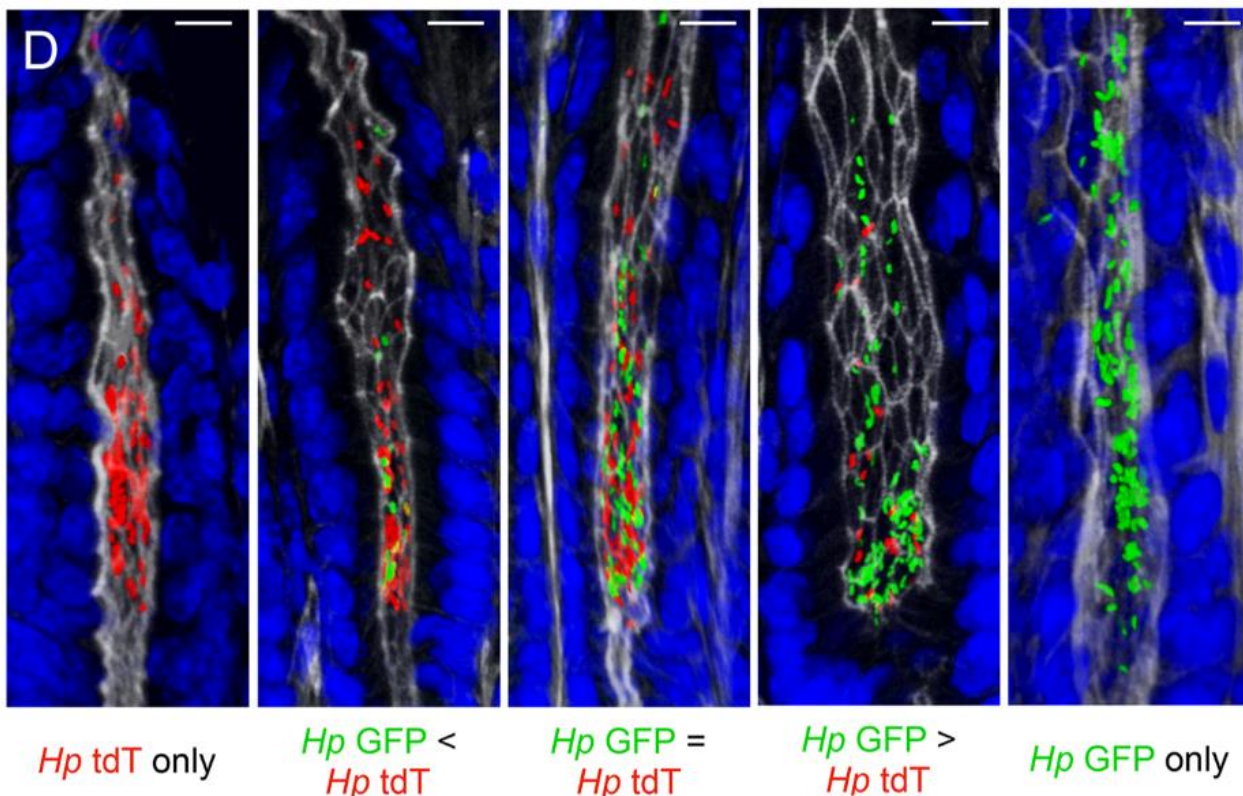


Figure 1.3. Mice's gastric glands were co-infected with 2 different labelled (green fluorescence protein – GFP and tdTomato – tdT) *H. pylori* strains. Images showed that different *H. pylori* strains compete for niches in gastric glands. The scale bar represents 10 μm [26].

2. Treatment of *Helicobacter pylori*

2.1. Current clinical treatments of *H. pylori* infection

The treatment of *H. pylori* is the combination of antibiotics, such as clarithromycin (CLA), amoxicillin (AMO), metronidazole (MET), tetracycline (TET) or tinidazole (TIN), with a proton-pump inhibitor (PPI) [27]. Several guidelines recommend the application of a triple therapy consisting of a PPI, CLA and AMO or PPI, CLA and MET in low clarithromycin resistance areas [28]. In high CLA resistance areas, the treatment is more complicated. The first-line therapy in high CLA resistance areas includes the use of 10-14 days of bismuth quadruple therapy (PPI, bismuth salt, 2 types of antibiotics such as MET and TET) and the use of 10-14 days of non-bismuth concomitant therapy (PPI and 3 types of antibiotics, usually AMO, MET and CLA). Both mentioned first-line therapies results in >90% of eradication rate in Europe [28]. In Asia, while China recommends 10-14 days of bismuth quadruple therapy as the empiric treatment, Korean and Japan still use triple therapy as the first-line treatment [28]. In 2015 in Japan, vonoprazan – a new gastric acid suppressant, has been launched. The triple therapy having vonoprazan, AMO and CLA, has an eradication rate of 93% in a clinical trial [29]. So, the 7-day vonoprazan-based triple therapy has been widely practiced in Japan as the primary treatment [30].

While providing a sufficient eradication rate, the current treatment of *H. pylori* has some limitations. The broad use of antibiotics leads to antibiotic resistance, which is already a problem with *H. pylori* treatment [31]. The World Health Organization (WHO) classified *H. pylori* as high priority for the research and development of antibiotics in 2017 [32]. The application of multiple antibiotics in the treatment increases the risk of antibiotic resistance to several types of antibiotics. Another problem is the dysbiosis of gut microbiota due to *H. pylori* treatment. Both PPI and antibiotics can influence importantly the function of gut microbiota, therefore, contribute to the change in metabolism and digestion after the eradication of *H. pylori* [28]. In a randomized trial, both alpha and beta diversity of gut microbiota in patients treated with concomitant therapy and bismuth quadruple therapy were not fully recovered after 1 year [33]. Therefore, new treatments for *H. pylori* are needed to reduce the dose of antibiotics by local delivery of drugs and targeting the bacteria directly in the stomach.

2.2. Current drug delivery strategies for *H. pylori* treatment in research

The current research about *H. pylori* treatments focuses on the delivery of drugs or nanoparticles directly to the bacteria in the stomach to reduce the required amount of antibiotics and to increase the treatment efficiency. In general, the strategies are gastroretentive system to improve retention time in the stomach, micro and nanotechnology to improve the penetration into mucus layer and to replace the use of antibiotics in case of metallic nanoparticles. Since the start of this doctoral project in October 2019, several comprehensive literature reviews about drug delivery systems for *H. pylori* treatment have been published [34–38], and we recommend readers these reviews for more details. In the frame of our project, we review recent drug delivery systems taking advantage of *H. pylori* survival factors mentioned above to eliminate them.

Since *H. pylori* takes advantage of the gastric mucus layer to hide from acid, mucoadhesive systems adhere directly to this location to deliver antibiotics [39–46]. Thombre and Gide reported the fabrication of a core-shell polymer beads having bio-adhesion property to eliminate *H. pylori* [39]. The shell is chitosan to facilitate the adhesion to the gastric mucus. The core is made of *Caesalpinia pulcherrima* galactomannan (a natural polymer)-alginate to load amoxicillin. The developed beads had a mucoadhesion efficiency *in vitro* of 61-89% and *in vivo* of 85% after 7 hours. The beads showed the inhibition of *H. pylori in vitro*. The elimination of the bacteria in the rat model was also achieved, however, only after 10 weeks of treatment. Similarly, in another research, by using chitosan as a mucoadhesive polymer, furazolidone-loaded chitosan microparticles were fabricated using spray drying techniques [40]. While the glutaraldehyde was used as the crosslinking agent to strengthen the chitosan stability in acid media, the high concentration of glutaraldehyde reduced the mucoadhesive efficiency. After optimization, the chitosan microparticles had the mucoadhesion efficiency after 6 hours of 87% at pH 4.5 and 60% at pH 1.2. The drug release was almost

immediate in pH 1.2 and could only be sustainable over 5h in pH 4.5. So, the optimal pH for the activity of chitosan microparticles in this report was 4.5. In addition to the mucoadhesive property, chitosan can adhere to the *H. pylori* membrane (illustrated in Figure 1.4) [47–49]. *In vitro* experiments showed that the chitosan microsphere can adhere to the *H. pylori* adhesin BabA and SabA [47]. The addition of chitosan microsphere to gastric cells pre-incubated with *H. pylori* reduced the adhesion of bacteria to cells [47]. Moreover, chitosan microparticles reduced the amount of *H. pylori* in the mice model by 88% after 14 days of treatment [48].

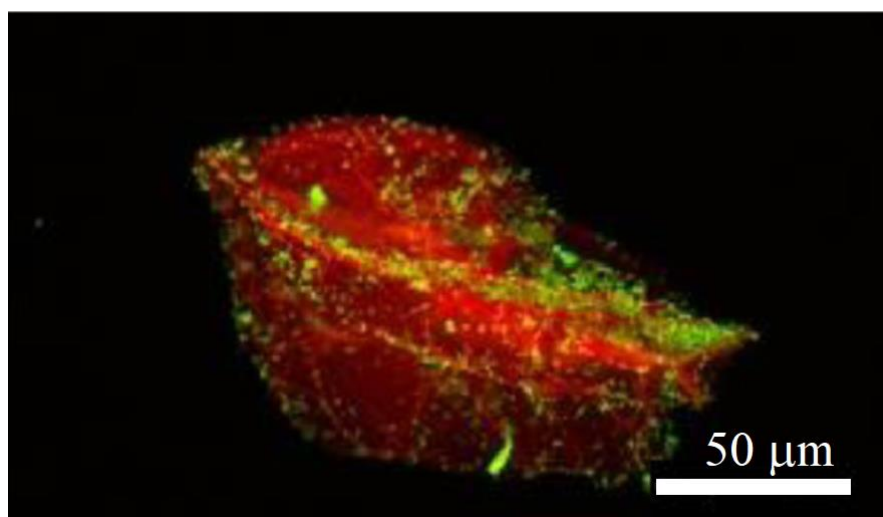


Figure 1.4. *H. pylori* (green) adheres to a chitosan bead (red), photo taken under confocal microscopy, figure adapted from ref. [48].

Besides chitosan, Carbopol 943P was also used frequently as the mucoadhesive polymer [42,44]. For example, Hardenia et al. reported the fabrication of polymer microparticles from Carbopol 934 and ethyl cellulose [42]. Amoxicillin – an antibiotic and famotidine – histamine H₂-receptor antagonist, usually for gastric ulcer treatment, were co-loaded inside the polymer microparticles, aiming to treat gastric ulcers and *H. pylori* at the same time. The bacteria elimination efficiency *in vivo* of the polymer microparticles was twice higher than the amoxicillin solution. The mucoadhesive efficiency *in vivo* of the polymer microparticles was 80% after 1h and remained at 74% after 10h, indicating the high retention and treatment efficiency of the formulation. Similarly, in another report, amoxicillin and clarithromycin were co-loaded inside polymer microparticles [44]. The polymer particles were made from Carbopol 974P, HPMC K4M and Eudragit RS 100 and had the mucoadhesive property. Interestingly, the *in vivo* experiment showed that after 3 days of treatment, the eradication rate of rats treated by the polymer microparticles was 100%, while it was only 60% for rats treated with the solution of antibiotic. While the mucoadhesive property was not demonstrated, the formulation helped to increase the treatment efficiency of antibiotics.

Taking advantage of the receptor on the membrane of *H. pylori*, several targeting drug delivery systems have been reported, with the idea to increase the interaction between the bacteria and drug carriers, adhering the carriers to the bacteria and increasing the bacteria elimination efficiency [50–57]. Targeting the urea-transporting protein UreI, ureido-conjugated chitosan nanoparticles had been prepared using sodium tripolyphosphate as crosslinking agent [51]. Amoxicillin was chosen as the antibiotic to load inside the ureido-conjugated chitosan nanoparticles. In an experiment, *H. pylori* was incubated in media containing both the ureido-conjugated chitosan nanoparticles and urea. The result showed ureido-conjugated chitosan nanoparticles could be recognized by the urea-transporting protein UreI of the bacteria, however, could not compete with urea. While the drug-loaded ureido-conjugated chitosan nanoparticles had higher elimination efficiency than unmodified drug-loaded chitosan nanoparticles, the competition of urea reduced the antibacterial efficiency of the ureido-conjugated chitosan nanoparticles. In another report of the same group, an *in vivo* experiment showed that after 7 days of treatment with amoxicillin ureido-conjugated chitosan nanoparticles, the CFU of *H. pylori* in mice model reduced 10 times compared to mice treated with PBS buffer [50].

Targeting the carbohydrate receptor of *H. pylori*, gliadin nanoparticles coated with lectin were reported to bind to the bacteria and inhibit the binding of bacteria to human gastric cells [53]. Acetohydroxamic acid (AHA) was used as the drug to load inside the gliadin nanoparticles, due to its urease inhibition activity, leading to the prevention of *H. pylori* development [53]. The AHA-loaded lectin-conjugated gliadin nanoparticles showed an increase in the bacterial inhibition efficiency compared to AHA-loaded nanoparticles that did not have lectin.

Targeting the BabA adhesin, pectin-coated liposome was reported to bind to the membrane of *H. pylori* and bind to the gastric mucus layer, demonstrating both the active targeting and mucoadhesive properties (Figure 1.5) [54]. Amoxicillin was used as the antibiotic to load inside the liposome. The pectin-coated liposome could inhibit the development of the bacteria *in vitro* and showed the adhesion to the bacteria under confocal microscopy. However, in simulated gastric fluid, with the presence of pepsin and low pH, the pectin coating was not stable and came out of the liposome.

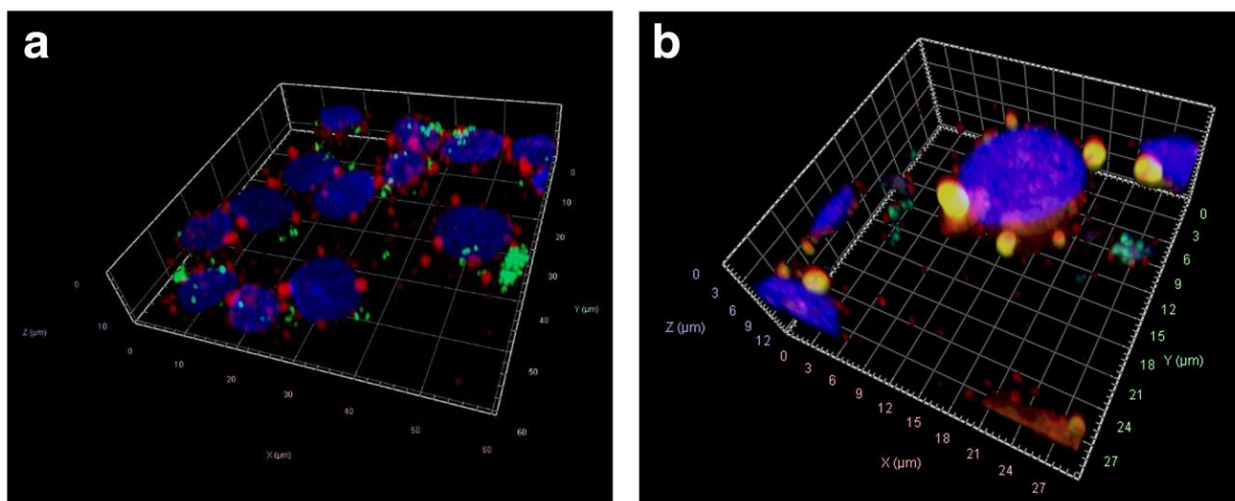


Figure 1.5. 3D reconstruction confocal laser scanning microscopy images of adenocarcinoma epithelial (AGS) cells infected by *H. pylori* incubated with (a) uncoated liposome and (b) pectin-coated liposome. AGS cell's DNA is blue, *H. pylori* is green, liposome is red. The overlap of green and red in figure b shows the interaction between pectin-coated liposome and *H. pylori*. The figure is adapted from ref. [54].

Using directly gastric epithelial cell membrane as the coating for polymer nanoparticles, Angsantikul et al. made biomimetic poly(lactic-co-glycolic acid) (PLGA) nanoparticles that could adhere to the bacteria naturally [57]. The coating of the gastric cell membrane helped increase the interaction between nanoparticles with the bacteria, visualized by confocal microscopy. Clarithromycin could be loaded inside the PLGA nanoparticles. An *in vivo* experiment showed that after 5 days of administration of cell membrane coated nanoparticles and PPI, the number of bacteria in the treated group was 3 times lower than the untreated group. Interestingly, this research group also fabricated *H. pylori* membrane coated PLGA nanoparticles, aiming to compete with the *H. pylori* in the stomach and prevent them from sticking to gastric epithelial cells [56]. While this is not an active targeting formulation, the idea is interesting. However, the bacterial membrane coated nanoparticles needed to be administered before the addition of bacteria to have a better effect. In the case of co-administration of bacteria membrane coated nanoparticles and bacteria, to have similar competition and inhibition effects to the nanoparticles pre-administrated case, the concentration of nanoparticles needed to be increased 10 times.

3. Conclusion

In summary, *H. pylori* evolved and developed several survival factors to survive in the human stomach. It can neutralize the acid by degrading urea using urease to create a buffer environment around it. It can sense and swim toward urea, while avoiding acid, to find the gastric epithelial layer. In contact with the mucus layer, it penetrates through the mucus layer and then attaches to gastric epithelial cells. To establish the persistent infection, the bacteria form niches in gastric glands. When the gastric epithelial cells

shred, some bacteria follow to the surface and colonize other glands. The interaction between *H. pylori* and the gastric glands promotes inflammation, leading to gastric ulcers, and may lead to gastric cancer in long-term infection patients.

Taking advantage of *H. pylori* survival factors, several drug delivery systems have been fabricated. Some systems use mucoadhesive polymers to stick to the mucus layer and improve the retention time of the antibiotics carrier in the stomach. Other systems target receptors on the surface of the bacteria to adhere the drug carriers on the bacterial membrane. However, to our knowledge, there is not any system that uses the chemotaxis behavior of *H. pylori* to attract it to the drug carriers. In the following chapter, we will review and analyze targeted drug delivery systems in the literature that mimic or use the natural taxis behavior of micro-organisms.

References

- [1] D.M. Parkin, International variation, *Oncogene*. 23 (2004) 6329–6340.
<https://doi.org/10.1038/sj.onc.1207726>.
- [2] J.K.Y. Hooi, W.Y. Lai, W.K. Ng, M.M.Y. Suen, F.E. Underwood, D. Tanyingoh, P. Malfertheiner, D.Y. Graham, V.W.S. Wong, J.C.Y. Wu, F.K.L. Chan, J.J.Y. Sung, G.G. Kaplan, S.C. Ng, Global Prevalence of *Helicobacter pylori* Infection: Systematic Review and Meta-Analysis, *Gastroenterology*. 153 (2017) 420–429.
<https://doi.org/10.1053/j.gastro.2017.04.022>.
- [3] I.F.N. Hung, B.C.Y. Wong, Assessing the risks and benefits of treating *Helicobacter pylori* infection, *Ther. Adv. Gastroenterol.* 2 (2009) 141–147.
<https://doi.org/10.1177/1756283X08100279>.
- [4] C.-Y. Kao, B.-S. Sheu, J.-J. Wu, *Helicobacter pylori* infection: An overview of bacterial virulence factors and pathogenesis, *Biomed. J.* 39 (2016) 14–23.
<https://doi.org/10.1016/j.bj.2015.06.002>.
- [5] J. Calam, J.H. Baron, ABC of the upper gastrointestinal tract: Pathophysiology of duodenal and gastric ulcer and gastric cancer, *BMJ*. 323 (2001) 980–982.
<https://doi.org/10.1136/bmj.323.7319.980>.
- [6] A. Debraekeleer, H. Remaut, Future perspective for potential *Helicobacter pylori* eradication therapies, *Future Microbiol.* 13 (2018) 671–687.
<https://doi.org/10.2217/fmb-2017-0115>.
- [7] H.L.T. Mobley, G.L. Mendz, S.L. Hazell, eds., *Helicobacter pylori: physiology and genetics*, ASM Press, Washington, DC, 2001.
- [8] D.R. Scott, E.A. Marcus, Y. Wen, S. Singh, J. Feng, G. Sachs, Cytoplasmic Histidine Kinase (HP0244)-Regulated Assembly of Urease with Urel, a Channel for Urea and

Its Metabolites, CO₂, NH₃, and NH₄⁺, Is Necessary for Acid Survival of *Helicobacter pylori*, *J. Bacteriol.* 192 (2010) 94–103. <https://doi.org/10.1128/JB.00848-09>.

- [9] J. Seong Kim, J. Hoon Chang, S. Il Chung, J. Sun Yum, Molecular Cloning and Characterization of the *Helicobacter pylori* *fliD* Gene, an Essential Factor in Flagellar Structure and Motility, *J. Bacteriol.* 181 (1999) 6969–6976. <https://doi.org/10.1128/JB.181.22.6969-6976.1999>.
- [10] C.-Y. Kao, B.-S. Sheu, S.-M. Sheu, H.-B. Yang, W.-L. Chang, H.-C. Cheng, J.-J. Wu, Higher Motility Enhances Bacterial Density and Inflammatory Response in Dyspeptic Patients Infected with *Helicobacter pylori*, *Helicobacter.* 17 (2012) 411–416. <https://doi.org/10.1111/j.1523-5378.2012.00974.x>.
- [11] K. Terry, S.M. Williams, L. Connolly, K.M. Ottemann, Chemotaxis Plays Multiple Roles during *Helicobacter pylori* Animal Infection, *Infect. Immun.* 73 (2005) 803–811. <https://doi.org/10.1128/IAI.73.2.803-811.2005>.
- [12] P. Lertsethtakarn, K.M. Ottemann, D.R. Hendrixson, Motility and Chemotaxis in *Campylobacter* and *Helicobacter*, *Annu. Rev. Microbiol.* 65 (2011) 389–410. <https://doi.org/10.1146/annurev-micro-090110-102908>.
- [13] O.A. Cerda, F. Núñez-Villena, S.E. Soto, J.M. Ugalde, R. López-Solís, H. Toledo, *tlpA* gene expression is required for arginine and bicarbonate chemotaxis in *Helicobacter pylori*, *Biol. Res.* 44 (2011) 277–282. <https://doi.org/10.4067/S0716-97602011000300009>.
- [14] M. Valenzuela, O. Cerda, H. Toledo, Overview on chemotaxis and acid resistance in *Helicobacter pylori*, *Biol. Res.* 36 (2003) 1399–1404. <https://doi.org/10.4067/S0716-97602003000300014>.
- [15] J.Y. Huang, E. Goers Sweeney, K. Guillemin, M.R. Amieva, Multiple Acid Sensors Control *Helicobacter pylori* Colonization of the Stomach, *PLOS Pathog.* 13 (2017) e1006118. <https://doi.org/10.1371/journal.ppat.1006118>.
- [16] J.Y. Huang, E.G. Sweeney, M. Sigal, H.C. Zhang, S.J. Remington, M.A. Cantrell, C.J. Kuo, K. Guillemin, M.R. Amieva, Chemodetection and Destruction of Host Urea Allows *Helicobacter pylori* to Locate the Epithelium, *Cell Host Microbe.* 18 (2015) 147–156. <https://doi.org/10.1016/j.chom.2015.07.002>.
- [17] M.A. Machuca, K.S. Johnson, Y.C. Liu, D.L. Steer, K.M. Ottemann, A. Roujeinikova, *Helicobacter pylori* chemoreceptor TlpC mediates chemotaxis to lactate, *Sci. Rep.* 7 (2017) 14089. <https://doi.org/10.1038/s41598-017-14372-2>.
- [18] T. Takahashi, T. Matsumoto, M. Nakamura, H. Matsui, K. Tsuchimoto, H. Yamada, L-Lactic Acid Secreted from Gastric Mucosal Cells Enhances Growth of

Helicobacter pylori, *Helicobacter*. 12 (2007) 532–540. <https://doi.org/10.1111/j.1523-5378.2007.00524.x>.

- [19] S. Iwatani, H. Nagashima, R. Reddy, S. Shiota, D.Y. Graham, Y. Yamaoka, Identification of the genes that contribute to lactate utilization in *Helicobacter pylori*, *PloS One*. 9 (2014) e103506. <https://doi.org/10.1371/journal.pone.0103506>.
- [20] D. Ilver, A. Arnqvist, J. Ögren, I.-M. Frick, D. Kersulyte, E.T. Incecik, D.E. Berg, A. Covacci, L. Engstrand, T. Borén, *Helicobacter pylori* Adhesin Binding Fucosylated Histo-Blood Group Antigens Revealed by Retagging, *Science*. 279 (1998) 373–377. <https://doi.org/10.1126/science.279.5349.373>.
- [21] B.-S. Sheu, S. Odenbreit, K.-H. Hung, C.-P. Liu, S.-M. Sheu, H.-B. Yang, J.-J. Wu, Interaction Between Host Gastric Sialyl-Lewis X and *H. pylori* SabA Enhances *H. pylori* Density in Patients Lacking Gastric Lewis B Antigen, *Am. J. Gastroenterol.* 101 (2006) 36–44.
- [22] D.J. Evans, D.G. Evans, T. Takemura, H. Nakano, H.C. Lampert, D.Y. Graham, D.N. Granger, P.R. Kviety, Characterization of a *Helicobacter pylori* neutrophil-activating protein., *Infect. Immun.* 63 (1995) 2213–2220. <https://doi.org/10.1128/IAI.63.6.2213-2220.1995>.
- [23] A. Polenghi, F. Bossi, F. Fischetti, P. Durigutto, A. Cabrelle, N. Tamassia, M.A. Cassatella, C. Montecucco, F. Tedesco, M. de Bernard, The Neutrophil-Activating Protein of *Helicobacter pylori* Crosses Endothelia to Promote Neutrophil Adhesion *In vivo*, *J. Immunol.* 178 (2007) 1312–1320. <https://doi.org/10.4049/jimmunol.178.3.1312>.
- [24] C.-Y. Lin, Y.-S. Huang, C.-H. Li, Y.-T. Hsieh, N.-M. Tsai, P.-J. He, W.-T. Hsu, Y.-C. Yeh, F.-H. Chiang, M.-S. Wu, C.-C. Chang, K.-W. Liao, Characterizing the polymeric status of *Helicobacter pylori* heat shock protein 60, *Biochem. Biophys. Res. Commun.* 388 (2009) 283–289. <https://doi.org/10.1016/j.bbrc.2009.07.159>.
- [25] A. Tanaka, T. Kamada, K. Yokota, A. Shiotani, J. Hata, K. Oguma, K. Haruma, *Helicobacter pylori* heat shock protein 60 antibodies are associated with gastric cancer, *Pathol. - Res. Pract.* 205 (2009) 690–694. <https://doi.org/10.1016/j.prp.2009.04.008>.
- [26] C. Fung, S. Tan, M. Nakajima, E.C. Skoog, L.F. Camarillo-Guerrero, J.A. Klein, T.D. Lawley, J.V. Solnick, T. Fukami, M.R. Amieva, High-resolution mapping reveals that microniches in the gastric glands control *Helicobacter pylori* colonization of the stomach, *PLOS Biol.* 17 (2019) e3000231. <https://doi.org/10.1371/journal.pbio.3000231>.

- [27] E. Garza-González, A review of *Helicobacter pylori* diagnosis, treatment, and methods to detect eradication, *World J. Gastroenterol.* 20 (2014) 1438. <https://doi.org/10.3748/wjg.v20.i6.1438>.
- [28] S. Suzuki, C. Kusano, T. Horii, R. Ichijima, H. Ikehara, The Ideal *Helicobacter pylori* Treatment for the Present and the Future, *Digestion.* 103 (2022) 62–68. <https://doi.org/10.1159/000519413>.
- [29] K. Murakami, Y. Sakurai, M. Shiino, N. Funao, A. Nishimura, M. Asaka, Vonoprazan, a novel potassium-competitive acid blocker, as a component of first-line and second-line triple therapy for *Helicobacter pylori* eradication: a phase III, randomised, double-blind study, *Gut.* 65 (2016) 1439–1446. <https://doi.org/10.1136/gutjnl-2015-311304>.
- [30] H. Deguchi, A. Uda, K. Murakami, Current Status of *Helicobacter pylori* Diagnosis and Eradication Therapy in Japan Using a Nationwide Database, *Digestion.* 101 (2020) 441–449. <https://doi.org/10.1159/000500819>.
- [31] for the Taiwan Gastrointestinal Disease and Helicobacter Consortium, J.-M. Liou, P.-Y. Chen, Y.-T. Kuo, M.-S. Wu, Toward population specific and personalized treatment of *Helicobacter pylori* infection, *J. Biomed. Sci.* 25 (2018) 70. <https://doi.org/10.1186/s12929-018-0471-z>.
- [32] WHO publishes list of bacteria for which new antibiotics are urgently needed, (n.d.). <https://www.who.int/news/item/27-02-2017-who-publishes-list-of-bacteria-for-which-new-antibiotics-are-urgently-needed> (accessed September 30, 2022).
- [33] J.-M. Liou, C.-C. Chen, C.-M. Chang, Y.-J. Fang, M.-J. Bair, P.-Y. Chen, C.-Y. Chang, Y.-C. Hsu, M.-J. Chen, C.-C. Chen, J.-Y. Lee, T.-H. Yang, J.-C. Luo, C.-Y. Chen, W.-F. Hsu, Y.-N. Chen, J.-Y. Wu, J.-T. Lin, T.-P. Lu, E.Y. Chuang, E.M. El-Omar, M.-S. Wu, Taiwan Gastrointestinal Disease and Helicobacter Consortium, Long-term changes of gut microbiota, antibiotic resistance, and metabolic parameters after *Helicobacter pylori* eradication: a multicentre, open-label, randomised trial, *Lancet Infect. Dis.* 19 (2019) 1109–1120. [https://doi.org/10.1016/S1473-3099\(19\)30272-5](https://doi.org/10.1016/S1473-3099(19)30272-5).
- [34] M.P.C. de Souza, B.A.F. de Camargo, L. Spósito, G.C. Fortunato, G.C. Carvalho, G.D. Marena, A.B. Meneguín, T.M. Bauab, M. Chorilli, Highlighting the use of micro and nanoparticles based-drug delivery systems for the treatment of *Helicobacter pylori* infections, *Crit. Rev. Microbiol.* 47 (2021) 435–460. <https://doi.org/10.1080/1040841X.2021.1895721>.
- [35] T. Safarov, B. Kiran, M. Bagirova, A.M. Allahverdiyev, E.S. Abamor, An overview of nanotechnology-based treatment approaches against *Helicobacter pylori*, *Expert Rev. Anti Infect. Ther.* (2019). <https://www.tandfonline->

com.inc.bib.cnrs.fr/doi/abs/10.1080/14787210.2019.1677464 (accessed September 6, 2022).

- [36] S. Khan, M. Sharaf, I. Ahmed, T.U. Khan, S. Shabana, M. Arif, S.S.U.H. Kazmi, C. Liu, Potential utility of nano-based treatment approaches to address the risk of *Helicobacter pylori*, *Expert Rev. Anti Infect. Ther.* (2021). [https://www-tandfonline-com.inc.bib.cnrs.fr/doi/abs/10.1080/14787210.2022.1990041](https://www.tandfonline-com.inc.bib.cnrs.fr/doi/abs/10.1080/14787210.2022.1990041) (accessed September 6, 2022).
- [37] Y. Qin, Y.-H. Lao, H. Wang, J. Zhang, K. Yi, Z. Chen, J. Han, W. Song, Y. Tao, M. Li, Combatting *Helicobacter pylori* with oral nanomedicines, *J. Mater. Chem. B.* 9 (2021) 9826–9838. <https://doi.org/10.1039/D1TB02038B>.
- [38] R. Grosso, M.-V. de-Paz, Scope and Limitations of Current Antibiotic Therapies against *Helicobacter pylori*: Reviewing Amoxicillin Gastroretentive Formulations, *Pharmaceutics.* 14 (2022) 1340. <https://doi.org/10.3390/pharmaceutics14071340>.
- [39] N.A. Thombre, P.S. Gide, Floating-bioadhesive gastroretentive Caesalpinia pulcherrima-based beads of amoxicillin trihydrate for *Helicobacter pylori* eradication, *Drug Deliv.* 23 (2016) 405–419. <https://doi.org/10.3109/10717544.2014.916766>.
- [40] M.I. Alam, T. Paget, Amal.A. Elkordy, Characterization of furazolidone-chitosan based spray dried microparticles regarding their drug release and mucin adsorptive properties, *Powder Technol.* 295 (2016) 175–179. <https://doi.org/10.1016/j.powtec.2016.03.026>.
- [41] S. Arora, R.D. Budhiraja, Chitosan-alginate microcapsules of amoxicillin for gastric stability and mucoadhesion, *J. Adv. Pharm. Technol. Res.* 3 (2012) 68–74. <https://doi.org/10.4103/2231-4040.93555>.
- [42] A. Hardenia, *In vitro* and *In vivo* Evaluation of Mucoadhesive Microspheres for Treatment of *Helicobacter pylori* and Its Associated Diseases, *Asian J. Pharm. AJP.* 10 (2016). <https://doi.org/10.22377/ajp.v10i03.766>.
- [43] M.S. Ali, V. Pandit, M. Jain, K.L. Dhar, Mucoadhesive microparticulate drug delivery system of curcumin against *Helicobacter pylori* infection: Design, development and optimization, *J. Adv. Pharm. Technol. Res.* 5 (2014) 48–56. <https://doi.org/10.4103/2231-4040.126996>.
- [44] V. .N, S. Ramanathan, P. Perumal, *In vivo* Evaluation of Amoxicillin Trihydrate and Clarithromycin-Loaded Mucoadhesive Microspheres for *H. pylori* Eradication, *Trop. J. Pharm. Res.* 12 (2013). <https://doi.org/10.4314/tjpr.v12i2.2>.

- [45] Y.-H. Lin, J.-H. Lin, S.-C. Chou, S.-J. Chang, C.-C. Chung, Y.-S. Chen, C.-H. Chang, Berberine-loaded targeted nanoparticles as specific *Helicobacter pylori* eradication therapy: *in vitro* and *in vivo* study, *Nanomed.* 10 (2015) 57–71. <https://doi.org/10.2217/nnm.14.76>.
- [46] Y.-H. Lin, S.-C. Tsai, C.-H. Lai, C.-H. Lee, Z.S. He, G.-C. Tseng, Genipin-cross-linked fucose-chitosan/heparin nanoparticles for the eradication of *Helicobacter pylori*, *Biomaterials.* 34 (2013) 4466–4479. <https://doi.org/10.1016/j.biomaterials.2013.02.028>.
- [47] I.C. Gonçalves, A. Magalhães, M. Fernandes, I.V. Rodrigues, C.A. Reis, M.C.L. Martins, Bacterial-binding chitosan microspheres for gastric infection treatment and prevention, *Acta Biomater.* 9 (2013) 9370–9378. <https://doi.org/10.1016/j.actbio.2013.07.034>.
- [48] H. Patricia C., Orally administrated chitosan microspheres bind *Helicobacter pylori* and decrease gastric infection in mice, *Acta Biomater.* (2020) 15.
- [49] I. Goncalves, Bacterial-binding chitosan microspheres for gastric infection treatment and prevention, *Acta Biomater.* (2013) 9.
- [50] M. Luo, Y.-Y. Jia, Z.-W. Jing, C. Li, S.-Y. Zhou, Q.-B. Mei, B.-L. Zhang, Construction and optimization of pH-sensitive nanoparticle delivery system containing PLGA and UCCs-2 for targeted treatment of *Helicobacter pylori*, *Colloids Surf. B Biointerfaces.* 164 (2018) 11–19. <https://doi.org/10.1016/j.colsurfb.2018.01.008>.
- [51] Z.-W. Jing, Y.-Y. Jia, N. Wan, M. Luo, M.-L. Huan, T.-B. Kang, S.-Y. Zhou, B.-L. Zhang, Design and evaluation of novel pH-sensitive ureido-conjugated chitosan/TPP nanoparticles targeted to *Helicobacter pylori*, *Biomaterials.* 84 (2016) 276–285. <https://doi.org/10.1016/j.biomaterials.2016.01.045>.
- [52] Z.-W. Jing, M. Luo, Y.-Y. Jia, C. Li, S.-Y. Zhou, Q.-B. Mei, B.-L. Zhang, Anti-*Helicobacter pylori* effectiveness and targeted delivery performance of amoxicillin-UCCs-2/TPP nanoparticles based on ureido-modified chitosan derivative, *Int. J. Biol. Macromol.* 115 (2018) 367–374. <https://doi.org/10.1016/j.ijbiomac.2018.04.070>.
- [53] R.B. Umamaheshwari, N.K. Jain, Receptor mediated targeting of lectin conjugated gliadin nanoparticles in the treatment of *Helicobacter pylori*, *J. Drug Target.* 11 (2003) 415–423; discussion 423–424. <https://doi.org/10.1080/10611860310001647771>.
- [54] M. Gottesmann, F.M. Goycoolea, T. Steinbacher, T. Menogni, A. Hensel, Smart drug delivery against *Helicobacter pylori*: pectin-coated, mucoadhesive liposomes

with antiadhesive activity and antibiotic cargo, *Appl. Microbiol. Biotechnol.* 104 (2020) 5943–5957. <https://doi.org/10.1007/s00253-020-10647-3>.

- [55] Y. Ping, X. Hu, Q. Yao, Q. Hu, S. Amini, A. Miserez, G. Tang, Engineering bioinspired bacteria-adhesive clay nanoparticles with a membrane-disruptive property for the treatment of *Helicobacter pylori* infection, *Nanoscale.* 8 (2016) 16486–16498. <https://doi.org/10.1039/C6NR05551F>.
- [56] Y. Zhang, Y. Chen, C. Lo, J. Zhuang, P. Angsantikul, Q. Zhang, X. Wei, Z. Zhou, M. Obonyo, R.H. Fang, W. Gao, L. Zhang, Inhibition of Pathogen Adhesion by Bacterial Outer Membrane-Coated Nanoparticles, *Angew. Chem. Int. Ed.* 58 (2019) 11404–11408. <https://doi.org/10.1002/anie.201906280>.
- [57] P. Angsantikul, S. Thamphiwatana, Q. Zhang, K. Spiekermann, J. Zhuang, R.H. Fang, W. Gao, M. Obonyo, L. Zhang, Coating nanoparticles with gastric epithelial cell membrane for targeted antibiotic delivery against *Helicobacter pylori* infection, *Adv. Ther.* 1 (2018) 1800016. <https://doi.org/10.1002/adtp.201800016>.

Chapter 2. Targeted drug delivery therapies inspired by natural taxes

Hung V. Nguyen, Vincent Faivre*

Université Paris-Saclay, CNRS, Institut Galien Paris-Saclay, 5 rue JB Clément, 92296 Châtenay-Malabry, France.

* corresponding author

Tel. + 33 1 46 83 54 65

Fax. + 33 1 46 83 53 12

e-mail: vincent.faivre@u-psud.fr

Abstract

A taxis is the movement responding to a stimulus of an organism. This behavior helps organisms to migrate, to find food or to avoid dangers. By mimicking and using natural taxes, many bio-inspired and bio-hybrid drug delivery systems have been synthesized. Under the guidance of physical and chemical stimuli, drug-loaded carriers are led to a target, for example tumors, then locally release the drug, inducing a therapeutic effect without influencing other parts of the body. On the other hand, for moving targets, for example metastasis cancer cells or bacteria, taking advantage of their taxes behavior is a solution to capture and to eliminate them. For instance, several traps and ecological niches have been fabricated to attract cancer cells by releasing chemokines. Cancer cells are then eliminated by drug loaded inside the trap, by radiotherapy focusing on the trap location or by simply removing the trap. Further research is needed to deeply understand the taxis behavior of organisms, which is essential to ameliorate the performance of taxes-inspired drug delivery application.

Keywords

Targeting, Taxes, Physical stimulus, Chemotaxis, Micromotors

The article has been published in *Journal of Controlled Release*, [Volume 322](#), 10 June 2020, Pages 439-456, DOI: <https://doi.org/10.1016/j.jconrel.2020.04.005>

1. Introduction

Targeted delivery is a huge issue in the field of active pharmaceutical ingredient (API) delivery and controlled release. The main objective of this approach is to concentrate the API in the tissue of interest in order to increase its efficacy and reduce side effects due to the wide distribution in the body [1]. Antibody-drug conjugates (ADC) are targeted drugs that combine potent anti-cancer agents with monoclonal antibodies specific to antigens of particular tumor cells thanks to chemical linkers. Several ADC have been approved last years (Kadcyla[®], Adcetris[®], ...) and many others are in phase II/III clinical trials [2]. In the field of drug formulation, targeting strategies are mainly associated with the growing domain of nanotechnologies that allow, besides controlled delivery, to protect API by their encapsulation. During the last decades, mainly two approaches were developed in the nanoworld, passive and active targeting [3]. Both are based on API encapsulation into nanocarriers and surface modification of nanoparticles in order to favor the delivery at the desired place. Passive targeting consists of an accumulation of the nanocarriers in the region of interest, e.g. tumor site, thanks to the enhanced permeation and retention effect (EPR) due to extravasation through the leaky tumor vasculature. By reducing opsonization by blood proteins, the coating of the nanocarriers with some polymers (polyethylene oxide, polysaccharides...) reduces the clearance by the mononuclear phagocytic system, increases the circulation time and then, statistically, improves extravasation. Despite studies showing limitations in clinics [4,5], this accumulation property is used in approved and commercial products (Doxil/Caelyx[®], Visudyne[®],...) [6]. Conversely, despite more than 40,000 studies published in the last 10 years, nano-products dealing with active targeting strategy have not reached the market yet to our knowledge [7]. This strategy requires the carrier coating with affinity ligands that will increase retention and uptake at the target site through biochemical interactions with specific receptors of the diseased tissues. However, ligand recognition by the receptor is only possible at very short distances, probably not more than few Angströms, and requires first efficient extravasation [8]. Moreover, after IV administration, it is well known that nanocarriers will be coated by a protein corona that modifies, among others, their surface properties and potentially shields the targeting ligands [9,10]. At best, ligand grafting allows better retention at the considered site than a real active targeting with guidance properties.

In nature, organisms always interact with the environment around to survive. They follow physical and chemical signals to find food, optimal living condition and potential mating partners. Moreover, they also have the ability to detect and avoid toxic and unfavorable environments. This capacity of migration under the influence of a stimulus is called taxis. The stimulus can be physical or chemical. Mimicking natural taxis, designing a drug carrier that moves under a stimulus is interesting for targeted drug delivery. Following external or cell-produced stimuli, taxis-inspired drug carriers can move toward specific environments or specific cells, then release drugs in that region, facilitating the interaction of drugs and cells, reducing toxicity to other parts of the

human body. In this review, we introduce some kinds of taxes and their corresponding bio-inspired drug delivery systems to improve the interaction between the therapeutic system and target. As demonstrated in figure 2.1, we summarize 2 strategies: guiding therapeutic systems to targets and attracting targets to therapeutic systems. In the first strategy, the therapeutic systems (e.g. drug-loaded nanoparticles, gene delivery vesicles...) are functionalized and loaded with therapeutic agents to locate and to attach to targets (e.g. tumors, human organs...), facilitating the drug delivery process and reducing systemic effects. In contrast, the latter strategy exploits the mobility and natural tactic behavior of targets (e.g. human cells, pathogens...). Targets are attracted and guided to a drug reservoir, which eliminates them when they penetrate inside.

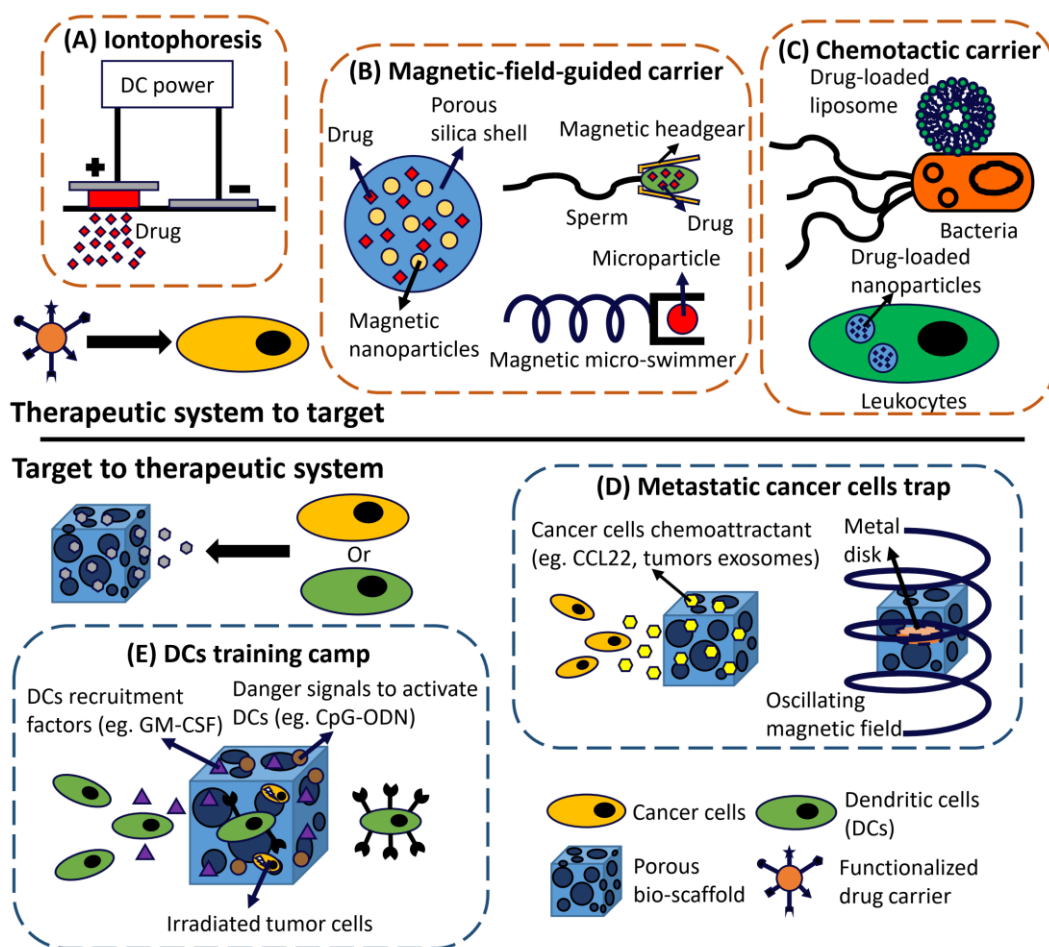


Figure 2.1. Summary of taxes-inspired targeted drug delivery therapies

1.1. Physical stimulus responsive taxis

Physical factors of the environment affect organisms in several ways. For example, many organisms' activities are dependent on the day/night period or light/shadow area. The ability to sense light intensity gradient and to move accordingly is called phototaxis. This behavior is commonly observed in insects like moths, when they fly toward or away from light sources [11]. Phototaxis is also found in microorganisms, such as *Serratia*

marcescens and *Tetrahymena pyriformis* [12]. In *Euglena*, combining with sensing light, they sense gravity direction to find optimal niches in water [13]. This behavior is called gravitaxis, which is the ability to follow and to align along the gravity vector. Furthermore, many organisms also react to a temperature gradient, namely thermotaxis behavior. Taking advantage of the thermotactic movement of sperm, high-quality sperms can be separated and selected to improve the fertility [14]. In the human body, cells also respond to the gradient of stiffness, namely durotaxis behavior. For example, cancer cells migration is affected by the stiffness of the extracellular environment, which may be related to the increase in the stiffness of tumors over time [15]. In this review, we only focus on tactic behaviors that have been based on to innovate new drug delivery and release strategies.

1.1.1. Magnetotaxis

Magnetotaxis is the ability to detect and to follow a magnetic field of an organism. This behavior is found in magnetotactic bacteria, which are a group of bacteria that lie along the magnetic field of the Earth. Magnetotactic bacteria were first discovered by Bellini in 1963 [16] and rediscovered independently by Blakemore in 1975 [17]. Their alignment along Earth's magnetic field characteristic comes from an organelle called magnetosome, which contains chains of magnetic iron oxide (Fe_3O_4) or iron sulfide (Fe_3S_4) nanocrystals with the size of 35-120 nm [18–20]. These magnetic nanocrystals introduce a magnetic force to the bacteria and align them along the magnetic field of the Earth. Therefore, magnetotactic bacteria usually swim along this alignment [17]. Death bacteria, despite of not being able to swim, continue to align along the magnetic field. Some researchers believe that the magnetotaxis behavior of bacteria helps them to migrate to areas of optimal oxygen concentration [21–23]. The high iron uptake of bacteria to synthesize magnetic nanocrystal also helps to detoxify toxic oxygen free radical [24,25].

1.1.2. Electrotaxis

Electrotaxis or galvanotaxis is the migration behavior of organisms along an electric field. In mammals, electric fields were measured at wound sites [26,27]. For example, immediately after being injured, a large rise in the electric field strength was measured at the wound edge of a guinea pig [28]. The electric field is generated from the trans-epithelial potential on mammalian skin. This voltage is positive on the skin basal layer and negative on the skin apical layer [27]. The cut through the skin creates a short circuit, driving a positively charge current toward the wound edge [29]. It acts as a cue to guide cells to the wound site, increasing the regeneration rate [26,27,29]. However, in experiments, not all types of cells move in the same direction under an electric field. In general, cells move toward the cathode, for example, bovine corneal epithelial cells, bovine aortic vascular endothelial cells, human keratinocytes... [30]. Meanwhile, some cell types move toward the anode, such as human granulocytes, human vascular

endothelial cells [30]. Interestingly, primary human lens epithelial cells move toward the cathode, while the transformed human lens epithelial cells move in the opposite direction [31]. Moreover, stronger metastatic and weakly metastatic prostatic cancer cell lines migrate in opposite directions while being under the same applied electric field and conditions [32]. Understanding electrotaxis in cells is very important to investigate the metastasis of cancer cells. In addition, the healing rate of wounds may be improved using electrotaxis by applying an optimized electric field to the wound site.

1.2. Chemical stimulus responsive taxis

1.2.1. Chemotaxis

Chemotaxis is the movement of an organism toward or away from a chemical concentration gradient. This behavior helps organisms migrate to the rich nutrition areas, optimal living condition regions or detect and avoid dangerous substances. For example, *Escherichia coli* (*E. coli*) swims toward high glucose concentration regions [33]. In humans, chemotaxis is extremely important in the development and the self-defense of body, such as, the movement of leukocytes toward injured and inflamed sites or the migration of sperms toward eggs. Microorganisms sense chemical cues using their receptor proteins, which detect 2 types of signals: chemoattractants and chemorepellents. They migrate to high chemoattractants concentration regions and flee from high chemorepellents regions. For example, a chemoattractant of leukocytes - formyl peptide, which is released by some types of bacteria, attracts leukocytes like neutrophils or macrophages to the disease sites [34]. This is an immune reaction to protect the human body from the invasion of pathogens. On the other hand, chemorepellents repel microorganisms. In the case of *Helicobacter pylori* (*H. pylori*) - bacteria that live in the human stomach, they sense acid concentration and migrate away from low pH regions [35]. Understanding the chemotactic behavior of human cells is very important to investigate how diseases work and affect the human body. For example, the environment inside tumors has lower pH, lower oxygen concentration, higher resting temperature and higher hydrogen peroxide concentration compared to normal tissues [36–38]. Taking advantage of these special properties, chemotaxis-inspired drug carriers can be designed to specifically target tumors by sensing and following chemical cues, such as the gradient of hydrogen peroxide concentration, the gradient of pH or the gradient of oxygen concentration.

2. Targeted drug delivery therapies inspired by natural taxes

2.1. Guiding carriers to a target

Aiming to synthesize a “magical bullet”, which can reach any places in the body then locally increase drug concentration and release to treat the disease without affecting other healthy parts of the human body, several strategies to guide drug carriers to a target have been proposed and investigated by many research groups in the world.

Recently, there are some reviews about the use of micro-/nanomotors for drug delivery application, which propose several advantages compared to the nanoparticles system due to their high mobility [39–41]. However, some micro-/nanomotors move randomly, which does not offer any benefits for the drug delivery application. Aiming to improve the interaction between the target and the drug carriers, herein, we summarize 3 popular methods to guide and to control drug carriers to a target: using a magnetic field, using an electric field and using a chemical concentration gradient.

2.1.1. Using a magnetic field

Inspired by magnetotaxis bacteria, several drug delivery systems use a magnetic field as the navigation and/or the moving force to guide drug carriers to the desired location (Figure 2.1B). The core of these systems is magnetic particles, which are able to orient and/or move along an applied magnetic field. The driving force of the magnetic drug carrier can be magnetic force or the combination of magnetic force and a self-propelling force. Magnetic particles may also serve as imaging agents using magnetic resonance imaging (MRI), enabling the tracking of the magnetic carriers while driving them inside patients' bodies [42]. In addition, under an alternating magnetic field exposure, magnetic nanoparticles are heated, leading to an increase of the local temperature. This effect may trigger physiological reactions of cells such as necrosis or even carbonization, aiding tumor treatment process [43].

2.1.1.1. Magnetic nanoparticles – Magnetic force as the driven factor

One simple magnetic drug delivery system is individual magnetic particles. In general, after the identification of the destination for drug carriers, for example, a tumor's location, the patients are injected with drug-loaded magnetic carriers. Then an external magnetic field is used to control and guide these magnetic carriers to the desired destination. Several groups synthesized functionalized magnetic nanoparticles [44–48]. The drug is attached to the nanoparticles by functional groups. Interestingly, some other groups have reported the synthesis of porous magnetic nanoparticles [49–51]. The drug is loaded by physical adsorption inside the pore network. The high porosity increases the specific surface area, increasing the amount of drug that can be loaded. For example, Chen et al. have reported the synthesis of mesoporous $M_xFe_{3-x}O_4$ (with $M = Fe, Co, Zn$) microspheres [51]. The loading efficiency of VP16 (Etoposide) in their particles is up to 64.8%. The drug release can be controlled using microwave radiation.

Directly taken from magnetotactic bacteria, magnetosome is gaining interest as drug carriers [52]. Magnetosome is a membranous, intracellular organelle containing magnetic iron oxide particles which has a pivotal role in the magnetotactic behavior of bacteria. Magnetosomes have several advantages in drug delivery applications, such as the narrow size distribution, which can be genetically controlled, and the high purity of iron oxide nanoparticles [52]. In addition, magnetosomes are already covered by a membrane, which offers facile functionalization, controllable drug release rate and

biocompatibility [52]. Moreover, magnetosomes can be produced at large scale with high quality [53,54]. There are several amino groups or chimeric proteins in the case of engineered magnetosomes on the magnetosomes' membrane, enabling the drug coupling via linkers [52]. So, drug or model molecule-loading into magnetosomes is achieved by surface functionalization [52,55–58]. For example, bacterial magnetosomes have been used as doxorubicin carriers for cancer treatment [58]. In this report, the research group of Li et al. showed the biocompatibility of magnetosomes and stability in the circulatory system *in vitro* [58]. The loaded doxorubicin was released effectively from the magnetosomes and killed cancer cells [58]. Tested in EMT-6 and HL60 cell lines, the IC₅₀ value of DOX-functionalized magnetosomes (3.114 mg/mL for EMT-6 and 0.050 mg/mL for HL60) was smaller than that of magnetosomes (very high for EMT-6 and 4.112 mg/mL for HL60) and of free DOX (7.205 mg/mL for EMT-6 and 0.381 mg/mL for HL60).

However, it is not easy to control the movement of single magnetic nanoparticle or single magnetosome, due to their low magnetization, therefore weak magnetic force [59]. In addition, the magnetic force applied to the magnetic carriers is proportional to the volume of magnetic materials [42]. With the nano-size particles, the magnetic force would be very small and may not overcome the circulation drag force inside the body. However, to keep the unique property of nanoparticles, the size of magnetic nanoparticles should be kept at the nanoscale. For example, superparamagnetic nanoparticles lose their superparamagnetic properties at a size larger than approximately 20 nm [60,61]. For ferromagnetic property, the formation of multiple magnetic domains, which reduces the remanent magnetization, occurs at the size threshold of approximately 128 nm for Fe₃O₄, 55 nm for nickel, 15 nm for iron and hexagonal close-packed cobalt and 7 nm for face-centered cubic cobalt [62,63]. To deal with this problem, a strategy is mimicking the magnetosome of magnetotactic bacteria, where the magnetic nanocrystals are organized in one or more chains. Therefore, drug carriers containing clusters of small magnetic nanoparticles are fabricated. Under the same magnetic field, the magnetic force of the assembly system is higher than that of individual nanoparticles. The system consists of several magnetic nanoparticles encapsulated in a matrix, for example, silica [64–68] or liposome [69–82], where the drug is usually loaded.

The magnetic nanoparticles assembly core – silica shell structure combines the advantage of both types of materials. The silica shell, which can be made to be mesoporous, not only protects the core from the outside environment, but also provides a large surface area for drug loading. Silica nanoparticles are also well-known for their biocompatibility [83–86], which further enhances the potential of this drug delivery system. For example, the group of Lu et al. reported the synthesis of mesoporous organosilica nanoparticles encapsulating with Fe₃O₄ nanocrystals clusters [66]. Thanks to the addition of organosilica precursors during the synthesis, NH₂ functional groups are on the surface of the organosilica layer. NH₂ groups bind with the

drug (aspirin and ibuprofen), hence reducing the release rate. This strategy not only increases the magnetization of the carriers, but also embeds the high mesoporosity, functionalization and the biocompatibility of silica into the drug delivery system.

Magnetic nanoparticles functionalized liposomes, also called magnetoliposomes, is another very interesting drug delivery system. This strategy introduces controllable mobility property and MRI imaging into liposomes. In addition, due to the hyperthermia effect of magnetic nanoparticles, the crystal structure of liposome can be controlled by applying an alternating magnetic field, thus regulating the drug release rate [69]. It is synthesized by loading several magnetic nanoparticles inside the lumen [70–75], or inside the lipid layer [76–79] or on the surface of liposome [77]. The location of magnetic nanoparticles inside liposomes can be controlled by changing their surface functional groups [69]. The position between lipid bi-layers could be favorable in some situations, since the heat from the hyperthermia effect will be delivered directly to the lipid to change the structure. By combining the large drug loading capacity and biocompatibility of liposome with the high mobility, MRI imaging and hyperthermia effect of magnetic nanoparticles, a wide range of applications is opened for magnetoliposomes.

Precise control of individual magnetic nanoparticles *in vivo* is hard to achieve, since they tend to form chains and aggregation under an external magnetic field [87]. Several *in vivo* studies about the guidance of magnetic nanoparticles to site of interests have been reported [88–90]. However, the accumulation of particles in the site of interest is achieved more than a long-distance guidance demonstration. The penetration depth of 100 nm magnetic particles inside tumors *in vivo* was reported to be only 7 cm [88]. Therefore, the injection of magnetic drug carriers near the site of interests seems required.

2.1.1.2. Magnetic micro-swimmers – Self-propelling force as the driven factor

While the encapsulation of several magnetic nanoparticles inside a drug carrier increases the magnetic force of magnetic fields applied to it, the aggregation may lead to the loss of superparamagnetism. Another approach is introducing a self-propelling force into the magnetic carriers. In this case, the magnetic field only acts as a navigator. Carriers move forward by their own propelling force. This approach does not require too strong magnetic fields, and does not depend on the magnetic force [42]. The self-propelling force can be from a bacterium, a sperm or a micron-size magnetic motor.

Using a rotating magnetic field, a mechanical rotation movement may be created. Inspired by the bacterial flagella, screw-shaped magnetic micro-motors for drug delivery are fabricated. The micro-motors (also called micro-swimmers) can swim steadily, pick up drug-loaded cargos and release them into cells. This drug delivery system offers many advantages: high controllability, drug loading and release on demand, possibility to synthesize in large scale, no fuel needed and low magnetic field

strength requirement compared to magnetic-force-driven systems... [42]. For instance, Wang et al. reported the synthesis of Ni-Ag micro-swimmers, which can move with a speed of 10 $\mu\text{m/s}$ [91]. The cargos, which are drug-loaded magnetic polymer microparticles, are stuck to the swimmers by magnetic force. The system can directly deliver the drug-loaded particles to cancer cells *in vitro*. Similarly, helix-shaped Ni/Ti bilayer coated polymeric micro-swimmers were synthesized by the group of Nelson et al. [92,93]. Their micro-swimmers can be functionalized with lipoplexes to deliver genes into cells [92] or pick up microparticles (around 6 μm in diameter) using a basket-shaped head [93], offering a wide range of applications. This micro-swimmer has a screw-shaped and rotates under an alternating magnetic field (Figure 2.2A and 2.2B). It moves in a wobbling motion; the wobbling angle is determined by the frequency of the magnetic field. When the wobbling angle is very small, the moving behavior is corkscrew. The speed of the micro-swimmer is ranging from 20 to 200 $\mu\text{m/s}$ depending on the size, shape and design.

Having the self-powered ability, living microorganisms are promising candidates for drug carriers. Compared to the speed of synthetic micro-swimmers, the speed of some microorganisms, for example bacteria, is higher, since their movement in biological environments is naturally optimized [42]. In addition, they have better bio-adaptability, for example, sperms adapt well to the environment inside the female reproductive system [95]. Moreover, they have the ability of trans-membrane transport, which is not available in synthetic micro-motors [42]. In the case of microorganisms having magnetic property, they are functionalized with drug carriers [94,96]. For example, Stanton et al. integrated ciprofloxacin-loaded silica microtubes into magnetotactic bacteria *Magnetospirillum gryphiswalense* (MSR-1) and demonstrated the controllability of this system using a magnetic field [94]. The drug delivery system was created simply by incubation of bacteria with silica microtubes. The drug-loaded microtubes-MSR-1 was magnetically guided to an *E. coli* biofilm, whose pH is acidic, facilitating the release of CFX. As shown in Figure 2.2C, the drug-release rate of CFX in low pH is much higher than in high pH. In addition, under magnetic field control, the bacteria can push the *E. coli* biofilm and be trapped inside it, providing more chances for drug release (Figure 2.2C). For microorganisms that do not naturally have magnetic particles inside, such as sperm or *E. coli*, they are loaded with drugs and functionalized with magnetic "gears" [95,97]. For example, taking advantage of the motility of sperms, Xu et al. loaded doxorubicin into sperms and put a magnetic cap around their heads [95]. Using a magnetic field, the magnetic caps around sperms orient and point them to the destination. When sperms arrive at the tumor, they penetrate inside it, leaving the caps behind. The drug-loaded modified sperms (approximately 15 pg of DOX-HCl per sperm) could swim for a suitable time, distance for drug delivery, and showed a high tumor cell elimination efficiency. Using HeLa spheroid model, the percentage of live cells after 24h when the spheroids were incubated with free DOX-HCl and with DOX-HCl-loaded sperms were 45% and 47%, respectively. The difference in percentage of live cells between these 2 cases were negligible after 72h, showing that the integration of drug

into sperms did not affect its therapeutic efficiency. Having almost equal cancer cells elimination efficiency with free DOX-HCl, DOX-HCl-loaded-sperms also possess targeting property, reducing systemic effect while keeping the same toxicity toward cancer cells.

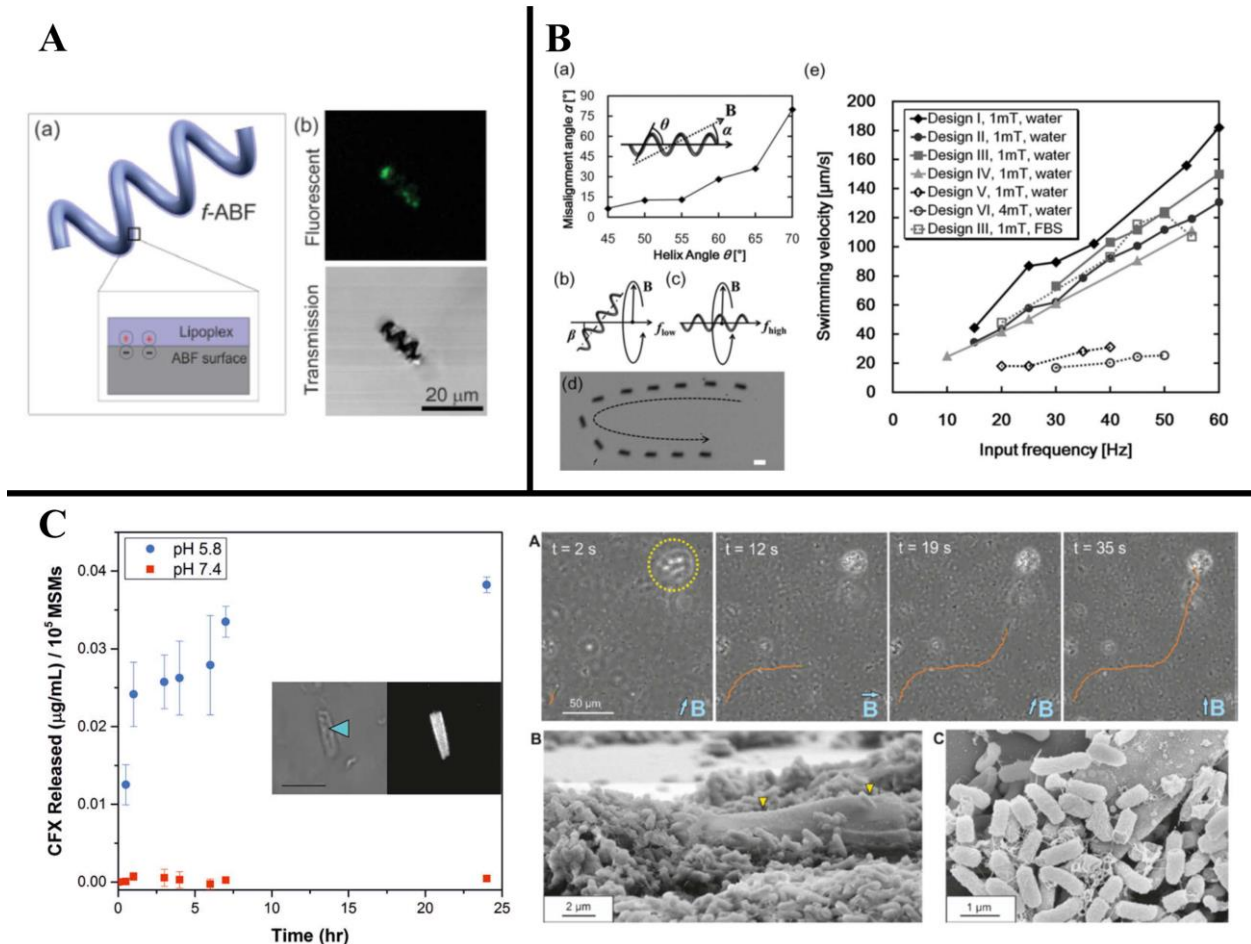


Figure 2.2. (A) Illustrative, fluorescence and TEM images of magnetically guided micro-swimmer show the screw shape and the success in *p*-DNA loading, marked with green fluorescence. (B) The wobbling moving behavior of a screw-shaped swimmer and its moving speed are dependent on the magnetic field frequency and the helix angle. (C) The ciprofloxacin release rate from drug-loaded silica microtubules and the photo of magnetotactic bacteria carrying those microtubules; drug-carrying magnetotactic bacteria can be guided to an *E. coli* biofilm using a magnetic field.

(A) Reproduced with permission from ref. [92]

(B) Reproduced with permission from ref. [93]

(C) Reproduced with permission from ref. [94]

While there have been many reported drug delivery strategies using controllable magnetic carriers, there are still many problems remaining unsolved. Practically, the

strongest, yet safe for human health, external magnetic field generated from a magnet can penetrate up to only 5 cm below human skin, limiting the application of magnetic drug carriers for deep targets [98]. To enhance the penetration depth of the magnetic field, superconducting magnets used in MRI are required. However, these magnets are very bulky and hard to move, raising the problem of controlling the direction of the magnetic field. Martel communicated an idea about moving the patient instead, but further investigation and experiments are needed [42].

Besides the problem of magnetic field penetration in deep targets, there is also a problem with the movement of drug carriers *in vivo*. Due to the no-slip boundary condition at the blood vessel wall, the highest circulation drag force is in the middle of the blood vessels, while it is 0 near the wall [98]. Therefore, if a magnetic field pushes the magnetic drug carriers out of the center, they would accumulate and form a film of magnetic particles on the blood vessel wall, while they should be deep inside a tumor. The aggregation would terminate the superparamagnetic property of nanoparticles. The film also requires a stronger magnetic field to move. MRI can be applied to know the location of magnetic carriers and to detect the formation of the film. However, this division of duty between control mode and imaging mode leads to the loss in carriers' driving effectiveness [98]. These problems *in vivo* can be solved if the magnetic carriers have their own propelling force; since they do not require a too strong magnetic field to move, and they can escape from the film by themselves. While the bio-hybrid carriers made from microorganisms have better bio-adaptability and moving speed than artificial micromotors, they would trigger the human immune system. In addition, with the micro size of bacteria and some types of microswimmers, it would be hard to penetrate deep inside a tumor.

2.1.2. Using an electric field

Similar to electrotaxis in many organisms, the use of electric fields to guide drugs to the desired location is a potential therapeutic strategy to cure diseases. Since a strong electric field is harmful to cells and tissues, only weak electric fields are applicable, leading to the low penetration depth of electric fields into the human body. Therefore, electric fields can only be used to guide drugs through epithelial barriers (such as skin) to improve the permeability of drugs. This technique is called iontophoresis (Figure 2.1A), which is not only applied to treat skin-related diseases, but also to eliminate deep tumors that are not suitable to be operated via implantation of iontophoresis devices.

Due to the ease of access, transdermal approaches of iontophoresis can be applied for several applications, such as the treatment of skin cancer [99–104] and local anesthetics [105,106]. The electric field helps drugs to go through the skin layer, improving treatment efficiency. For local anesthetics application, Manjunatha et al. reported the delivery of Lidocaine Hydrochloride (HCl) using iontophoresis through *ex vivo* human skin and *in vivo* mice skin [106]. The Lidocaine HCl concentration penetrated into human

skin of continuous direct current (DC) iontophoresis application group was 4 times higher than that of passive diffusion group. By applying pulsed DC current, the drug concentration penetrated into human skin was only 3 times higher than the drug concentration in passive diffusion application group, but the skin damage investigated in mice was highly reduced, suggesting the potential application of pulsed DC iontophoresis for local anesthetics application. In cancer treatment, Huber et al. used iontophoresis of nanoparticles drug formulation to improve the penetration depth of doxorubicin (DOX) to treat squamous cell carcinoma in mice [101]. In their report, under passive diffusion condition, the penetration depth in viable epidermis *in vitro* of DOX solid lipid nanoparticles (DOX-SLNs, 136 nm in diameter) was approximately 3.4 times higher than that of DOX solution. The penetration efficiency can be further improved by the application of iontophoresis. In viable epidermis layer, the penetration depth of DOX-SLNs in iontophoresis condition was 45 times higher than that of DOX-SLNs in passive diffusion condition. In combination, the use of iontophoresis for nanoparticles drug formulation highly increased the penetration depth of DOX into skin. For skin cancer treatment efficiency investigation, *in vivo* study in mice was conducted. The tumor growth inhibition rate in mice treated with iontophoresis of DOX-SLNs was higher than that of DOX solution. In addition, the use of iontophoresis of DOX-SLNs reduced the amount of undifferentiated cancer cells, compared to both non-treated mice group and mice group treated with the iontophoresis of DOX solution. These achievements show the very high potential of electric-field-guided drug treatment for skin cancers.

Although iontophoresis has shown its high performance in skin cancers treatment in both preclinical and clinical trials, it cannot be applied for tumors lying deep inside the body due to the access difficulty of iontophoresis devices. Specifically for bladder, intravesical delivery is one of the approaches for post-surgery treatment of bladder cancers. The electrode and drugs are inserted into the bladder through urinal tracts, helping to deliver drugs deep inside the bladder wall. The delivery of mitomycin C using iontophoresis into the bladder reduces recurrences in patients [104]. In an *ex vivo* experiment of human bladder tissue, after 15 minutes, the amount of drug delivered by iontophoresis was approximately 6 times higher than that by passive diffusion [107]. Several clinical trials gave positive results for the use of iontophoresis to deliver drugs intravesically for bladder cancer treatment [104,108]. For example, Gan et al. reported a clinical trial using sequential bacillus Calmette-Guérin (BCG)/iontophoresis of mitomycin C to treat high risk, nonmuscle invasive bladder cancer [109]. The treatment was successful in 87% of patients (90 of 104 people). After 1 year, nearly 87% of patients did not develop recurrence (75 of 86 people). After 2 years, approximately 93% of 1-year-disease-free patients continued to be disease-free (66 of 71 people).

Because of the shallow penetration of applied electric fields, iontophoresis devices have to be implanted inside the body to reach deep targets. The use of implanted devices helps to concentrate drugs on the implanted location and to reduce systemic

drugs. This approach is suitable for unable to be operated tumors, such as in the case of pancreatic cancer. In the advanced state of pancreatic cancer, many patients have locally advanced cancer, leading to the invasion of the tumor to the adjacent blood vessels, creating difficulties for surgery [110,111]. Byrne et al. fabricated a biocompatible iontophoresis device, which was then implanted inside the pancreatic cancer xenograft mouse model [110]. After 7 weeks, the tumor size of mice treated by implanted gemcitabine-releasing iontophoresis device was 1.7 times smaller than the initial. Meanwhile, the tumors of mice treated by intravenous gemcitabine, intravenous saline and saline-releasing iontophoresis device continued to develop for 7 weeks. In another report, the implanted iontophoresis device for local drug delivery showed a better tumor response than intravenous drugs [112].

The main challenge with the use of electric fields to guide drug is the danger of high strength electric fields, lowering the electric force inducing on the drug. Therefore, only small molecules can be guided by iontophoretic, while antibodies, nanoparticles are excluded from this treatment method due to their big size [104]. The penetration depth of molecules in tumors is improved by electric field, but still too small for large size tumors. For example, the drug is found up to 12 mm [113], 10 mm [104] or only 5 mm [114] from the electrode surface. In addition, at high depth, the quantity of drug may not be sufficient for therapeutic purposes. Although the electrode can be put in the desired location (for example, on tumors), the drug still diffuses to healthy surrounding tissues, raising the concern about toxicity, especially in sensitive areas. For instance, pancreatitis may develop if drugs are delivered directly to the pancreas [104].

2.1.3. Using a chemical concentration gradient

Chemotaxis is very important in the development of an organism. Bacteria, human cells sense chemical cues to migrate, to find food and to avoid dangers. Taking advantage of chemotaxis, many targeted drug delivery systems use chemical cues released from the target to migrate there (Figure 2.1C). In addition, these taxis behavior can be further engineered to increase the sensitivity or to fit the application. Unlike magnetically guided carriers or electric guided therapies, in which the location of action must be well known, chemotactic guided drug carriers spontaneously follow the chemoattractant to the desired location.

2.1.3.1. Self-driven micromotors

Micromotors can transfer chemical reaction energy to mechanical movements. They interact with chemicals that exist in their surrounding environment to move, equipping them the capacity to sense and move toward high reactants/catalysts concentration regions. This behavior is similar to chemotaxis in living organisms, giving micromotors a very high potential in the targeted drug delivery application. Using fuels like hydrogen peroxide [115–120], or catalysts like pH [121,122], which are overproduced in tumors [123,124], micromotors are able to move specifically toward cancer cells.

Polymerization reactions also can be used to move micromotors [125], giving them the chemotactic movement toward high monomer concentration. Interestingly, a glucose-fueled nanomotor system has demonstrated the improvement in mice blood-brain barrier penetration *in vivo* [126]. The nanomotor showed the chemotactic movement toward high glucose concentration. The nanomotors are polymersomes containing glucose oxidase and catalase, which catalyze glucose oxidation reaction and decomposition of H_2O_2 to form O_2 , pushing the nanomotor forward. The directional movement of polymersomes was achieved due to the asymmetric configuration. Via *in situ* brain perfusion, the amount of chemotactic polymersomes in the central nervous system of rat was 4 times higher than that of non-chemotactic polymersomes (20% and 5% of injected dose, respectively) – consisting of symmetric polymersomes, asymmetric but empty polymersomes. Drug-loaded micromotors moving specifically in acidic pH have been reported for drug delivery in the stomach [121,122]. Wang et al. showed the improvement in the *Helicobacter pylori* elimination rate *in vivo* when using clarithromycin-loaded micromotors compared to non-moving microparticles [122]. As shown in Figure 2.3A, the micromotor main component is the Mg core, which reacts with HCl in mice's stomach to move. The directional movement is achieved by the configuration of the TiO_2 shell, which covers partly the Mg core, leaving space for the bubble forming reaction. In Figure 2.3B, the amount of *H. pylori* in mice treated with Mg motor is comparable to mice treated with the conventional method (antibiotic and proton pump inhibitor), confirming the drug-protection capacity of the motor.

Researches about micromotors are mostly conducted in non-biological environments. There are not many investigations *in vivo*, especially the behavior of micromotors in blood, maybe because of their remaining disadvantages. Hydrogen peroxide – the fuel of many micromotor systems, has a very low concentration in blood (1-5 μM at normal state [127]), while the needed H_2O_2 concentration to activate H_2O_2 -fueled micromotors movement is at least 64 mM (0.15% v/v) [115]. Therefore, a direct administration of micromotors to the surrounding site of interest is required. In addition, micromotors are easily recognized and caught by macrophages in the blood, since they do not have any stealth coating. The addition of a stealth layer would cover the reaction site of micromotors, hindering their movement.

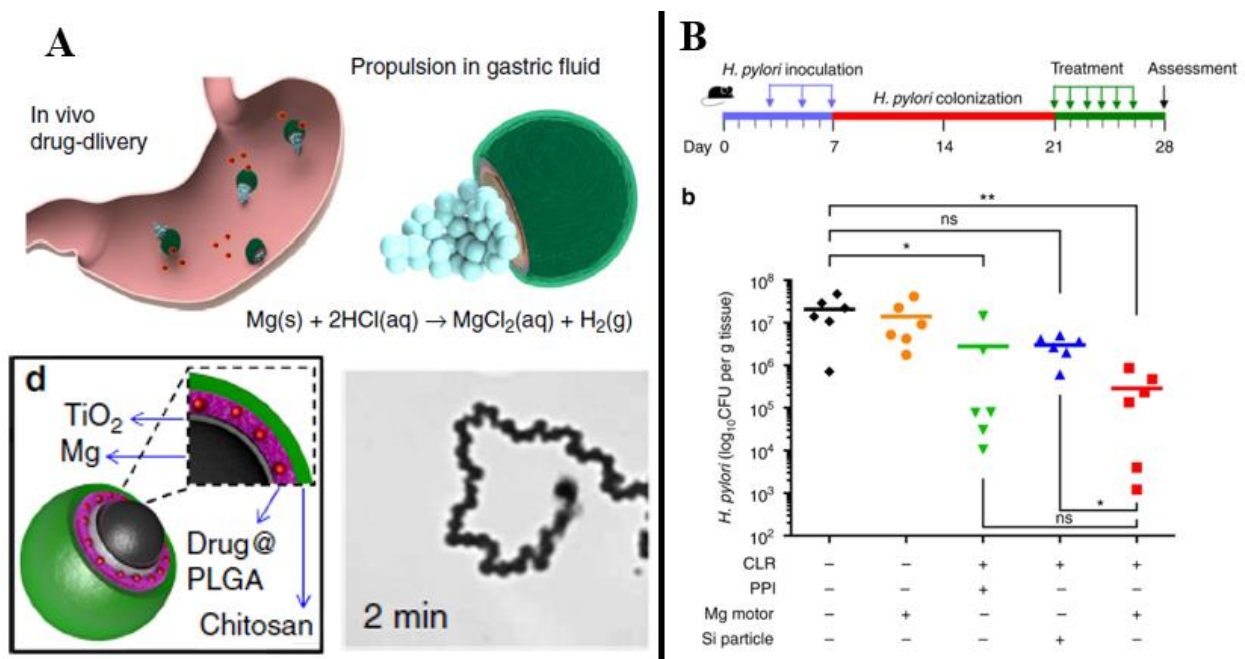


Figure 2.3. (A) Structure and moving mechanism of Mg micro-motor in acidic environments; (B) The application of clarithromycin-loaded micromotors in *H. pylori* treatment in mice shows comparable performance to the combination of clarithromycin and proton pump inhibitor. Reproduced with open-access permission from ref. [122]

2.1.3.2. Biological and bio-hybrid drug carriers

2.1.3.2.1. Bacteria

Bacteria is a potential candidate to carry drugs. They have the ability to locate, target and then to proliferate inside tumors thanks to their chemotactic sensing [128]. Bacteria find the tumor's location by following the chemoattractants in necrotic regions produced by cancer cells, such as aspartate, serine, citrate, ribose and galactose [129]. Then they enter tumors via the leaky vascular networks. Because oxygen acts as a chemorepellant for certain types of bacteria, tumors are perfect niches for them to replicate because of the hypoxia, rich nutrition and lack of immune system environment [128]. Bacteria have been reported to be carriers of proteins [130–133], DNA [134–140] and micro/nanoparticles [141–145] for tumors elimination.

Bacteria can be genetically modified to have the capacity to produce desired therapeutic proteins. The interested proteins, such as anti-tumor cytotoxic agents, are directly expressed in bacteria. The modification procedure is well known and easy to manipulate [146]. With the ability to target and accumulate inside tumors by following chemotactic signals, bacteria enter tumors and express therapeutic proteins, which act as drugs, prodrugs or immune stimulation agents [133]. The combinational therapy involving many drugs can be achieved by integrating several proteins of interest at the same time on bacteria. This *in vivo* production of therapeutic agents reduces the drug purification step in drug production, hence reducing the cost of treatment. In addition,

since the bacteria migrate and express proteins only inside tumors, the systematic toxicity is highly decreased. For example, Tangney et al. reported the use of probiotic bacteria to on-site produce prodrug [132]. *In vitro* and *in vivo* experiments on mice showed the reduction in tumor size and the increase of mice survival rate, indicating the potential of this strategy. In another example, Zheng et al. reported the use of an attenuated *Salmonella Typhimurium* strain, which was genetically engineered to secrete *Vibrio vulnificus* flagellin B (FlaB), to target tumors in mice model [147]. FlaB triggered the recruitment of immune cells, which eliminated and suppressed tumor cells. 55% of mice treated with modified bacteria no longer had tumor after 52 days. Meanwhile, mice treated with PBS or purified FlaB did not show any sign of tumor regression and died before the experiment ended, indicating the importance of the targeting property of bacteria. The secretion of FlaB from engineered bacteria also can prevent metastasis of orthotopic human colon cancer in nude mice. In mice treated with engineered *S. Typhimurium*, only 4 metastasis lesions were found in 3 mice, while 91 lesions were found in PBS treated mice. However, when bacteria express eukaryotic proteins, the lack of post-translational modification, the formation of inclusion bodies, incomplete protein folding or codon usage bias inactivate the produced proteins or reduce the yield rate [148].

Instead of proteins, the delivery of DNA directly into cancer cells using bacteria is an effective strategy to kill cancer cells, which is called bactofection. In comparison to other types of gene delivery vector, the use of bacteria has lower cost and more simple preparation, while still keeps a high delivery load [146]. The gene is embedded into a bacteria plasmid. Then, it is transferred to the host cell nucleus after the internalization of bacteria. Therefore, the most popular choice of plasmid carrier is intracellular bacteria, for example, *Listeria monocytogenes* (*L. monocytogenes*), due to their ability to internalize, live in the cytoplasm and to spread from cells to cells without going through extracellular matrix [146,149]. Proteins of interest are then synthesized and expressed by mammalian cells. This strategy produces more stable expression compared to proteins expressed directly on bacteria [146]. Bactofection has been reported for *in vivo* delivery of therapeutic DNA to inflamed tissue for treatment of inflammatory bowel disease [137], the delivery of herpes simplex virus thymidine kinase and ganciclovir (called suicide gene therapy) to bladder cancer cells, leading to their apoptosis [138–140]. Nevertheless, bactofection is also well-known for its application in the delivery of DNA vaccines, which is a plasmid encoding antigen that provides mammalian cells the immunity against pathogens and cancer cells [134–136]. For example, *L. monocytogenes* have been used to deliver melanoma, cervical and breast cancer antigens to T-cells for cancer immunotherapy [134]. However, not all cancer cells express therapeutic antigens, leading to the uncompleted elimination of cancer cells [150]. Thus, a combination of therapy would be necessary to totally cure a disease.

Using bacteria to deliver protein or DNA requires genetic modification, which can be affected by mutation, hence reducing the efficiency of this method. To avoid this

problem, a division in the responsibility of drug loading and transport is needed. So, the drug is loaded inside a cargo, for example liposomes or nanoparticles, and the duty of bacteria is only carrying the cargo to the desired destination by following chemotactic cues. The cargos can carry any drugs or imaging agents without harming the bacteria. The linkage between cargos and bacteria can be formed without or with very little modification of bacterial membrane, leading to the simplicity in the fabrication of the delivery systems. The cargos-bacteria bond can be bioaffinity [142–144], such as streptavidin-biotin and antibody-antigen, or covalent interaction [151]. For example, Nguyen et al. have reported the attachment of paclitaxel-loaded liposome to *Salmonella Typhimurium* bacteria for tumor targeting and elimination (Figure 2.4) [144]. The paclitaxel-loaded liposome was coated with streptavidin, which could adhere to biotin on the bacteria membrane. Therefore, no complicated modification was needed on bacteria. The drug release rate of the drug-loaded liposomes is similar to the liposome-bacteria system, showing the minor influence of bacteria on the drug release property of liposomes. Thanks to the mobility of bacteria, the liposomes-bacteria system had a higher speed than the only-liposomes formulation, which possessed only Brownian motion (3.09 $\mu\text{m/s}$ and 0.4 $\mu\text{m/s}$, respectively). With the liposomes' size of 2.25 μm , the number of bacteria adhering to one liposome was from 1 to 3. In addition, the bacteria provided the tumors-targeting ability to the system, hence increasing the therapeutic efficiency. *In vitro*, the IC_{50} of the liposome-bacteria system was significantly lower than that of only-liposomes, indicating the high potential of the system. While the strategy of attaching drug-loaded cargos to bacteria ignores the high functionality of bacteria, the simplification in the production process brings the therapy closer to the realization [146].

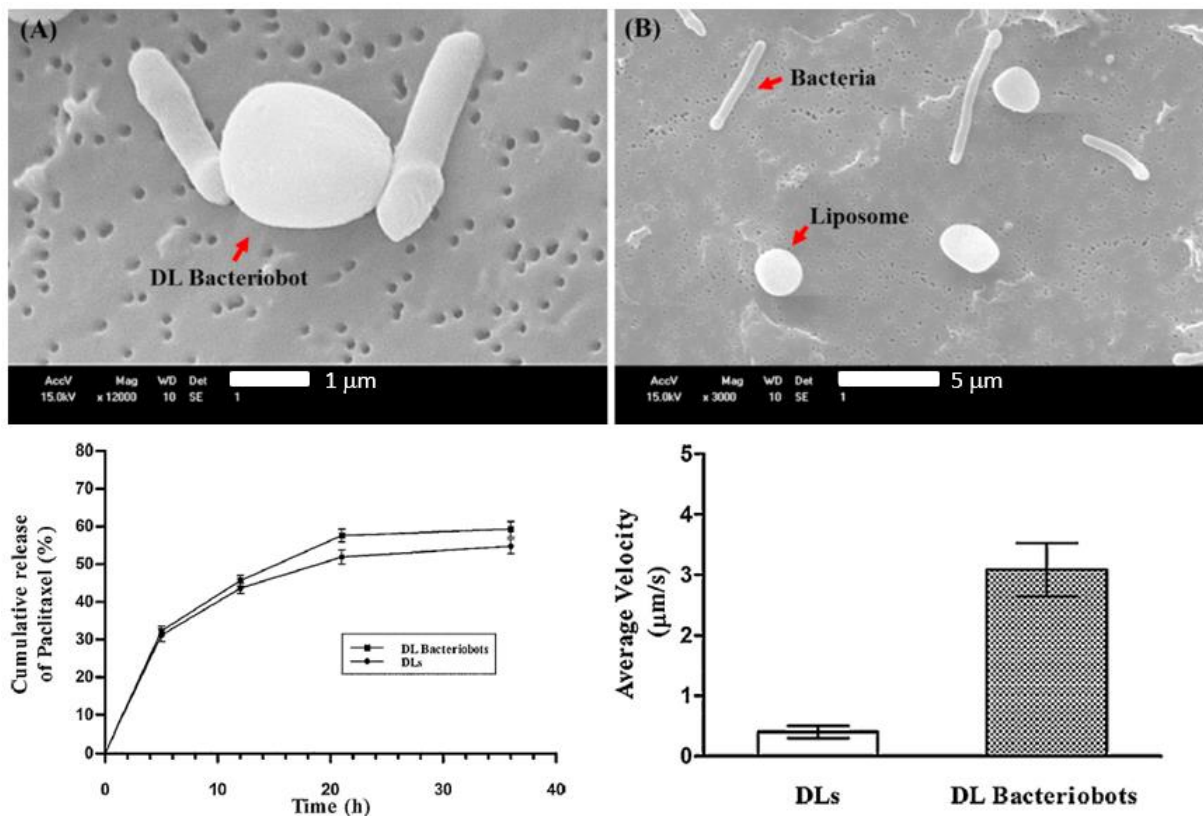


Figure 2.4. Images of *Salmonella Typhimurium* carrying paclitaxel-loaded liposomes; The drug release rate of liposomes and of bacteria carrying liposomes are almost identical, while the moving speed of the bacteria-liposome system is higher than single liposomes. Reproduced with permission from ref. [144]

2.1.3.2.2. Human cells

Besides the same advantages as bacteria in drug delivery applications, human cells also offer the compatibility with the human immune system. With the ability to follow chemotactic signals, immunocytes and stem cells can migrate to injured, inflamed or cancerous sites. For example, the inflammation process recruits many mononuclear phagocytes to inflamed sites [152]. Macrophages and monocytes also accumulate in the hypoxic region of tumors, as reported in prostate and breast cancer [153,154]. In addition, they can pass through biological barriers, such as the blood-brain or blood tumors barrier, then release the loaded drug, enhancing the therapeutic efficacy [155,156]. Another advantage of the human cell drug delivery system is the simple drug loading process. In general, drugs are loaded inside a cargo, for example, nanoparticles, liposomes. Then, the drug-loaded cargos are endocytosed by human cells during the incubation of the cells [157]. Human cells like leukocytes are known to store many compounds in their intracellular vesicles, which is then released via exocytosis at the disease site [158]. Drugs are then released following these chemicals. Human cells acting as promising drug carriers are leukocytes [159–163] and stem cells [164–167] due to their homing property to disease sites. Although red blood cells hold many

advantages to be potential drug carriers, they do not possess any important intrinsic chemotactic movements. Therefore, we do not discuss about them in this review.

Leukocytes hold great potential for targeted drug delivery applications due to their well-known homing behavior to inflammation or pathogens' sites. From the fact that neutrophils have the ability to track, hunt and follow *E. coli*, Qiang He et al. loaded drugs into neutrophils and showed that they could carrier drugs toward an *E. coli* gel via chemotactic movement [159]. The drug – doxorubicin (DOX) was loaded inside mesoporous silica nanoparticles (MSNs), which had high biocompatibility and high specific surface area for drug loading. To reduce drug leakage and increase MSNs uptake by neutrophils, MSNs were coated with a layer of *E. coli* membrane (EM) (Figure 2.5A). EM@MSNs uptake rate by neutrophils was 97.36%, higher than the uptake rate of MSNs (32.58%). The drug leakage rate was significantly reduced in both neutral and acidic pH after the coating of EM. Figure 2.5B shows the directional movement of EM@MSNs carrying neutrophils towards an *E. coli* gel over 8 minutes, with a velocity of 0.165 $\mu\text{m/s}$. In addition to chasing after bacteria, the chemotactic behavior of leukocytes also brings leukocytes in blood or in bone marrows specifically to injured, inflamed locations [168]. Leukocytes were also found inside tumors [169]. Tumor cells undergo inflammation process and secret chemoattractants to attract a high amount of leukocytes, mainly macrophages and T cells [170,171]. Moreover, in the inflammation environment, cell adhesion molecules are overexpressed on the surface of epithelial cells, facilitating the attachment of leukocytes to the epithelial layer, which is highly favorable for drug release [168,172]. Taking advantage of these properties, when leukocytes are loaded with a drug, they carriers the drug to the disease site, accumulate in that region and release the drug, enhancing the therapeutic efficacy. For example, Zhang et al. have reported the use of neutrophils to carry paclitaxel-loaded liposomes to target inflamed brain tumors [160]. Liposome-carried neutrophils migrate to the tumors following inflammatory chemoattractants, penetrate the brain and reduce the recurrence of malignant glioma in mice. However, cancer in mice was not fully cured, even when the chemotactic attraction of cells to disease site was observed. Probably, the drug encapsulation capacity of cells was not high [158]. In addition, leukocytes like macrophage cannot penetrate too far into the tumor. The drug then cannot reach tumor cores. When the size of tumors reduces, hypoxia and other inflammatory signals from the tumor reduced, hence reducing the recruitment of leukocyte and slowing down the treatment [173]. Moreover, macrophages accumulation on the tumor surface would make the size of tumors nearly unchanged [173]. Therefore, the combination of therapies in addition to the use of leukocytes is needed for complete eradication.

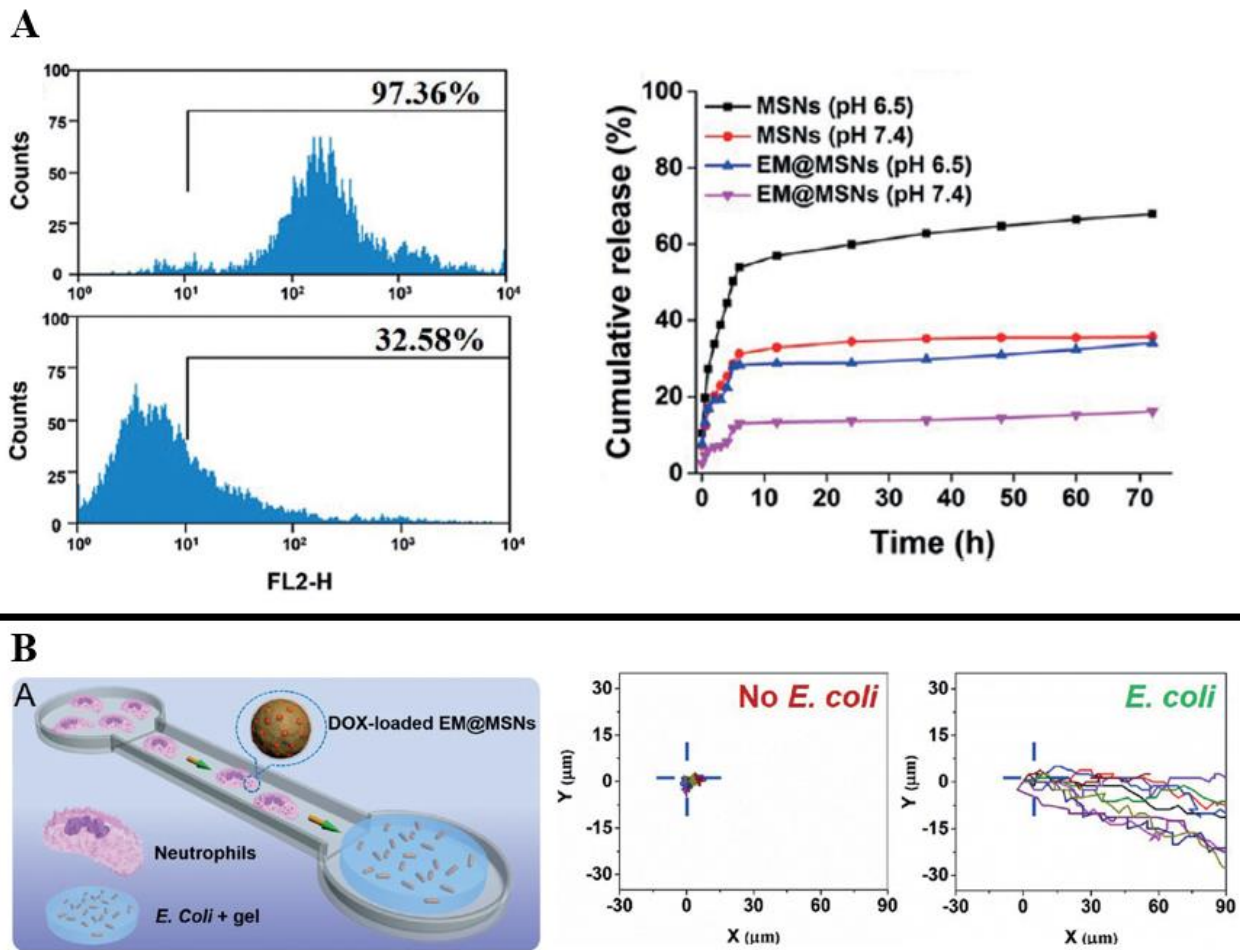


Figure 2.5. (A) EM@MSNs (top-left) and MSNs (bottom-left) uptake percentage by neutrophils characterized by flow cytometry. The release rate of loaded DOX inside each system in different pH shows that the *E. coli* membrane coating reduces the leakage of drug. (B) Trajectories of 10 neutrophils carrying drugs over 8 minutes in the absence or the presence of an *E. coli* gel. Reproduced with permission from ref. [159]

Just like leukocytes, stem cells have the property of homing to inflammation and tumors site. Stem cells surface interacts with chemokines and cytokines secreted by injured tissues [174]. They then migrate, adhere and penetrate into that site [174]. The targeting capacity of stem cells can be improved by overexpressing chemoattractant receptors [174]. In addition to their chemotactic behavior, stem cells are also interesting due to their regenerative function. They can release trophic factors to repair damaged neurons and facilitate recovery [175]. So, they are applied intensively in the treatment of neurodegenerative diseases [176,177]. To enhance the healing capacity of stem cells for angiogenesis improvement, vascular endothelial growth factor (VEGF)-loaded nanoparticles was integrated inside stem cells [167]. After intramuscular injection of modified stem cells and delivery of VEGF, muscle degeneration and tissue fibrosis were highly reduced. This approach would be highly effective for injuries recovery and tissue regeneration. Stem cells are also applied in targeted-delivery of genes. Menon et al. transduced a lentivirus vector of tumor necrosis factor-related apoptosis-inducing

ligand (TRAIL) into mesenchymal stromal cells [166]. After injection, engineered mesenchymal stromal cells migrated to glioma tumors, locally expressed TRAIL to kill cancer cells, leading to the high suppression rate of glioma tumor growth (81.6%) and the high survival rate of the tested animals.

The drug delivery systems using human cells also possess disadvantages. In general, human cells have low drug loading capacity [158]. In addition, both leukocyte and stem cells have the ability to disintegrate and destroy loaded therapeutic agents, leading to even lower loading capacity [158,178]. The drug formulation must also be safe for carrying cells, since they still need to function normally and migrate toward the desired destination. The uptake of nanoparticles modifies cellular membrane, influences the differentiation process and cellular migration [178–180]. For example, after endocytosed titanium oxides nanoparticles, the migration distance of stem cells was reduced [180]. The large TiO₂ nanoparticles inhibit more severely the migration behavior of cells than small nanoparticles [180,181]. Furthermore, after the injection of cells, not all drug-loaded cells migrate to injured sites, leading to the need of overexpressing cellular chemoattractants receptors, which complicates the therapeutic procedure. After the penetration, drug-loaded cells remain inside tumors or disease sites and block new-coming cells, reducing the influence of drugs to the center of the location. Finally, when the tumor's size reduces, the chemotactic signals secreted by cancer cells also decreases, leading to the lower attraction of drug-loaded leukocytes or stem cells [173]. Thus, the total eradication of cancer cells must be realized by other supplementary therapeutic methods.

The sensing ability using chemotaxis only works at short range and cannot be precisely controlled *in vivo*, since the chemical cues source is originated from the desired destination, leading to the low concentration at far distances. Therefore, the injection of drug-loaded bacteria or cells must be near the site of interest. So, using additional guidance, such as a magnetic field, is a strategy to overcome the problem. The external guidance helps the biological carriers get close to the destination, enough to activate the chemotactic sensing. Then, the carriers move along the chemical signal to the site of action. For example, magnetotactic bacteria have both chemotactic and magnetotactic behavior. Felfoul et al. used a magnetic field to guide liposome-loaded magnetotactic bacteria to the tumor region, where the oxygen concentration is suitable for the activation of their aerotactic behavior [96]. The number of bacteria found inside tumors increased approximately 4 times when a magnetic field was applied.

2.2. Attracting targets to a desired location

“Magical bullets” can only be shot at well-defined targets, for example a tumor, or an inflammation site. However, this is not the case for problems like circulating cancer cells, whose location is not always obvious. Using cellular natural taxis behavior, guiding these moving targets to a trap is another strategy to eliminate residual cancer cells or

harmful bacteria living in the body and for disease diagnostics. In another application, the scaffold can be used as a training camp, which attracts, modifies and equips dendritic cells with tumor antigens to increase anti-cancer immunity.

2.2.1. Cancer cells trap

The first strategy is establishing an artificial scaffold to catch metastasis cancer cells to prevent the adhesion of cancer cells, to reduce the metastasis burden for human organs and to detect circulating cancer cells for early detection of cancer metastasis (Figure 2.1D). This niche or trap simulates an optimal environment for cancer cells, deceives and redirects them from their original destination [182–185]. Benefiting the chemotactic behavior of cells, the trap may be loaded with chemokines to enhance cancer cells attraction efficiency. Cancer cells are guided to the trap by extracted exosomes [186,187], cells encapsulated inside the trap [184,188], hypoxia environment creating compound [182], proteins [183,189–191] or nanofibers [192]. The location to install traps is determined based on the information that certain types of cancer cells only migrate and metastasize to certain organs. For example, the bone marrow is a favorite site of metastasis in breast or prostate cancer cases [183], or the peritoneal cavity is a metastasis site of ovarian and colorectal cancer cells [186,188]. Hence, traps are set up in the predicted metastasis destination. Cancer cells stuck inside the traps will be then removed by removing the traps [186,188], be killed by drugs loaded inside the traps [192], by *in situ* hyperthermia [193] or irreversible electroporation activation [194].

The cancer cell traps are applied for early diagnosis of cancer metastasis, by detecting them in the early state, when the metastasis tumors haven't formed [191,195]. Azarin et al. fabricated CCL22 chemokine loaded scaffolds and investigated its behavior using the orthotopic breast cancer metastasis model [191]. CCL22 loaded inside the trap recruits immune cells to trigger an immune response at the scaffold, which facilitates the recruitment of cancer cells. Using inverse spectroscopic optical coherence tomography, the invasion of circulating tumor cells to the trap can be detected via the changes in tissue architecture. After 28 days, the amount of metastasis cancer cells detected in the lung was 88% lower in trap-implanted mice compared to sham treated group, showing that the trap also reduced the metastasis burden.

After the colonization of cancer cells inside traps, the trap removal step is necessary to improve the survival duration of cancer patients. For example, knowing that peritoneal cancer is developed when ovarian cancer cells metastasize to the cavity of peritoneal, the group of De Wever synthesized engineered niches from cancer-associated fibroblasts encapsulated microparticles, which attract peritoneal cancer cells and prevent the adhesion of them to mesothelial cells, delaying tumors formation rate [188]. After being saturated with cancer cells, the microparticles niches were then removed magnetically thanks to an iron oxide coating on the surface. *In vitro*

experiments showed that the system can trap effectively several cell lines and have higher cell attractiveness than an *in vitro* model of the peritoneal wall (64% reduction of cells adhering after the introduction of microparticles). In the xenograft peritoneal cancer model, the group of mice treated with microparticles survived for 67 days, longer than sham-treated mice (50 days), indicating the potential of this treatment. Applying a similar strategy but using scaffolds containing exosomes extracted from ovarian cancer patients, Abal et al. reported the delay of peritoneal cancer metastasis in murine ovarian cancer model [186]. The metastasis trap became a favored destination for metastasis, which distracted circulating cancer cells away from their migration pathway, preventing the occurrence of peritoneal metastasis. With the implantation of the trap, the survival duration increased from 117 days to 199 days, indicating the therapeutic effect of the trap. The presence of the trap delays the metastasis and reduces the burden for the peritoneal cavity. Interestingly, if the trap was removed after one month, the survival duration increased to 309 days, showing the importance of trap removal after the colonization of cancer cells into it.

The removal of tumor traps requires surgery, which may not be favorable for some patients. In addition, the total removal of traps is not easy, especially when many trap systems are micro-size. If trap residual stays inside the human body, they may act as a metastasis enhancement source [188]. Therefore, eliminating cancer cells *in situ* inside traps is a strategy to avoid these problems. Jain et al. encapsulated anti-tumor drugs inside a hydrogel scaffold and guided brain tumors cells there using aligned polycaprolactone nanofibers [192]. From primary brain tumors, cancer cells attached then migrated along nanofibers to the trap. They then underwent apoptosis inside the trap due to the influence of loaded cycloamine. Eighteen days after the implantation of the trap, the tumor volume was approximately 12 times smaller than the tumor volume of the non-treated case. However, in clinical, the insertion of such a large device proposes several difficulties. In another strategy, in which the elimination of cancer cells trapped inside a scaffold is controlled externally, micro-size traps are equipped with metal mesh to induce irreversible electroporation [194] or metal disk to have the heating ability via electromagnetic induction [193].

In clinical, the implantation, the removal and replacement of cancer cell traps require surgery, which is not always possible for patients and may negatively affect their health. The wound site created after surgery is an attractive location for the colonization of cancer cells due to the excessive secretion of growth factors [188]. Thus, this therapeutic approach is not suitable in all cases. After the installation of scaffolds, the *in vivo* monitoring of the trap to quantify the amount of recruited cancer cells need to be done carefully. The saturation of the scaffold leads to the escape of cancer cells, reducing the efficiency of the trap [186]. The residual of scaffolds due to incomplete removal may act as a source of metastasis to enhance tumor progress [188]. The *in situ* elimination of trapped cancer cells strategy using electroporation and electromagnetic induction heating also requires surgery to remove metal parts after the treatment.

Concerning another aspect, cancer cells chemoattractants must be well-characterized and have a high specificity toward cancer cells. The use of cells and exosomes ensures the tumor cells attraction selectivity; however, it complicates the fabrication procedure of tumor traps. Proteins as chemoattractants are easier to manipulate in the procedure of trap synthesis. However, in the case of SDF-1 (also called CXCL12), it also attracts stem cells, speeding up the saturation of the trap [196,197]. In addition, SDF-1 is associated with the process of tumor progression, survival, angiogenesis and metastasis [198].

2.2.2. Immune cells training camp

The rise of cancer is partly originated from the failure of the human immune system. Instead of introducing chemical drugs into the body, training the immune system by equipping them with essential gears is one of the approaches to treat the disease. The *ex vivo* modification of dendritic cells (DCs) approach has been investigated for a long time. It is however an expensive, complicated procedure with inconsistent success rate, and often leads to failures in phase III of clinical trials [199]. The explanations are proposed to be the low number of *ex vivo* modified DCs migration to lymph node and the limitation in the function of *ex vivo* differentiated DCs [199]. To avoid these problems, the *in vivo* modification of DCs method is investigated as a solution. In detail, bio-scaffolds, acting as training camps for dendritic cells, are installed around the body, aiming to expose them with tumor antigens (Figure 2.1E). The key factor for this approach is the chemoattractants loaded inside the scaffold, which attract DCs to the training camps for surface antibody modification and maturation. In addition, drug-loaded bio-scaffolds provide residence sites for DCs, highly improve the therapeutic efficiency compared to bolus formulation [200]. For example, Kumamoto et al. co-implanted MIP-3 β chemokines-loaded and tumor-lysates-loaded polymer rods in the abdominal skin of mice to attract epidermal Langerhans cells [201]. Firstly, the release of MIP-3 β chemokine was controlled to recruits DCs to the polymer rods, with >70% of MIP-3 β released after 48h. Then, the entrapped DCs were exposed to tumor lysates, which helped to modify DCs. In the last step, dinitrofluorobenzene (DNFB) was injected to induce DCs maturation and emigration from the epidermis to lymph nodes. *In vivo* experiments using fibrosarcoma tumor and lung carcinoma mouse model, mice received implanted rods had a significantly lower tumor growth rate compared to non-treated groups, indicating the promising application of this approach. Similarly, Ali et al. loaded into scaffolds granulocyte-macrophage colony-stimulating factor (GM-CSF) as a DCs recruitment factor, cytosine guanosine oligonucleotide (CpG-ODN) as a danger signal to activate DCs and tumor lysates containing tumor antigens [200]. To keep a long-term attraction of DCs, GM-CSF release was controlled to be continuous for 10 days, while CpG-ODN was formulated with polyethylenimine to form cationic charged nanoparticles, improving adhesion to scaffolds, resulting in 80% retention after 25 days. The co-loading of CpG-ODN and GM-CSF into scaffolds increased the amount of activated DCs by 2.5 times, compared to scaffolds loaded only with GM-CSF. Using the

melanoma mouse model, 90% of scaffold-implanted mice survived after 90 days, while non-treated mice survival time was up to 25 days. In the following studies, Ali et al. investigated the therapeutic efficiency of scaffold loaded different chemokines like GM-CSF, Flt3L, CCL20 and adjuvants like Poly-(I:C) and CpG-ODN [202,203]. Different chemokines recruited and activated different subsets of DCs, resulting in different therapeutic efficiency [202]. In the melanoma mouse model, the survival rate of CCL20-loaded scaffold implanted mice after 120 days was approximately 60%, while those of GM-CSF-loaded scaffold and Flt3L-loaded scaffold implanted mice were about 76% and 90%, respectively. Besides melanoma, this approach was tested and showed positive results in glioma mouse [204,205] and Lewis lung carcinoma model [203]. The feasibility of the strategy can be further improved by using injectable bio-scaffold, reducing the side effects of surgery on patients. Using cryo-gelation hydrogel as the scaffold material, several groups have reported the *in vivo* installation of DCs recruitment camps via intramuscular injection [206] or subcutaneous injection method [207–210]. The high porosity and elasticity of hydrogel provide high chemokines encapsulation efficiency and a suitable living environment for DCs [199]. For example, Liu et al. injected GM-CSF-loaded hydrogel into the melanoma mouse model and investigated its therapeutic efficiency [207]. The scaffold recruited a high amount of both DCs and macrophages, peaked at 4 million cells after 1 week; however, most of DCs were inactive. The recruited DCs were then programmed and activated with tumor antigen via the injection of viral or non-viral vectors into the scaffold. The implantation of hydrogel improved cancer immunity in murine melanoma model. The hydrogel-injected mice had a higher survival rate and much lower tumor development rate than non-treated mice. While non-treated mice could not survive for more than 30 days, the survival duration of vaccinated mice was from 40 to 46 days. Similarly, Mooney et al. loaded GM-CSF, CpG and irradiated breast cancer cells into cryogel scaffold, which was then implanted near inguinal lymph nodes of mice [209]. After a burst release initially, the release rate of GM-CSF and CpG from the scaffold was sustained for at least 14 days, long enough for the application (Figure 2.6A). As demonstrated in Figure 2.6A, thanks to the release of GM-CSF, the amount of recruited DCs cells and neutrophils in the chemokines-loaded scaffold was much higher than in the blank scaffold. However, the blank scaffold recruited more macrophages than the GM-CSF-loaded scaffold. To evaluate the efficiency of the vaccine scaffold, it was implanted inside mice, which were challenged with tumor 30 days after vaccination (Figure 2.6B). Vaccinated mice had a higher level of anti-HER2 antibody than mice that were implanted with the blank scaffold. This level of anti-tumor antibody was maintained for at least 37 days after implantation. Interestingly, the scaffold implantation location highly affected the immunity and the survival rate of mice. After 150 days, the survival rate of mice that had scaffold near inguinal lymph nodes was 80%, much higher than mice had scaffold far from inguinal lymph nodes (40%).

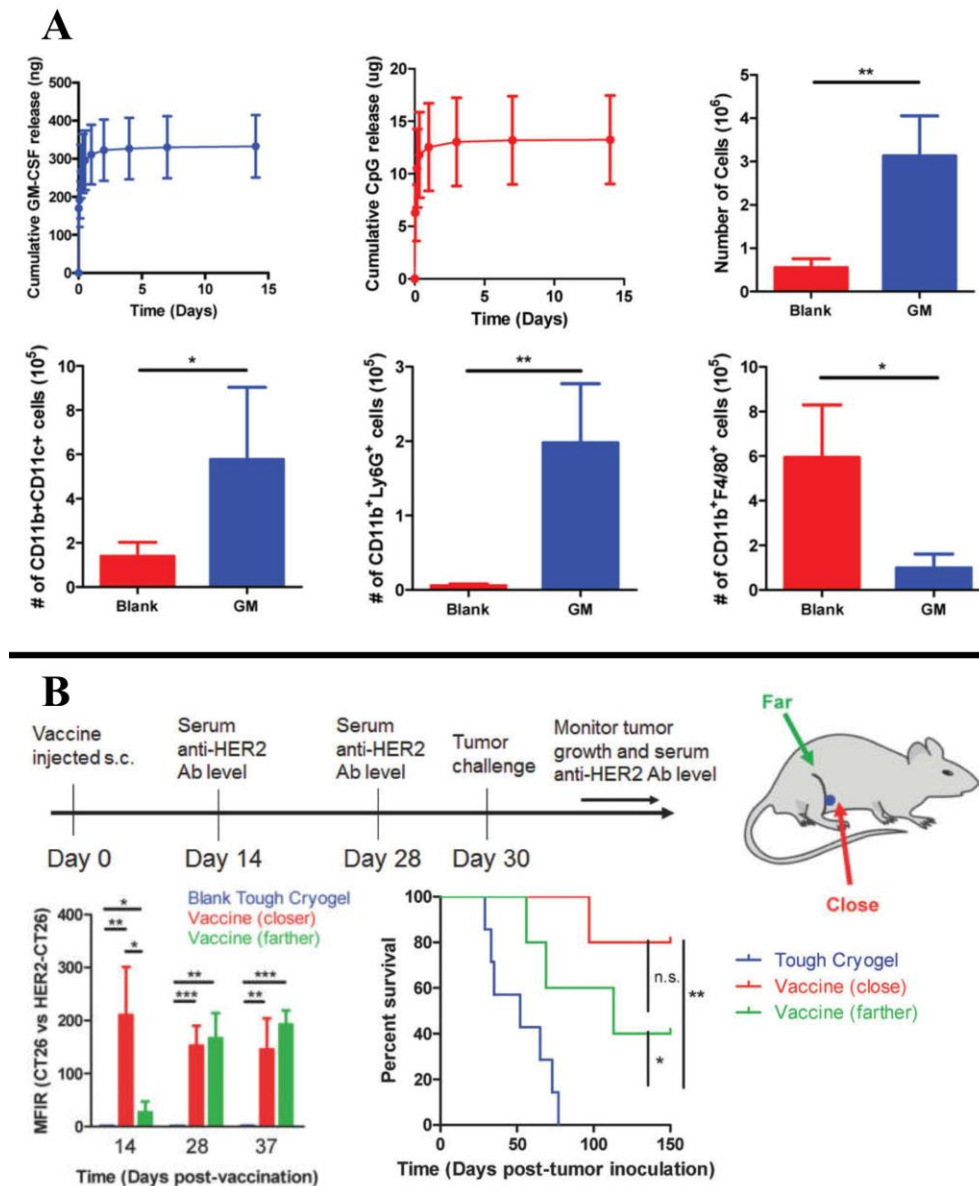


Figure 2.6. (A) The release rate of GM-CSF and CpG from the scaffold; GM-CSF-loaded scaffold recruits more neutrophils and DCs, but fewer macrophages than the blank scaffold. (B) The implantation of the vaccine scaffold improves the production of anti-cancer antibody; the location of implantation (near or far from the draining inguinal lymph nodes) influences the kinetics of antibody response, resulting in the difference in survival rates after 150 days. Reproduced with permission from ref. [209]

While preclinical studies of immune cell training camp strategy have shown a very high potential for cancer treatment and prevention, this strategy cannot prevent the case of tumors escape, which is one main reason for cancer relapse and metastasis. Tumor has mechanisms to escape from the surveillance of the immune system, avoiding the attack of immune cells and facilitating metastasis [211,212]. Whereas immunotherapy boosts the ability of the immune system to fight against tumors, cancer cells can alter the behavior of host immune system via the recruitment of immunosuppressive cells,

which reduce the activity of immune cells and create a tumor immunosuppressive microenvironment [211]. These immunosuppressive cells disturb the surface antigens recognition of DCs, inactivate T and B cells while prevent their proliferation, and inhibit activities of natural killer cells and cytotoxic T lymphocytes [213]. In another strategy, cancer cells can change their antigenicity to hide from DCs. The change and loss of tumor antigenicity are proposed to be originated from the immune selection of mutated cancer cells or from the defects in antigen presentation [212]. To solve the problem of tumor escape, the combination of “training camp” strategy with other immunotherapies is necessary. Calmeiro et al. suggested two potential strategies for the combination, which are using immune checkpoint inhibitors and equipping DCs with specific neoantigens from patient tumors [199]. By delivering immune checkpoint inhibitory molecules, the tumor immunosuppression is inhibited, blocking one of the main routes of tumor escape. Neoantigens can be predicted by studying the frequency of cancer mutation [212]. While several clinical trials of using neoantigens and using immune checkpoint inhibitors have been conducted, the combination of them with a scaffold-based system to boost the treatment efficiency has not been investigated [199]. Further research in these directions are needed to investigate this promising therapy.

3. Future prospects and conclusion

We have reported two targeted taxis-inspired therapeutic strategies: guiding drug carriers to a target and guiding targets to an immobilized drug reservoir. To guide carriers to a target, electric field, magnetic field, and chemical concentration gradient are applied. On the other hand, two types of bio-scaffold to attract tumor cells and DCs are reviewed.

Strategy using magnetic fields to guide drug carriers showed potential results in pre-clinical studies. We have reported the application of two types of magnetic system in targeted drug delivery: magnetic nanoparticles and magnetic micro-swimmers. It has been shown that magnetic nanoparticles systems have less controllability than magnetic micro-swimmers. However, to drive micro-swimmers, we need to know their position and their current orientation, which are only possible under microscope, hindering their application in clinical research. Therefore, while the use of magnetic micro-swimmers for drug delivery stays in *in vitro* research, several magnetic nanoparticles-based drugs have already been investigated in clinical trials. Whereas many of magnetic nanoparticles systems exploited the hyperthermia effect [214–216], certain clinical trials tried to focus magnetic nanoparticles to a site of interest using permanent magnets [217]. Under the guidance of magnetic fields, the penetration depth of drug carriers was indeed increased, but only few centimeters, due to the weak magnetic field of permanent magnets. So, only tumors near or on skin were eligible for this method. To improve the depth of drug delivery, the strength of magnetic field should be increased, and the control of magnetic field direction should be more precise.

The ideas of using superconductor coils magnets, complicated magnets configuration, such as moving magnets, or combination of electromagnets and permanent magnets, were communicated by several groups [42,217]. Yet, due to several difficulties, such as the large size of magnets, or the complication of the configuration, these magnet systems have not been investigated in any clinical studies. Moreover, even if we can control the magnetic field perfectly, the exact location of diseases to guide drugs to is needed. This location is not always obvious, for example, in the case of bone, skin and blood cancer. In addition, the complexity of the blood vessel network complicates the position control of the magnetic nanoparticles.

Electric field guided therapy has shown the improvement in drug delivery through epithelial layers. However, because of the harm of strong electric field, iontophoresis using weak electric field can only reach shallow targets. To get to deeper targets, device implantation is needed, which raises several difficulties of surgery. Iontophoresis has been applied in clinical trials of several diseases like skin, bladder and eyes related diseases [104,108,218], which resulted in very promising results.

Chemical concentration gradient is also a signal to guide drug carriers. Inspired by the chemotactic behavior of organisms, chemical-fueled micromotors moving toward specific molecules are reported with high controllability. However, several improvements are needed to increase their biocompatibility before they can be applied in clinical trials. While the stealth coating is necessary for drug carriers to move in the bloodstream, this coating layer would cover the reaction site of the motor, blocking its movement. Having chemotactic behavior, bacteria and human cells can carry drugs, proteins or genes and delivered them to the desired destination. Several clinical trials have been conducted to investigate the potential of using bacteria in the treatment of cancer [146]. While many promising results were reported, certain clinical trials had to be stopped due to the problem with bacteria's toxicity [146]. In addition, a high dose of bacteria may trigger patient's immune response, clearing all bacteria in the body. Since bacteria may provoke the immune response of the human body, the use of human cells seems to be the more appropriate solution. Exploiting chemotactic behavior of human cells, several therapies using human cells such as immunotherapy or regenerative therapy have been investigated in clinical trials [219–221]. However, there have not been any clinical trials about the use of drug-loaded human cells. With very promising results in pre-clinical studies, this strategy is potential for clinical studies, however, several disadvantages need to be improved to complete the treatment method. Firstly, the stability of human cells-drugs formulation is not high, because drugs may be degraded by human cells after being endocytosed. In addition, the loading of drug, such as nanoparticles, hinders the movement and the migration behavior of cells. Besides, in general, chemotactic behavior only works at short distances from the signal source, due to the low signal concentration at high distances from the source. The combination of chemotactic guided carriers and another guiding approach, for example, magnetic field guided carriers, is necessary to improve the targeting efficiency.

In contrast to the “magic bullet” concept, cancer cells trap, and immune cell training camp are two strategies that use chemotaxis to attract cells to scaffolds pre-installed in the human body. Cancer cells trap attracts metastasis cancer cells and eliminates them, reducing the metastasis burden for organs. Having high biocompatibility, high efficiency in preclinical studies, it is interesting to conduct clinical trials with this strategy to prevent metastasis in cancer patients. The safety and efficiency of a cancer cell trap called M-trap have been investigated in a clinical trial (NCT03085238). Being implanted by surgery in the peritoneal cavity of patients having advanced ovarian cancer, M-trap captured metastasis cells and was removed after 18 months, or after cancer recurrence was detected. From the newest updated results (January 27, 2020), among all recurrent patients, at least 25% of recurrent tumor was captured by the M-trap in 64.3% of patients (10/14 of recurrent patients). During the clinical trial, only 4.3% of patient (1/23 people) had M-trap removal due to device-related adverse events. Instead of attracting cancer cells, immune cells training camp attracts DCs to the scaffold and modifies them with tumor antigens, enhancing anti-cancer immunity. This strategy opens a new way for immunotherapy, and has very positive results in preclinical studies. Until now, a phase I clinical trial is conducting to study the therapeutic efficiency of a PLGA scaffold loaded with patient’s tumor lysate, GM-CSF and CpG in treatment of melanoma (NCT01753089). It will be very interesting to see the results of this study in the future.

Throughout the review, we emphasize that there is no perfect drug delivery system. The combination to cover the disadvantages of each individual strategy is necessary to have an optimized drug carrier. Following this direction, we propose an ideal structure consisting of a “macro-targeting” component and a “micro-targeting” component. When using physical stimuli to guide drug carriers, the location of carriers can be controlled, facilitating the accumulation of drugs to the site of interest. However, it is hard for physical stimuli to penetrate deeply into the human body and to act at cellular resolution. On the other hand, since chemical signals are released from cells, chemotaxis-inspired carriers can reach deep location, increase the interaction between carriers and cells, improve carriers’ retention effect, providing chances for ligand-receptor coupling. Yet, their application is limited due to the low concentration of signals at far distances. These two limitations strongly suggest that real guidance from the entry point to the cellular target requires a two-level strategy: firstly, a “macro-targeting” toward the region of interest, thanks to a physical stimulus as magnetic field; and secondly, a “micro-targeting”, refining the final destination and essentially based on chemo-attraction. Consequently, the ideal carrier should be strongly multifunctional and complex with a physical stimulus-responsive part, a chemical stimulus-responsive domain, a drug reservoir, and a ligands coating layer for active targeting. A possible way to simplify the design of the carrier is to avoid the macro-targeting step. From a certain point of view, the EPR effect is a macro-targeting approach but seems not efficient enough. The injection of drugs carriers near signal sources or the application of drugs in more confined systems than blood circulation (i.e. specific segments of the digestive

tract, bladder, lung...) would increase the success rate. It results from the analysis of the literature, that the most important questionings on nano-/micromotors for drug delivery purposes are the renewal of the fuel, their miniaturization towards nanoscale devices and the biocompatibility of the materials. Drug loading and release did not show any particular difficulties.

In a reverse strategy, the interaction between cells and drugs can be further enhanced when cells move towards drugs. This is the concept of attracting target to a drug-loaded scaffold. Nowadays, this approach is mainly investigated to trap circulating tumor cells in order to reduce metastasis risk. As a lot of bacteria or viruses are highly sensitive to chemo-attractants and developed sophisticated tools to swim through gradients, a similar strategy should be considered for such pathogens. Nonetheless, the scaffold's location is fixed in one location, hence requiring a long time to recruit targets and cannot be applied in the case of low mobility targets.

Whatever the strategy, the development of these bio-inspired drug delivery therapies based on natural taxes requires also models that mimic the conditions of drainage, i.e. blood flow for IV administration or specific dynamics for local administrations. The conditions for success will only be met if the driven forces induced by the chemical or physical stimuli are able to overcome the biological fluid flux in the region of interest.

References

- [1] V.P. Torchilin, Drug targeting, *Eur. J. Pharm. Sci.* 11 (2000) S81–S91. [https://doi.org/10.1016/S0928-0987\(00\)00166-4](https://doi.org/10.1016/S0928-0987(00)00166-4).
- [2] M.-R. Nejadmoghaddam, A. Minai-Tehrani, R. Ghahremanzadeh, M. Mahmoudi, R. Dinarvand, A.-H. Zarnani, Antibody-Drug Conjugates: Possibilities and Challenges, *Avicenna J. Med. Biotechnol.* 11 (2019) 3–23.
- [3] K. Park, Controlled drug delivery systems: Past forward and future back, *J. Controlled Release.* 190 (2014) 3–8. <https://doi.org/10.1016/j.jconrel.2014.03.054>.
- [4] F. Danhier, To exploit the tumor microenvironment: Since the EPR effect fails in the clinic, what is the future of nanomedicine?, *J. Controlled Release.* 244 (2016) 108–121. <https://doi.org/10.1016/j.jconrel.2016.11.015>.
- [5] S. Wilhelm, A.J. Tavares, Q. Dai, S. Ohta, J. Audet, H.F. Dvorak, W.C.W. Chan, Analysis of nanoparticle delivery to tumours, *Nat. Rev. Mater.* 1 (2016) 1–12. <https://doi.org/10.1038/natrevmats.2016.14>.
- [6] L. Salvioni, M.A. Rizzuto, J.A. Bertolini, L. Pandolfi, M. Colombo, D. Prospero, Thirty Years of Cancer Nanomedicine: Success, Frustration, and Hope, *Cancers.* 11 (2019) 1855. <https://doi.org/10.3390/cancers11121855>.

- [7] D. Rosenblum, N. Joshi, W. Tao, J.M. Karp, D. Peer, Progress and challenges towards targeted delivery of cancer therapeutics, *Nat. Commun.* 9 (2018) 1–12. <https://doi.org/10.1038/s41467-018-03705-y>.
- [8] Y.H. Bae, K. Park, Targeted drug delivery to tumors: Myths, reality and possibility, *J. Controlled Release.* 153 (2011) 198–205. <https://doi.org/10.1016/j.jconrel.2011.06.001>.
- [9] D. Baimanov, R. Cai, C. Chen, Understanding the Chemical Nature of Nanoparticle–Protein Interactions, *Bioconj. Chem.* 30 (2019) 1923–1937. <https://doi.org/10.1021/acs.bioconjchem.9b00348>.
- [10] V.H. Nguyen, B.-J. Lee, Protein corona: a new approach for nanomedicine design, *Int. J. Nanomedicine.* 12 (2017) 3137–3151. <https://doi.org/10.2147/IJN.S129300>.
- [11] A.C.S. Owens, S.M. Lewis, The impact of artificial light at night on nocturnal insects: A review and synthesis, *Ecol. Evol.* 8 (2018) 11337–11358. <https://doi.org/10.1002/ece3.4557>.
- [12] M. Kim, A.A. Julius, *Microbiorobotics: Biologically Inspired Microscale Robotic Systems*, William Andrew, 2012.
- [13] D.-P. Häder, R. Hemmersbach, Gravitaxis in *Euglena*, *Adv. Exp. Med. Biol.* 979 (2017) 237–266. https://doi.org/10.1007/978-3-319-54910-1_12.
- [14] S. Pérez-Cerezales, R. Laguna-Barraza, A.C. de Castro, M.J. Sánchez-Calabuig, E. Cano-Oliva, F.J. de Castro-Pita, L. Montoro-Buils, E. Pericuesta, R. Fernández-González, A. Gutiérrez-Adán, Sperm selection by thermotaxis improves ICSI outcome in mice, *Sci. Rep.* 8 (2018). <https://doi.org/10.1038/s41598-018-21335-8>.
- [15] B.J. DuChes, A.D. Doyle, E.K. Dimitriadis, K.M. Yamada, Durotaxis by Human Cancer Cells, *Biophys. J.* 116 (2019) 670–683. <https://doi.org/10.1016/j.bpj.2019.01.009>.
- [16] S. Bellini, On a unique behavior of freshwater bacteria, *Chin. J. Oceanol. Limnol.* 27 (2009) 3–5. <https://doi.org/10.1007/s00343-009-0003-5>.
- [17] R. Blakemore, Magnetotactic bacteria, *Science.* 190 (1975) 377–379. <https://doi.org/10.1126/science.170679>.
- [18] R.B. Frankel, D.A. Bazylinski, D. Schüler, Biomineralization of magnetic iron minerals in bacteria, *Supramol. Sci.* 5 (1998) 383–390. [https://doi.org/10.1016/S0968-5677\(98\)00036-4](https://doi.org/10.1016/S0968-5677(98)00036-4).

- [19] D.A. Bazylinski, R.B. Frankel, Magnetosome formation in prokaryotes, *Nat. Rev. Microbiol.* 2 (2004) 217–230. <https://doi.org/10.1038/nrmicro842>.
- [20] T. Prozorov, D.A. Bazylinski, S.K. Mallapragada, R. Prozorov, Novel magnetic nanomaterials inspired by magnetotactic bacteria: Topical review, *Mater. Sci. Eng. R Rep.* 74 (2013) 133–172. <https://doi.org/10.1016/j.mser.2013.04.002>.
- [21] R.B. Frankel, D.A. Bazylinski, M.S. Johnson, B.L. Taylor, Magneto-aerotaxis in marine coccoid bacteria, *Biophys. J.* 73 (1997) 994–1000. [https://doi.org/10.1016/S0006-3495\(97\)78132-3](https://doi.org/10.1016/S0006-3495(97)78132-3).
- [22] R.B. Frankel, T.J. Williams, D.A. Bazylinski, Magneto-Aerotaxis, in: D. Schüler (Ed.), *Magnetoreception Magnetosomes Bact.*, Springer, Berlin, Heidelberg, 2007: pp. 1–24. https://doi.org/10.1007/7171_2006_036.
- [23] D.B. Dusenbery, *Living at micro scale*, Harvard University Press, Cambridge, 2011.
- [24] R.P. Blakemore, Magnetotactic Bacteria, *Annu. Rev. Microbiol.* 36 (1982) 217–238. <https://doi.org/10.1146/annurev.mi.36.100182.001245>.
- [25] F.F. Guo, W. Yang, W. Jiang, S. Geng, T. Peng, J.L. Li, Magnetosomes eliminate intracellular reactive oxygen species in *Magnetospirillum gryphiswaldense* MSR-1, *Environ. Microbiol.* 14 (2012) 1722–1729. <https://doi.org/10.1111/j.1462-2920.2012.02707.x>.
- [26] Electric fields and wound healing, *Clin. Dermatol.* 2 (1984) 34–44. [https://doi.org/10.1016/0738-081X\(84\)90025-7](https://doi.org/10.1016/0738-081X(84)90025-7).
- [27] G. Tai, B. Reid, L. Cao, M. Zhao, Electrotaxis and Wound Healing: Experimental Methods to Study Electric Fields as a Directional Signal for Cell Migration, in: T. Jin, D. Hereld (Eds.), *Chemotaxis*, Humana Press, Totowa, NJ, 2009: pp. 77–97. https://doi.org/10.1007/978-1-60761-198-1_5.
- [28] A.T. Barker, L.F. Jaffe, J.W. Vanable, The glabrous epidermis of cavies contains a powerful battery, *Am. J. Physiol.-Regul. Integr. Comp. Physiol.* 242 (1982) R358–R366. <https://doi.org/10.1152/ajpregu.1982.242.3.R358>.
- [29] B. Reid, B. Song, C.D. McCaig, M. Zhao, Wound healing in rat cornea: the role of electric currents, *FASEB J.* 19 (2005) 379–386. <https://doi.org/10.1096/fj.04-2325com>.
- [30] M.E. Mycielska, M.B.A. Djamgoz, Cellular mechanisms of direct-current electric field effects: galvanotaxis and metastatic disease, *J. Cell Sci.* 117 (2004) 1631–1639. <https://doi.org/10.1242/jcs.01125>.

- [31] E. Wang, M. Zhao, J.V. Forrester, C.D. MCCAig, Re-orientation and Faster, Directed Migration of Lens Epithelial Cells in a Physiological Electric Field, *Exp. Eye Res.* 71 (2000) 91–98. <https://doi.org/10.1006/exer.2000.0858>.
- [32] S.P. Fraser, J.A. Grimes, M.B.A. Djamgoz, Effects of voltage-gated ion channel modulators on rat prostatic cancer cell proliferation: Comparison of strongly and weakly metastatic cell lines, *The Prostate.* 44 (2000) 61–76. [https://doi.org/10.1002/1097-0045\(20000615\)44:1<61::AID-PROS9>3.0.CO;2-3](https://doi.org/10.1002/1097-0045(20000615)44:1<61::AID-PROS9>3.0.CO;2-3).
- [33] P.J. Mears, S. Koirala, C.V. Rao, I. Golding, Y.R. Chemla, *Escherichia coli* swimming is robust against variations in flagellar number, *ELife.* 3 (2014). <https://doi.org/10.7554/eLife.01916>.
- [34] E. Schiffmann, B.A. Corcoran, S.M. Wahl, N-formylmethionyl peptides as chemoattractants for leucocytes., *Proc. Natl. Acad. Sci. U. S. A.* 72 (1975) 1059–1062.
- [35] J.Y. Huang, E. Goers Sweeney, K. Guillemin, M.R. Amieva, Multiple Acid Sensors Control *Helicobacter pylori* Colonization of the Stomach, *PLOS Pathog.* 13 (2017) e1006118. <https://doi.org/10.1371/journal.ppat.1006118>.
- [36] I.F. Tannock, Acid pH in Tumors and Its Potential for Therapeutic Exploitation, (n.d.) 13.
- [37] R.N. Lawson, M.S. Chughtai, Breast Cancer and Body Temperature, *Can. Med. Assoc. J.* 88 (1963) 68–70.
- [38] M. López-Lázaro, Dual role of hydrogen peroxide in cancer: Possible relevance to cancer chemoprevention and therapy, *Cancer Lett.* 252 (2007) 1–8. <https://doi.org/10.1016/j.canlet.2006.10.029>.
- [39] J. Li, B. Esteban-Fernández de Ávila, W. Gao, L. Zhang, J. Wang, Micro/nanorobots for biomedicine: Delivery, surgery, sensing, and detoxification, *Sci. Robot.* 2 (2017) eaam6431. <https://doi.org/10.1126/scirobotics.aam6431>.
- [40] M. Medina-Sánchez, H. Xu, O.G. Schmidt, Micro- and nano-motors: the new generation of drug carriers, *Ther. Deliv.* 9 (2018) 303–316. <https://doi.org/10.4155/tde-2017-0113>.
- [41] L. Sonntag, J. Simmchen, V. Magdanz, Nano-and Micromotors Designed for Cancer Therapy, *Molecules.* 24 (2019) 3410. <https://doi.org/10.3390/molecules24183410>.
- [42] S. Martel, Magnetic therapeutic delivery using navigable agents, *Ther. Deliv.* 5 (2014) 189–204. <https://doi.org/10.4155/tde.13.147>.

- [43] A. Jordan, R. Scholz, P. Wust, H. Fähling, Roland Felix, Magnetic fluid hyperthermia (MFH): Cancer treatment with AC magnetic field induced excitation of biocompatible superparamagnetic nanoparticles, *J. Magn. Magn. Mater.* 201 (1999) 413–419. [https://doi.org/10.1016/S0304-8853\(99\)00088-8](https://doi.org/10.1016/S0304-8853(99)00088-8).
- [44] S.C. McBain, H.H. Yiu, J. Dobson, Magnetic nanoparticles for gene and drug delivery, *Int. J. Nanomedicine.* 3 (2008) 169–180.
- [45] M.M. Yallapu, S.P. Foy, T.K. Jain, V. Labhasetwar, PEG-Functionalized Magnetic Nanoparticles for Drug Delivery and Magnetic Resonance Imaging Applications, *Pharm. Res.* 27 (2010) 2283–2295. <https://doi.org/10.1007/s11095-010-0260-1>.
- [46] O. Veisoh, J.W. Gunn, M. Zhang, Design and fabrication of magnetic nanoparticles for targeted drug delivery and imaging, *Adv. Drug Deliv. Rev.* 62 (2010) 284–304. <https://doi.org/10.1016/j.addr.2009.11.002>.
- [47] J. Mačiulaitis, M. Deveikytė, S. Rekštytė, M. Bratchikov, A. Darinskas, A. Šimbelytė, G. Daunoras, A. Laurinavičienė, A. Laurinavičius, R. Gudas, M. Malinauskas, R. Mačiulaitis, Preclinical study of SZ2080 material 3D microstructured scaffolds for cartilage tissue engineering made by femtosecond direct laser writing lithography, *Biofabrication.* 7 (2015) 015015. <https://doi.org/10.1088/1758-5090/7/1/015015>.
- [48] Z. Luo, K. Cai, Y. Hu, J. Li, X. Ding, B. Zhang, D. Xu, W. Yang, P. Liu, Redox-Responsive Molecular Nanoreservoirs for Controlled Intracellular Anticancer Drug Delivery Based on Magnetic Nanoparticles, *Adv. Mater.* 24 (2012) 431–435. <https://doi.org/10.1002/adma.201103458>.
- [49] S. Guo, D. Li, L. Zhang, J. Li, E. Wang, Monodisperse mesoporous superparamagnetic single-crystal magnetite nanoparticles for drug delivery, *Biomaterials.* 30 (2009) 1881–1889. <https://doi.org/10.1016/j.biomaterials.2008.12.042>.
- [50] T. Fuchigami, R. Kawamura, Y. Kitamoto, M. Nakagawa, Y. Namiki, A magnetically guided anti-cancer drug delivery system using porous FePt capsules, *Biomaterials.* 33 (2012) 1682–1687. <https://doi.org/10.1016/j.biomaterials.2011.11.016>.
- [51] P. Chen, B. Cui, Y. Bu, Z. Yang, Y. Wang, Synthesis and characterization of mesoporous and hollow-mesoporous $MxFe_3-xO_4$ (M=Mg, Mn, Fe, Co, Ni, Cu, Zn) microspheres for microwave-triggered controllable drug delivery, *J. Nanoparticle Res.* 19 (2017) 398. <https://doi.org/10.1007/s11051-017-4096-z>.

- [52] J. Sun, Y. Li, X.-J. Liang, P.C. Wang, Bacterial Magnetosome: A Novel Biogenetic Magnetic Targeted Drug Carrier with Potential Multifunctions, *J. Nanomater.* 2011 (2011) 1–13. <https://doi.org/10.1155/2011/469031>.
- [53] Y. Liu, G.R. Li, F.F. Guo, W. Jiang, Y. Li, L.J. Li, Large-scale production of magnetosomes by chemostat culture of *Magnetospirillum gryphiswaldense* at high cell density, *Microb. Cell Factories.* 9 (2010) 99. <https://doi.org/10.1186/1475-2859-9-99>.
- [54] J.-B. Sun, F. Zhao, T. Tang, W. Jiang, J. Tian, Y. Li, J.-L. Li, High-yield growth and magnetosome formation by *Magnetospirillum gryphiswaldense* MSR-1 in an oxygen-controlled fermentor supplied solely with air, *Appl. Microbiol. Biotechnol.* 79 (2008) 389. <https://doi.org/10.1007/s00253-008-1453-y>.
- [55] T. Matsunaga, R. Sato, S. Kamiya, T. Tanaka, H. Takeyama, Chemiluminescence enzyme immunoassay using ProteinA-bacterial magnetite complex, *J. Magn. Magn. Mater.* 194 (1999) 126–131. [https://doi.org/10.1016/S0304-8853\(98\)00575-7](https://doi.org/10.1016/S0304-8853(98)00575-7).
- [56] Noriyuki. Nakamura, J. Grant. Burgess, Kaoru. Yagiuda, Satoko. Kudo, Toshifumi. Sakaguchi, Tadashi. Matsunaga, Detection and removal of *Escherichia coli* using fluorescein isothiocyanate conjugated monoclonal antibody immobilized on bacterial magnetic particles, *Anal. Chem.* 65 (1993) 2036–2039. <https://doi.org/10.1021/ac00063a018>.
- [57] N. Nakamura, T. Matsunaga, Highly sensitive detection of allergen using bacterial magnetic particles, *Anal. Chim. Acta.* 281 (1993) 585–589. [https://doi.org/10.1016/0003-2670\(93\)85018-F](https://doi.org/10.1016/0003-2670(93)85018-F).
- [58] J.-B. Sun, J.-H. Duan, S.-L. Dai, J. Ren, L. Guo, W. Jiang, Y. Li, Preparation and anti-tumor efficiency evaluation of doxorubicin-loaded bacterial magnetosomes: Magnetic nanoparticles as drug carriers isolated from *Magnetospirillum gryphiswaldense*, *Biotechnol. Bioeng.* 101 (2008) 1313–1320. <https://doi.org/10.1002/bit.22011>.
- [59] S. Kralj, T. Potrc, P. Kocbek, S. Marchesan, D. Makovec, Design and Fabrication of Magnetically Responsive Nanocarriers for Drug Delivery, *Curr. Med. Chem.* 24 (2017) 454–469. <https://doi.org/10.2174/0929867323666160813211736>.
- [60] C.T. Yavuz, J.T. Mayo, W.W. Yu, A. Prakash, J.C. Falkner, S. Yean, L. Cong, H.J. Shipley, A. Kan, M. Tomson, D. Natelson, V.L. Colvin, Low-Field Magnetic Separation of Monodisperse Fe₃O₄ Nanocrystals, *Science.* 314 (2006) 964–967. <https://doi.org/10.1126/science.1131475>.
- [61] Y. Jun, Y.-M. Huh, J. Choi, J.-H. Lee, H.-T. Song, Kim, S. Yoon, K.-S. Kim, J.-S. Shin, J.-S. Suh, J. Cheon, Nanoscale Size Effect of Magnetic Nanocrystals and Their

Utilization for Cancer Diagnosis via Magnetic Resonance Imaging, *J. Am. Chem. Soc.* 127 (2005) 5732–5733. <https://doi.org/10.1021/ja0422155>.

- [62] X. Batlle, A. Labarta, Finite-size effects in fine particles: magnetic and transport properties, *J. Phys. Appl. Phys.* 35 (2002) R15–R42. <https://doi.org/10.1088/0022-3727/35/6/201>.
- [63] A.-H. Lu, E.L. Salabas, F. Schüth, Magnetic Nanoparticles: Synthesis, Protection, Functionalization, and Application, *Angew. Chem. Int. Ed.* 46 (2007) 1222–1244. <https://doi.org/10.1002/anie.200602866>.
- [64] E. Ruiz-Hernández, A. López-Noriega, D. Arcos, M. Vallet-Regí, Mesoporous magnetic microspheres for drug targeting, *Solid State Sci.* 10 (2008) 421–426. <https://doi.org/10.1016/j.solidstatesciences.2007.11.026>.
- [65] F.-H. Chen, L.-M. Zhang, Q.-T. Chen, Y. Zhang, Z.-J. Zhang, Synthesis of a novel magnetic drug delivery system composed of doxorubicin-conjugated Fe₃O₄ nanoparticle cores and a PEG-functionalized porous silica shell, *Chem. Commun.* 46 (2010) 8633. <https://doi.org/10.1039/c0cc02577a>.
- [66] L. Zhang, S.Z. Qiao, Y.G. Jin, Z.G. Chen, H.C. Gu, G.Q. Lu, Magnetic Hollow Spheres of Periodic Mesoporous Organosilica and Fe₃O₄ Nanocrystals: Fabrication and Structure Control, *Adv. Mater.* 20 (2008) 805–809. <https://doi.org/10.1002/adma.200700900>.
- [67] E. Ruiz-Hernández, A. López-Noriega, D. Arcos, I. Izquierdo-Barba, O. Terasaki, M. Vallet-Regí, Aerosol-Assisted Synthesis of Magnetic Mesoporous Silica Spheres for Drug Targeting, *Chem. Mater.* 19 (2007) 3455–3463. <https://doi.org/10.1021/cm0705789>.
- [68] K.C. Souza, J.D. Ardisson, E.M.B. Sousa, Study of mesoporous silica/magnetite systems in drug controlled release, *J. Mater. Sci. Mater. Med.* 20 (2008) 507. <https://doi.org/10.1007/s10856-008-3592-1>.
- [69] C.A. Monnier, D. Burnand, B. Rothen-Rutishauser, M. Lattuada, A. Petri-Fink, Magnetoliposomes: opportunities and challenges, *Eur. J. Nanomedicine.* 6 (2014). <https://doi.org/10.1515/ejnm-2014-0042>.
- [70] M.R. Faria, M.M. Cruz, M.C. Gonçalves, A. Carvalho, G. Feio, M.B.F. Martins, Synthesis and characterization of magnetoliposomes for MRI contrast enhancement, *Int. J. Pharm.* 446 (2013) 183–190. <https://doi.org/10.1016/j.ijpharm.2013.02.025>.
- [71] J.-P. Fortin-Ripoche, M.S. Martina, F. Gazeau, C. Ménager, C. Wilhelm, J.-C. Bacri, S. Lesieur, O. Clément, Magnetic Targeting of Magnetoliposomes to Solid Tumors

with MR Imaging Monitoring in Mice: Feasibility, *Radiology*. 239 (2006) 415–424. <https://doi.org/10.1148/radiol.2392042110>.

- [72] D. Frascione, C. Diwoky, G. Almer, P. Opriessnig, C. Vonach, K. Gradauer, G. Leitinger, H. Mangge, R. Stollberger, R. Prassl, Ultrasmall superparamagnetic iron oxide (USPIO)-based liposomes as magnetic resonance imaging probes, *Int. J. Nanomedicine*. 7 (2012) 2349–2359. <https://doi.org/10.2147/IJN.S30617>.
- [73] S. García-Jimeno, E. Escribano, J. Queralt, J. Estelrich, Magnetoliposomes prepared by reverse-phase followed by sequential extrusion: Characterization and possibilities in the treatment of inflammation, *Int. J. Pharm.* 405 (2011) 181–187. <https://doi.org/10.1016/j.ijpharm.2010.11.044>.
- [74] B. Garnier, S. Tan, S. Miraux, E. Bled, A.R. Brisson, Optimized synthesis of 100 nm diameter magnetoliposomes with high content of maghemite particles and high MRI effect, *Contrast Media Mol. Imaging*. 7 (2012) 231–239. <https://doi.org/10.1002/cmimi.487>.
- [75] J. Giri, S. Guha Thakurta, J. Bellare, A. Kumar Nigam, D. Bahadur, Preparation and characterization of phospholipid stabilized uniform sized magnetite nanoparticles, *J. Magn. Mater.* 293 (2005) 62–68. <https://doi.org/10.1016/j.jmmm.2005.01.044>.
- [76] Y. Chen, A. Bose, G.D. Bothun, Controlled Release from Bilayer-Decorated Magnetoliposomes via Electromagnetic Heating, *ACS Nano*. 4 (2010) 3215–3221. <https://doi.org/10.1021/nn100274v>.
- [77] A. Floris, A. Ardu, A. Musinu, G. Piccaluga, A. M. Fadda, C. Sinico, C. Cannas, SPION@liposomes hybrid nanoarchitectures with high density SPION association, *Soft Matter*. 7 (2011) 6239–6247. <https://doi.org/10.1039/C1SM05059A>.
- [78] C. Bonnaud, C.A. Monnier, D. Demurtas, C. Jud, D. Vanhecke, X. Montet, R. Hovius, M. Lattuada, B. Rothen-Rutishauser, A. Petri-Fink, Insertion of Nanoparticle Clusters into Vesicle Bilayers, *ACS Nano*. 8 (2014) 3451–3460. <https://doi.org/10.1021/nn406349z>.
- [79] E. Amstad, J. Kohlbrecher, E. Müller, T. Schweizer, M. Textor, E. Reimhult, Triggered Release from Liposomes through Magnetic Actuation of Iron Oxide Nanoparticle Containing Membranes, *Nano Lett.* 11 (2011) 1664–1670. <https://doi.org/10.1021/nl2001499>.
- [80] H. Marie, L. Lemaire, F. Franconi, S. Lajnef, Y.-M. Frapart, V. Nicolas, G. Frébourg, M. Trichet, C. Ménager, S. Lesieur, Superparamagnetic Liposomes for MRI Monitoring and External Magnetic Field-Induced Selective Targeting of Malignant

Brain Tumors, *Adv. Funct. Mater.* 25 (2015) 1258–1269.
<https://doi.org/10.1002/adfm.201402289>.

- [81] M.-S. Martina, J.-P. Fortin, C. Ménager, O. Clément, G. Barratt, C. Grabielle-Madelmont, F. Gazeau, V. Cabuil, S. Lesieur, Generation of Superparamagnetic Liposomes Revealed as Highly Efficient MRI Contrast Agents for *in vivo* Imaging, *J. Am. Chem. Soc.* 127 (2005) 10676–10685. <https://doi.org/10.1021/ja0516460>.
- [82] E. Millart, S. Lesieur, V. Faivre, Superparamagnetic lipid-based hybrid nanosystems for drug delivery, *Expert Opin. Drug Deliv.* 15 (2018) 523–540. <https://doi.org/10.1080/17425247.2018.1453804>.
- [83] D. Tarn, C.E. Ashley, M. Xue, E.C. Carnes, J.I. Zink, C.J. Brinker, Mesoporous Silica Nanoparticle Nanocarriers: Biofunctionality and Biocompatibility, *Acc. Chem. Res.* 46 (2013) 792–801. <https://doi.org/10.1021/ar3000986>.
- [84] F. Tang, L. Li, D. Chen, Mesoporous Silica Nanoparticles: Synthesis, Biocompatibility and Drug Delivery, *Adv. Mater.* 24 (2012) 1504–1534. <https://doi.org/10.1002/adma.201104763>.
- [85] T. Asefa, Z. Tao, Biocompatibility of Mesoporous Silica Nanoparticles, *Chem. Res. Toxicol.* 25 (2012) 2265–2284. <https://doi.org/10.1021/tx300166u>.
- [86] Q. He, J. Shi, Mesoporous silica nanoparticle based nano drug delivery systems: synthesis, controlled drug release and delivery, pharmacokinetics and biocompatibility, *J. Mater. Chem.* 21 (2011) 5845–5855. <https://doi.org/10.1039/C0JM03851B>.
- [87] B. Ramaswamy, S.D. Kulkarni, P.S. Villar, R.S. Smith, C. Eberly, R.C. Araneda, D.A. Depireux, B. Shapiro, Movement of Magnetic Nanoparticles in Brain Tissue: Mechanisms and Safety, *Nanomedicine Nanotechnol. Biol. Med.* 11 (2015) 1821–1829. <https://doi.org/10.1016/j.nano.2015.06.003>.
- [88] M. Mohseni, J.J. Connell, C. Payne, P.S. Patrick, R. Baker, Y. Yu, B. Siow, M. Zaw-Thin, T.L. Kalber, Q.A. Pankhurst, M.F. Lythgoe, Scalable magnet geometries enhance tumour targeting of magnetic nano-carriers, *Mater. Des.* 191 (2020) 108610. <https://doi.org/10.1016/j.matdes.2020.108610>.
- [89] D.N. Price, L.R. Stromberg, N.K. Kunda, P. Muttill, *In vivo* Pulmonary Delivery and Magnetic-Targeting of Dry Powder Nano-in-Microparticles, *Mol. Pharm.* 14 (2017) 4741–4750. <https://doi.org/10.1021/acs.molpharmaceut.7b00532>.
- [90] K.T. Al-Jamal, J. Bai, J.T.-W. Wang, A. Protti, P. Southern, L. Bogart, H. Heidari, X. Li, A. Cakebread, D. Asker, W.T. Al-Jamal, A. Shah, S. Bals, J. Sosabowski, Q.A. Pankhurst, Magnetic Drug Targeting: Preclinical *in vivo* Studies, *Mathematical*

Modeling, and Extrapolation to Humans, *Nano Lett.* 16 (2016) 5652–5660.
<https://doi.org/10.1021/acs.nanolett.6b02261>.

- [91] W. Gao, D. Kagan, O.S. Pak, C. Clawson, S. Campuzano, E. Chuluun-Erdene, E. Shipton, E.E. Fullerton, L. Zhang, E. Lauga, J. Wang, Cargo-Towing Fuel-Free Magnetic Nanoswimmers for Targeted Drug Delivery, *Small*. 8 (2012) 460–467.
<https://doi.org/10.1002/sml.201101909>.
- [92] F. Qiu, S. Fujita, R. Mhanna, L. Zhang, B.R. Simona, B.J. Nelson, Magnetic Helical Microswimmers Functionalized with Lipoplexes for Targeted Gene Delivery, *Adv. Funct. Mater.* 25 (2015) 1666–1671. <https://doi.org/10.1002/adfm.201403891>.
- [93] S. Tottori, L. Zhang, F. Qiu, K.K. Krawczyk, A. Franco-Obregón, B.J. Nelson, Magnetic Helical Micromachines: Fabrication, Controlled Swimming, and Cargo Transport, *Adv. Mater.* 24 (2012) 811–816.
<https://doi.org/10.1002/adma.201103818>.
- [94] M.M. Stanton, B.-W. Park, D. Vilela, K. Bente, D. Faivre, M. Sitti, S. Sánchez, Magnetotactic Bacteria Powered Biohybrids Target *E. coli* Biofilms, *ACS Nano*. 11 (2017) 9968–9978. <https://doi.org/10.1021/acsnano.7b04128>.
- [95] H. Xu, M. Medina-Sánchez, V. Magdanz, L. Schwarz, F. Hebenstreit, O.G. Schmidt, Sperm-Hybrid Micromotor for Targeted Drug Delivery, *ACS Nano*. 12 (2018) 327–337. <https://doi.org/10.1021/acsnano.7b06398>.
- [96] O. Felfoul, M. Mohammadi, S. Taherkhani, D. de Lanauze, Y. Zhong Xu, D. Loghin, S. Essa, S. Jancik, D. Houle, M. Lafleur, L. Gaboury, M. Tabrizian, N. Kaou, M. Atkin, T. Vuong, G. Batist, N. Beauchemin, D. Radzioch, S. Martel, Magneto-aerotactic bacteria deliver drug-containing nanoliposomes to tumour hypoxic regions, *Nat. Nanotechnol.* 11 (2016) 941–947.
<https://doi.org/10.1038/nnano.2016.137>.
- [97] B.-W. Park, J. Zhuang, O. Yasa, M. Sitti, Multifunctional Bacteria-Driven Microswimmers for Targeted Active Drug Delivery, *ACS Nano*. 11 (2017) 8910–8923. <https://doi.org/10.1021/acsnano.7b03207>.
- [98] B. Shapiro, Towards dynamic control of magnetic fields to focus magnetic carriers to targets deep inside the body, *J. Magn. Magn. Mater.* 321 (2009) 1594–1599. <https://doi.org/10.1016/j.jmmm.2009.02.094>.
- [99] V.V.K. Venuganti, M. Saraswathy, C. Dwivedi, R.S. Kaushik, O.P. Perumal, Topical gene silencing by iontophoretic delivery of an antisense oligonucleotide-dendrimer nanocomplex: the proof of concept in a skin cancer mouse model, *Nanoscale*. 7 (2015) 3903–3914. <https://doi.org/10.1039/c4nr05241b>.

- [100] M. Toyoda, S. Hama, Y. Ikeda, Y. Nagasaki, K. Kogure, Anti-cancer vaccination by transdermal delivery of antigen peptide-loaded nanogels via iontophoresis, *Int. J. Pharm.* 483 (2015) 110–114. <https://doi.org/10.1016/j.ijpharm.2015.02.024>.
- [101] L.A. Huber, T.A. Pereira, D.N. Ramos, L.C.D. Rezende, F.S. Emery, L.M. Sobral, A.M. Leopoldino, R.F.V. Lopez, Topical Skin Cancer Therapy Using Doxorubicin-Loaded Cationic Lipid Nanoparticles and Iontophoresis, (2015). <https://doi.org/info:doi/10.1166/jbn.2015.2139>.
- [102] C.N. Lemos, J.G. de Souza, P.S. Simão, R.F.V. Lopez, Iontophoresis Improved Growth Reduction of Invasive Squamous Cell Carcinoma in Topical Photodynamic Therapy, *PLoS ONE*. 11 (2016). <https://doi.org/10.1371/journal.pone.0145922>.
- [103] R. Petrilli, J.O. Eloy, F.P. Saggiaro, D.L. Chesca, M.C. de Souza, M.V.S. Dias, L.L.P. daSilva, R.J. Lee, R.F.V. Lopez, Skin cancer treatment effectiveness is improved by iontophoresis of EGFR-targeted liposomes containing 5-FU compared with subcutaneous injection, *J. Controlled Release*. 283 (2018) 151–162. <https://doi.org/10.1016/j.jconrel.2018.05.038>.
- [104] J.D. Byrne, J.J. Yeh, J.M. DeSimone, Use of iontophoresis for the treatment of cancer, *J. Controlled Release*. 284 (2018) 144–151. <https://doi.org/10.1016/j.jconrel.2018.06.020>.
- [105] F. Liu, L. Liu, Iontophoretic delivery of lignocaine in healthy volunteers: effect of concentration of epinephrine on local anesthesia, (2017). <https://www.biomedres.info/abstract/iontophoretic-delivery-of-lignocaine-in-healthy-volunteers-effect-of-concentration-of-epinephrine-on-local-anesthesia-6282.html> (accessed March 23, 2020).
- [106] R.G. Manjunatha, R. Prasad, S. Sharma, R.P. Narayan, V. Koul, Iontophoretic delivery of lidocaine hydrochloride through ex-vivo human skin, *J. Dermatol. Treat.* 31 (2020) 191–199. <https://doi.org/10.1080/09546634.2019.1589640>.
- [107] S.M.D. Stasi, G. Vespasiani, A. Giannantoni, R. Massoud, S. Dolci, F. Micali, Electromotive Delivery of Mitomycin C into Human Bladder Wall, *Cancer Res.* 57 (1997) 875–880.
- [108] S.M. Di Stasi, C. Verri, F. Celestino, F. De Carlo, V. Pagliarulo, Intravesical Electro-Osmotic Administration of Mitomycin C, *Urol. J.* 83 (2016) 18–23. <https://doi.org/10.5301/uro.5000202>.
- [109] C. Gan, S. Amery, K. Chatterton, M.S. Khan, K. Thomas, T. O'Brien, Sequential bacillus Calmette-Guérin/Electromotive Drug Administration of Mitomycin C as the Standard Intravesical Regimen in High Risk Nonmuscle Invasive Bladder Cancer: 2-

Year Outcomes, *J. Urol.* 195 (2016) 1697–1703.

<https://doi.org/10.1016/j.juro.2016.01.103>.

- [110] J.D. Byrne, M.N. R. Jajja, A.T. O'Neill, L.R. Bickford, A.W. Keeler, N. Hyder, K. Wagner, A. Deal, R.E. Little, R.A. Moffitt, C. Stack, M. Nelson, C.R. Brooks, W. Lee, J.C. Luft, M.E. Napier, D. Darr, C.K. Anders, R. Stack, J.E. Tepper, A.Z. Wang, W.C. Zamboni, J.J. Yeh, J.M. DeSimone, Local iontophoretic administration of cytotoxic therapies to solid tumors, *Sci. Transl. Med.* 7 (2015) 273ra14-273ra14. <https://doi.org/10.1126/scitranslmed.3009951>.
- [111] D. Li, K. Xie, R. Wolff, J.L. Abbruzzese, Pancreatic cancer, *The Lancet.* 363 (2004) 1049–1057. [https://doi.org/10.1016/S0140-6736\(04\)15841-8](https://doi.org/10.1016/S0140-6736(04)15841-8).
- [112] J.D. Byrne, M.R.N. Jajja, A.N. Schorzman, A.W. Keeler, J.C. Luft, W.C. Zamboni, J.M. DeSimone, J.J. Yeh, Iontophoretic device delivery for the localized treatment of pancreatic ductal adenocarcinoma, *Proc. Natl. Acad. Sci.* 113 (2016) 2200–2205. <https://doi.org/10.1073/pnas.1600421113>.
- [113] C.R. Anderson, R.L. Morris, S.D. Boeh, P.C. Panus, W.L. Sembrowich, Effects of iontophoresis current magnitude and duration on dexamethasone deposition and localized drug retention, *Phys. Ther.* 83 (2003) 161–170.
- [114] D.O. Draper, M. Coglianese, C. Castel, Absorption of Iontophoresis-Driven 2% Lidocaine With Epinephrine in the Tissues at 5 mm Below the Surface of the Skin, *J. Athl. Train.* 46 (2011) 277–281.
- [115] F. Peng, Y. Tu, J.C.M. van Hest, D.A. Wilson, Self-Guided Supramolecular Cargo-Loaded Nanomotors with Chemotactic Behavior towards Cells, *Angew. Chem. Int. Ed.* 54 (2015) 11662–11665. <https://doi.org/10.1002/anie.201504186>.
- [116] S. Nakata, M. Nomura, H. Yamamoto, S. Izumi, N.J. Suematsu, Y. Ikura, T. Amemiya, Periodic Oscillatory Motion of a Self-Propelled Motor Driven by Decomposition of H₂O₂ by Catalase, *Angew. Chem.* 129 (2017) 879–882. <https://doi.org/10.1002/ange.201609971>.
- [117] L. Baraban, S.M. Harazim, S. Sanchez, O.G. Schmidt, Chemotactic Behavior of Catalytic Motors in Microfluidic Channels, *Angew. Chem. Int. Ed.* 52 (2013) 5552–5556. <https://doi.org/10.1002/anie.201301460>.
- [118] G. Zhao, M. Pumera, Geometric asymmetry driven Janus micromotors, *Nanoscale.* 6 (2014) 11177–11180. <https://doi.org/10.1039/C4NR02393E>.
- [119] W. Gao, M. D'Agostino, V. Garcia-Gradilla, J. Orozco, J. Wang, Multi-Fuel Driven Janus Micromotors, *Small.* 9 (2013) 467–471. <https://doi.org/10.1002/sml.201201864>.

- [120] X. Ma, S. Jang, M.N. Popescu, W.E. Uspal, A. Miguel-López, K. Hahn, D.-P. Kim, S. Sánchez, Reversed Janus Micro/Nanomotors with Internal Chemical Engine, *ACS Nano*. 10 (2016) 8751–8759. <https://doi.org/10.1021/acsnano.6b04358>.
- [121] J. Li, P. Angsantikul, W. Liu, B. Esteban-Fernández de Ávila, S. Thamphiwatana, M. Xu, E. Sandraz, X. Wang, J. Delezuk, W. Gao, L. Zhang, J. Wang, Micromotors Spontaneously Neutralize Gastric Acid for pH-Responsive Payload Release, *Angew. Chem. Int. Ed.* 56 (2017) 2156–2161. <https://doi.org/10.1002/anie.201611774>.
- [122] B.E.-F. de Ávila, P. Angsantikul, J. Li, M. Angel Lopez-Ramirez, D.E. Ramírez-Herrera, S. Thamphiwatana, C. Chen, J. Delezuk, R. Samakapiruk, V. Ramez, M. Obonyo, L. Zhang, J. Wang, Micromotor-enabled active drug delivery for *in vivo* treatment of stomach infection, *Nat. Commun.* 8 (2017) 272. <https://doi.org/10.1038/s41467-017-00309-w>.
- [123] T.P. Szatrowski, C.F. Nathan, Production of Large Amounts of Hydrogen Peroxide by Human Tumor Cells, *Cancer Res.* 51 (1991) 6.
- [124] Y. Kato, S. Ozawa, C. Miyamoto, Y. Maehata, A. Suzuki, T. Maeda, Y. Baba, Acidic extracellular microenvironment and cancer, *Cancer Cell Int.* 13 (2013) 89. <https://doi.org/10.1186/1475-2867-13-89>.
- [125] R.A. Pavlick, S. Sengupta, T. McFadden, H. Zhang, A. Sen, A Polymerization-Powered Motor, *Angew. Chem. Int. Ed.* 50 (2011) 9374–9377. <https://doi.org/10.1002/anie.201103565>.
- [126] A. Joseph, C. Contini, D. Cecchin, S. Nyberg, L. Ruiz-Perez, J. Gaitzsch, G. Fullstone, X. Tian, J. Azizi, J. Preston, G. Volpe, G. Battaglia, Chemotactic synthetic vesicles: Design and applications in blood-brain barrier crossing, *Sci. Adv.* 3 (2017) e1700362. <https://doi.org/10.1126/sciadv.1700362>.
- [127] H.J. Forman, A. Bernardo, K.J.A. Davies, What is the concentration of hydrogen peroxide in blood and plasma?, *Arch. Biochem. Biophys.* 603 (2016) 48–53. <https://doi.org/10.1016/j.abb.2016.05.005>.
- [128] J. Cummins, M. Tangney, Bacteria and tumours: causative agents or opportunistic inhabitants?, *Infect. Agent. Cancer.* 8 (2013) 11. <https://doi.org/10.1186/1750-9378-8-11>.
- [129] C.K. Baban, M. Cronin, D. O'Hanlon, G.C. O'Sullivan, M. Tangney, Bacteria as vectors for gene therapy of cancer, *Bioeng. Bugs.* 1 (2010) 385–394. <https://doi.org/10.4161/bbug.1.6.13146>.
- [130] M.M. Seavey, Z.-K. Pan, P.C. Maciag, A. Wallecha, S. Rivera, Y. Paterson, V. Shahabi, A Novel Human Her-2/neu Chimeric Molecule Expressed by *Listeria*

monocytogenes Can Elicit Potent HLA-A2 Restricted CD8-positive T cell Responses and Impact the Growth and Spread of Her-2/neu-positive Breast Tumors, *Clin. Cancer Res.* 15 (2009) 924–932. <https://doi.org/10.1158/1078-0432.CCR-08-2283>.

- [131] J. Theys, O. Pennington, L. Dubois, G. Anlezark, T. Vaughan, A. Mengesha, W. Landuyt, J. Anné, P.J. Burke, P. Dûrre, B.G. Wouters, N.P. Minton, P. Lambin, Repeated cycles of Clostridium -directed enzyme prodrug therapy result in sustained antitumour effects *in vivo*, *Br. J. Cancer.* 95 (2006) 1212–1219. <https://doi.org/10.1038/sj.bjc.6603367>.
- [132] P. Lehouritis, M. Stanton, F.O. McCarthy, M. Jeavons, M. Tangney, Activation of multiple chemotherapeutic prodrugs by the natural enzymolome of tumour-localised probiotic bacteria, *J. Controlled Release.* 222 (2016) 9–17. <https://doi.org/10.1016/j.jconrel.2015.11.030>.
- [133] N.S. Forbes, Engineering the perfect (bacterial) cancer therapy, *Nat. Rev. Cancer.* 10 (2010) 785–794. <https://doi.org/10.1038/nrc2934>.
- [134] L.M. Wood, P.D. Guirnalda, M.M. Seavey, Y. Paterson, Cancer immunotherapy using *Listeria monocytogenes* and listerial virulence factors, *Immunol. Res.* 42 (2008) 233–245. <https://doi.org/10.1007/s12026-008-8087-0>.
- [135] I. Gentshev, G. Dietrich, S. Spreng, A. Kolb-Mäurer, V. Brinkmann, L. Grode, J. Hess, S.H.E. Kaufmann, W. Goebel, Recombinant attenuated bacteria for the delivery of subunit vaccines, *Vaccine.* 19 (2001) 2621–2628. [https://doi.org/10.1016/S0264-410X\(00\)00502-8](https://doi.org/10.1016/S0264-410X(00)00502-8).
- [136] G. Sciaranghella, S.K. Lakhashe, M. Ayash-Rashkovsky, S. Mirshahidi, N.B. Siddappa, F.J. Novembre, V. Velu, R.R. Amara, C. Zhou, S. Li, Z. Li, F.R. Frankel, R.M. Ruprecht, A live attenuated *Listeria monocytogenes* vaccine vector expressing SIV Gag is safe and immunogenic in macaques and can be administered repeatedly, *Vaccine.* 29 (2011) 476–486. <https://doi.org/10.1016/j.vaccine.2010.10.072>.
- [137] R. Palffy, R. Gardlik, M. Behuliak, P. Jani, D. Balakova, L. Kadası, J. Turna, P. Celec, Salmonella-mediated gene therapy in experimental colitis in mice, *Exp. Biol. Med.* 236 (2011) 177–183. <https://doi.org/10.1258/ebm.2010.010277>.
- [138] X. Yin, B. Yu, Z. Tang, B. He, J. Ren, X. Xiao, W. Tang, Bifidobacterium infantis - mediated HSV-TK/GCV suicide gene therapy induces both extrinsic and intrinsic apoptosis in a rat model of bladder cancer, *Cancer Gene Ther.* 20 (2013) 77–81. <https://doi.org/10.1038/cgt.2012.86>.
- [139] L. Jiang, J. Ren, X. Xiao, Y.-Y. Tang, H.-Q. Weng, Q. Yang, M.-J. Wu, W. Tang, Proteomic analysis of bladder cancer by iTRAQ after Bifidobacterium infantis-

mediated HSV-TK/GCV suicide gene treatment, *Biol. Chem.* 394 (2013) 1333–1342. <https://doi.org/10.1515/hsz-2013-0201>.

- [140] X. Xiao, R. Jin, J. Li, Y. Bei, T. Wei, The Antitumor Effect of Suicide Gene Therapy Using *Bifidobacterium infantis*-mediated Herpes Simplex Virus Thymidine Kinase/Ganciclovir in a Nude Mice Model of Renal Cell Carcinoma, *Urology*. 84 (2014) 982.e15-982.e20. <https://doi.org/10.1016/j.urology.2014.05.020>.
- [141] C.-H. Luo, C.-T. Huang, C.-H. Su, C.-S. Yeh, Bacteria-Mediated Hypoxia-Specific Delivery of Nanoparticles for Tumors Imaging and Therapy, *Nano Lett.* 16 (2016) 3493–3499. <https://doi.org/10.1021/acs.nanolett.6b00262>.
- [142] M. Kojima, Z. Zhang, M. Nakajima, K. Ooe, T. Fukuda, Construction and evaluation of bacteria-driven liposome, *Sens. Actuators B Chem.* 183 (2013) 395–400. <https://doi.org/10.1016/j.snb.2013.03.127>.
- [143] Z. Zhang, Z. Li, W. Yu, K. Li, Z. Xie, Z. Shi, Propulsion of liposomes using bacterial motors, *Nanotechnology*. 24 (2013) 185103. <https://doi.org/10.1088/0957-4484/24/18/185103>.
- [144] V.D. Nguyen, J.-W. Han, Y.J. Choi, S. Cho, S. Zheng, S.Y. Ko, J.-O. Park, S. Park, Active tumor-therapeutic liposomal bacteriobot combining a drug (paclitaxel)-encapsulated liposome with targeting bacteria (*Salmonella Typhimurium*), *Sens. Actuators B Chem.* 224 (2016) 217–224. <https://doi.org/10.1016/j.snb.2015.09.034>.
- [145] S.J. Park, S.-H. Park, S. Cho, D.-M. Kim, Y. Lee, S.Y. Ko, Y. Hong, H.E. Choy, J.-J. Min, J.-O. Park, S. Park, New paradigm for tumor theranostic methodology using bacteria-based microrobot, *Sci. Rep.* 3 (2013) 1–8. <https://doi.org/10.1038/srep03394>.
- [146] Z. Hosseinidoust, B. Mostaghaci, O. Yasa, B.-W. Park, A.V. Singh, M. Sitti, Bioengineered and biohybrid bacteria-based systems for drug delivery, *Adv. Drug Deliv. Rev.* 106 (2016) 27–44. <https://doi.org/10.1016/j.addr.2016.09.007>.
- [147] J.H. Zheng, V.H. Nguyen, S.-N. Jiang, S.-H. Park, W. Tan, S.H. Hong, M.G. Shin, I.-J. Chung, Y. Hong, H.-S. Bom, H.E. Choy, S.E. Lee, J.H. Rhee, J.-J. Min, Two-step enhanced cancer immunotherapy with engineered *Salmonella Typhimurium* secreting heterologous flagellin, *Sci. Transl. Med.* 9 (2017). <https://doi.org/10.1126/scitranslmed.aak9537>.
- [148] G.L. Rosano, E.A. Ceccarelli, Recombinant protein expression in *Escherichia coli*: advances and challenges, *Front. Microbiol.* 5 (2014). <https://doi.org/10.3389/fmicb.2014.00172>.

- [149] S.H.E. Kaufmann, Immunity to Intracellular Bacteria, *Annu. Rev. Immunol.* 11 (1993) 129–163. <https://doi.org/10.1146/annurev.iy.11.040193.001021>.
- [150] R. Gardlik, J.H. Fruehauf, Bacterial vectors and delivery systems in cancer therapy, *IDrugs Investig. Drugs J.* 13 (2010) 701–706.
- [151] S. Taherkhani, M. Mohammadi, J. Daoud, S. Martel, M. Tabrizian, Covalent Binding of Nanoliposomes to the Surface of Magnetotactic Bacteria for the Synthesis of Self-Propelled Therapeutic Agents, *ACS Nano.* 8 (2014) 5049–5060. <https://doi.org/10.1021/nn5011304>.
- [152] T.J. Kindt, B.A. Osborne, R.A. Goldsby, Kuby Immunology, Sixth Edition, 6th edition, W. H. Freeman & Company, New York, 2006.
- [153] R.D. Leek, C.E. Lewis, R. Whitehouse, M. Greenall, J. Clarke, A.L. Harris, Association of Macrophage Infiltration with Angiogenesis and Prognosis in Invasive Breast Carcinoma, *Cancer Res.* 56 (1996) 4625–4629.
- [154] J.S. Lewis, R.J. Landers, J.C.E. Underwood, A.L. Harris, C.E. Lewis, Expression of vascular endothelial growth factor by macrophages is up-regulated in poorly vascularized areas of breast carcinomas, *J. Pathol.* 192 (2000) 150–158. [https://doi.org/10.1002/1096-9896\(2000\)9999:9999<::AID-PATH687>3.0.CO;2-G](https://doi.org/10.1002/1096-9896(2000)9999:9999<::AID-PATH687>3.0.CO;2-G).
- [155] Y. Persidsky, A. Ghorpade, J. Rasmussen, J. Limoges, X.J. Liu, M. Stins, M. Fiala, D. Way, K.S. Kim, M.H. Witte, M. Weinand, L. Carhart, H.E. Gendelman, Microglial and Astrocyte Chemokines Regulate Monocyte Migration through the Blood-Brain Barrier in Human Immunodeficiency Virus-1 Encephalitis, *Am. J. Pathol.* 155 (1999) 1599–1611. [https://doi.org/10.1016/S0002-9440\(10\)65476-4](https://doi.org/10.1016/S0002-9440(10)65476-4).
- [156] D.C. Anthony, S.J. Bolton, S. Fearn, V.H. Perry, Age-related effects of interleukin-1 beta on polymorphonuclear neutrophil-dependent increases in blood-brain barrier permeability in rats., *Brain.* 120 (1997) 435–444. <https://doi.org/10.1093/brain/120.3.435>.
- [157] M.-R. Choi, R. Bardhan, K.J. Stanton-Maxey, S. Badve, H. Nakshatri, K.M. Stantz, N. Cao, N.J. Halas, S.E. Clare, Delivery of nanoparticles to brain metastases of breast cancer using a cellular Trojan horse, *Cancer Nanotechnol.* 3 (2012) 47–54. <https://doi.org/10.1007/s12645-012-0029-9>.
- [158] E.V. Batrakova, H.E. Gendelman, A.V. Kabanov, Cell-mediated drug delivery, *Expert Opin. Drug Deliv.* 8 (2011) 415–433. <https://doi.org/10.1517/17425247.2011.559457>.

- [159] J. Shao, M. Xuan, H. Zhang, X. Lin, Z. Wu, Q. He, Chemotaxis-Guided Hybrid Neutrophil Micromotors for Targeted Drug Transport, *Angew. Chem. Int. Ed.* 56 (2017) 12935–12939. <https://doi.org/10.1002/anie.201706570>.
- [160] J. Xue, Z. Zhao, L. Zhang, L. Xue, S. Shen, Y. Wen, Z. Wei, L. Wang, L. Kong, H. Sun, Q. Ping, R. Mo, C. Zhang, Neutrophil-mediated anticancer drug delivery for suppression of postoperative malignant glioma recurrence, *Nat. Nanotechnol.* 12 (2017) 692–700. <https://doi.org/10.1038/nnano.2017.54>.
- [161] A.M. Brynskikh, Y. Zhao, R.L. Mosley, S. Li, M.D. Boska, N.L. Klyachko, A.V. Kabanov, H.E. Gendelman, E.V. Batrakova, Macrophage delivery of therapeutic nanozymes in a murine model of Parkinson's disease, *Nanomed.* 5 (2010) 379–396. <https://doi.org/10.2217/nnm.10.7>.
- [162] M.T. Stephan, J.J. Moon, S.H. Um, A. Bershteyn, D.J. Irvine, Therapeutic cell engineering with surface-conjugated synthetic nanoparticles, *Nat. Med.* 16 (2010) 1035–1041. <https://doi.org/10.1038/nm.2198>.
- [163] W.-C. Huang, W.-H. Chiang, Y.-H. Cheng, W.-C. Lin, C.-F. Yu, C.-Y. Yen, C.-K. Yeh, C.-S. Chern, C.-S. Chiang, H.-C. Chiu, Tumortropic monocyte-mediated delivery of echogenic polymer bubbles and therapeutic vesicles for chemotherapy of tumor hypoxia, *Biomaterials.* 71 (2015) 71–83. <https://doi.org/10.1016/j.biomaterials.2015.08.033>.
- [164] M. Roger, A. Clavreul, M.-C. Venier-Julienne, C. Passirani, L. Sindji, P. Schiller, C. Montero-Menei, P. Menei, Mesenchymal stem cells as cellular vehicles for delivery of nanoparticles to brain tumors, *Biomaterials.* 31 (2010) 8393–8401. <https://doi.org/10.1016/j.biomaterials.2010.07.048>.
- [165] J. Ma, S. Zhang, J. Liu, F. Liu, F. Du, M. Li, A.T. Chen, Y. Bao, H.W. Suh, J. Avery, G. Deng, Y. Zhou, P. Wu, K. Sheth, H. Wang, J. Zhou, Targeted Drug Delivery to Stroke via Chemotactic Recruitment of Nanoparticles Coated with Membrane of Engineered Neural Stem Cells, *Small.* 15 (2019) 1902011. <https://doi.org/10.1002/smll.201902011>.
- [166] L.G. Menon, K. Kelly, H.W. Yang, S.-K. Kim, P.M. Black, R.S. Carroll, Human Bone Marrow-Derived Mesenchymal Stromal Cells Expressing S-TRAIL as a Cellular Delivery Vehicle for Human Glioma Therapy, *STEM CELLS.* 27 (2009) 2320–2330. <https://doi.org/10.1002/stem.136>.
- [167] F. Yang, S.-W. Cho, S.M. Son, S.R. Bogatyrev, D. Singh, J.J. Green, Y. Mei, S. Park, S.H. Bhang, B.-S. Kim, R. Langer, D.G. Anderson, Genetic engineering of human stem cells for enhanced angiogenesis using biodegradable polymeric

nanoparticles, *Proc. Natl. Acad. Sci.* 107 (2010) 3317–3322.
<https://doi.org/10.1073/pnas.0905432106>.

- [168] L. Pang, C. Zhang, J. Qin, L. Han, R. Li, C. Hong, H. He, J. Wang, A novel strategy to achieve effective drug delivery: exploit cells as carrier combined with nanoparticles, *Drug Deliv.* 24 (2017) 83–91.
<https://doi.org/10.1080/10717544.2016.1230903>.
- [169] S.I. Grivennikov, F.R. Greten, M. Karin, *Immunity, Inflammation, and Cancer*, *Cell.* 140 (2010) 883–899. <https://doi.org/10.1016/j.cell.2010.01.025>.
- [170] U. Steinfeld, C. Pauli, N. Kaltz, C. Bergemann, H.-H. Lee, T lymphocytes as potential therapeutic drug carrier for cancer treatment, *Int. J. Pharm.* 311 (2006) 229–236. <https://doi.org/10.1016/j.ijpharm.2005.12.040>.
- [171] M.-R. Choi, K.J. Stanton-Maxey, J.K. Stanley, C.S. Levin, R. Bardhan, D. Akin, S. Badve, J. Sturgis, J.P. Robinson, R. Bashir, N.J. Halas, S.E. Clare, A Cellular Trojan Horse for Delivery of Therapeutic Nanoparticles into Tumors, *Nano Lett.* 7 (2007) 3759–3765. <https://doi.org/10.1021/nl072209h>.
- [172] D. Wong, R. Prameya, K. Dorovini-Zis, Adhesion and migration of polymorphonuclear leukocytes across human brain microvessel endothelial cells are differentially regulated by endothelial cell adhesion molecules and modulate monolayer permeability, *J. Neuroimmunol.* 184 (2007) 136–148.
<https://doi.org/10.1016/j.jneuroim.2006.12.003>.
- [173] M.R. Owen, H.M. Byrne, C.E. Lewis, Mathematical modelling of the use of macrophages as vehicles for drug delivery to hypoxic tumour sites, *J. Theor. Biol.* 226 (2004) 377–391. <https://doi.org/10.1016/j.jtbi.2003.09.004>.
- [174] Y.-L. Hu, Y.-H. Fu, Y. Tabata, J.-Q. Gao, Mesenchymal stem cells: A promising targeted-delivery vehicle in cancer gene therapy, *J. Controlled Release.* 147 (2010) 154–162. <https://doi.org/10.1016/j.jconrel.2010.05.015>.
- [175] C.V. Borlongan, L.E. Glover, N. Tajiri, Y. Kaneko, T.B. Freeman, The great migration of bone marrow-derived stem cells toward the ischemic brain: Therapeutic implications for stroke and other neurological disorders, *Prog. Neurobiol.* 95 (2011) 213–228. <https://doi.org/10.1016/j.pneurobio.2011.08.005>.
- [176] B. Huang, Y. Tabata, J.-Q. Gao, Mesenchymal stem cells as therapeutic agents and potential targeted gene delivery vehicle for brain diseases, *J. Controlled Release.* 162 (2012) 464–473. <https://doi.org/10.1016/j.jconrel.2012.07.034>.
- [177] F. Yin, L. Guo, C. Meng, Y. Liu, R. Lu, P. Li, Y. Zhou, Transplantation of mesenchymal stem cells exerts anti-apoptotic effects in adult rats after spinal cord

ischemia-reperfusion injury, *Brain Res.* 1561 (2014) 1–10.
<https://doi.org/10.1016/j.brainres.2014.02.047>.

- [178] M. Wei, S. Li, W. Le, Nanomaterials modulate stem cell differentiation: biological interaction and underlying mechanisms, *J. Nanobiotechnology.* 15 (2017).
<https://doi.org/10.1186/s12951-017-0310-5>.
- [179] S. Behzadi, V. Serpooshan, W. Tao, M.A. Hamaly, M.Y. Alkawareek, E.C. Dreaden, D. Brown, A.M. Alkilany, O.C. Farokhzad, M. Mahmoudi, Cellular Uptake of Nanoparticles: Journey Inside the Cell, *Chem. Soc. Rev.* 46 (2017) 4218–4244.
<https://doi.org/10.1039/c6cs00636a>.
- [180] Q. Sun, K. Kanehira, A. Taniguchi, PEGylated TiO₂ nanoparticles mediated inhibition of cell migration via integrin beta 1, *Sci. Technol. Adv. Mater.* 19 (2018) 271–281. <https://doi.org/10.1080/14686996.2018.1444318>.
- [181] Y. Hou, K. Cai, J. Li, X. Chen, M. Lai, Y. Hu, Z. Luo, X. Ding, D. Xu, Effects of titanium nanoparticles on adhesion, migration, proliferation, and differentiation of mesenchymal stem cells, *Int. J. Nanomedicine.* 8 (2013) 3619–3630.
<https://doi.org/10.2147/IJN.S38992>.
- [182] H.R. Lee, F. Pelaez, A.M. Silbaugh, F. Leslie, E. Racila, S.M. Azarin, Biomaterial Platform To Establish a Hypoxic Metastatic Niche *in vivo*, *ACS Appl. Bio Mater.* 2 (2019) 1549–1560. <https://doi.org/10.1021/acsabm.8b00837>.
- [183] F.P. Seib, J.E. Berry, Y. Shiozawa, R.S. Taichman, D.L. Kaplan, Tissue engineering a surrogate niche for metastatic cancer cells, *Biomaterials.* 51 (2015) 313–319.
<https://doi.org/10.1016/j.biomaterials.2015.01.076>.
- [184] F. Bersani, J. Lee, M. Yu, R. Morris, R. Desai, S. Ramaswamy, M. Toner, D.A. Haber, B. Parekkadan, Bioengineered Implantable Scaffolds as a Tool to Study Stromal-Derived Factors in Metastatic Cancer Models, *Cancer Res.* 74 (2014) 7229–7238. <https://doi.org/10.1158/0008-5472.CAN-14-1809>.
- [185] M. Najberg, M. Haji Mansor, F. Boury, C. Alvarez-Lorenzo, E. Garcion, Reversing the Tumor Target: Establishment of a Tumor Trap, *Front. Pharmacol.* 10 (2019) 887. <https://doi.org/10.3389/fphar.2019.00887>.
- [186] A. de la Fuente, L. Alonso-Alconada, C. Costa, J. Cueva, T. Garcia-Caballero, R. Lopez-Lopez, M. Abal, M-Trap: Exosome-Based Capture of Tumor Cells as a New Technology in Peritoneal Metastasis, *J. Natl. Cancer Inst.* 107 (2015) djv184.
<https://doi.org/10.1093/jnci/djv184>.
- [187] H. Peinado, M. Alečković, S. Lavotshkin, I. Matej, B. Costa-Silva, G. Moreno-Bueno, M. Hergueta-Redondo, C. Williams, G. García-Santos, C.M. Ghajar, A.

Nitadori-Hoshino, C. Hoffman, K. Badal, B.A. Garcia, M.K. Callahan, J. Yuan, V.R. Martins, J. Skog, R.N. Kaplan, M.S. Brady, J.D. Wolchok, P.B. Chapman, Y. Kang, J. Bromberg, D. Lyden, Melanoma exosomes educate bone marrow progenitor cells toward a pro-metastatic phenotype through MET, *Nat. Med.* 18 (2012) 883–891. <https://doi.org/10.1038/nm.2753>.

- [188] E. De Vlieghere, F. Gremontprez, L. Verset, L. Mariën, C.J. Jones, B. De Craene, G. Berx, B. Descamps, C. Vanhove, J.-P. Remon, W. Ceelen, P. Demetter, M. Bracke, B.G. De Geest, O. De Wever, Tumor-environment biomimetics delay peritoneal metastasis formation by deceiving and redirecting disseminated cancer cells, *Biomaterials*. 54 (2015) 148–157. <https://doi.org/10.1016/j.biomaterials.2015.03.012>.
- [189] M. Haji Mansor, M. Najberg, A. Contini, C. Alvarez-Lorenzo, E. Garcion, C. Jérôme, F. Boury, Development of a non-toxic and non-denaturing formulation process for encapsulation of SDF-1 α into PLGA/PEG-PLGA nanoparticles to achieve sustained release, *Eur. J. Pharm. Biopharm.* 125 (2018) 38–50. <https://doi.org/10.1016/j.ejpb.2017.12.020>.
- [190] S. Giarra, C. Ierano, M. Biondi, M. Napolitano, V. Campani, R. Pacelli, S. Scala, G. De Rosa, L. Mayol, Engineering of thermoresponsive gels as a fake metastatic niche, *Carbohydr. Polym.* 191 (2018) 112–118. <https://doi.org/10.1016/j.carbpol.2018.03.016>.
- [191] S.M. Azarin, J. Yi, R.M. Gower, B.A. Aguado, M.E. Sullivan, A.G. Goodman, E.J. Jiang, S.S. Rao, Y. Ren, S.L. Tucker, V. Backman, J.S. Jeruss, L.D. Shea, *In vivo* capture and label-free detection of early metastatic cells, *Nat. Commun.* 6 (2015) 8094. <https://doi.org/10.1038/ncomms9094>.
- [192] A. Jain, M. Betancur, G.D. Patel, C.M. Valmikinathan, V.J. Mukhatyar, A. Vakharia, S.B. Pai, B. Brahma, T.J. MacDonald, R.V. Bellamkonda, Guiding intracortical brain tumour cells to an extracortical cytotoxic hydrogel using aligned polymeric nanofibres, *Nat. Mater.* 13 (2014) 308–316. <https://doi.org/10.1038/nmat3878>.
- [193] F. Pelaez, N. Manuchehrabadi, P. Roy, H. Natesan, Y. Wang, E. Racila, H. Fong, K. Zeng, A.M. Silbaugh, J.C. Bischof, S.M. Azarin, Biomaterial scaffolds for non-invasive focal hyperthermia as a potential tool to ablate metastatic cancer cells, *Biomaterials*. 166 (2018) 27–37. <https://doi.org/10.1016/j.biomaterials.2018.02.048>.
- [194] F. Pelaez, Q. Shao, P. Ranjbarkehrani, T. Lam, H.R. Lee, S. O’Flanagan, A. Silbaugh, J.C. Bischof, S.M. Azarin, Optimizing Integrated Electrode Design for Irreversible Electroporation of Implanted Polymer Scaffolds, *Ann. Biomed. Eng.* (2020). <https://doi.org/10.1007/s10439-019-02445-4>.

- [195] S.S. Rao, G.G. Bushnell, S.M. Azarin, G. Spicer, B.A. Aguado, J.R. Stoehr, E.J. Jiang, V. Backman, L.D. Shea, J.S. Jeruss, Enhanced Survival with Implantable Scaffolds That Capture Metastatic Breast Cancer Cells *In vivo*, *Cancer Res.* 76 (2016) 5209–5218. <https://doi.org/10.1158/0008-5472.CAN-15-2106>.
- [196] Y. Hu, J. Ran, Z. Zheng, Z. Jin, X. Chen, Z. Yin, C. Tang, Y. Chen, J. Huang, H. Le, R. Yan, T. Zhu, J. Wang, J. Lin, K. Xu, Y. Zhou, W. Zhang, Y. Cai, P. Dominique, B.C. Heng, W. Chen, W. Shen, H.-W. Ouyang, Exogenous stromal derived factor-1 releasing silk scaffold combined with intra-articular injection of progenitor cells promotes bone-ligament-bone regeneration, *Acta Biomater.* 71 (2018) 168–183. <https://doi.org/10.1016/j.actbio.2018.02.019>.
- [197] Y. Wang, X. Sun, J. Lv, L. Zeng, X. Wei, L. Wei, Stromal Cell-Derived Factor-1 Accelerates Cartilage Defect Repairing by Recruiting Bone Marrow Mesenchymal Stem Cells and Promoting Chondrogenic Differentiation, *Tissue Eng. Part A.* 23 (2017) 1160–1168. <https://doi.org/10.1089/ten.tea.2017.0046>.
- [198] B.A. Teicher, S.P. Fricker, CXCL12 (SDF-1)/CXCR4 Pathway in Cancer, *Clin. Cancer Res.* 16 (2010) 2927–2931. <https://doi.org/10.1158/1078-0432.CCR-09-2329>.
- [199] J. Calmeiro, M. Carrascal, C. Gomes, A. Falcão, M.T. Cruz, B.M. Neves, Biomaterial-based platforms for in situ dendritic cell programming and their use in antitumor immunotherapy, *J. Immunother. Cancer.* 7 (2019) 238. <https://doi.org/10.1186/s40425-019-0716-8>.
- [200] O.A. Ali, N. Huebsch, L. Cao, G. Dranoff, D.J. Mooney, Infection-mimicking materials to program dendritic cells in situ, *Nat. Mater.* 8 (2009) 151–158. <https://doi.org/10.1038/nmat2357>.
- [201] T. Kumamoto, E.K. Huang, H.J. Paek, A. Morita, H. Matsue, R.F. Valentini, A. Takashima, Induction of tumor-specific protective immunity by in situ Langerhans cell vaccine, *Nat. Biotechnol.* 20 (2002) 64–69. <https://doi.org/10.1038/nbt0102-64>.
- [202] O.A. Ali, P. Tayalia, D. Shvartsman, S. Lewin, D.J. Mooney, Inflammatory Cytokines Presented from Polymer Matrices Differentially Generate and Activate DCs In Situ, *Adv. Funct. Mater.* 23 (2013) 4621–4628. <https://doi.org/10.1002/adfm.201203859>.
- [203] O.A. Ali, C. Verbeke, C. Johnson, R.W. Sands, S.A. Lewin, D. White, E. Doherty, G. Dranoff, D.J. Mooney, Identification of Immune Factors Regulating Antitumor Immunity Using Polymeric Vaccines with Multiple Adjuvants, *Cancer Res.* 74 (2014) 1670–1681. <https://doi.org/10.1158/0008-5472.CAN-13-0777>.
- [204] O.A. Ali, E. Doherty, W.J. Bell, T. Fradet, J. Hudak, M.-T. Laliberte, D.J. Mooney, D.F. Emerich, The efficacy of intracranial PLG-based vaccines is dependent on

direct implantation into brain tissue, *J. Controlled Release*. 154 (2011) 249–257. <https://doi.org/10.1016/j.jconrel.2011.06.021>.

- [205] O.A. Ali, E. Doherty, W.J. Bell, T. Fradet, J. Hudak, M.-T. Laliberte, D.J. Mooney, D.F. Emerich, Biomaterial-Based Vaccine Induces Regression of Established Intracranial Glioma in Rats, *Pharm. Res.* 28 (2011) 1074–1080. <https://doi.org/10.1007/s11095-010-0361-x>.
- [206] A. Singh, H. Qin, I. Fernandez, J. Wei, J. Lin, L.W. Kwak, K. Roy, An injectable synthetic immune-priming center mediates efficient T-cell class switching and T-helper 1 response against B cell lymphoma, *J. Controlled Release*. 155 (2011) 184–192. <https://doi.org/10.1016/j.jconrel.2011.06.008>.
- [207] Y. Liu, L. Xiao, K.-I. Joo, B. Hu, J. Fang, P. Wang, In Situ Modulation of Dendritic Cells by Injectable Thermosensitive Hydrogels for Cancer Vaccines in Mice, *Biomacromolecules*. 15 (2014) 3836–3845. <https://doi.org/10.1021/bm501166j>.
- [208] S.A. Bencherif, R.W. Sands, O.A. Ali, W.A. Li, S.A. Lewin, T.M. Braschler, T.-Y. Shih, C.S. Verbeke, D. Bhatta, G. Dranoff, D.J. Mooney, Injectable cryogel-based whole-cell cancer vaccines, *Nat. Commun.* 6 (2015) 1–13. <https://doi.org/10.1038/ncomms8556>.
- [209] T.-Y. Shih, S.O. Blacklow, A.W. Li, B.R. Freedman, S. Bencherif, S.T. Koshy, M.C. Darnell, D.J. Mooney, Injectable, Tough Alginate Cryogels as Cancer Vaccines, *Adv. Healthc. Mater.* 7 (2018) 1701469. <https://doi.org/10.1002/adhm.201701469>.
- [210] J. Kim, W.A. Li, Y. Choi, S.A. Lewin, C.S. Verbeke, G. Dranoff, D.J. Mooney, Injectable, spontaneously assembling, inorganic scaffolds modulate immune cells *in vivo* and increase vaccine efficacy, *Nat. Biotechnol.* 33 (2015) 64–72. <https://doi.org/10.1038/nbt.3071>.
- [211] Y. Liu, X. Cao, Immunosuppressive cells in tumor immune escape and metastasis, *J. Mol. Med.* 94 (2016) 509–522. <https://doi.org/10.1007/s00109-015-1376-x>.
- [212] G.L. Beatty, W.L. Gladney, Immune Escape Mechanisms as a Guide for Cancer Immunotherapy, *Clin. Cancer Res.* 21 (2015) 687–692. <https://doi.org/10.1158/1078-0432.CCR-14-1860>.
- [213] D. Mittal, M.M. Gubin, R.D. Schreiber, M.J. Smyth, New insights into cancer immunoediting and its three component phases—elimination, equilibrium and escape, *Curr. Opin. Immunol.* 27 (2014) 16–25. <https://doi.org/10.1016/j.coi.2014.01.004>.

- [214] A.B. Salunkhe, V.M. Khot, S.H. Pawar, Magnetic Hyperthermia with Magnetic Nanoparticles: A Status Review, *Curr. Top. Med. Chem.* 14 (2014) 572–594. <https://doi.org/10.2174/1568026614666140118203550>.
- [215] S. Luo, L. Wang, W. Ding, H. Wang, J. Zhou, H. Jin, S. Su, W. Ouyang, Clinical trials of magnetic induction hyperthermia for treatment of tumours, *Crit. Rev.* (2014) 6.
- [216] D. Bobo, K.J. Robinson, J. Islam, K.J. Thurecht, S.R. Corrie, Nanoparticle-Based Medicines: A Review of FDA-Approved Materials and Clinical Trials to Date, *Pharm. Res.* 33 (2016) 2373–2387. <https://doi.org/10.1007/s11095-016-1958-5>.
- [217] Y.-L. Liu, D. Chen, P. Shang, D.-C. Yin, A review of magnet systems for targeted drug delivery, *J. Controlled Release.* 302 (2019) 90–104. <https://doi.org/10.1016/j.jconrel.2019.03.031>.
- [218] V.L. Perez, B. Wirostko, M. Korenfeld, S. From, M. Raizman, Ophthalmic Drug Delivery Using Iontophoresis: Recent Clinical Applications, *J. Ocul. Pharmacol. Ther.* 36 (2019) 75–87. <https://doi.org/10.1089/jop.2019.0034>.
- [219] J. Galipeau, L. Sensébé, Mesenchymal Stromal Cells: Clinical Challenges and Therapeutic Opportunities, *Cell Stem Cell.* 22 (2018) 824–833. <https://doi.org/10.1016/j.stem.2018.05.004>.
- [220] A.E. Firor, A. Jares, Y. Ma, From humble beginnings to success in the clinic: Chimeric antigen receptor-modified T-cells and implications for immunotherapy, *Exp. Biol. Med.* 240 (2015) 1087–1098. <https://doi.org/10.1177/1535370215584936>.
- [221] G. Orive, E. Santos, D. Poncelet, R.M. Hernández, J.L. Pedraz, L.U. Wahlberg, P. De Vos, D. Emerich, Cell encapsulation: technical and clinical advances, *Trends Pharmacol. Sci.* 36 (2015) 537–546. <https://doi.org/10.1016/j.tips.2015.05.003>.

Chapter 3. Lyotropic lipid particles formulation for co-encapsulation of both hydrophilic and lipophilic drugs

Hung V. Nguyen, Vincent Faivre*

Université Paris-Saclay, CNRS, Institut Galien Paris-Saclay, 5 rue JB Clément, 92296 Châtenay-Malabry, France.

1. Introduction

In our project, it is essential to load 2 types of drugs in 1 formulation. The challenge is to load 2 types of molecules having opposite solubilities. We aim to design a carrier having a lipophilic domain for lipophilic drugs and a hydrophilic domain for hydrophilic drugs. In this 2-domain carrier, the interaction between the lipid part and the water part needs to be clarified and well understood. In this chapter, we will present different lyotropic forms of lipids with water. We then describe recent research about lipid particles formulations that have both lipophilic and hydrophilic domains.

In a mixture of 2 immiscible substances, for example, oil and water, there are 2 immiscible domains: oil and water. The mixture has 2 possible morphologies: oil-in-water (o/w) and water-in-oil (w/o). Usually, the type of morphology is determined by looking at the continuous phase. If the continuous phase is water, the mixture is o/w and vice versa. However, this method would be difficult to use in the case of bicontinuous structures, which have 2 continuous phases. In a more general way, if the curvature of the interface oil-water towards oil, then it is an o/w mixture and vice versa. The exact determination of morphology can be done by calculating the average curvature H of the interface between oil and water. In 3D, if the average curvature H calculated from the oil's view is convex, the morphology is o/w and vice versa. The convention in literature is that "type 1" mesostructure is o/w and "type 2" is w/o [1].

In the case of lyotropic structures of an amphiphilic molecule with water, we can predict the tendency to form type 1 or type 2 morphology by looking at its shape. For example, if the hydrophobic chains of the molecule are bulky and larger than the hydrophilic head, when we "pack" the molecules head-to-head and tail-to-tail, the morphology is likely to be type 2 (w/o). In detail, from the dimension of the molecule, we can calculate the critical packing parameter (CPP) to predict the lyotropic morphology. The critical packing parameter (CPP) " s " of the molecule can be estimated from the area per surfactant molecule at the head-group/chain interface " a ", the chain length of the molecule " L " and the chain volume " v " [1].

$$s = \frac{v}{a \times L} \text{ (Equation 3.1)}$$

The value of “a”, which is from the interface between head-group/chain (not head-group/water interface), can be estimated very roughly from the area per linear hydrocarbon chain, which is around 30 – 35 Å² [1]. The value a is however highly dependent on the hydration rate, temperature, ionization state, counter ions in solution, etc.

For each linear hydrocarbon chain, its length and volume can be estimated using Tanford’s formulae [1]:

$$v = (27.4 + 26.9 \times n^3) \text{ \AA}^3 \text{ (Equation 3.2)}$$

$$L = (1.5 + 1.26 \times n) \text{ \AA} \text{ (Equation 3.3)}$$

with n being the number of carbon atoms in the hydrocarbon chain.

Figure 3.1 shows the morphology of amphiphilic molecules in a water and oil mixture. Generally, if the CPP value is larger than 1, the morphology is likely to be type 2 (w/o) and otherwise, if the CPP value is smaller than 1, the morphology is likely to be type 1 (o/w).

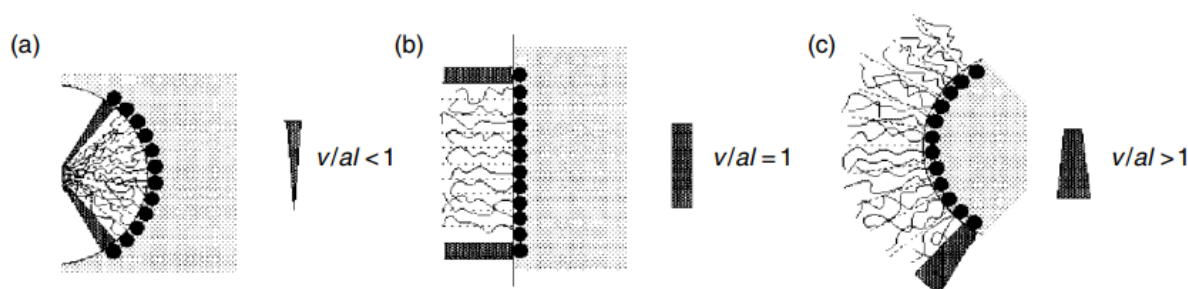


Figure 3.1. Morphology of amphiphilic molecules in water and oil mixture: (a) type 1 - w/o, (b) lamellar phase, (c) type 2 - o/w. The shaded area represents water. The image is adapted from ref. [1].

2. Lyotropic crystals

In water or polar solvents, amphiphilic molecules can self-assemble into different lyotropic structures to minimize their surface energy. The term lyotropic is made from “lyo”, which means “solvent” and “tropic”, which means “form”. Herein, we describe different lyotropic crystals that may form from the mixture of amphiphilic molecules with water.

2.1. Lamellar mesophase

Lamellar mesophase consists of several lipid bilayers stacking periodically together. Water is located between these layers. The thickness of all water planes is the same. The illustration of the structure is in Figure 3.2. This structure is commonly found in molecules having CPP equal to 1. In the structure, the hydrophilic heads of the

molecules face toward the water, while the lipophilic chains face toward themselves. Because the CPP is 1, the molecules pack together to form a plane. The structure is stabilized by the hydrophobic interaction between hydrophobic chains, and hydrophilic interaction and hydration force between hydrophilic heads and water. The thickness of the water layer can be influenced by the concentration of water, the introduction of charges in the lipid bilayer, or the change in pH etc. The lamellar structure can be identified by a series of peaks in X-ray scattering data, with the d-spacing being a , $2*a$, $3*a$, $4*a$ etc, with a being the spacing between 2 adjacent lipid bilayers.

The lamellar mesophase can be categorized into fluid lamellar mesophase and gel lamellar mesophase. In fluid lamellar mesophase, the hydrocarbon chain is in a liquid state. In X-ray scattering data, we may have only 1 wide and large diffuse scattering peak at the wavevector $q \sim 14 \text{ nm}^{-1}$ ($d = 0.45 \text{ nm}$), which is the characteristic of in-plane spacing between molten chains [1,2]. In gel lamellar mesophase, the hydrocarbon chains are in a solid state. Due to the crystalline state of the hydrocarbon chains, the X-ray scattering data typically has a sharp peak at the wavevector $q \sim 15\text{-}15.3 \text{ nm}^{-1}$ ($d = 0.41 - 0.42 \text{ nm}$) [1]. In this case, the hydrocarbon chains are arranged in a hexagonal arrangement, and the distance between chains is $0.41 - 0.42 \text{ nm}$.

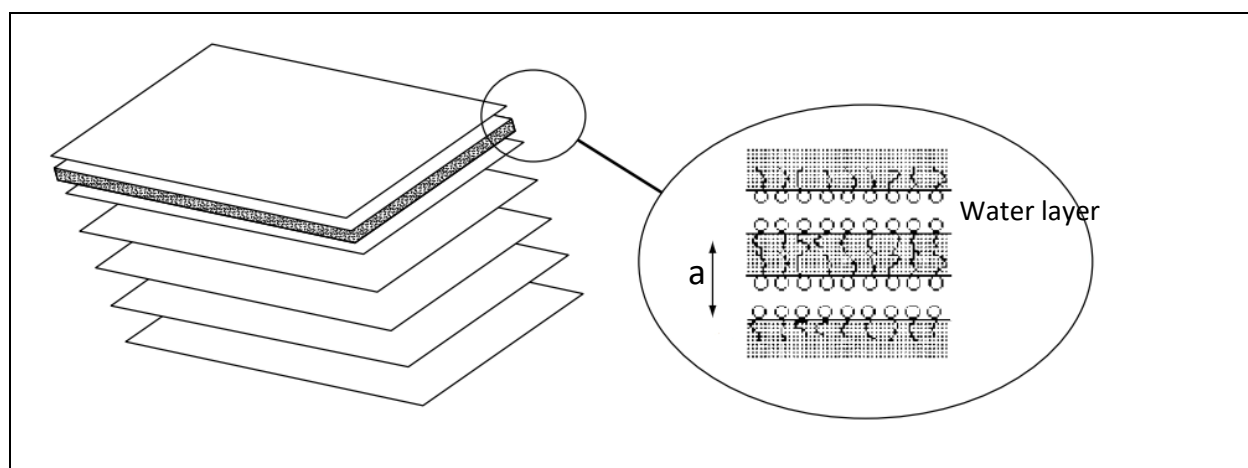


Figure 3.2. Illustration of lyotropic lamellar mesophase, adapted from ref. [1]

2.2. Columnar mesophase

The columnar mesophase consists of densely packed cylindrical micelles. When the cylindrical micelles are arranged in hexagonal morphology, the mesophase is called hexagonal mesophases (H_1 and H_2 for hexagonal mesophase type 1 and type 2, respectively). Usually, molecules having a CPP value of 0.5 result in H_1 mesophase, while molecules having $CPP > 1$ form H_2 mesophase. The hexagonal mesophase can be determined by X-ray scattering, which shows a series of peaks having a wavevector ratio of $1:\sqrt{3}:\sqrt{4}:\sqrt{7}$ etc. The illustration of H_2 mesophase is in Figure 3.3a. The top view shows the hydrophobic interaction between chains of adjacent cylindrical micelles. Those cylindrical micelles are arranged in a hexagonal lattice, with the lattice parameter a .

Another columnar mesophase is ribbon mesophase (Figure 3.3b), which was reported as a variation or a deformed hexagonal mesophase [1]. The ribbon mesophase has cylindrical micelles arranged in a rectangular lattice, leading to several possibilities of rectangular symmetry. The illustration in Figure 3.3 is only an example of the centered mesophase. The ribbon mesophase is described as less homogenous than the hexagonal mesophase and is expected to be found in multi-component systems.

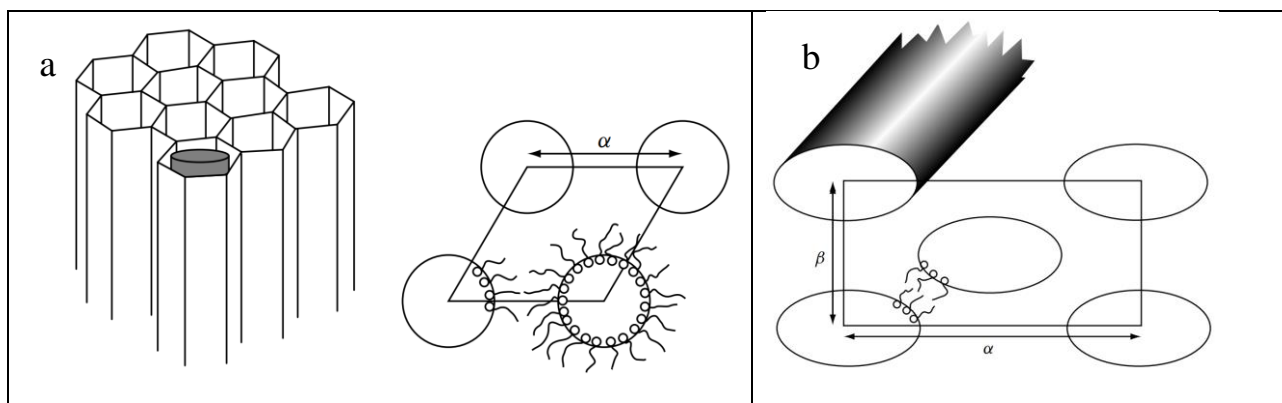


Figure 3.3. Illustration of (a) hexagonal mesophase type 2 (H_2) side view and top view with lattice parameter α ; (b) ribbon mesophase type 2, centered configuration, with lattice parameters a and β . The figure is adapted from ref. [1].

2.3. Globular mesophases

Globular mesophase is created from the aggregation of globular micelles, which self-assemble into 3D crystalline structures. Globular mesophase is also called discrete micellar mesophase. The notation is I_1 for globular mesophase type 1, and I_2 for globular mesophase type 2. One of the common forms is the body-centered cubic (bcc) 3D lattice of micelles (Figure 3.4). Other forms were also found such as face-centered cubic (fcc) or clathrate. Usually, to form globular mesophase type 1, the CPP of the molecule is $\sim 1/3$, while globular mesophase type 2 requires molecules having CPP > 1 .

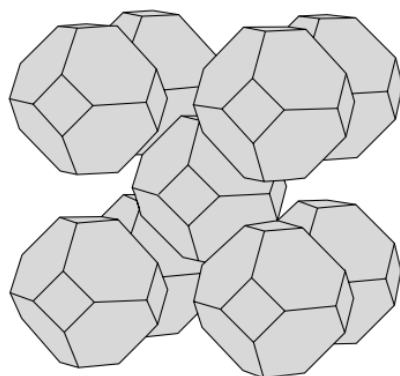


Figure 3.4. Globular body-centered cubic (bcc) mesophase in an exploded view, each cell contains a micelle. The figure is adapted from ref. [1].

2.4. Bicontinuous mesophases

Bicontinuous mesophases can be visualized as wrapped lamellar phase, with the idea that a bicontinuous mesophase crystal is one lipid bilayer having hyperbolic geometry. The fold of lipid bilayers in bicontinuous mesophase is to minimize the surface, creating homogenous zero mean curvature (minimal surfaces) structures. Unlike in the case of globular mesophases, which have discontinuous, closed micelles, the term bicontinuous means we have 2 continuous phases, polar and non-polar. The polar and non-polar phases in a bicontinuous mesophase crystal create 2 distinct networks inside a crystal.

2.4.1. Cubic ordered bicontinuous mesophase

Taking the name of 3 minimal surfaces P (primitive), D (diamond), and Gyroid (G), there are 3 discovered cubic bicontinuous mesophase: P phase ($Im\bar{3}m$ space group), D phase ($Pn\bar{3}m$ space group) and G phase ($Ia\bar{3}d$ space group) (Figure 3.5). To determine the type of mesophase, we can imagine the lipid bilayer as a film, and the bicontinuous mesophase as a wrapped, folded thick film. If the film is filled with water, the bicontinuous mesophase is type 1, and if the film is filled with hydrocarbon chains, it is type 2. The notation for cubic bicontinuous mesophase is V_1 for type 1 and V_2 for type 2. In X-ray scattering experiments, the P phase shows the peaks ratio of $\sqrt{2}:\sqrt{4}:\sqrt{6}:\sqrt{8}:\sqrt{10}$ etc, D phase shows $\sqrt{2}:\sqrt{3}:\sqrt{4}:\sqrt{6}:\sqrt{8}$ etc, G phase shows $\sqrt{6}:\sqrt{8}:\sqrt{14}:\sqrt{16}:\sqrt{18}:\sqrt{20}$ etc [1]. Usually, to have cubic bicontinuous mesophases, the CPP of the molecules is around $2/3$ for type 1, and around larger than 1 for type 2.

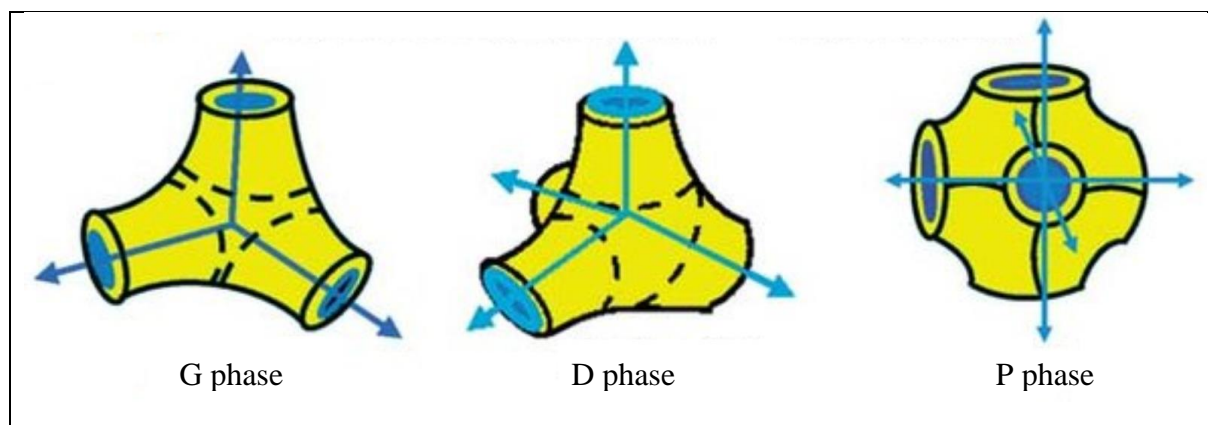


Figure 3.5. Morphology of type 2 cubic bicontinuous mesophases, the figure is adapted from ref. [3].

2.4.2 Mesh-ordered bicontinuous mesophases

Another ordered bicontinuous mesophase is mesh, which can be visualized as a stack of holey bilayers. In 1 bilayer, the holes are arranged in a 2D lattice, which can be a hexagonal array (rhombohedral mesh mesophase) or square array (tetragonal mesh mesophase, Figure 3.6). The holey lipid bilayers form mesh mesophase by making a

stack, with a distance parameter c between bilayers. It is very hard to predict the formation of mesh mesophase from CPP, due to the large variability of CPP that may form mesh mesophase.

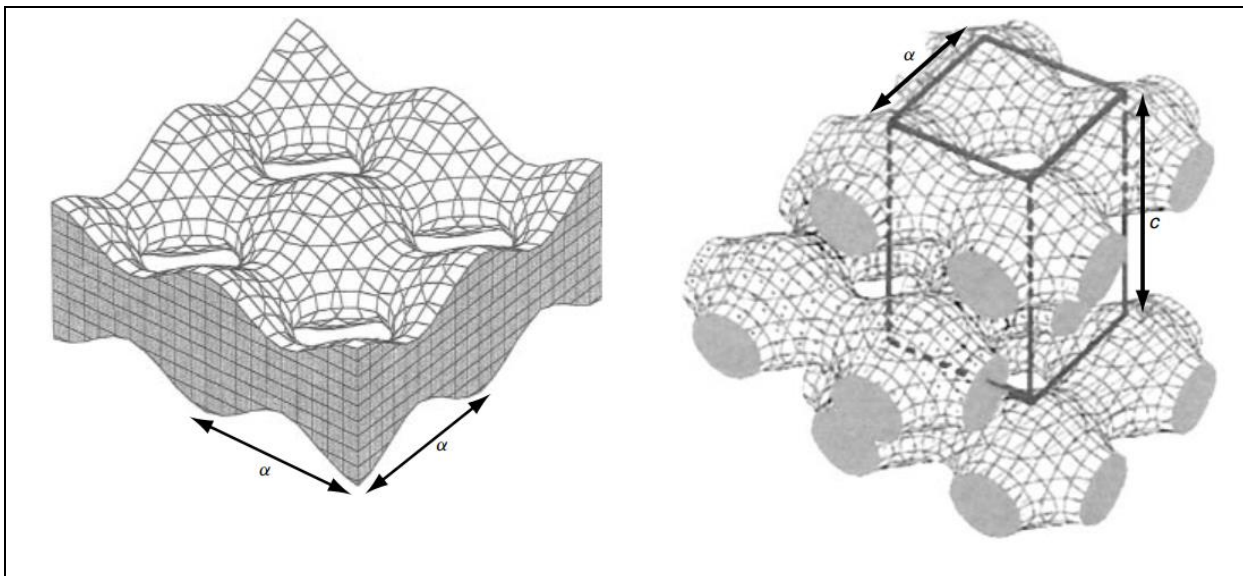


Figure 3.6. Morphology of mesh bicontinuous mesophases in tetragonal geometry, with the lattice parameters a and c . The figure is adapted from ref. [1].

2.5. Sponge-disordered bicontinuous mesophase

The sponge is a complex, disordered bicontinuous mesophase, which may form from the fusion of ordered bicontinuous mesophase (Figure 3.7). A sponge may have local mesostructures, but the domain's size is not large enough to define a lattice. It can be visualized as an aggregation of molten bicontinuous mesophases. In a phase diagram, the formation of the sponge phase is usually between lamellar mesophase and cubic bicontinuous mesophase. Because the sponge mesophase is disordered, there aren't any sharp peaks in X-ray scattering experiments. There might be a wide peak in small-angle x-ray scattering data, with a distance similar to the thickness of the lipid bilayer [4]. Under a polarized light microscope, the sponge phase is anisotropic when flowing, while it is isotropic at rest [1].

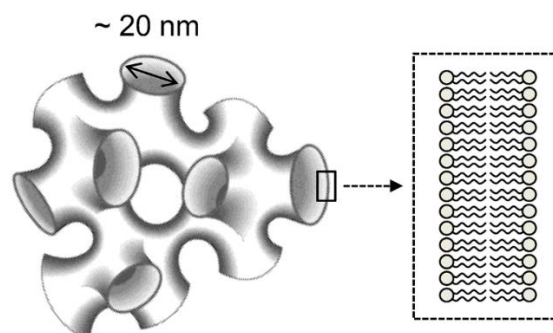


Figure 3.7. Illustration of a sponge having folded continuous lipid bilayer, creating connected aqueous channels. The figure is adapted from ref. [5].

3. Water-containing drug delivery systems from lyotropic lipid structures

After understanding different lyotropic lipid structures, in this part, we summarize research about lipid particles containing both hydrophilic and lipophilic domains. Figure 3.8 shows the different lyotropic structures mentioned above and their particulate form observed by cryogenic electron microscopy (cryo-EM). In our project, we are interested in water-containing lipid particles and only present them in this chapter. So, some other lipid particles like bicelles, emulsion, or solid lipid particles are not included. In addition, all lipid particle types presented in Figure 3.8 are stable upon dilution.

The sponge particle in Figure 3.8 was fabricated by a low-energy top-down method from sponge mesophase [6]. The sponge particles cryo-EM image shows disordered-structured particles having both water and oil channels. The particle size is around 100-200 nm, and the size of the water channels is around 13 nm, making it a suitable system for our application.

The cubosome, which is the lipid particle in bicontinuous cubic mesophase, is shown in Figure 3.8. In this case, the structure is P-phase, determined by the X-ray scattering technique [7]. Cubosomes have ordered networks of water and oil, suitable for loading both hydrophilic and hydrophobic drugs.

From lamellar mesophase, 2 types of lipid particles can be fabricated. They are α -gel emulsion and liposome. The α -gel emulsion is fabricated from the gel lamellar phase, in which the hydrocarbon chains are solid. In Figure 3.8, we can see layers of lamellar structure in an emulsion sample [8]. The formulation has a lipophilic phase in oil and a hydrophilic phase in between lamellar sheets. If the hydrocarbon chain of the lamellar mesophase is in the liquid state, liposomes may be obtained. The liposome is a vesicle made from lipid bilayers. In liposomes, the hydrophilic domain is in the core, while the lipophilic domain is in the lipid layers. Figure 3.8 shows a multi-walled liposome, which may be suitable for our project.

Hexosomes are particles having hexagonal mesophase type 2. The hexosome has tubes of water and hydrocarbon chains around those tubes. The hexosome structure can be visualized as the aggregation of channels of water in a hexagonal arrangement, the space between the water channels is filled with hydrocarbon chains. The hexosome in Figure 3.8 has a hexagonal shape and scattering characteristic of hexagonal phase [9]. Hexosome is also an interesting system for our project.

Multiple emulsion is a system of a w/o emulsion inside an o/w emulsion droplet, which is called water-in-oil-in-water (w/o/w) emulsion. The system has oil droplets stabilized in water, inside the oil droplets, there are water droplets. So hydrophilic compounds can be loaded inside the water droplets, while hydrophobic compounds are loaded inside the oil region around those water droplets. Figure 3.8 shows a micro-size w/o/w

multiple emulsion sample [10], in which we can clearly observe water droplets inside the oil droplet. Multiple emulsions may also be a strategy for our project.

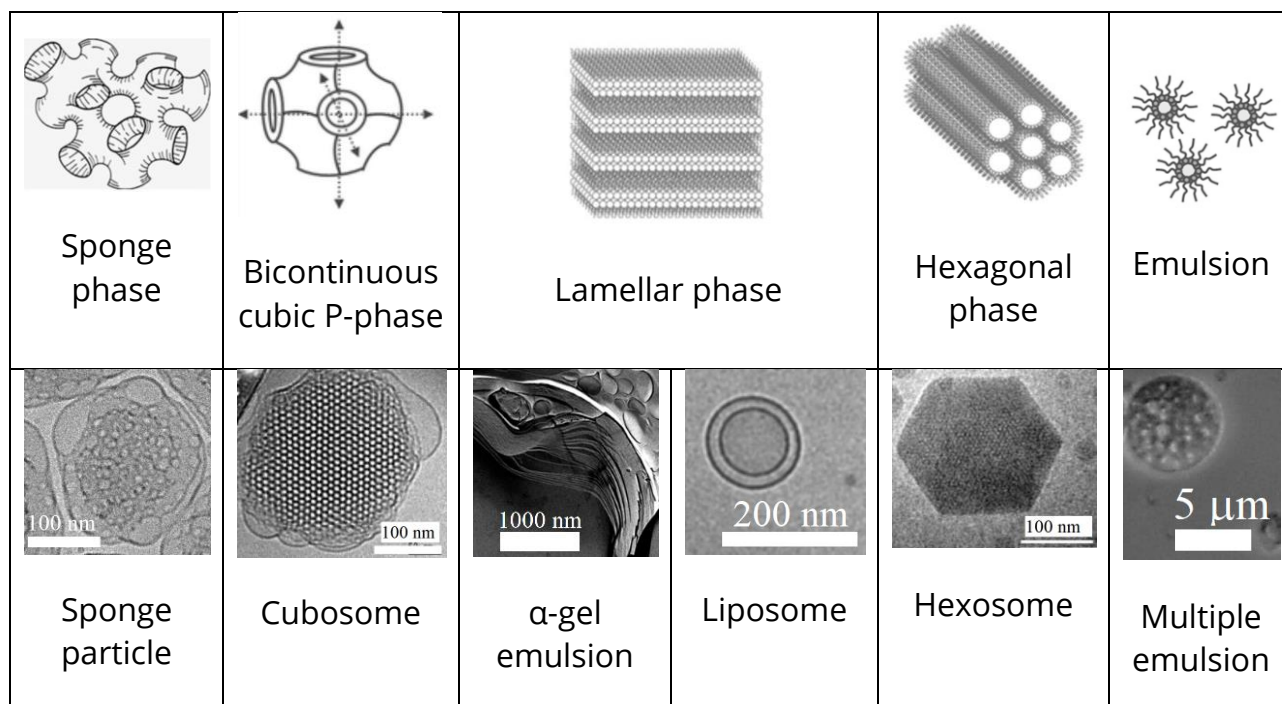


Figure 3.8. Lyotropic lipid structures and examples of their particulate forms, only water-containing lipid particles are presented. Lipid lyotropic structure illustrations are adapted from ref. [11]. From left to right, cryo-EM images of a sponge particle [6], cubosome [7], α -gel emulsion [8], liposome [12], hexosome [9], and multiple emulsion [10] are adapted from the corresponding references.

In the following sections, we will present in detail the materials, fabrication methods, and the structures of mentioned lipid particle systems. We also comment on their potential as a drug delivery system and the ability to load hydrophilic and lipophilic drugs.

3.1. Multiple emulsion

An emulsion is a mixture of lipids and an aqueous solution, commonly used in the pharmaceutical, cosmetic and food industries. Emulsions are formed by the dispersion of oil particles in water, making o/w emulsion, or by the dispersion of water particles in oils, making w/o emulsion. In the case of o/w emulsions, they help to solubilize lipophilic compounds in water, by solubilizing active compounds in oils, then dispersing oil in water. Multiple emulsions are emulsions of emulsions, meaning that the dispersed phase (for example, oil in o/w emulsions) is an emulsion itself. In the case of w/o/w multiple emulsions, they can have both lipophilic and hydrophilic compounds solubilized in 1 oil particle.

Interestingly, in the case of internal phase separation of multiple emulsions, a structure called Janus particles could be created when 2 phases still stay intact in 1 particle (Figure 3.9) [13]. This Janus-structured lipid particle was patented by our team, enabling the loading of both hydrophilic and lipophilic drugs in one particle.

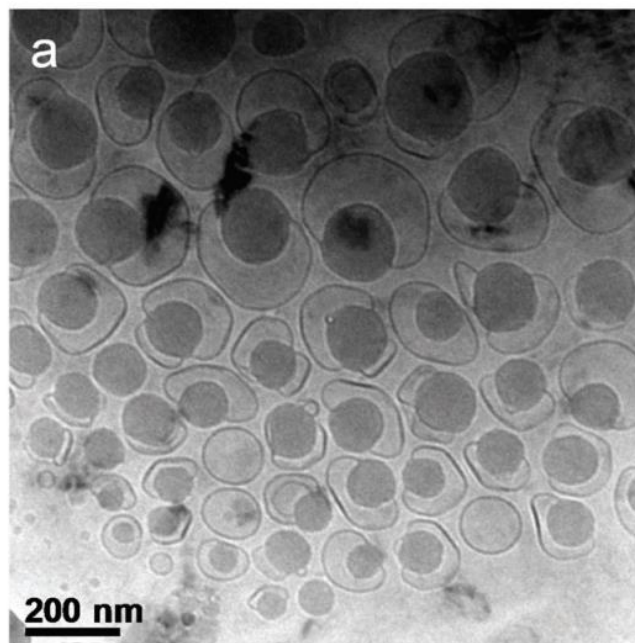


Figure 3.9. Janus lipid nanoparticles under Cryo-EM, figure adapted from ref. [13].

3.1.1. Composition of multiple emulsion

Multiple emulsions have 4 main components: lipid, water, lipophilic surfactant, and hydrophilic surfactant. While the lipid can be chosen according to the application and lipophilic active compounds, the choice of 2 types of surfactants is crucial for the formation of a stable multiple emulsion. The existence of small-size emulsion is not thermodynamically favorable, due to the high interfacial surface energy of the curvature. To stabilize the emulsion, the interfacial surface energy needs to be reduced via the activity of surfactants. Based on the amphiphilic characteristics of the surfactants, there are 2 types of surfactants: lipophilic surfactant and hydrophilic surfactant. The amphiphilic characteristic can be determined by the value hydrophilic-lipophilic balance (HLB). The HLB value can be calculated from the morphology of the molecule. The HLB scale range from 0 to 20 for non-ionic surfactant. The surfactant is called lipophilic if its HLB value is <10 , while it is called hydrophilic if its HLB value is >10 [14]. For ionic surfactants, the effective HLB can be very high, up to 40, due to the hydrophilicity of ionic groups [14]. The lipophilic surfactants (low HLB) favor the formation of w/o emulsion, while the hydrophilic surfactants (high HLB) favor the formation of o/w emulsion. So, to stabilize a multiple emulsion, the choice of a combination of surfactants and the optimization of their concentration is very

important. The oil phase can be made to crystallize by using high melting point lipids, such as those containing long-chain saturated triglycerides, diglycerides, monoglycerides, free fatty acids, hard fats, and waxes. Several works have demonstrated that this approach can improve the stability and functional properties of this kind of structured emulsion-based delivery system [15,16].

3.1.2. Fabrication methods of multiple emulsion

The mechanism of the formation of multiple emulsions is overcoming the interfacial energy barrier to create a metastable state of dispersion. In the ideal case, the multiple emulsion should be the metastable state which has a lower energy state than the formation of a normal emulsion, promoting the formation of multiple emulsions and preventing the coalescence of phases. To understand the fabrication of multiple emulsions, we first present the fabrication of normal emulsions. There are 2 main methods to fabricate normal emulsion: high-energy emulsification and spontaneous emulsification (also called phase inversion method). The high-energy emulsification method applies high stress to the water-lipid mixture to overcome the interfacial surface energy. The technique can be high-shear mixing, high-pressure homogenization, high-pressure microfluidic and ultra-sonication etc. As the interfacial surface energy increases with the decrease of the droplets' size, the higher the energy, the smaller the droplets. Spontaneous emulsification is the process of slowly adding the desired continuous phase (for example, water in the case of o/w emulsion) to the monophasic mixture (for example, oil in the case of o/w emulsion). Up to the phase boundary point, when the nucleation of nucleate droplets occurs, the monophasic mixture nucleates in the continuous phase and grows larger until the phase separation completes. In the presence of surfactants, the interfacial surface tension decreases and favors the stabilization of small droplets instead of the total phase separation.

In the fabrication of multiple emulsions, the sequential mixing of components is usually applied [14]. For example, to make a w/o/w emulsion, in the first step, a w/o emulsion is prepared using a lipophilic surfactant. Then, the prepared w/o emulsion is added to an aqueous solution containing hydrophilic surfactant to form the w/o/w emulsion. To mix the components, a high-energy mixing can be applied to obtain small-size droplets. However, high-energy mixing usually cannot control the size of the particles. In addition, the high energy may rupture the first emulsion, resulting in a normal emulsion. Sequential mixing can also be performed using microfluidic devices. The size of the droplet of multiple emulsions fabricated in this method, which is typically >10 μm , is dependent on the device geometry and capillary size [14].

Multiple emulsions can also be fabricated by the one-step mixing method. Using the engulfment mechanism, the emulsion is created using high-energy emulsification. The droplets are deformed by the high-energy mixing and a part of the continuous phase internalizes the droplet, making a multiple emulsion. The engulfment using high-energy

emulsification usually creates core-shell morphology droplets. In this method, the optimization of the surfactant ratio, surfactant concentration and volume of 2 phases are crucial [17,18].

3.1.3. Application of multiple emulsions in drug delivery research

Large-size multiple emulsions are widely used in the food industry and chemical preparation [14]. However, in pharmaceutical research, specifically in our project, we prefer micro- to nano-scale multiple emulsions. Herein, we summarize some examples of using nano-size multiple emulsions for drug delivery. Nano-size multiple emulsions can be used to load both hydrophobic and hydrophilic drugs.

Using nanosize w/o/w emulsion to load hydrophilic drugs, the release rate of hydrophilic drugs can be controlled [19,20]. For example in cancer treatment, a w/o/w emulsion was used to contain 5-fluorouracil (5-FU), an anticancer drug, to control its release rate in oral administration [20]. The *in vitro* release of 5-FU can be prolonged up to more than 60 minutes, depending on the formulation. The use of nano w/o/w emulsion to load hydrophilic drugs also improves drug penetration through the skin. By loading aciclovir, a hydrophilic drug, in a w/o/w emulsion, the amount of drug from w/o/w emulsion penetrated through the skin in a Franc cell experiment is larger than the amount of drug from an aqueous drug solution [19].

As an example of using nanosize w/o/w emulsion to load both hydrophilic and lipophilic drugs, oxaliplatin (OXA), a lipophilic anticancer drug, and 5-FU, a hydrophilic anticancer drug, have been loaded inside a nano-size w/o/w emulsion [21]. Authors used industrial excipients to fabricate w/o/w emulsion using 2 steps spontaneous emulsification method. In the 1st emulsion, Capryol 90 was used as the oil phase, Labrasol and Transcutol HP were used as the surfactant and co-surfactant. To make the w/o/w emulsion, the 1st emulsion was dispersed in water containing Cremophor EL and Transcutol HP as the surfactant and co-surfactant. The ratio of all components was optimized to maximize the yield of w/o/w emulsion. The w/o/w emulsion showed higher efficiency in tumor suppression than the control group of drugs only.

3.2. Liposome and α -gel particle

Liposomes are closed lipid vesicles made from lipid bilayers. Liposomes are fabricated from amphiphilic lipids having CPP of 1, which have a lamellar structure in water. Liposomes have been discovered since the mid-1960s, and there are already pharmaceutical, cosmetic and food commercial products using liposomes [22,23]. In the literature, there are several comprehensive reviews about liposome and its development [22,23]. We would like to refer readers to them for detailed information and experts' opinions. In this part, we present briefly the structure, fabrication process and application of liposomes, which may be applicable to our project. Liposomes are lipid particles having lipid bilayers membrane, which can load hydrophilic drugs, and

an aqueous core, which can load hydrophilic drugs. Liposomes can be uni-lamellar, meaning that the vesicle has only 1 membrane, or multi-lamellar, meaning that the vesicle has more than 1 membrane. The size of liposomes can be from 30 nm to micrometer scale.

Similar to liposomes, α -gel particles are also assembled from amphiphilic lipids having CPP of 1; however, α -gel particles are not closed vesicles. The difference is in the state of the hydrocarbon chain of the amphiphilic lipids used to make the particles. In liposomes, the hydrocarbon chain of the lipids is generally in the liquid state, leading to the fluid lamellar mesophase. In α -gel particles, the hydrocarbon chain of lipids is in the solid state, leading to the gel lamellar mesophase. Similar to liposomes, α -gel-based particles and emulsions are widely used in the pharmaceutical, cosmetic and food industries [24–26]. In α -gel particles, hydrophilic drugs can be loaded in between lamellar membranes, while lipophilic drugs can be loaded inside hydrocarbon chains, or in oil droplets in the case of α -gel based emulsions (Figure 3.10).

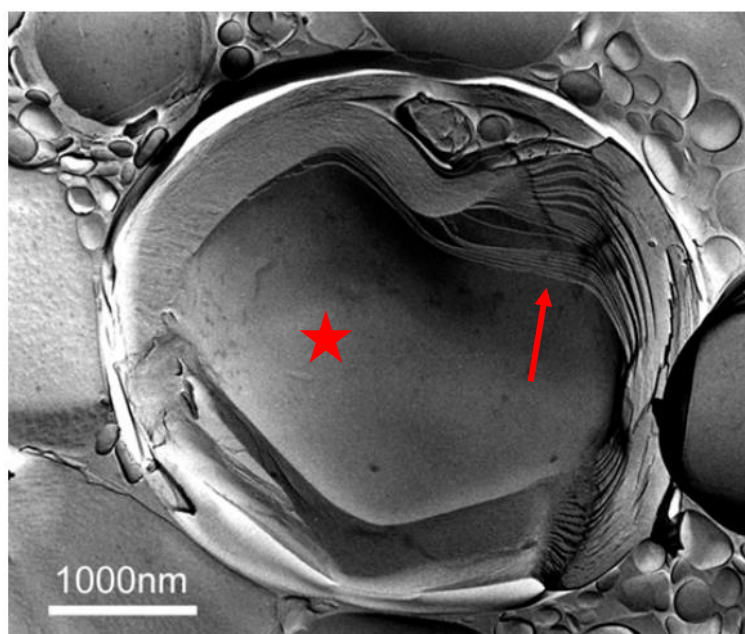


Figure 3.10. α -gel based emulsion under Cryo-EM, the arrow points to the α -gel region, the star indicates the oil droplet, the figure is adapted from ref. [8].

3.2.1. Composition of liposome and α -gel particle

To fabricate liposomes and α -gel particles, amphiphilic lipids having CPP of 1 are required to create lamellar mesophase. In the case of liposomes, glycerolphospholipid (GP), sphingomyelin (SM) and cholesterol (Chol) are basic components of current products in the market (Figure 3.11) [22]. The hydrophilic head of phospholipids is chosen to have negative, positive or neutral charges in the working pH, according to the requirement of the application. GPs are the key component of liposomes that form lipid bilayers. The choice of GPs affects the drug encapsulation efficiency, stability, and drug

release behavior of liposomes. For example, the morphology of the hydrocarbon chain of GPs (unsaturation degree, branching, length etc) influences the fluidity and the phase transition temperature of the lipid bilayer. The long hydrocarbon chain may tighten the membrane, increasing the drug retention efficiency. When the glycerol of GPs is replaced by the sphingosine group, the SMs are obtained. When using SMs to form liposomes instead of GPs, the stability of liposomes in acid increases, due to the slower hydrolysis rate in acid of SMs compared to GPs [22]. Chol promotes the packing of lipid chains and helps the formation of lipid bilayer via the change in the fluidity of the membrane. The addition of Chol may control the drug release rate and the stability of liposomes [22]. In addition to GP, SM and Chol, other additives or additional components may be added to functionalize liposomes. For example, the polyethylene glycol (PEG) group may be functionalized on the surface of liposomes by using PEG-lipid to increase the circulation time and protect drugs from metabolic degradation [23]. The cellular intake efficiency of liposomes can be increased by functionalizing ligands like antibodies, proteins, and nucleic acids on the surface of liposomes [23].

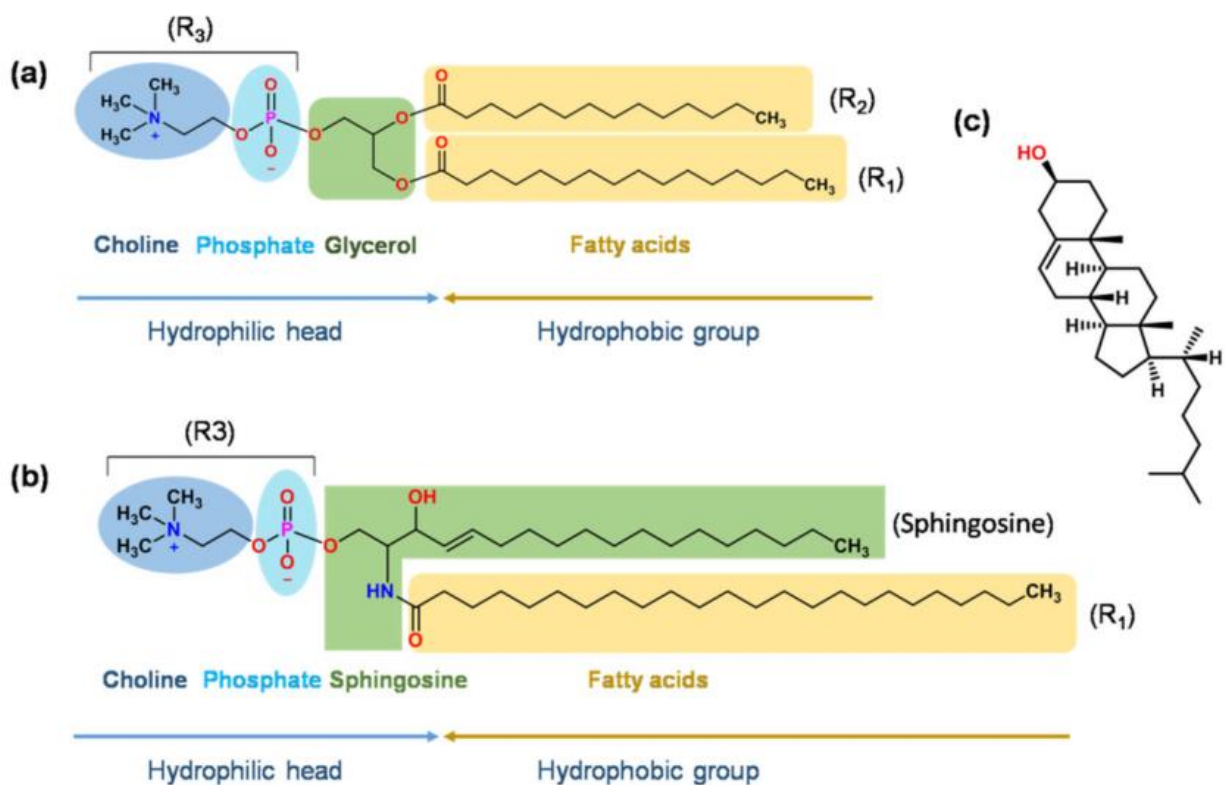


Figure 3.11. The main components of liposome (a) glycerolphospholipid, R1 and R2 are fatty acids, such as decanoic acid, lauric acid, palmitic acid, oleic acid, myristic acid, stearic acid, and erucic acid, R3 can be phosphatidylcholine (PC), phosphatidyl ethanolamine (PE), phosphatidyl serine (PS), phosphatidyl inositol (PI), phosphatidic acid (PA), phosphatidylglycerol (PG), and cardiolipin. (b) sphingomyelin and (c) cholesterol. The figure is adapted from ref. [22].

α -gel particles and α -gel based emulsions can be fabricated from lamellar gel phase lipids having CPP of 1, such as monoglycerides, a mixture of fatty alcohols with hydrophilic surfactants, phospholipids, etc. [26]. The α -gel lamellar phase is usually used in the cream formulation, to stabilize oil droplets and form an α -gel network. When the α -gel lamellar phase is created by low HLB molecules, such as monoglycerides or fatty alcohols, the addition of a high HLB surfactant is required to create α -gel particle suspension.

3.2.2. Fabrication methods of liposome and α -gel particle

The fabrication of liposomes can be described in 2 main steps: liposomes formation and size reduction. There are several liposome formation methods [23]; herein, we only briefly introduce widely used methods, which are film hydration, solvent injection, and emulsification [22,27].

The thin film hydration method starts with the dissolution of lipids in an organic solvent. The solution is then evaporated under a vacuum using a rotary evaporator to create a thin film of lipids. Multiple lamellar vesicles are then formed by adding an aqueous solution to hydrate the thin film. This method can be applied to all kinds of lipids; however, it is difficult to scale up and has a low encapsulation efficiency for water-soluble drugs [23].

The solvent injection method starts with the dissolution of lipids in a water-miscible solvent, usually ethanol or ether. The lipid solution is then injected into a large quantity of aqueous buffer solution. Liposomes are then formed spontaneously in the aqueous solution. Another modified version of this method is the use of microfluidic devices to mix the organic phase and aqueous phase to form liposomes. This method is simple and reproducible. However, it is not suitable for ethanol-sensitive proteins, and the removal of ethanol is difficult.

The emulsification method starts by mixing an organic solvent, water, and lipids to form a water-in-organic solvent emulsion. The solvent is then removed slowly using a rotary evaporator. Liposomes will form around water droplets. This method is simple and has a high encapsulation efficiency. However, it requires a large volume of organic solvent and cannot be applied to load fragile molecules.

After the formation of liposomes, the size reduction step is usually conducted. The high energy is applied to the liposomes to cut them into smaller particles, which self-assemble again to form small liposomes. The techniques usually used are ultrasonication, French press, extrusion and high-pressure homogenization. In commercial products, extrusion and high-pressure homogenization are widely used due to their simplicity and large-scale production capacity [22].

The fabrication of α -gel particles or α -gel-based emulsion is similar to the fabrication of emulsion, which is described above. Since the lamellar gel phase can be formed easily by mixing lipids with water, the formation of particles is done by high-energy mixing methods, such as sonication or homogenizer to generate α -gel lipid particles.

3.2.3. Application of liposome and α -gel particle in drug delivery research

The amount of publication about α -gel particles or α -gel-based emulsions in drug delivery applications is still limited, despite their wide use in several industries. Probably because amphiphilic surfactants having lamellar gel phases, such as fatty alcohols or monoglycerides, are usually identified as co-surfactants or additives in a formulation. In addition, according to Iwata [26], the technology of the lamellar gel phase has been maintained as a trade secret by companies. In contrast, there are several reports about the use of liposomes to co-encapsulate both hydrophilic and lipophilic drugs and we present here some examples of them.

Chen et al. encapsulated both Epigallocatechin-3-gallate (EGCG), a hydrophilic compound, and quercetin, a hydrophobic compound in liposomes for antioxidant application [28]. The liposomes were prepared using the thin film hydration method, with quercetin added during the thin film-making process, and EGCG added during the thin film hydration step. Both ingredients were encapsulated successfully in the liposomes, with EGCG in the aqueous core and quercetin in the lipid bilayer. The liposomes showed the synergistic antioxidant property *in vitro*.

Liu et al. encapsulated vitamin C, a hydrophilic compound, and β -carotene (BC), a hydrophobic compound in liposomes for oral administration [29]. The liposomes were prepared using the solvent injection method, with BC dissolved in a dichloromethane-ethanol (1:2 v/v) mixture, and vitamin C dissolved in an aqueous buffer solution. After the fabrication, vitamin C was in the aqueous core and BC was in the lipid bilayer. In the *in vitro* release study, both ingredients were released slowly in simulated gastric fluid pH 1.2 during the 1st 2 hours, then released faster in simulated intestinal fluid, reaching 72% cumulative release rate after 4 hours. The study showed the protection efficiency of liposomes for both hydrophilic and hydrophobic compounds against gastric acid.

Wong et al. encapsulated vincristine, a hydrophilic anticancer drug, and quercetin, a hydrophobic compound, in liposomes for the parental route [30]. Liposomes were prepared using the thin film hydration method, with quercetin added to the lipid solution in an organic solvent. Vincristine was loaded inside the liposomes after the formation of liposomes using an ionophore-mediated proton gradient. The liposomes showed a synergistic effect against cancer cells *in vitro*, with much higher cell elimination efficiency than free drugs. The liposomes also showed high efficiency *in vivo* experiments. The volume of tumors in mice treated with co-encapsulated liposomes was only 36% of the untreated groups, while the value for the group treated with free vincristine/quercetin combination was 49%. This study demonstrated the potential of

liposomes for co-encapsulation of both lipophilic and hydrophilic, promoting the treatment efficiency.

3.3. Hexosome, cubosome and sponge particle

Cubosome, hexosome and sponge particles are non-lamellar lipid particles. They all have both lipophilic and hydrophilic domains. The cubosome is a particle having bicontinuous cubic mesophase type 2, giving cubosome ordered hydrophilic and lipophilic networks. Sponge particle is particles having bicontinuous sponge mesophase, in which the hydrophilic and lipophilic networks are disordered. The hexosome is a particle having hexagonal mesophase type 2, in which the hydrophilic domain is in cylindrical micellar tubes, while the lipophilic domain is located around those tubes. We present them in the same section, because the transformation between bicontinuous cubic mesophase, hexagonal mesophase and sponge mesophase can be tuned by the change in temperature, pH, ionic strength or other environmental and fabrication parameters. In addition, they have a non-lamellar structure, meaning that the CPP of the molecules used to make them is usually larger than 1.

3.3.1. Composition of cubosome, hexosome and sponge particle

Non-lamellar lipid particles are made from amphiphilic lipids, additives, and stabilizers. The common amphiphilic lipids are phospholipids, monoglycerides, PEGylated phospholipids, glycolipids [31]. Due to the variability in the CPP, they may form different mesophases in water. In the fabrication of cubosome, hexosome and sponge particles, glycerol monooleate (GMO), phytantriol (PHYT) and the related structures are used frequently due to the high stability of their mesophases in excess water [31]. The structure of GMO and PHYT are shown in Figure 3.12. GMO is a natural lipid, which has been applied to make pharmaceutical and cosmetic formulations. The glycerol head contributes to its hydrophilicity, while the hydrocarbon chains give it the lipophilicity. Compared to PHYT, GMO is less stable, due to the possible oxidation of the ester bond and the unsaturated hydrocarbon chain. PHYT has similar physicochemical properties to GMO, however, is more stable. While PHYT is also biocompatible, PHYT-based formulation is shown to be more cytotoxic than GMO-based formulation in one study [32].

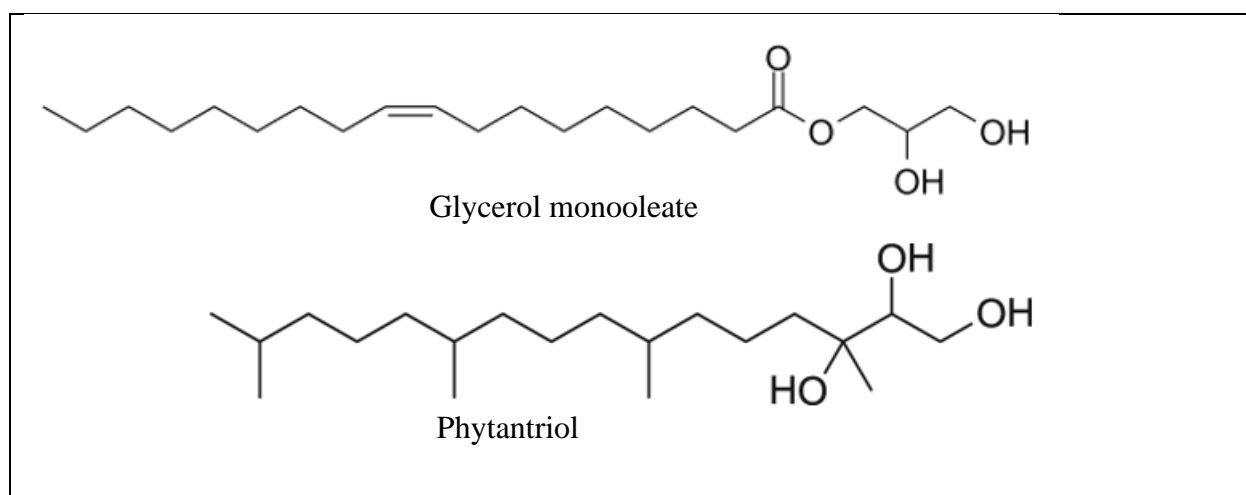


Figure 3.12. The molecular structure of glycerol monooleate (GMO) and phytantriol (PHYT)

While GMO and PHYT can form stable mesophases in excess water, the addition of surfactants, or drug molecules may change the mesophases and the stability [31]. To stable the structure and introduce functionality, additives may be added to the formulation. Fatty acids, phospholipids, glycolipids, mono- and diglycerides are commonly used [31]. For example, the formation of hexosomes, cubosomes and sponge phase particles can be controlled by the change in ratio and/or addition of glycerol dioleate and diglycerol monooleate to the main matrix of GMO [7].

Stabilizers are needed to stabilize lipid crystalline particles in water, reduce the viscosity and prevent the aggregation of particles. Block co-polymers, especially Pluronic F127 (also known as Poloxamer 407, P407) are frequently used as the stabilizer for cubosomes, hexosomes, and sponge phase particles [31]. Amphiphilic proteins, bile salts, PEGylated surfactants are also reported to maintain the stability of the dispersion [31]. P407 is a triblock hydrophilic co-polymer having 2 polyethylene glycol blocks and 1 polypropylene glycol block. P407 is used as a steric stabilizer via the adsorption of the polypropylene glycol block on the surface of the lipid particles in the case of PHYT-based cubosomes, and via the integration into the lipid inner structure in the case of GMO-based cubosomes [33]. The concentration of P407 can be used to control the size of the cubosomes [31]. Concerning safety issues, cubosomes stabilized by P407 caused cytotoxicity in certain cell lines. Discussion about other steric stabilizers and their application in drug delivery can be found in the reference [34].

3.3.2. Fabrication methods of cubosome, hexosome, and sponge particle

Cubosome, hexosome and sponge particles can be fabricated using the top-down approach or the bottom-up approach. The top-down approach, in general, is making particles from bulk-size input materials. Meanwhile, the bottom-up approach is the assembly of the particles from lipid molecules.

In the top-down approach to fabricate cubosome, hexosome and sponge particles, firstly, the lipid is hydrated by water in a designed ratio of lipids, water, stabilizers to make its bulk self-assembly structure, such as bicontinuous cubic phase, hexagonal phase or sponge phase. Then a high-energy input, such as high-pressure homogenization or ultrasonication, is applied to the bulk self-assembly structure to shear and cut down to the desired particle size. The typical reported lipid particle size is in the range of 100 nm [31]. The drawback of the method is the heat produced during the high-energy process may degrade the sample, if there are any heat-sensitive components. Moreover, undesirable particles, such as vesicles, may be produced [31].

The bottom-up approach is also known as the hydrotrope approach. Firstly, the lipid is dissolved in hydrotropes, such as ethanol, to create a solution of lipid molecules. The lipid solution in hydrotropes is then poured into the aqueous phase containing stabilizers; the mixture is then agitated under a low-energy method such as vortex or stirring, until the complete formation of lipid particles. The bottom-up method has the advantage of low energy input, low working temperature, and a low percentage of undesirable particles. However, the control of the particle size is difficult. In addition, even with evaporation, residual hydrotropes may be present, posing toxicity problems. Some products, which are sensitive to chosen hydrotropes, may not be suitable for this method.

For drug loading, drugs can be pre-loaded inside the lipid matrix, post-loaded after the fabrication of lipid particles or pre-loaded inside hydrotropes [35]. In the pre-loading strategy, drugs are usually loaded inside lipids before the hydration step. This strategy ensures the encapsulation of drugs inside lipids and may increase the encapsulation efficiency. In the post-loading strategy, drugs are loaded via the adsorption on the surface of fabricated lipid particles. This strategy can be applied to hydrophilic drugs, which penetrate the water network inside cubosome, hexosome or sponge phase particles. In the hydrotrope-loading strategy, drugs are soluble in hydrotrope during the lipid solution preparation step. This strategy may be applied for drugs which are soluble in hydrotrope.

3.3.3. Application of cubosome, hexosome, and sponge particle in drug delivery research

Cubosome, hexosome and sponge phase particles can be applied in drug delivery applications. While cubosomes and hexosomes are widely used, the number of reports about sponge phase particles is low. We will report here the research about cubosomes, hexosomes and sponge phase particles to load hydrophilic and/or lipophilic drugs. Lipophilic drugs can be loaded inside the lipid bilayer, while hydrophilic drugs can be loaded inside aqueous networks, enabling a wide range of applications for cubosomes, hexosomes and sponge phase particles [31,35].

As an example of co-loading lipophilic compounds in cubosomes and sponge phase particles, the work of Rakotoarisoa et al. in our team showed the potential of using cubosomes and sponge phase particles loaded with curcumin and fish oil to protect cells against oxidative stress [36]. Both curcumin and fish oil were integrated inside the lipid matrix. By varying the quantity of fish oil, the mesophase of the lipid particles was tuned from bicontinuous cubic (low fish oil content) to sponge phase (high fish oil content). Both types of lipid particles had the antioxidative stress property *in vitro*, suggesting the potential for neuro-regenerative applications.

As an example of the loading of a hydrophilic drug in cubosome, 5-fluorouracil (5-FU), a hydrophilic anticancer drug, has been loaded inside cubosome made from GMO and P407 [37]. Because 5-FU is soluble water, a large quantity of 5-FU was outside of the particles, leading to an encapsulation efficiency of 31%. *In vitro*, after a burst release, the 5-FU was released slowly due to the diffusion mechanism from the aqueous network of cubosomes. *In vivo* study showed the accumulation of the drug in the liver when injecting 5-FU loaded cubosomes, 5 times higher than the accumulation of the drug in the case of injection of 5-FU solution, indicating the liver-targeting effect of cubosomes.

As an example of the co-loading of both hydrophilic and lipophilic active compounds in one carrier, Li et al. reported the fabrication of pH-responsive GMO-based cubosome and hexosome for the co-delivery of *Brucea javanica* oil (BJO) and doxorubicin (DOX) [38]. The main materials for the lipid particles were GMO and oleic acid, with pluronic F127 as the stabilizer. BJO was incorporated inside the lipid phase, while DOX was loaded inside the aqueous phase of the lipid particles. However, the presence of DOX also affected the lipid structure, indicated by the peak shift in the X-ray scattering experiment. The fabricated lipid particles were pH-responsive, as the mesophases changed with pH. In pH 7.4, pH 6.8, pH 5.3, the particles were hexosome, cubosome and emulsified microemulsion, respectively. The formulation had cytotoxic activity against cancer cells *in vitro*, suggesting its potential application.

4. Conclusion

By taking advantage of the lyotropic behavior of lipids, several types of particulate formulations can be created to load both hydrophilic and lipophilic compounds for drug delivery application. Each type of formulation has its own advantages and disadvantages. Therefore, careful analysis needs to be done to choose the most suitable type of formulation for the project.

Cubosomes, hexosomes and sponge phase particles are good candidates for the project; however, they have low gastrointestinal resistance [31]. The change in pH in the oral administration route would change the lipid mesophase, hence influencing the drug release property. Moreover, the optimization of the formulation ratio is essential for the formation of the desired mesophase. The purity of lipids is important for the

optimization purpose, since the impurity may change the phase behavior. So, the materials to make cubosome, hexosome and sponge phase particles are generally expensive due to their high purity. Similarly, for liposome fabrication, the quality of phospholipid and cholesterol in the formulation needs to be high to ensure the integrity of the lipid membrane. In addition, the lipid concentration in the case of cubosomes, hexosomes, sponge phase particles and liposomes is low (from 0.01 wt% to 10% wt% of the formulation) [39], hindering the amount of drug loaded inside the formulation.

Multiple emulsion has been used for a long time in industries. The pharmaceutical excipients for multiple emulsions such as surfactants and lipids are available in large quantities. Moreover, the fabrication process is simple and well-established. The concentration of lipids in emulsions is much higher, can be up to 30wt% of the formulation [40], leading to a high potential for drug loading. So, we conclude that the use of multiple emulsions would be interesting for the project. Furthermore, in order to avoid water droplet coalescence and/or drug leakage, our primary intention is to develop crystallizable multiple emulsions in the nanometric size range to favor our application.

References

- [1] K. Holmberg, D.O. Shah, M.J. Schwuger, eds., Handbook of applied surface and colloid chemistry, Wiley, Chichester, England ; New York, 2002.
- [2] T.T. Mills, G.E.S. Toombes, S. Tristram-Nagle, D.-M. Smilgies, G.W. Feigenson, J.F. Nagle, Order Parameters and Areas in Fluid-Phase Oriented Lipid Membranes Using Wide Angle X-Ray Scattering, *Biophys. J.* 95 (2008) 669–681. <https://doi.org/10.1529/biophysj.107.127845>.
- [3] C.V. Kulkarni, Lipid crystallization: from self-assembly to hierarchical and biological ordering, *Nanoscale.* 4 (2012) 5779–5791. <https://doi.org/10.1039/C2NR31465G>.
- [4] B. Angelov, A. Angelova, R. Mutafchieva, S. Lesieur, U. Vainio, V.M. Garamus, G.V. Jensen, J.S. Pedersen, SAXS investigation of a cubic to a sponge (L3) phase transition in self-assembled lipid nanocarriers, *Phys. Chem. Chem. Phys.* 13 (2011) 3073–3081. <https://doi.org/10.1039/C0CP01029D>.
- [5] FRAP to Characterize Molecular Diffusion and Interaction in Various Membrane Environments, *PLOS ONE.* 11 (2016) e0158457. <https://doi.org/10.1371/journal.pone.0158457>.
- [6] M. Valldeperas, M. Wiśniewska, M. Ram-On, E. Kesselman, D. Danino, T. Nylander, J. Barauskas, Sponge Phases and Nanoparticle Dispersions in Aqueous Mixtures of Mono- and Diglycerides, *Langmuir.* 32 (2016) 8650–8659. <https://doi.org/10.1021/acs.langmuir.6b01356>.

- [7] J. Barauskas, M. Johnsson, F. Tiberg, Self-Assembled Lipid Superstructures: Beyond Vesicles and Liposomes, *Nano Lett.* 5 (2005) 1615–1619. <https://doi.org/10.1021/nl050678i>.
- [8] T. Suzuki, Liquid Crystal and α -gel-Based Emulsion and Soft Gel formulations, *Acc. Mater. Surf. Res.* (2017), Vol.2, No.1, 21-40
- [9] A. Yagmur, L. de Campo, L. Sagalowicz, M.E. Leser, O. Glatter, Emulsified Microemulsions and Oil-Containing Liquid Crystalline Phases, *Langmuir.* 21 (2005) 569–577. <https://doi.org/10.1021/la0482711>.
- [10] F. Rebry, V. Nelis, K. Moens, K. Dewettinck, P. Van der Meeren, Production of reduced-fat whipped toppings by solid fat-based W/O/W double emulsions: proof of concept, *Int. J. Food Sci. Technol.* 55 (2020) 1950–1961. <https://doi.org/10.1111/ijfs.14449>.
- [11] C.V. Kulkarni, W. Wachter, G. Iglesias-Salto, S. Engelskirchen, S. Ahualli, Monoolein: a magic lipid?, *Phys. Chem. Chem. Phys.* 13 (2011) 3004–3021. <https://doi.org/10.1039/C0CP01539C>.
- [12] G. Bastiat, P. Oliger, G. Karlsson, K. Edwards, M. Lafleur, Development of Non-Phospholipid Liposomes Containing a High Cholesterol Concentration, *Langmuir.* 23 (2007) 7695–7699. <https://doi.org/10.1021/la700824m>.
- [13] T. Truong-Cong, E. Millart, L.T.C. Tran, H. Amenitsch, G. Frebourg, S. Lesieur, V. Faivre, A scalable process to produce lipid-based compartmented Janus nanoparticles with pharmaceutically approved excipients, *Nanoscale.* 10 (2018) 3654–3662. <https://doi.org/10.1039/C7NR08488A>.
- [14] T. Sheth, S. Seshadri, T. Prileszky, M.E. Helgeson, Multiple nanoemulsions, *Nat. Rev. Mater.* 5 (2020) 214–228. <https://doi.org/10.1038/s41578-019-0161-9>.
- [15] S. Herzi, W. Essafi, Crystallizable W/O/W double emulsions made with milk fat: Formulation, stability and release properties, *Food Res. Int.* 116 (2019) 145–156. <https://doi.org/10.1016/j.foodres.2018.08.023>.
- [16] J. Liu, H. Zhou, J.L. Muriel Mundo, Y. Tan, H. Pham, D.J. McClements, Fabrication and characterization of W/O/W emulsions with crystalline lipid phase, *J. Food Eng.* 273 (2020) 109826. <https://doi.org/10.1016/j.jfoodeng.2019.109826>.
- [17] M. Zhang, P.T. Corona, N. Ruocco, D. Alvarez, P. Malo de Molina, S. Mitragotri, M.E. Helgeson, Controlling Complex Nanoemulsion Morphology Using Asymmetric Cosurfactants for the Preparation of Polymer Nanocapsules, *Langmuir.* 34 (2018) 978–990. <https://doi.org/10.1021/acs.langmuir.7b02843>.

- [18] P. Malo de Molina, M. Zhang, A.V. Bayles, M.E. Helgeson, Oil-in-Water-in-Oil Multinanoemulsions for Templating Complex Nanoparticles, *Nano Lett.* 16 (2016) 7325–7332. <https://doi.org/10.1021/acs.nanolett.6b02073>.
- [19] J.C. Schwarz, V. Klang, S. Karall, D. Mahrhauser, G.P. Resch, C. Valenta, Optimisation of multiple W/O/W nanoemulsions for dermal delivery of aciclovir, *Int. J. Pharm.* 435 (2012) 69–75. <https://doi.org/10.1016/j.ijpharm.2011.11.038>.
- [20] F. Shakeel, N. Haq, A. Al-Dhfyhan, F. Alanazi, I. Alsarra, Double w/o/w nanoemulsion of 5-fluorouracil for self-nanoemulsifying drug delivery system, *J. Mol. Liq.* 200 (2014) 183–190. <https://doi.org/10.1016/j.molliq.2014.10.013>.
- [21] R. Pangen, S.W. Choi, O.-C. Jeon, Y. Byun, J.W. Park, Multiple nanoemulsion system for an oral combinational delivery of oxaliplatin and 5-fluorouracil: preparation and *in vivo* evaluation, *Int. J. Nanomedicine.* 11 (2016) 6379–6399. <https://doi.org/10.2147/IJN.S121114>.
- [22] P. Liu, G. Chen, J. Zhang, A Review of Liposomes as a Drug Delivery System: Current Status of Approved Products, Regulatory Environments, and Future Perspectives, *Molecules.* 27 (2022) 1372. <https://doi.org/10.3390/molecules27041372>.
- [23] V.V.S.N.L. Andra, S.V.N. Pammi, L.V.K.P. Bhatraju, L.K. Ruddaraju, A Comprehensive Review on Novel Liposomal Methodologies, Commercial Formulations, Clinical Trials and Patents, *BioNanoScience.* 12 (2022) 274–291. <https://doi.org/10.1007/s12668-022-00941-x>.
- [24] F.C. Wang, A.G. Marangoni, Advances in the application of food emulsifier α -gel phases: Saturated monoglycerides, polyglycerol fatty acid esters, and their derivatives, *J. Colloid Interface Sci.* 483 (2016) 394–403. <https://doi.org/10.1016/j.jcis.2016.08.012>.
- [25] G. Eccleston, Multiple-phase oil-in-water emulsion, *J Soc Cosmet Chem.* 41 (1990).
- [26] T. Iwata, Chapter 25 - Lamellar Gel Network, (n.d.) 33.
- [27] L. Šturm, N. Poklar Ulrih, Basic Methods for Preparation of Liposomes and Studying Their Interactions with Different Compounds, with the Emphasis on Polyphenols, *Int. J. Mol. Sci.* 22 (2021) 6547. <https://doi.org/10.3390/ijms22126547>.
- [28] W. Chen, M. Zou, X. Ma, R. Lv, T. Ding, D. Liu, Co-Encapsulation of EGCG and Quercetin in Liposomes for Optimum Antioxidant Activity, *J. Food Sci.* (2018) 1750-3841.14405. <https://doi.org/10.1111/1750-3841.14405>.

- [29] X. Liu, P. Wang, Y.-X. Zou, Z.-G. Luo, T.M. Tamer, Co-encapsulation of Vitamin C and β -Carotene in liposomes: Storage stability, antioxidant activity, and *in vitro* gastrointestinal digestion, *Food Res. Int.* 136 (2020) 109587. <https://doi.org/10.1016/j.foodres.2020.109587>.
- [30] M.-Y. Wong, G.N.C. Chiu, Liposome formulation of co-encapsulated vincristine and quercetin enhanced antitumor activity in a trastuzumab-insensitive breast tumor xenograft model, *Nanomedicine Nanotechnol. Biol. Med.* 7 (2011) 834–840. <https://doi.org/10.1016/j.nano.2011.02.001>.
- [31] C. Tan, S.F. Hosseini, S.M. Jafari, Cubosomes and Hexosomes as Novel Nanocarriers for Bioactive Compounds, *J. Agric. Food Chem.* 70 (2022) 1423–1437. <https://doi.org/10.1021/acs.jafc.1c06747>.
- [32] J. Zhai, R. Suryadinata, B. Luan, N. Tran, T.M. Hinton, J. Ratcliffe, X. Hao, C.J. Drummond, Amphiphilic brush polymers produced using the RAFT polymerisation method stabilise and reduce the cell cytotoxicity of lipid lyotropic liquid crystalline nanoparticles, *Faraday Discuss.* 191 (2016) 545–563. <https://doi.org/10.1039/C6FD00039H>.
- [33] Y.-D. Dong, I. Larson, T.J. Barnes, C.A. Prestidge, S. Allen, X. Chen, C.J. Roberts, B.J. Boyd, Understanding the interfacial properties of nanostructured liquid crystalline materials for surface-specific delivery applications, *Langmuir ACS J. Surf. Colloids.* 28 (2012) 13485–13495. <https://doi.org/10.1021/la302435g>.
- [34] J.Y.T. Chong, X. Mulet, B.J. Boyd, C.J. Drummond, Chapter Five - Steric Stabilizers for Cubic Phase Lyotropic Liquid Crystal Nanodispersions (Cubosomes), in: A. Iglič, C.V. Kulkarni, M. Rappolt (Eds.), *Adv. Planar Lipid Bilayers Liposomes*, Academic Press, 2015: pp. 131–187. <https://doi.org/10.1016/bs.adplan.2014.11.001>.
- [35] M.A.S. Abourehab, M.J. Ansari, A. Singh, A. Hassan, M.A. Abdelgawad, P. Shrivastav, B.M. Abualsoud, L.S. Amaral, S. Pramanik, Cubosomes as an emerging platform for drug delivery: a review of the state of the art, *J. Mater. Chem. B.* 10 (2022) 2781–2819. <https://doi.org/10.1039/D2TB00031H>.
- [36] M. Rakotoarisoa, B. Angelov, V.M. Garamus, A. Angelova, Curcumin- and Fish Oil-Loaded Spongosome and Cubosome Nanoparticles with Neuroprotective Potential against H₂O₂-Induced Oxidative Stress in Differentiated Human SH-SY5Y Cells, *ACS Omega.* 4 (2019) 3061–3073. <https://doi.org/10.1021/acsomega.8b03101>.
- [37] M. Nasr, M.K. Ghorab, A. Abdelazem, *In vitro* and *in vivo* evaluation of cubosomes containing 5-fluorouracil for liver targeting, *Acta Pharm. Sin. B.* 5 (2015) 79–88. <https://doi.org/10.1016/j.apsb.2014.12.001>.

- [38] Y. Li, A. Angelova, F. Hu, V.M. Garamus, C. Peng, N. Li, J. Liu, D. Liu, A. Zou, pH Responsiveness of Hexosomes and Cubosomes for Combined Delivery of Brucea javanica Oil and Doxorubicin, *Langmuir*. 35 (2019) 14532–14542. <https://doi.org/10.1021/acs.langmuir.9b02257>.
- [39] D. Carugo, E. Bottaro, J. Owen, E. Stride, C. Nastruzzi, Liposome production by microfluidics: potential and limiting factors, *Sci. Rep.* 6 (2016) 25876. <https://doi.org/10.1038/srep25876>.
- [40] D.H. Teitelbaum, I.F. Btaiche, A.G. Coran, Chapter 12 - Nutritional Support in the Pediatric Surgical Patient, in: A.G. Coran (Ed.), *Pediatr. Surg.* Seventh Ed., Mosby, Philadelphia, 2012: pp. 179–199. <https://doi.org/10.1016/B978-0-323-07255-7.00012-X>.

III. EXPERIMENTAL PART

Chapter 4. Excipients screening, pre-formulation and process parameters optimization.....	124
Chapter 5. Sorbitan stearate: from the hydration behavior to the preparation of α -gel based particles.....	147
Chapter 6. Solid lipid particles - chitosan nanocomposite for chemoattraction and elimination of <i>Helicobacter pylori</i>	182

Chapter 4. Excipients screening, pre-formulation and process parameters optimization

Hung V. Nguyen, Vincent Faivre

Université Paris-Saclay, CNRS, Institut Galien Paris Sud, 5 rue JB Clément, 92296 Châtenay-Malabry, France.

Abstract

This first chapter presents the work of materials screening and optimization of fabrication parameters. With the aim to create lipid particles that can load both hydrophilic and lipophilic drugs, we adopted the hot homogenization method. From 4 lipophilic surfactants and 2 lipids, we found the combination of 1 lipophilic surfactant and 1 lipid to be the main lipid matrix, which can load water with high stability. We have chosen and optimized the ratio of cocoa butter and sorbitan monostearate (Montane 60) in the emulsion to be 2/8. Then, sodium dodecyl sulfate (SDS) has been chosen to be the hydrophilic surfactant to stabilize the lipid particles and to charge them negatively. The temperature of fabrication and steps of fabrication have also been optimized to raise the robustness of the process. We then successfully fabricated lipid nanoparticles that can load water inside and are charged negatively.

1. Introduction

The first step of any formulation development process is choosing materials and performing materials characterization. In our team, while we have already developed strategies to load both hydrophilic and lipophilic drugs in one carrier, they are not suitable for our current application in this project [1]. Based on our expertise, we decided to screen and investigate existing industrial excipients to find suitable materials for the project. In our formulation, we need to load urea solution inside lipid nanoparticles. We envisioned the fabrication of a water-in-oil-in-water (w/o/w) nanoemulsion (also called multiple nanoemulsion) [2]. However, instead of using oil, we will try to use solid lipids. We hypothesized that the solid lipid multiple nanoemulsion can be produced using the 2-step emulsification method. The 1st step is making w/o emulsion by using a lipophilic surfactant to stabilize water inside the lipid matrix. The 2nd step is mixing the obtained w/o emulsion into a hydrophilic surfactant solution to make the w/o/w emulsion. The hydrophilic surfactant will stabilize the w/o lipid particles in water. Due to being solid, the lipid matrix will prevent the separation of water droplets in the lipid matrix. Lastly, we introduce charges on the surface of the lipid nanoparticles to prepare for the coating of polymers.

In this chapter, we will present the materials screening results and the optimization of the fabrication parameters. The characterization of materials and the interaction

between materials will also be reported. At the end of the chapter, we completed and established the fabrication process to make solid lipid nanoparticles that can load urea solution inside the particles.

2. Materials and methods

2.1. Materials

Cocoa butter was provided by Edna Group. Sorbitan monostearate and sorbitan monooleate were provided by Seppic under the trade name of Montane 60 (M60) and Montane 80. Sorbitan tristearate and sorbitan trioleate were provided by Croda under the trade name of Span 65 and Span 85. Precirol and Gelucire 50/13 were provided by Gattefosse. 1-Octadecylamine (ODA, 97%) was purchased from Alfa Aesar. Urea (Molecular Biology grade, Ultrapure, Batch 200927) was purchased from Thermo Scientific. Lecithin Phospholipon 90G (P90G) was provided by Lipoid GmbH. Erythromycin was purchased from Cooper. Sodium dodecyl sulfate (SDS, GPR Retapur®) was purchased from VWR chemical.

2.2. Taguchi's design of experiment for excipients screening

To optimize the choice of materials, we set up a Taguchi's design of experiment (DoE) to make a water-in-oil emulsion (w/o) from a lipid, a lipophilic surfactant, and a urea solution at the eutectic point (the use interest of urea eutectic solution will be explained in the following section). In terms of materials for the experiment, we investigated cocoa butter (triglyceride of mainly palmitic, stearic, and oleic acids) and Precirol® (diglycerides of palmitic and stearic acids) as the main lipid matrix, since the team already has some experience with them. Montane 60, Montane 80, span 65, or span 85 were chosen as the lipophilic surfactant to stabilize water inside the lipid matrix. By choosing these compounds, we established a series of lipophilic surfactants of the same family with different hydrophilic-lipophilic balance (HLB) values. The HLB value of Montane 60, Montane 80, Span 65 and Span 85 are 4.7, 4.3, 2.1, and 1.8, respectively [3–5]. Moreover, in the chocolate research field, sorbitan monostearate is often mixed as an additive in cocoa butter to reduce the blooming effect, hence proving that sorbitan monostearate is well fused in the matrix of cocoa butter [6]. The summary of the experiment design is shown in Table 4.1. To fabricate the w/o emulsion, in general, a lipid (cocoa butter or Precirol) and a surfactant (Montane 60, Montane 80, Span 65 or Span 85) were melted and mixed at 85°C. Then an amount of 85°C pre-heated urea solution at eutectic point (32.85 wt% [7]) was added to the lipid mixture. The mixture was then agitated using an Ultra-Turrax homogenizer IKA® for 5 minutes at level 5 (20000 rpm of no-load speed). The obtained w/o emulsion was then cooled to room temperature.

Surfactant	HLB	Surfactant concentration (wt%)	Hydration rate (%)	Lipid (0 = cocoa butter, 100 = Precirol)
Span 85	1.8	1	10	0
	1.8	5	20	0
	1.8	10	30	100
	1.8	15	40	100
Span 65	2.1	1	20	100
	2.1	5	10	100
	2.1	10	40	0
	2.1	15	30	0
Montane 80	4.3	1	30	0
	4.3	5	40	0
	4.3	10	10	100
	4.3	15	20	100
Montane 60	4.7	1	40	100
	4.7	5	30	100
	4.7	10	20	0
	4.7	15	10	0

Table 4.1. Summary of the factors and their levels in the design of experiment

The aim of the experiment was to find the right composition of lipid, surfactant, and hydration rate to have the highest urea solution loading percentage in the lipid matrix. In addition, since the final formulation is nanoscale, the size of urea solution droplets in the lipid matrix should be in the nanoscale. Because nano-size solution droplets freeze at a lower temperature than the solution in bulk form (explained by the nucleation theory), we can identify the amount of urea solution loaded inside the lipid matrix in the form of small droplets by differential scanning calorimetry (DSC) [8]. In the DSC experiment, we performed a cooling-heating cycle. The sample was cooled from 25°C to -45°C, kept at -45°C for 5 minutes, then heated to 25°C. The urea solution concentration was chosen at the eutectic point of urea-water. So, there was only 1 peak of freezing in the cooling step and 1 peak of melting in the heating step in DSC,

facilitating the data analysis. In the cooling step, only large-size urea solution droplets were frozen and identified by an exothermic peak at around -34°C. The enthalpy of melting of the melting peak in the heating step was used to calculate the enthalpy of fusion. We then calculated the ratio of the enthalpy of fusion of samples over the enthalpy of fusion of urea solution at the eutectic point. If the ratio was 1, all urea solution in the sample had been frozen at a temperature above -45°C, meaning that we did not have any small-size urea solution droplets in the lipid matrix. On the other hand, if the ratio was smaller than 1, the volume of urea solution that stayed in liquid at the end of cooling cycles was small droplets of urea solution. Therefore, we chose the response for the DoE is:

$$\text{enthalpy ratio (K)} = \frac{H_{\text{sample}}}{H_{\text{Urea sol. eutectic}}} \quad (\text{Equation 4.1})$$

with H_{sample} is the enthalpy of fusion calculated from the endothermic peaks in the heating cycle, $H_{\text{urea sol. eutectic}}$ is the enthalpy of fusion of urea solution at the eutectic point (found to be 269.23 J/g). K is ranging from 0 to 1.

2.3. DSC measurement of w/o emulsions

To find the response for the DoE, DSC measurement of all w/o emulsion samples was performed using a Diamond DSC machine (Perkin Elmer). The sample weight was about 10 mg. We set a cooling-heating cycle. In the 1st step, the temperature cooled from 20°C to -45°C at 2°C/min, then stayed at -45°C for 5 minutes, then raised from -45°C to 20°C at 2°C/min.

In the experiment to optimize the cocoa butter / Montane 60 ratio in the w/o emulsion, DSC measurement of all w/o emulsion samples was also performed using a Diamond DSC machine (Perkin Elmer). The sample weight was about 10 mg. We set a heating-cooling cycle. In the 1st step, the temperature increased from 20°C to 70°C at 2°C/min, then stayed at 70°C for 5 minutes, then decreased from 70°C to 20°C at 2°C/min.

In all DSC experiments, the time between the sample preparation and DSC measurement was overnight if not indicated. All samples were measured 3 times to ensure repeatability.

2.4. Sample morphology characterization by polarized light microscopy

To examine the structure and morphology of w/o emulsions, Nikon Eclipse E600 polarized light microscope was used. A homemade heater stage was used to observe the sample at different temperatures. A Mightex USB camera attached to the microscope was used to take photos.

2.5. Lipid structure characterization

The lipid structure was determined by the small- and wide-angle X-ray scattering technique (S-WAXS) using the Bruker MicroCalix machine. The S-WAXS patterns were acquired at the laboratory using a microfocus X-ray tube (I μ S, Incoatec), selecting the Cu K α radiation. It was used with an intensity of 1000 μ A and a voltage of 50 kV. The incident beam was focused at the detector with multilayer Montel optics and 2D Kratky block collimator. Small-angle (SAXS) and wide-angle (WAXS) X-ray scattering analyses were performed simultaneously using two position-sensitive linear detectors (Vantec-1, Bruker) set perpendicular to the incident beam direction, up to 7° (2 θ) and at 19° to 28° (2 θ) from it, respectively. The direct beam was stopped with a W-filter. The scattered intensity was reported as a function of the scattering vector

$$q=4\pi \sin \theta/\lambda \quad (\text{Equation 4.2})$$

where θ is half the scattering angle and λ is the wavelength of the radiation. The temperature of the samples was controlled by a Microcalix calorimeter cell (Bruker). Silver behenate and tristearin (β form) were used as standards to calibrate SAXS and WAXS detectors, respectively.

Samples for X-ray experiments were contained inside quartz glass capillary tubes (1.5 mm inner diameter) purchased from Glas Müller, Germany. The time between the sample preparation and measurement was overnight if not indicated. All samples were measured 3 times to ensure repeatability.

2.6. Fabrication of lipid nanoparticles

The fabrication of lipid nanoparticles has 2 steps, the 1st step of making w/o emulsion, and the 2nd step of making w/o/w emulsion. In the 1st step, cocoa butter, Montane 60, and water were melted and mixed at 85°C (the ratio of cocoa butter over Montane 60 CB/M60 is 6/4 or 2/8). Then an amount of 85°C pre-heated urea solution at the eutectic point was added to the lipid mixture, so that the hydration rate of Montane 60 is 30%. The mixture was then agitated using an Ultra-Turrax homogenizer IKA® for 5 minutes at level 5 (20000 rpm of no-load speed). In the 2nd step, the w/o emulsion was cooled down to the high-pressure homogenization (HPH) temperature (room temperature, 40°C or 85°C). Then it was mixed with a suspension of hydrophilic surfactants (P90G and Gelucire 50/13) so that the final weight percentage of lipid phase (cocoa butter plus Montane 60) was 10%, P90G was 1% and Gelucire 50/13 was 2%. The obtained suspension was called w/o/w suspension, which was homogenized by Ultra-Turrax for 5 minutes at level 5, then by a preheated high-pressure homogenizer (APV-2000 SPXFLOW) for 5 minutes at 600 bars. The choice of hydrophilic surfactant percentage and pressure in HPH were made from the experience of our group with the materials [1]. In the fabrication of w/o/w emulsion, we used water instead of urea solution, to be able to separate lipid phases using ultracentrifugation.

The obtained suspension after the HPH process was centrifuged at 40000 rpm, 4°C for 16 hours using an ultracentrifuge (Optima L-100K, Beckman Coulter), with the rotor 70.1 Ti to check the homogeneity of the suspension.

2.7. Particles' size and zeta potential measurement

The particle size and zeta potential were measured using Zetasizer Nano ZS90 (Malvern Panalytical Ltd.) at 25°C. To prepare the sample for measurements, the fabricated particle suspension was diluted 30 times in NaCl 3 mM solution. The final estimated particle concentration was 7 mg/ml. All measurements were repeated 3 times.

2.8. Solution surface tension measurement

SDS aqueous solutions from 0.005 to 0.3 wt% were prepared by the dilution of SDS mother solution 1 wt%. The surface tension was measured at 25°C by the Wilhelmy plate method, using a digital tensiometer (Krüss K10T, Germany). Before measurements, the surface of the solutions was cleaned using an absorbing paper and the platinum plate of the tensiometer was cleaned using concentrated sulfochromic acid. At the start of the experiment, the plate was brought into contact with the solution surface and the surface tension value was monitored until its value was considered stable. The error of the tensiometer measurement was 0.1 mN/m. The reported values of surface tensions are the average of 3 measurements.

2.9. Finding the solubility of erythromycin in SDS solution

Erythromycin was added in excess to a series of SDS aqueous solutions from 0.01 to 3 wt%. The solutions were mixed by a magnetic stirrer overnight to ensure the total solubility of erythromycin. Then they were filtered through a 200 nm syringe filter for the high-performance liquid chromatography (HPLC, Thermo UltiMate 3000 UHPLC system, Thermo Scientific™) measurement.

The dosage of erythromycin was adapted from the literature with some modifications [1]. We used a 150 x 4.6 mm I.D YMC-Triart C18 column (particle size of 3 µm and pore size of 12 nm). The mobile phase was acetonitrile (ACN) : 8 mM K₂HPO₄ solution in water at pH 9 (1:1) and flowed at 1 mL/min in the isocratic condition. The temperature of the column was kept at 50°C. The detection wavelength was 210 nm. The injection volume of samples was 20 µL. In running conditions, the stable pressure was 147 bar. Erythromycin retention time was 14 minutes. The running time was 30 minutes to be able to detect degraded products of erythromycin. The limit of detection (LOD) and limit of quantification (LOQ) of erythromycin were 4.1 µg/mL and 12.3 µg/mL, respectively. After each analytical sequence, the column was rinsed with ACN : H₂O (1:1) for 30 minutes, followed by ACN 100% for 30 minutes and stored in ACN.

3. Results and discussion

3.1. Input materials screening using DoE

Taguchi's design was chosen to screen input materials. The choice of the design was partially due to the low number of experiments that we needed to perform for multi-level factors. Since we have 3 factors having 4 levels and 1 factor having 2 levels, the number of experiments of a full factorial design would be 128. However, the decrease in the number of experiments causes the loss of information. Taguchi's design does not provide information about the interaction between factors. In addition, the aliasing of factors contributes to the response, and if it is significant, the main effect of factors would be false. The data analysis method of Taguchi is also controversial. A detailed discussion about the design of experiments would exceed the scope of this chapter, and we recommend the critical review of Taguchi's method found in the textbook of Montgomery [9]. Lastly, our response of enthalpy ratio K can identify the amount of small water droplets but cannot estimate their real size due to the lack of reference. By using an optical microscope and observing w/o emulsion samples having an enthalpy ratio significantly smaller than 1, we estimated the size of droplets that froze below -45°C was smaller than 10 microns. This is however an indirect method, since we cannot freeze the sample under the microscope. Therefore, the results obtained from our DoE are only for qualitative analysis to have a brief idea about the behavior of factors.

Figure 4.1 shows the effects of HLB, surfactant concentration, hydration rate and the choice of triglyceride materials (cocoa butter or Precirol) on the enthalpy ratio (the percentage of small-size droplets in the lipid mixture). The smaller the ratio, the higher percentage of small urea solution droplets in the sample. For example, Figure 4.2a shows the freezing and melting peaks of bulk-size urea solution at eutectic point urea-water, in this case, the enthalpy ratio is 1. Because the solution is at the eutectic point, there is only 1 peak of freezing and 1 peak of melting. The shape of the freezing peak is due to the fast crystallization rate of the solution, that the DSC equipment cannot catch up. Figure 4.2b shows the DSC signal from a w/o sample that had only small urea solution droplets. Since the sample only had urea solution in the form of small droplets, there was not any sharp peak of freezing at -34°C . We observed a small peak of freezing, which indicated the crystallization of a population of small-size droplets. In the heating step, we had the corresponding melting peak, which gave the enthalpy ratio of 0.04.

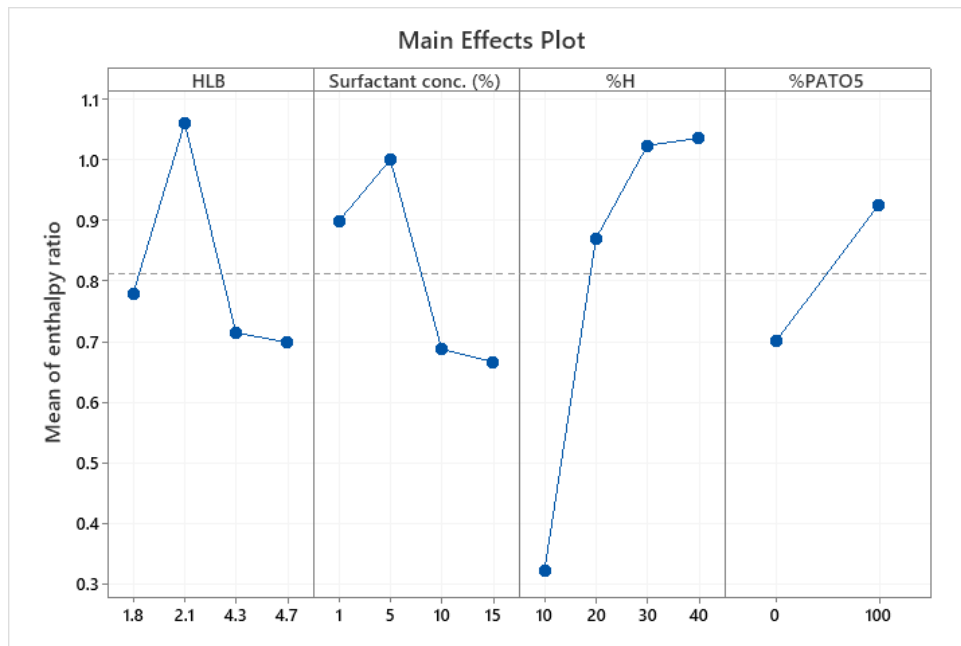


Figure 4.1. Summary of responses (enthalpy ratio) from main effects

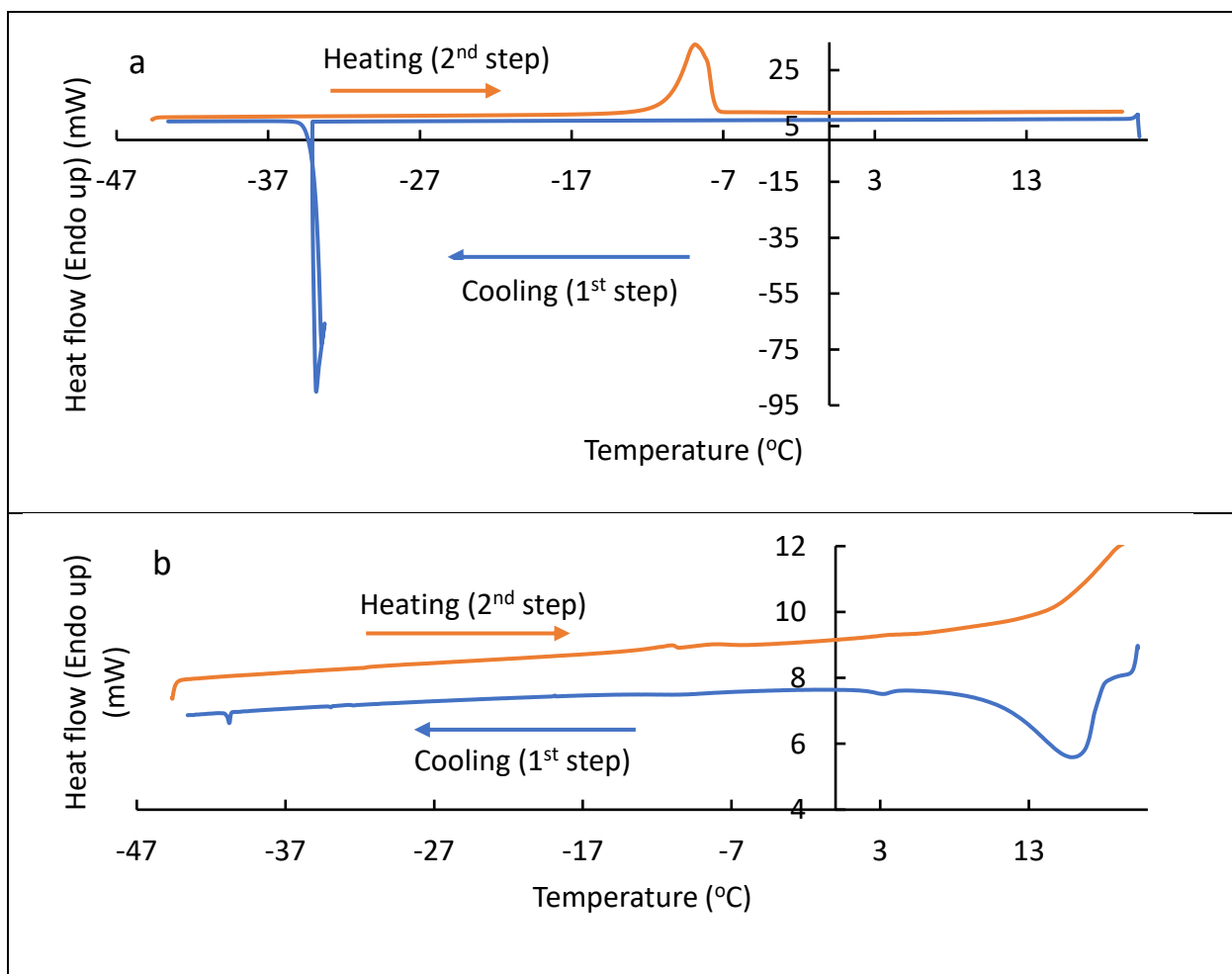


Figure 4.2. (a) DSC freezing and melting peaks of eutectic urea solution, (b) DSC freezing and melting peaks of urea solution in the sample (15 wt% Montane 60, 10% hydration rate, cocoa butter as lipid) which only had small urea solution droplet.

The hydration rate significantly influenced the response and could be identified as the most impactful factor. We obtained the tendency that the lower hydration rate was more favorable to have a high percentage of small urea solution droplets. It can be explained by the saturation of surfactants at the high hydration rate and the presence of urea solution outside the lipid matrix. Similarly, the high concentration of lipophilic surfactant concentration increased the amount of small-size urea solution droplets in the lipid matrix. For the type of lipid and surfactant, the influence was not so significant; however, we can see that the use of cocoa butter and Montane 60 (HLB = 4.7) was the most optimal. Therefore, we decided that the combination of cocoa butter and Montane 60 is interesting for further investigation. We then observed the w/o sample of cocoa butter and Montane 60 under a polarized light microscope (Figure 4.3). By varying the temperature, the components in the image could be identified. At 80°C, we have a w/o emulsion having microns-size droplets. At 45°C, when cocoa butter was still liquid, but Montane 60 had already solidified, we can confirm that the urea solution was stabilized by Montane 60. Montane 60 and water formed a gel-like structure when Montane 60 was solid. At 25°C, cocoa butter solidified, confirming that the background was cocoa butter.

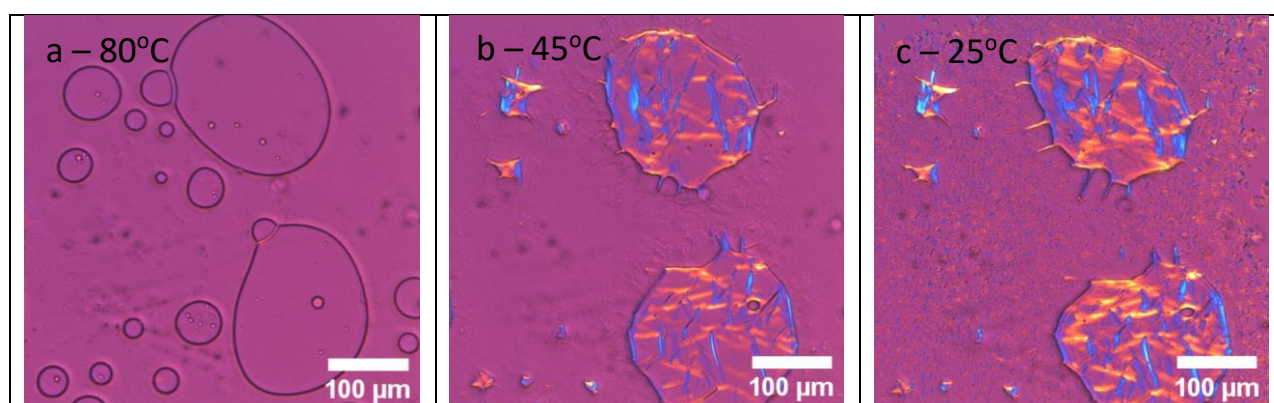


Figure 4.3. w/o emulsion (10% hydration rate) made from the mixture of cocoa butter, Montane 60 (15 wt%) and urea solution at (a) 80°C, (b) 45°C and (c) 25°C.

In summary, from the set of experiments, we have identified the input materials that are suitable for the loading of urea solution in a lipid. Cocoa butter is chosen as the lipid matrix, and Montane 60 is chosen as the lipophilic surfactant to stabilize the urea solution. In cocoa butter matrix, Montane 60 stabilizes urea solution by the formation of a gel-like hydrated structure. This structure is solid at room temperature. To maximize the urea solution loading capacity, the ratio of cocoa butter and Montane 60 needs to be optimized to maximize the quantity of gel-like structure in the lipid matrix. Then in the nanoparticle's fabrication process, we envisaged a top-down method to reduce the size of this gel-like structure from micro to nano-size.

3.2. Optimization of Montane 60 and cocoa butter ratio

To optimize the ratio of Montane 60 and cocoa butter in the emulsion, the lipid structure needs to be investigated. Figure 4.4 shows the S-WAXS spectra of cocoa butter, Montane 60 and hydrated Montane 60. The structure of cocoa butter has been well presented in the literature [10]. Cocoa butter is a mixture of triglycerides. The main fatty acids are palmitic (P), stearic (S) and oleic acids (O). The main triglycerides are POS, POP and SOS. There is also a smaller amount of linoleic and arachidic acid. Cocoa butter has a complex polymorphism. Its structure changes over time to the most stable structure β_V and the rate of structure transformation may depend on other components mixed inside its lipid matrix. Our native cocoa butter has a structure like in the literature. In the SAXS region, we detected a triple chain length (3L, peaks at 1 and 2 nm^{-1}) and a double chain length (2L, the peak at 1.5 nm^{-1}) lamellar structure. In the WAXS region, we identified that cocoa butter has the β_V structure. For Montane 60, while the name is sorbitan monostearate, it is a mixture of sorbitan esters with different degrees of esterification [11,12]. We detected in SAXS region 1 hydrophilic lamellar structure (peak at around 1 nm^{-1} in the anhydrous sample, shifting to 0.63 nm^{-1} in 30% hydrated Montane 60 sample) and 1 hydrophobic lamellar structure (peak at around 1.25 nm^{-1}) in Montane 60. The hydrophilic structure may come from sorbitan monostearate and distearate, while the hydrophobic structure may come from sorbitan tristearate and tetrastearate. In the WAXS region of Montane 60 and hydrated Montane 60, we detected only a peak at 15.12 nm^{-1} , indicating the H- α arrangement of lipid chains [13]. Details about the structure of Montane 60 can be found in the next chapter.

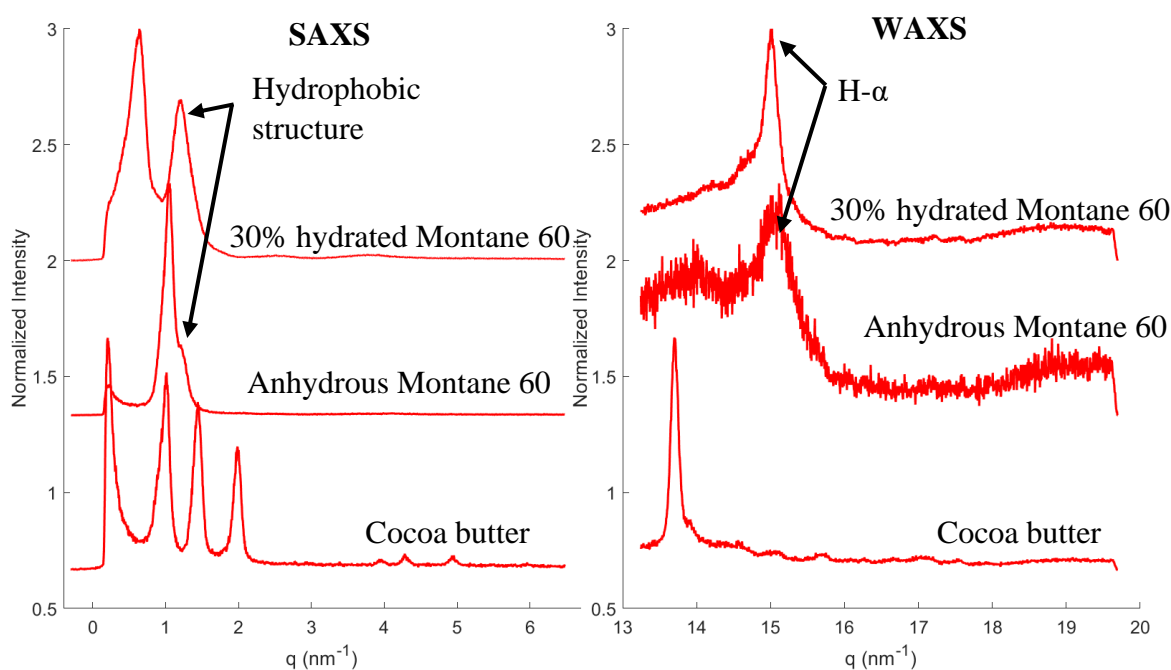


Figure 4.4. S-WAXS spectra of cocoa butter, Montane 60, and 30% hydrated Montane 60

When making the w/o emulsion, we fixed the hydration rate of Montane 60 to 30% due to the limitation of the SAXS machine. Above 30%, the lamellar distance of the hydrophilic structure of hydrated Montane 60 is too large to be in the wavevector range of the machine. In all w/o emulsion samples, the hydrated lamellar structure of Montane 60 was present, meaning that it was not affected by cocoa butter (Figure 4.5a). This is reasonable since cocoa butter is hydrophobic. In addition, triglycerides have 3 hydrocarbon chains, making it hard to blend in the sorbitan monostearate (1 hydrocarbon chain) hydrated matrix. However, the hydrophobic structure of Montane 60 may be mixed with cocoa butter. So, in samples having a low percentage of cocoa butter (CB/M60 = 4/6, 3/7 and 2/8), we could not detect anymore the β peak in the WAXS region. The hydrophobic part of Montane 60 (mainly sorbitan triesters and tetraesters) changed the crystallization behavior of cocoa butter, preventing the formation of β crystals. In contrast, in samples having a low quantity of Montane 60 (CB/M60 = 7/3, 6/4 and 5/5), 2 types of crystals, β (the peak at 13.68 nm^{-1}) and α (the peak at 15.12 nm^{-1}) were detected in WAXS region, indicating the co-existence of cocoa butter region and Montane 60 region.

We used DSC to determine the point that cocoa butter is fully integrated into the lipid matrix of Montane 60. Figure 4.5b shows that when we have both α peak and β peak, for example, at the ratio CB/M60 = 6/4, in DSC, we have the endothermic peak of melting of cocoa butter first, then the peaks of melting of Montane 60. DSC experiments showed that at the ratio CB/M60 = 2/8, cocoa butter had been fully integrated into the matrix of Montane 60, because the melting peak of cocoa butter had disappeared. The melting peak at around 42°C of Montane 60 was shifted to lower temperatures when cocoa butter was added to the emulsion, indicating the incorporation of cocoa butter in Montane 60.

In summary, if we want to make a w/o/w emulsion, the ratio CB/M60 = 6/4 would be interesting, since we may obtain nanoparticles having a cocoa butter shell and hydrated Montane 60 core. Meanwhile, if the purpose is to maximize the amount of urea solution loading, the ratio CB/M60 = 2/8 would be suitable, then we may obtain nanoparticles of gel-like hydrated lipid. Further investigation and optimization of the nanoparticle fabrication process are detailed in the section below.

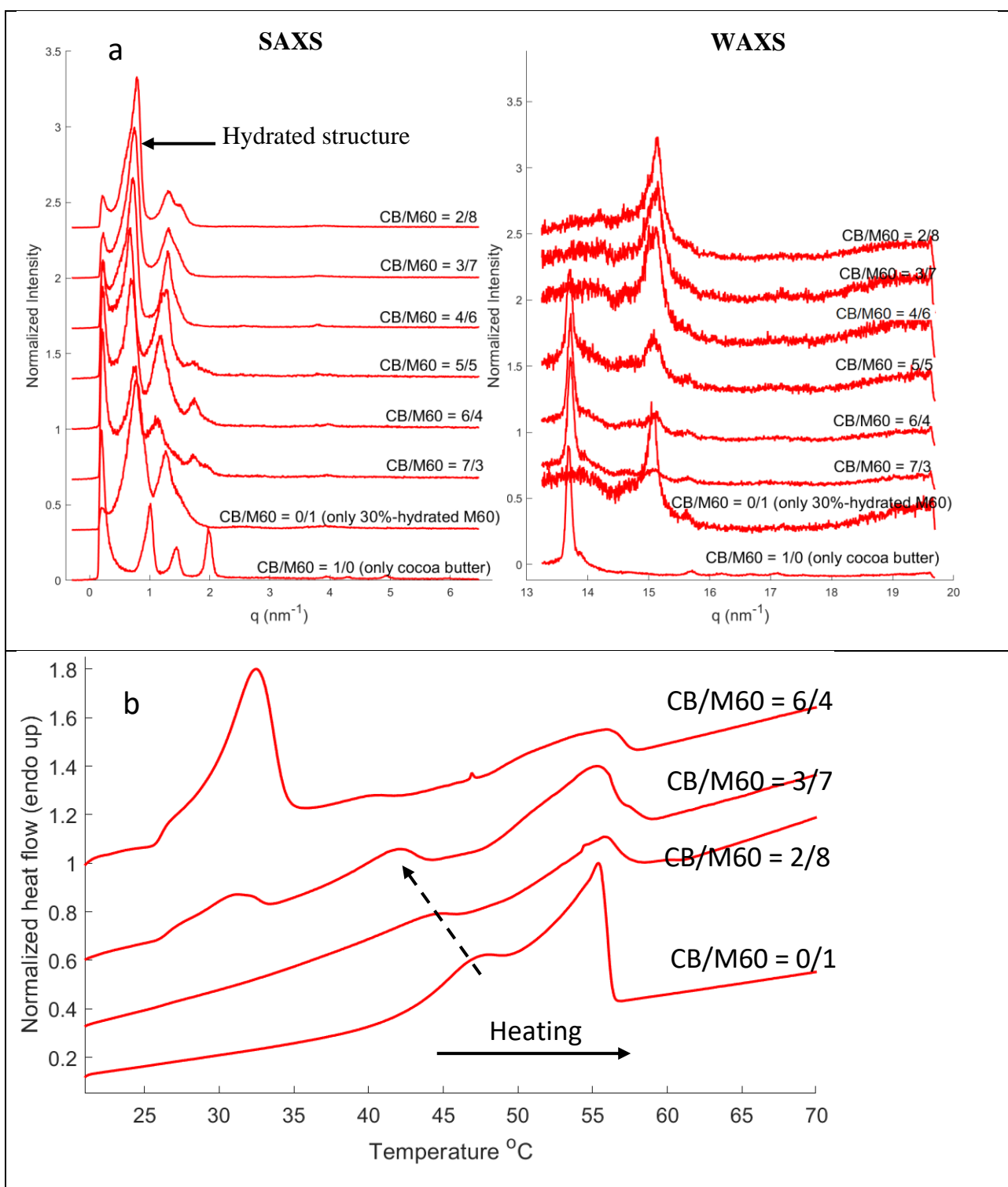


Figure 4.5. (a) S-WAXS spectra and (b) DSC signal in the heating step of w/o emulsions made of cocoa butter (CB), Montane 60 (M60) and urea solution, each thermogram is an emulsion with different ratio of CB/M60. The hydration rate of M60 in all samples is the same (at 30%). In figure a, the sample CB/M60 = 1/0 contained only CB and was not hydrated. The dashed arrow in figure b is only for eye guidance.

3.3. Optimization of nanoparticles fabrication parameters

When using the ratio CB/M60 = 6/4 to make w/o/w suspension as mentioned above, we could get nanoparticles by the high-pressure homogenization (HPH) method (the size and polydispersity index (PDI) are summarized in Table 4.2). However, using ultra-centrifugation, we observed that there were 2 populations of particles having different densities (photo in Figure 4.6b). After the ultra-centrifugation, we obtained a top layer (density lower than water) and a bottom pellet (density higher than water). Using S-WAXS, we can identify that the top layer is cocoa butter. We fabricated cocoa butter nanoparticles (without Montane 60) in the same condition to use as a reference (Figure 4.6a), which confirmed that the top layer of the centrifuged w/o/w suspension is cocoa butter. The cocoa butter particles layer showed in SAXS the 2L and 3L lamellar structure, in WAXS the β form peak at 13.68 nm^{-1} . The bottom layer is hydrated Montane 60, identified by the hydrated lamellar structure in SAXS and the α form peak in WAXS. So, when the w/o emulsion made of cocoa butter and Montane 60 (ratio CB/M60 = 6/4) was resuspended with the hydrophilic surfactant, under HPH, the cocoa butter domain was separated from the hydrated Montane 60 domain. Even when the HPH was at room temperature, meaning that cocoa butter was not fully melted during the fabrication process, we still had 2 layers of lipid after centrifugation. The existence of 2 populations of particles after HPH is due to the mechanism of the top-down approach. Because the w/o emulsion is broken down into nano-size pieces, when the cocoa butter domain is too large, it would be broken down into nano-size cocoa butter pieces. Similarly, the hydrated Montane 60 domain is broken down into nano-size hydrated Montane 60 pieces. So, after the fabrication process, we have 2 types of particles in the suspension. It may be hypothesized that the separation of particle populations is facilitated by the centrifugation force.

Ratio CB/M60	Temperature of HPH (°C)	Size (nm)	PDI	Number of layers after centrifugation	Observation
6/4	25	528	0.35	2 layers	Viscous suspension, hard to process
6/4	40	181	0.28	2 layers	
2/8	40	531	0.26	1 layer	Viscous suspension, hard to process
2/8	85	180	0.16	1 layer	

Table 4.2. Results summary of nanoparticles fabricated in different conditions

When using the ratio CB/M60 = 2/8, which is the ratio that cocoa butter is well integrated into the lipid matrix of Montane 60, we also obtained nanoparticles. As expected, when we have only 1 domain of lipid in w/o emulsion, the obtained suspension gave only 1

bottom layer after the ultracentrifugation (Figure 4.6c). This bottom layer is identical to the bottom layer of the suspension fabricated from the ratio CB/M60 = 6/4. Even when being homogenized at 85°C, when both cocoa butter and Montane 60 were melted, we still obtained suspension that had only 1 population after ultracentrifugation. This means that when cocoa butter is well integrated inside the matrix of Montane 60, the centrifugation force cannot separate cocoa butter from Montane 60. Therefore, the ratio CB/M60 = 2/8 is optimal for the suspension fabrication, since we can have homogenous suspension and a maximum loading rate of urea solution.

About the temperature of fabrication, we noted that in cold HPH, when the lipid phase is not melted, the suspensions both before and after HPH are very viscous. This high viscosity may indicate that the suspension is not homogenized in terms of particle size, is aggregated, or the particle size is too large (microns-size). The quantity of lipid inside the suspension is limited by the high viscosity, since in general, the higher the lipid percentage, the higher the viscosity. So, when fabricating the nanoparticles using the ratio CB/M60 = 2/8, we decided to fix the temperature to 85°C to facilitate the fabrication process. At 85°C, in addition to the fact that cocoa butter is not separated from Montane 60, the particle size is reduced to the nanoscale, and we can increase the percentage of lipid from 10 wt% to 20 wt%. Moreover, we can eliminate the 1st step of making w/o emulsion and mix directly molten lipid mixture (cocoa butter and Montane 60) to urea solution, since the mixing at 85°C also hydrates Montane 60.

In summary, the nanoparticle fabrication parameters have been fixed. We use the ratio CB/M60 = 2/8, the point that cocoa butter is integrated inside the matrix of Montane 60. This ratio also maximizes the possible hydration rate of particles. The temperature of fabrication is 85°C, which helps to reduce the particle size and to increase the percentage of lipid in the suspension to 20 wt% without changing the structure of lipid. The obtained suspension has a size of 180 nm, with a PDI of 0.16. In the next step, we will try to incorporate charges to the surface of nanoparticles, preparing for the polymer coating step.

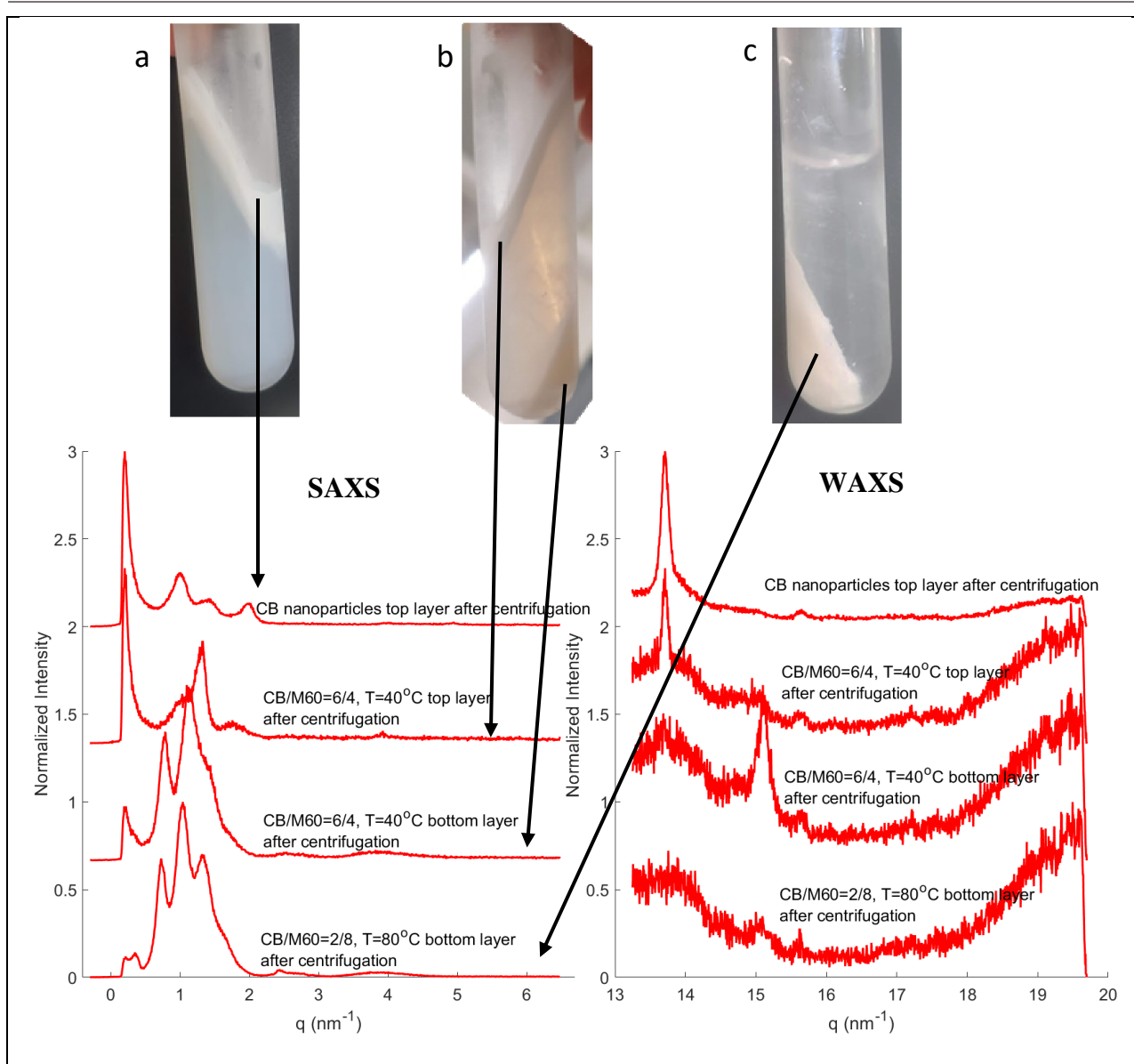


Figure 4.6. Structure of particles population found in nanoparticles fabricated in different conditions (a) $CB/M60 = 1/0$, $T = 40^{\circ}C$ - using as reference, (b) $CB/M60 = 6/4$, $T = 40^{\circ}C$, (c) $CB/M60 = 2/8$, $T = 85^{\circ}C$.

3.4. The incorporation of charge into lipid particles

To complete our formulation, we coat a layer of polymer on the surface of the nanoparticles. The polymer coating is for the active targeting purpose, helping the particles to stick to the surface of *H. pylori*. We will use the electrostatic interaction method for polymer coating. The challenge is to keep both lipid particles and polymers charged in the acidic pH of the stomach. If the lipid particles are positively charged, we will use fucoidan, which is negatively charged in $pH > 2.5$ (pKa of fucoidan is from 1 - 2.5 [14]). Fucoidan has been shown to interact with *H. pylori* [15]. If the lipid particles are negatively charged, we will use chitosan, which is positively charged in $pH < 6.5$ (pKa of chitosan is ~ 6.5) [16]. Chitosan has also been shown to interact with *H. pylori* [17].

So far, we have identified that the lipid used for the particle's fabrication is the mixture of cocoa butter and Montane 60 at the ratio CB/M60 = 2/8. This lipid mixture is charged negatively at pH 7, due to the presence of fatty acids in Montane 60 (data from manufacturer); however, in gastric acid, it would be neutral. In the first attempt, we wanted to introduce positive charges by mixing ODA in the lipid phase. However, the suspension was jellified and phase-separated upon the addition of ODA (starting from 2 wt% of ODA, earlier when the aqueous phase was a buffer pH7). Interestingly, this phase separation and jellification only happened at a high temperature (85°C), blocking the homogenization step. We suspected a change in the lipid structure at high temperatures, however, could not detect anything in S-WAXS experiments of mixture Montane 60, ODA and water in Figure 4.7 (the sample has 20% Montane 60, 2% ODA and 78% water, CB is not in the sample). Upon the addition of ODA, besides the increase in melting temperature, we did not find any structural changes.

We decided to charge the nanoparticles with negative charges, which would be difficult since the charge should stay negative even in gastric acid (pH 1.2 at the lowest). Sodium dodecyl sulfate (SDS) is chosen, because of its low pKa (-1.5), hence giving the particles negative charges even in highly acidic environments [18]. In the fabrication process, we change the hydrophilic surfactants (mixture of P90G and Gelucire 50/13) to only SDS, while keeping the same weight content of the surfactant in the formulation. Further investigation about the effect of SDS on the lipid structure will be discussed in the following chapter.

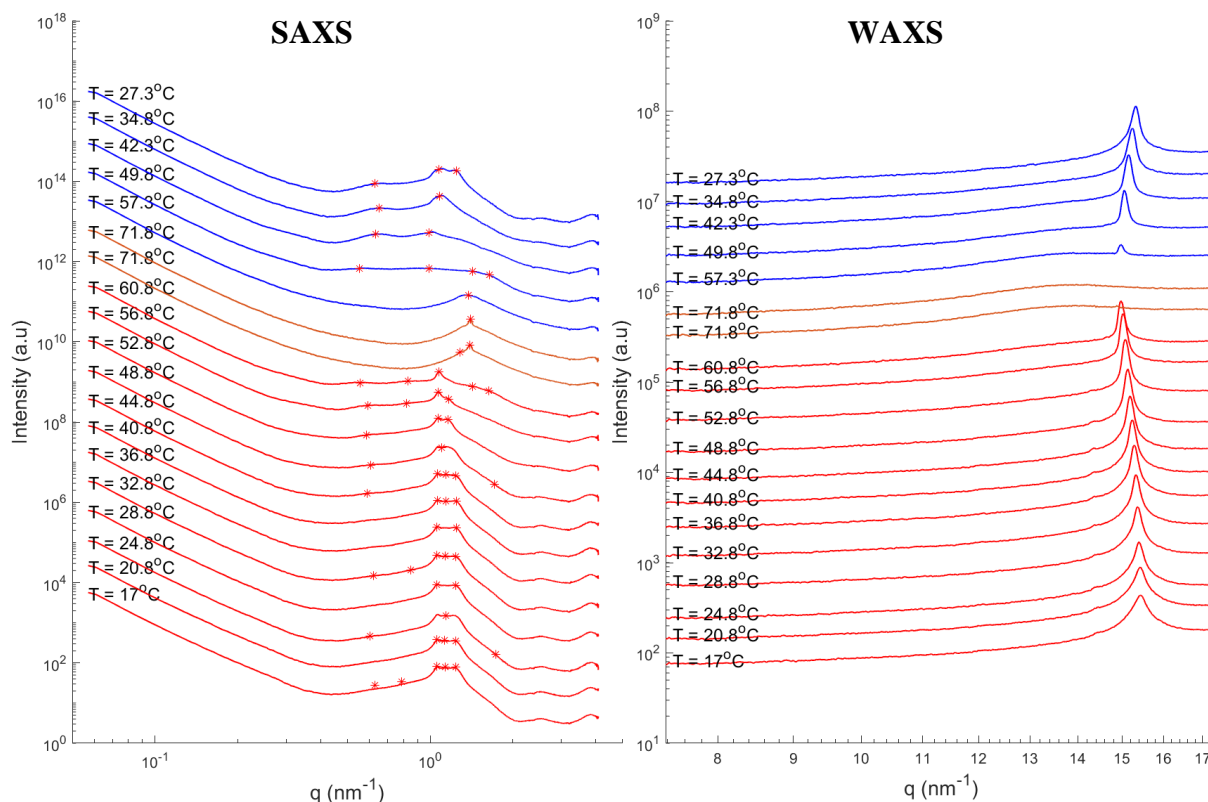


Figure 4.7. S-WAXS spectra at different temperatures of ODA-containing emulsion (20 wt% Montane 60, 2 wt% ODA, and 78 wt% water). The emulsion was heated from 17°C to 71.8°C at 2°C/min (red curves), kept at 71.8°C for 5 minutes (orange curves) and cooled down to 25°C at 5°C/min (blue curves). Red dots indicate the peaks position.

3.5. Characterization of the SDS, erythromycin, and urea

After finishing the finding and optimization of lipids, we characterize other components of the formulation and their interactions.

3.5.1. Critical micelle concentration (CMC) of SDS and urea in water

Using a plate tensiometer, the CMC of SDS in water at 25°C was found to be 0.13 wt% in water (~4.5 mM, Figure 4.8), lower than the reported value in literature (~8 mM) [19,20]. It may be due to the difference in the supplier and or the contamination in the SDS. Unexpectedly, we found that our urea is surface-active. The urea solution at the eutectic point (32.85 wt%) has a surface tension of 50.3 mN/m, lower than that of water (73 mN/m). It is contrary to the reported value, which is higher than water [21]. It may be due to the contamination of surfactant in the urea, which is however denied by the supplier. This unexpected property of our urea may increase the solubility of erythromycin in water, hence reducing the drug loading capacity of lipid particles. Therefore, the drug loading capacity and encapsulation efficiency of lipid particles need to be investigated carefully.

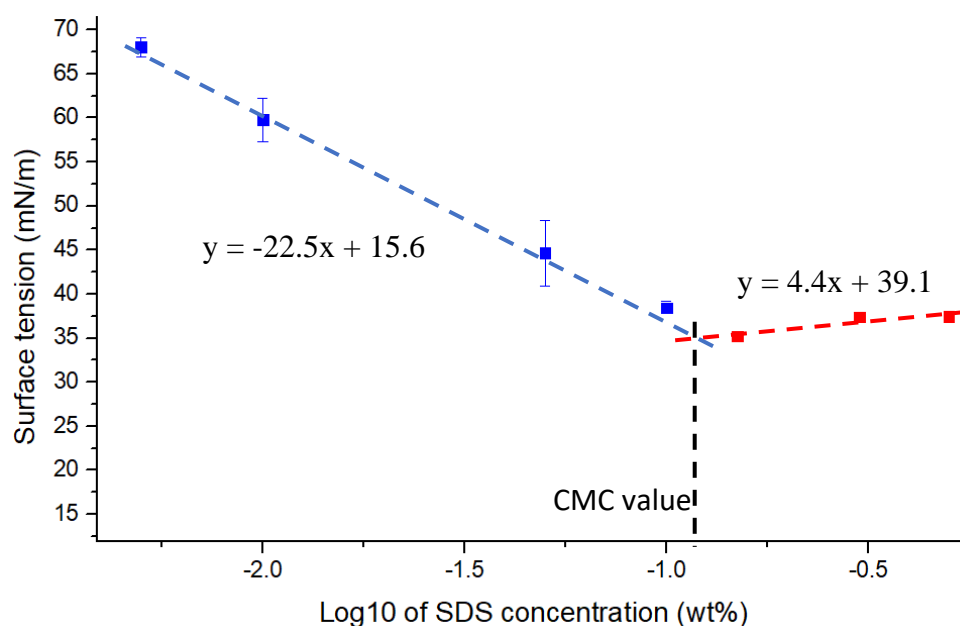


Figure 4.8. The surface tension of SDS solution at different concentrations, error bars present the standard deviation calculated from 3 measurements.

3.5.2. Solubility of erythromycin in SDS solution

SDS can increase the solubility of erythromycin in solution. The addition of SDS increases the amount of erythromycin in the water phase [22], hence decreasing the erythromycin loading capacity of lipid particles. Figure 4.9 shows the saturated erythromycin concentration in different SDS solutions. The concentration of erythromycin was determined by HPLC. We can confirm that the higher the SDS, the higher the saturated concentration of erythromycin. We also confirmed the solubility of erythromycin in water is 1.9 mg/mL, which agrees with the literature [22,23]. However, the solubility of erythromycin in water is influenced by its crystalline state and by the suppliers [24]. It has been found that when dissolving in water, amorphous erythromycin rapidly converts to the dihydrate crystal form, hence reducing the real solubility of amorphous erythromycin [24]. In our case, using S-WAXS, we confirm that our erythromycin is amorphous. So, when dissolving in water or SDS solution, an amount of erythromycin might convert to dihydrate crystal and was filtered away during the HPLC sample preparation. This may explain the reduction in erythromycin solubility below CMC of SDS, since the addition of SDS may facilitate the nucleation and conversion of erythromycin amorphous form to crystalline form.

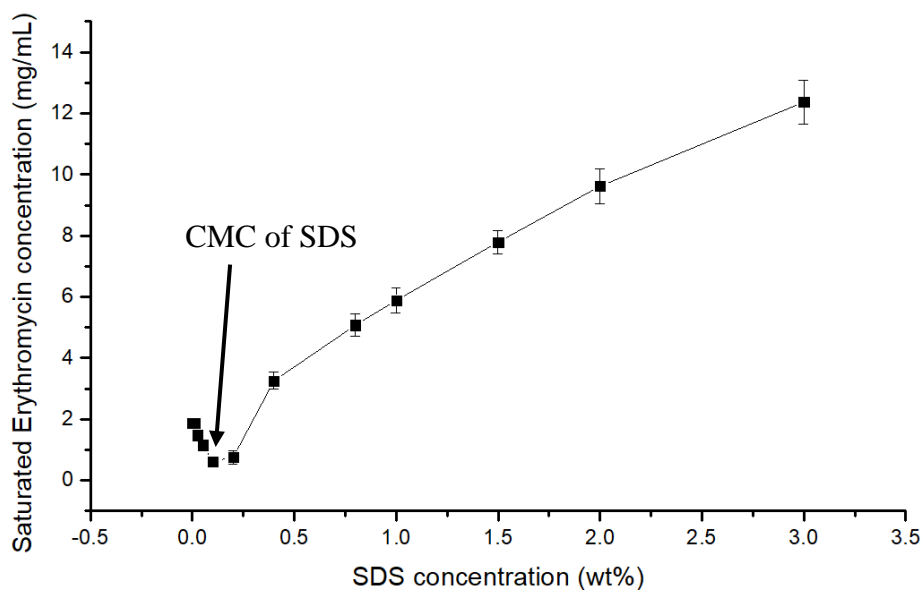


Figure 4.9. The saturated concentration of erythromycin in SDS solution, error bars present the standard deviation from 3 measurements.

The saturated erythromycin solution in SDS jellified over time. Figure 4.10 demonstrates the jellification of erythromycin saturated in 0.1wt% SDS solution. This jellification happened over time, normally taking a few days for a volume of 10mL like in the photo. We suspected it would be due to the formation of erythromycin dihydrate crystal, however, the jellified sample was found to be amorphous under S-WAXS measurement. We hypothesize that there is an interaction between erythromycin (positively charged in water) with SDS (negatively charged in water). Due to any reason, the erythromycin saturated in SDS solution is found to be jellified or crystallized, creating erythromycin gel or crystal in the aqueous phase of the nanoparticle suspension. Therefore, the elimination of free erythromycin in the aqueous phase of the nanoparticle suspension is necessary and should be done as soon as possible. Due to this reason, in our final fabrication process, the nanoparticles suspension is ultracentrifuged directly after the HPH process to eliminate the aqueous part.



Figure 4.10. Jellification of saturated erythromycin in 0.1 wt% SDS solution

3.5.3. Solubility of erythromycin in melted Montane 60 and cocoa butter

The solubility of erythromycin in solid lipid is hard to determine, since at room temperature, the lipid is solid state, trapping both soluble erythromycin and precipitation of erythromycin in lipid. We then determine the solubility of erythromycin in melted Montane 60 and cocoa butter, to ensure that we do not have erythromycin crystals precipitated during the fabrication step. To determine the solubility of erythromycin in Montane 60 and cocoa butter, we added slowly erythromycin in melted Montane 60 or cocoa butter at 85°C under agitation by a magnetic stirrer. We then observed the melted lipid at 85°C under a polarized light optical microscope equipped with a heater stage to find erythromycin crystals. The solubility of erythromycin in lipids is determined as the point that erythromycin crystals appeared in melted lipids. The result is in Table 4.3, which shows the high solubility of erythromycin in melted Montane 60. Meanwhile, erythromycin is less soluble in cocoa butter.

Lipid	Saturated Erythromycin concentration (mg/g lipid)
Montane 60	16.34
Cocoa butter	477.6

Table 4.3. Solubility of erythromycin in Montane 60 and cocoa butter at 85°C

4. Conclusion

We have finished the first step of the formulation development process is to choose the materials and optimize the fabrication parameters. Using DoE approaches, we found that the mixture of cocoa butter and Montane 60 at the ratio CB/M60 = 2/8 can hold water in form of gel, whose lipid structure is solid and stable at room temperature. SDS has been chosen as the hydrophilic surfactant to introduce negative charges on the surface of the lipid particles. Due to the hydration and viscous properties of the lipid mixture, we rejected the initial proposal of using 2 steps fabrication method of making w/o emulsion and then w/o/w emulsion. The optimized fabrication process is more simple, robust with only 1 step of hot homogenization at 85°C. We can increase the lipid content and reduce the size while keeping water inside the lipid matrix with the new process. Finally, the jellification of erythromycin with SDS over time is investigated, suggesting quick centrifugation after the suspension fabrication process to eliminate free erythromycin in the aqueous phase.

In the next chapter, we will analyze the structure and composition of Montane 60 and its interaction with SDS to form α -gel lipid particles. The hydration behavior of Montane 60, which is important for the loading of urea solution in the particles, will be investigated and discussed in depth.

References

- [1] L.T.C. Tran, Development of nanodispersions based on polyoxylglycerides to protect unstable molecules : Application to *Helicobacter pylori* treatment, These de doctorat, Paris 11, 2014. <http://www.theses.fr/2014PA114836> (accessed July 15, 2022).
- [2] T. Sheth, S. Seshadri, T. Prileszky, M.E. Helgeson, Multiple nanoemulsions, *Nat. Rev. Mater.* 5 (2020) 214–228. <https://doi.org/10.1038/s41578-019-0161-9>.
- [3] M. Nollet, H. Boulghobra, E. Calligaro, J.-D. Rodier, An efficient method to determine the Hydrophile-Lipophile Balance of surfactants using the phase inversion temperature deviation of CiEj/n-octane/water emulsions, *Int. J. Cosmet. Sci.* 41 (2019) 99–108. <https://doi.org/10.1111/ics.12516>.
- [4] Y.S. Mok, K.H. Lee, W.K. Lee, Control of swelling in liquid emulsion membranes employed for lactic acid separation, *J. Chem. Technol. Biotechnol.* 65 (1996) 309–316. [https://doi.org/10.1002/\(SICI\)1097-4660\(199604\)65:4<309::AID-JCTB434>3.0.CO;2-I](https://doi.org/10.1002/(SICI)1097-4660(199604)65:4<309::AID-JCTB434>3.0.CO;2-I).
- [5] G.A. Abdelbary, M.M. Amin, M.Y. Zakaria, Ocular ketoconazole-loaded proniosomal gels: formulation, *ex vivo* corneal permeation and *in vivo* studies, *Drug Deliv.* 24 (2017) 309–319. <https://doi.org/10.1080/10717544.2016.1247928>.
- [6] M.H.M. Buscato, L.M. Hara, É.C. Bonomi, G. de A. Calligaris, L.P. Cardoso, R. Grimaldi, T.G. Kieckbusch, Delaying fat bloom formation in dark chocolate by adding sorbitan monostearate or cocoa butter stearin, *Food Chem.* 256 (2018) 390–396. <https://doi.org/10.1016/j.foodchem.2018.02.127>.
- [7] L. Yuan, S. Clevers, N. Couvrat, Y. Cartigny, V. Dupray, G. Coquerel, Precise Urea/Water Eutectic Composition by Temperature-Resolved Second Harmonic Generation, *Chem. Eng. Technol.* 39 (2016) 1326–1332. <https://doi.org/10.1002/ceat.201600032>.
- [8] C. Dalmazzone, C. Noïk, D. Clause, Application of DSC for Emulsified System Characterization, *Oil Gas Sci. Technol. - Rev. IFP.* 64 (2009) 543–555. <https://doi.org/10.2516/ogst:2008041>.
- [9] D.C. Montgomery, Design and analysis of experiments, Ninth edition, John Wiley & Sons, Inc, Hoboken, NJ, 2017.
- [10] N. De Clercq, Changing the functionality of cocoa butter, dissertation, Ghent University, 2011. <http://hdl.handle.net/1854/LU-1909786> (accessed August 30, 2022).

- [11] EFSA Panel on Food Additives and Nutrient Sources added to Food (ANS), A. Mortensen, F. Aguilar, R. Crebelli, A. Di Domenico, B. Dusemund, M.J. Frutos, P. Galtier, D. Gott, U. Gundert-Remy, J. Leblanc, O. Lindtner, P. Moldeus, P. Mosesso, D. Parent-Massin, A. Oskarsson, I. Stankovic, I. Waalkens-Berendsen, R.A. Woutersen, M. Wright, M. Younes, P. Boon, D. Chrysafidis, R. Gürtler, P. Tobback, A. Altieri, A.M. Rincon, C. Lambré, Re-evaluation of sorbitan monostearate (E 491), sorbitan tristearate (E 492), sorbitan monolaurate (E 493), sorbitan monooleate (E 494) and sorbitan monopalmitate (E 495) when used as food additives, EFSA J. 15 (2017). <https://doi.org/10.2903/j.efsa.2017.4788>.
- [12] T. Cottrell, J.V. Peij, Sorbitan Esters and Polysorbates, in: R.J. Whitehurst (Ed.), Emuls. Food Technol., Blackwell Publishing Ltd, Oxford, UK, 2004: pp. 162–185. <https://doi.org/10.1002/9780470995747.ch7>.
- [13] C. Himawan, V.M. Starov, A.G.F. Stapley, Thermodynamic and kinetic aspects of fat crystallization, Adv. Colloid Interface Sci. 122 (2006) 3–33. <https://doi.org/10.1016/j.cis.2006.06.016>.
- [14] P.X. Sheng, Y.-P. Ting, J.P. Chen, L. Hong, Sorption of lead, copper, cadmium, zinc, and nickel by marine algal biomass: characterization of biosorptive capacity and investigation of mechanisms, J. Colloid Interface Sci. 275 (2004) 131–141. <https://doi.org/10.1016/j.jcis.2004.01.036>.
- [15] P. Bardonnnet, V. Faivre, P. Boullanger, J. Piffaretti, F. Falson, Pre-formulation of liposomes against *Helicobacter pylori*: Characterization and interaction with the bacteria, Eur. J. Pharm. Biopharm. 69 (2008) 908–922. <https://doi.org/10.1016/j.ejpb.2008.01.018>.
- [16] M.A. Mohammed, J.T.M. Syeda, K.M. Wasan, E.K. Wasan, An Overview of Chitosan Nanoparticles and Its Application in Non-Parenteral Drug Delivery, Pharmaceutics. 9 (2017) 53. <https://doi.org/10.3390/pharmaceutics9040053>.
- [17] H. Patricia C., Orally administrated chitosan microspheres bind *Helicobacter pylori* and decrease gastric infection in mice, Acta Biomater. (2020) 15.
- [18] K.D. Ristroph, R.K. Prud'homme, Hydrophobic ion pairing: encapsulating small molecules, peptides, and proteins into nanocarriers, Nanoscale Adv. 1 (2019) 4207–4237. <https://doi.org/10.1039/C9NA00308H>.
- [19] S.S. Sakhawat, Ejaz-ur-Rehman, Effect of Temperature and Aprotic Solvents on the CMC of Sodium Dodecyl Sulphate, in: H. Kleeberg (Ed.), Interact. Water Ion. Nonion. Hydrates, Springer Berlin Heidelberg, Berlin, Heidelberg, 1987: pp. 251–255. https://doi.org/10.1007/978-3-642-72701-6_45.

- [20] A. Chatterjee, S.P. Moulik, S.K. Sanyal, B.K. Mishra, P.M. Puri, Thermodynamics of Micelle Formation of Ionic Surfactants: A Critical Assessment for Sodium Dodecyl Sulfate, Cetyl Pyridinium Chloride and Dioctyl Sulfosuccinate (Na Salt) by Microcalorimetric, Conductometric, and Tensiometric Measurements, *J. Phys. Chem. B.* 105 (2001) 12823–12831. <https://doi.org/10.1021/jp0123029>.
- [21] S. Halonen, T. Kangas, M. Haataja, U. Lassi, Urea-Water-Solution Properties: Density, Viscosity, and Surface Tension in an Under-Saturated Solution, *Emiss. Control Sci. Technol.* 3 (2017) 161–170. <https://doi.org/10.1007/s40825-016-0051-1>.
- [22] P.A. Bhat, A.A. Dar, G.M. Rather, Solubilization Capabilities of Some Cationic, Anionic, and Nonionic Surfactants toward the Poorly Water-Soluble Antibiotic Drug Erythromycin, *J. Chem. Eng. Data.* 53 (2008) 1271–1277. <https://doi.org/10.1021/je700659g>.
- [23] Z. Wang, J. Wang, M. Zhang, L. Dang, Solubility of Erythromycin A Dihydrate in Different Pure Solvents and Acetone + Water Binary Mixtures between 293 K and 323 K, *J. Chem. Eng. Data.* 51 (2006) 1062–1065. <https://doi.org/10.1021/je0505265>.
- [24] K.S. Murthy, N.A. Turner, R.U. Nesbitt, M.B. Fawzi, Characterization of Commercial Lots of Erythromycin Base, *Drug Dev. Ind. Pharm.* 12 (1986) 665–690. <https://doi.org/10.3109/03639048609043484>.

Chapter 5. Sorbitan stearate: from the hydration behavior to the preparation of α -gel based particles

Hung V. Nguyen¹, Audrey Solgadi², Bastien Prost², Vincent Faivre¹

¹Université Paris-Saclay, CNRS, Institut Galien Paris-Saclay, 5 rue JB Clément, 92296 Châtenay-Malabry, France.

²Université Paris-Saclay, Inserm, CNRS, Ingénierie et Plateformes au Service de l'Innovation Thérapeutique, 92296, Châtenay-Malabry, France.

Abstract

Multi-compartmented nanoparticles for combination therapy are being researched intensively because of the need to load more than one drug in one drug carrier. In this article, we report the fabrication of lipid α -gel particles from sorbitan monostearate - an industrial excipient. The α -gel particles have both hydrophobic and lipophilic sites, showing the potential for loading substances having opposite solubilities. The hydration rate of sorbitan monostearate can be very high, with a very thick lamellar distance (up to 42.5 nm at 90% hydration rate). The swelling behavior of sorbitan monostearate α -gel structure in water can be controlled by changing the pH, ionic strength, and adding surfactants. Interestingly, at high temperatures, the hydrated lamellar layer may be stabilized by the combination of electrostatic and undulation effects. Thanks to the monomorphism of their constituents, the α -gel structure and α -gel suspension are stable for a long period of time. All these assets of sorbitan monostearate α -gel suspension make it a potential candidate for advanced drug delivery systems for applications requiring pH-sensitive or local activation properties.

1. Introduction

Combination therapy in cancer treatment is the co-delivery of two or more drugs, which may produce synergetic effects and improve the final treatment results. This approach reduces the resistance to chemotherapy and prevents the development of multi-drug resistance [1,2]. In addition, the high-dose side effect coming from only one drug can be reduced by lowering the dose of individual drugs used in the therapy [2]. While the combination treatment has been used widely in clinical, several obstacles are still present, for example, the variation in the pharmacokinetics of different drugs [1]. Currently, achievement in nanotechnology has shown the potential of using nanoparticles to control the pharmacokinetic profile through prolonged circulation time in the bloodstream, controlled drug release, and enhanced tumor retention [1]. However, most works on nanoparticles for combination therapy reports the

encapsulation of drug having similar solubility, noticeably hydrophilic drugs [1]. To tackle this problem, multi-compartmented nanoparticles have been developed to load drugs having opposite solubility, such as lipid Janus nanoparticles and block copolymers nanoparticles [3,4].

Having both lipophilic and hydrophilic domains, lipid α -gel nanoparticles have the potential for the loading and delivery of drugs having opposite solubility [5]. α -gel is a hydrated lipid bilayer crystal structure. It has periodically repeated bilayers of lipid (and/or surfactant) with interlamellar water layers. This structure can be obtained by mixing amphiphilic molecules (such as some fatty alcohols or their mixtures with other surfactants, monoglycerides, sorbitan monostearate [6,7]) with water. The hydrophilic heads face to water, while the hydrophobic chains align together and face others. The lipid chains are in the solid state, and arranged in hexagonal form (also called H- α [8]). α -gel is generally used to stabilize the oil phase in cosmetic and pharmaceutical products [6,9]. It is also used as a foam stabilizer in the food industry [9]. In several systems, α -gel is a metastable state. For example, in glycerol monostearate, α -gel is formed by cooling the liquid crystal state to below the Krafft temperature [9]. Over time, the lipid chain arrangement changes from α to β , forming coagel (β crystal) which does not contain water [9]. On the other hand, while having a similar structure to glycerol monostearate, sorbitan monostearate forms a stable α -gel state in water due to its monomorphism [7]. This property makes sorbitan monostearate a potential material for the loading of drugs with opposite solubility.

Herein, we reported a scalable fabrication process of lipid α -gel nanoparticles from Montane 60 - an industrial excipient. We investigate the hydration behavior of Montane 60, its interaction with surfactants, and the particle formation mechanism. The obtained α -gel particles have a tunable size from micro- to nano-scale, and both lipophilic and hydrophilic domains, enabling the capacity to load both lipophilic and hydrophilic drugs in one particle.

2. Materials and methods

2.1. Materials

Sorbitan monostearate was provided by Seppic under the trade name Montane 60 (M60). Sorbitan tristearate was provided by Croda under the trade name Span 65. Sodium dodecyl sulfate (SDS, GPR Retapur®) was purchased from VWR chemical. Lecithin Phospholipon 90G (P90G) was provided by Lipoid GmbH. Glacial acetic acid (CH_3COOH) was purchased from Sigma-Aldrich. Sodium hydroxide (NaOH) was purchased from Carl Roth. Sodium chloride (NaCl) was purchased from Carlo Erba.

2.2. Montane 60 chemical composition analysis method

Liquid chromatography-mass spectrometry (LC-MS) was used to qualitatively determine the chemical composition of Montane 60. Span 65 was also analyzed and used as a reference to compare to Montane 60. The analytical method was consulted from the literature [10,11] and applied with modification.

For M60 sample preparation, a 5 mg/mL stock solution of M60 was prepared by dissolving M60 in a mixture of tetrahydrofuran (THF, LC-MS grade) and isopropanol (IPA, LC-MS grade) (ratio 1:2 v/v). Then, the concentration of M60 samples for injection was 3 mg/mL, prepared by diluting the 5 mg/mL M60 stock solution in IPA. For Span 65 sample preparation, a 5 mg/mL stock solution of Span 65 was prepared by dissolving Span 65 in a mixture of THF and IPA (ratio 1:1 v/v). The concentration of Span 65 samples for injection was 3 mg/mL, prepared by diluting 5 mg/mL Span 65 stock solution in IPA. The ratios of THF:IPA to dissolve Montane 60 and Span 65 in stock solutions were optimized experimentally. Non-dissolved solids were observed if only THF or IPA was used. This observation is opposite to some other articles, which reported the total dissolution of Span 60 and Span 65 in only THF or IPA at a concentration >2 mg/mL [10,12,13]. Moreover, it also shows the complexity of the composition of Span 60/Montane 60 and Span 65 and the differences between manufacturers.

Regarding the liquid chromatographic condition, a 150 x 4.6 mm I.D YMC-Triart C18 column (particle size of 3 μ m and pore size of 12 nm) was used. The chromatographic separation was performed at 30°C, using a gradient elution process composed of IPA/water (ratio 60/40, solvent A) and IPA (solvent B). If the negative ion mode was chosen, solvents containing 0.1% v/v of formic acid were used. The gradient elution program was 0-4 minutes: 100% A, 0.4 ml/min; 4-15 minutes: 100% B, 0.4 ml/min; 15-22 minutes: 100% A, 0.4ml/min. The first step is to eliminate THF in the sample and bring out hydrophilic compounds in the sample (for example, residual fatty acids or sorbitol), while hydrophobic compounds (esters of sorbitan) stay inside the column. The next step using 100% IPA as the mobile phase is to separate and drive out esters of sorbitan. The last step is to re-condition the column for the next injection.

LTQ-Orbitrap Velos Pro system (Thermo Fisher Scientific, United States) was used for the LC/HR-MSⁿ analyses. The system is made of a double linear trap and an orbital trap. The analysis was performed in positive ion mode (electrospray ionization - ESI⁺) under the following conditions: the source voltage was 3.4 kV, the source and the capillary temperatures were 300°C and 350°C, respectively. Sheath gas and auxiliary gas nitrogen flows were 40 and 20 arbitrary units, respectively. S-lens was set at 60%. The normalized collision was 35 for high-resolution fragmentation studies. The mass range of 150–1300 amu was applied for the Full Scan in the Orbitrap. The chosen full width at half maximum (measured at fifty percent of the maximum peak height) was

100,000 for all stages of HRMS. Instrumentation calibration was carried out daily based on the recommendations of the manufacturer of the mass spectrometer and using the Pierce™ LTQ Velos ESI positive ion calibration solution (ThermoFisher, United States). The MS data were handled using Xcalibur® software (version 2.2 SP 1.48).

2.3. Sorbitan stearate spontaneous hydration method

In order to visualize the hydration behavior of M60 and Span 65, solid grains of M60 and Span 65 were submerged in DI water and pH5 buffer at ambient temperature. The pH5 buffer solution was prepared from CH₃COOH and CH₃COONa, whose concentrations are 17.12 mM and 29.75 mM, respectively. The mass of the grain was measured over time to calculate the hydration rate. Several grains were observed at the same time to ensure repeatability.

2.4. Acquisition of the synchrotron radiation computed microtomography (SR μ CT) dataset

SR μ CT measurements were conducted at the SYRMEP beamline of Elettra using a multi-scale approach [14]. At SYRMEP the X-ray beam is delivered by a bending magnet source and experiments were performed in a filtered white-beam configuration (filters: 1.5 mm Si + 0.025 mm Mo) with a mean energy of ~27 keV (estimated entrance dose of the order of kiloGray). Projections were recorded with a macroscope camera based on a 16-bit, water-cooled sCMOS detector (2048 × 2048 pixels) coupled to a 15 μ m-thick LSO:Tb scintillator screen. Using the optical zoom of the detecting system, an effective pixel size of 0.9 μ m was set corresponding to a field of view of about 1.8 × 1.8 mm.

For each scan, we acquired 1800 projections over a 180° rotation with an exposure time/projection of 500 ms. The experiment was conducted in propagation-based phase-contrast mode with the sample-to-detector distance set to 150 mm for all measurements. The slice reconstruction was carried out using the custom-developed SYRMEP Tomo Project (STP) software. Before reconstruction, a ring-removal algorithm was applied. Then, projections were processed by a single-distance phase-retrieval algorithm with a δ/β parameter (ratio between the real and imaginary parts of the refraction index of the material $n = 1 - \delta - i\beta$) chosen on an ad hoc basis for a good visualization of fine details in the tooth enamel balancing between contrast and spatial resolution. In our case, the δ/β ratio was set to 100.

2.5. Montane 60 hot hydration method

M60 was melted at 85°C. Then, pre-heated water (or pH5 buffer solution) at 85°C was added to melted M60 to favor dispersion. The pH5 buffer solution was prepared from CH₃COOH and CH₃COONa, whose concentrations are 17.12 mM and 29.75 mM, respectively. The volume of water (or pH5 buffer solution) depends on the hydration rate. The mixture was then agitated vigorously at 85°C using an Ultra-Turrax

homogenizer IKA® for 5 minutes at level 5 (20000 rpm of no-load speed). The hydrated samples were cooled in room condition and characterized after one night.

To verify if the hot hydration method separates components of M60, hydrated M60 samples were centrifuged at 40000 rpm, 4°C for 16 hours using an ultracentrifuge (Optima L-90K, Beckman Coulter), with the rotor 70.1 Ti to separate the components by their density.

2.6. α -gel particles fabrication process

α -gel particles were fabricated by the homogenization method. SDS or P90G was added to melted M60 at 85°C. The melted lipid mixture was mixed slightly until the color was clear, indicating the solubilization of SDS or P90G in M60. Pre-heated 85°C water was then poured into the mixture. The suspension was agitated by Ultra Turrax at 85°C for 5 minutes at level 5 (20000 rpm of no-load speed) to obtain M60 microparticles (MPs), and then homogenized by a high-pressure homogenizer (Homogenising systems Ltd.) at 1000 bar, 85°C for 5 cycles to obtain M60 nanoparticles (NPs). The obtained M60 particles were then cooled down in ice for 5 minutes and characterized after one night. The composition of M60 particles is shown in Table 5.1.

Material	Composition (wt%)
Montane 60	20
SDS or P90G	0.1, 0.25, 0.5, 1, 2, 3, 4 or 5
Water	Add up to 100

Table 5.1. Composition of M60 particles

2.7. Lipid crystal structure determination method

The lipid structure was determined by the small- and wide-angle X-ray scattering technique (S-WAXS) using the Bruker MicroCalix machine. The S-WAXS patterns were acquired at the laboratory using a microfocus X-ray tube ($1\mu\text{S}$, Incoatec), selecting the Cu K α radiation. It was used with an intensity of 1000 μA and a voltage of 50 kV. The incident beam was focused at the detector with multilayer Montel optics and 2D Kratky block collimator. Small-angle (SAXS) and wide-angle (WAXS) X-ray scattering analyses were performed simultaneously using two position-sensitive linear detectors (Vantec-1, Bruker) set perpendicular to the incident beam direction, up to 7° (2θ) and at 19° to 28° (2θ) from it, respectively. The direct beam was stopped with a W-filter. The temperature of the samples was controlled by a Microcalix calorimeter cell (Bruker). Silver behenate and tristearin (β form) were used as standards to calibrate SAXS and WAXS detectors, respectively.

For samples having large lamellar distances, which could not be observed in the MicroCalix machine, they were measured at the SAXS beamline, ELETTRA Synchrotron Trieste, Italy. The beam photon energy was 8 kV (wavelength 0.154 nm). The distances from the sample to SAXS and WAXS detectors were 1764 mm and 379 mm, respectively. Silver behenate and p-bromobenzoic acid were used as calibrants for SAXS and WAXS detectors. An in-line differential scanning calorimeter (DSC) was used as the sample holder. To investigate the change in the structure of the sample with the temperature, the sample was heated from 20°C to 75°C at the rate of 2°C/min, then kept at 75°C for 5 minutes and cooled down to 20°C at the rate of 5°C/min. One diffractogram was acquired every 30 seconds, with an exposure time of 20 seconds. So, in the heating process, we recorded one frame every degree C, while in the cooling process, it was one frame every 2.5°C.

The scattered intensity was reported as a function of the scattering vector:

$$q=4\pi \sin \theta/\lambda \quad (\text{Equation 5.1})$$

where θ is half the scattering angle and λ is the wavelength of the radiation. The d-spacing can be calculated from the scattering vectors:

$$d = 2\pi/q \quad (\text{Equation 5.2})$$

where q is the scattering vector.

Samples for X-ray experiments were contained inside quartz glass capillary tubes (1.5 mm inner diameter) purchased from Glas Müller, Germany. All samples were measured 3 times to ensure repeatability.

2.8. Particles' size and zeta potential measurement

The particle size and zeta potential were measured using Zetasizer Nano ZS90 (Malvern Panalytical Ltd.) at 25°C. To prepare the sample for measurements, the fabricated particle suspension was diluted 30 times in NaCl 3 mM solution. The final estimated particle concentration was 7 mg/ml. All measurements were repeated 3 times.

3. Results and discussion

3.1. Chemical composition analysis of Montane 60

Several articles have pointed out that sorbitan monostearate is not pure, but a mixture of mono-, di-, tri-, and tetra-ester of sorbitan [15,16]. Moreover, the fatty acid used to fabricate sorbitan monostearate is usually a mixture of stearic acid and palmitic acid [15]. However, the quantification of each component is difficult due to the lack of pure standard references. For a long time, several groups have tried to separate and identify all components of Span 60 and Span 65 using high-performance liquid chromatography (HPLC) with an assumption that mono-, di- and tri-esters of sorbitan have different retention times due to the difference in polarity [12,13]. Gas chromatography (GC) was

also applied to separate and quantify the composition of M60. However, the identification of sorbitan esters peaks was also based on the retention time [17]. By only identifying the different degrees of esterification, these results ignore the fact that both sorbitan and sorbitan esters have different isomers [15,18,19], which may have significantly different polarity. So, the integration of the peak to find the percentage of components may produce errors. In addition, in previous reports, the response of sorbitan esters to detectors is considered equal, or determined from the response factor of glycerides [12,13,17]. To improve the analysis of sorbitan esters, peaks in HPLC or GC need to be identified by mass spectrometry (MS) to confirm the separation efficiency of the method. Moreover, the response factor of different esters of sorbitan needs to be clarified. Considering all these problems, a deep analysis of sorbitan monostearate requires an enormous amount of work and is out of the context of this article.

We applied a slightly modified published LC-MS method to analyze our sorbitan monostearate (Montane 60) sample qualitatively in comparison with a sorbitan tristearate (Span 65) sample [10,11]. While the separation of all components of sorbitan monostearate using HPLC is reported to be impossible [17], the MS detector helps to detect and identify further different molecules. However, the quantification in percentage is still not possible since the response factor of different molecules is different in MS. For example, a correlation between molecular volume and ESI ionization efficiency has been reported [20]. In the case of sorbitan esters, the addition of a fatty acid chain may significantly change the volume of different sorbitan esters. Therefore, the calculation of the percentage of different esters of Montane 60 and Span 65 is solely for the purpose of comparison between sorbitan monostearate and sorbitan tristearate samples in this report.

The mass spectra of Montane 60 and Span 65 are shown in Figure 5.1. In both samples, we detected 2 types of monoester, 3 types of diester, 4 types of triester, and 5 types of tetraester of sorbitan and their associated dehydrated products (one H₂O molecule less in the molecular weight). In the chromatogram (Figure 5.2), we observed that while all components of Montane 60 are separated, the separation is not perfect. Interestingly, the difference in retention time for the same molecular weight species was noted (Figure 5.2), probably due to the existence of isomers of sorbitan and/or isomers of sorbitan esters. For example, for the same molecule sorbitan tetrapalmitate (sorbitan tetraester (C16:0)₄), there are 3 separated peaks at 12.89, 14.34 and 14.77 minutes, showing that there are at least 3 isomers having different polarity. Interestingly, the peak at 12.89 minutes overlaps with the peaks of sorbitan triesters. Hence, while our method did not separate well all sorbitan esters, our results suggest that isomers of sorbitan esters have very different polarity and the use of only retention time to identify the degree of esterification may not be sufficient.

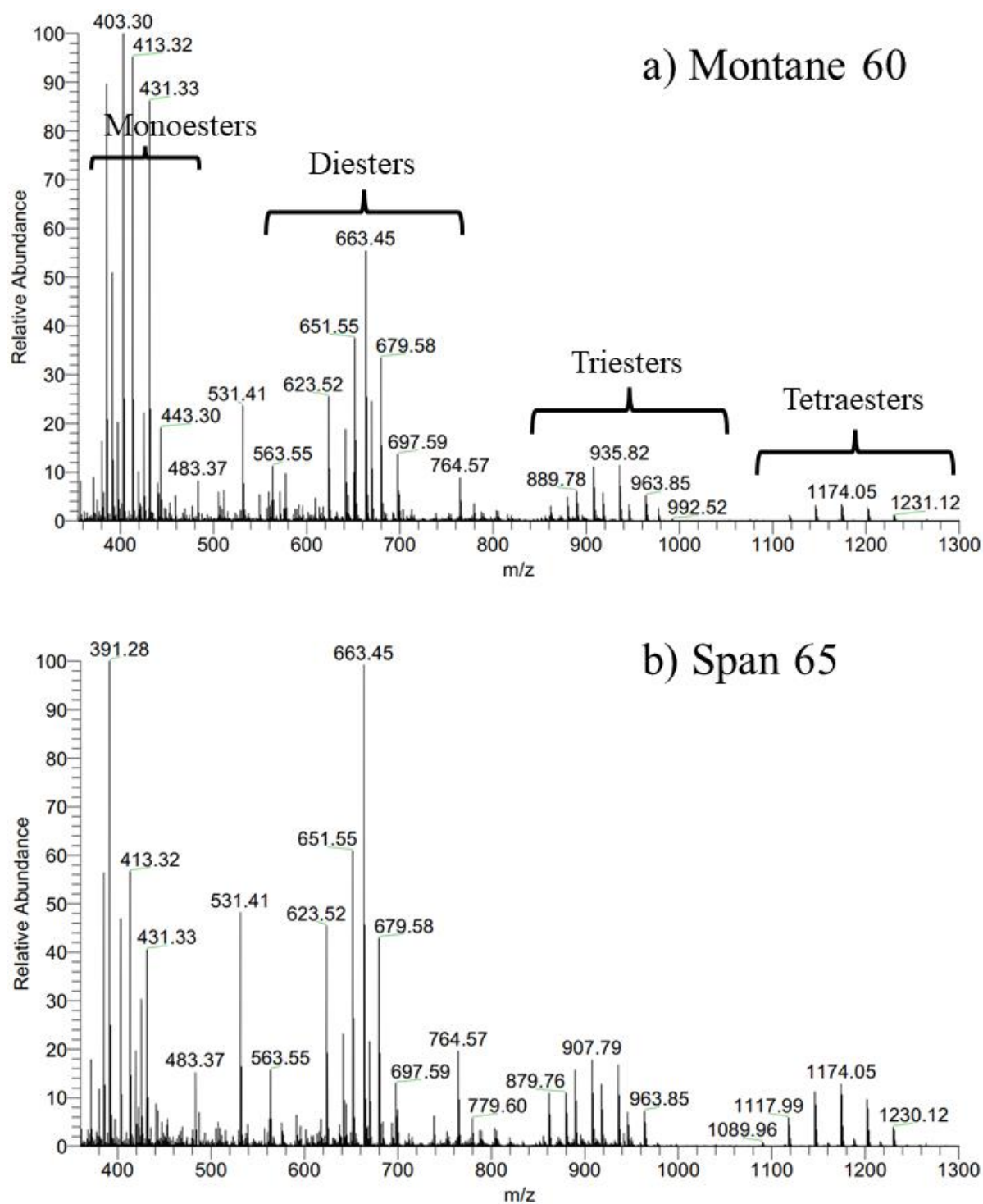


Figure 5.1. Mass spectra of (a) Montane 60 and (b) Span 65

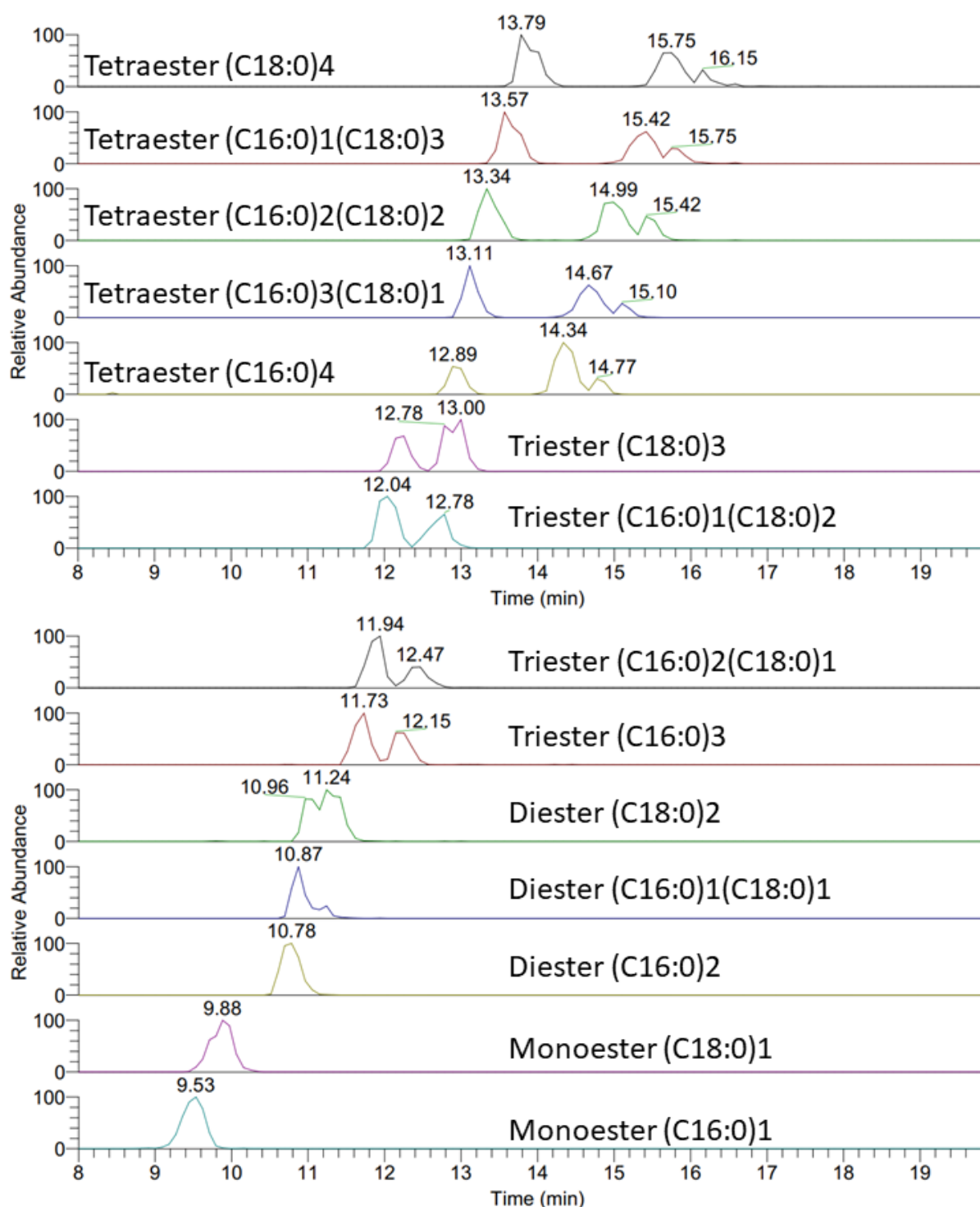


Figure 5.2. The retention time of different sorbitan esters detected in Montane 60

Figure 5.3 shows the MS peak area of different types of esters in Montane 60 and Span 65. The contribution of esters of sorbitan with both palmitic acid and stearic acid is included. We can see that the amount of di-ester in Montane 60 and Span 65 are almost equal (19.66% and 23.22%, respectively). In Montane 60, the amount of tri-esters is one-half of that in Span 65. So, there is a nonnegligible amount of hydrophobic substance in Montane 60. In contrast, in Span 65, there is a significant amount of amphiphilic

sorbitan monopalmitate and sorbitan monostearate, whose percentage is approximately one-half of those in Montane 60.



Figure 5.3. The estimated composition of Montane 60 and Span 65 calculated from LC-MS peaks' area

3.2. Spontaneous hydration of Montane 60 and Span 65

The spontaneous hydration experiments at ambient temperature visualize the hydration behavior of M60 and Span 65 and may estimate their maximum hydration rate. As shown in Figure 5.4a, Montane 60 grains took up water rapidly and became saturated at around 90% of hydration rate after 3 days, meaning that the weight of the grains increased by 10 times. Meanwhile, the hydration rate of Span 65 grain after 3 days was only about 3%. The fully hydrated M60 grain in comparison with the anhydrous M60 grain is shown in Figure 5.4b. We can see that the M60 grain was swollen with water, showing the high capacity of holding water inside the lipid matrix. In contrast, there was not any increase in the size of Span 65 grain. Using SR μ CT, we can confirm that the increase in size and weight of the M60 grain is not because of the porosity of the grain. Figure 5.4c and Figure 5.4d show the SR μ CT photos of anhydrous M60 grain and hydrated M60 grain, respectively. In both photos, the M60 grains are dense macroscopically. There are not any water-containing pores or domains, indicating that water has entered the microscopic lipid structure of the M60 grain. As a comparison, Figure 5.4e shows the SR μ CT photo of lipid microspheres that contain water pores. The water pores are visible inside lipid microspheres.

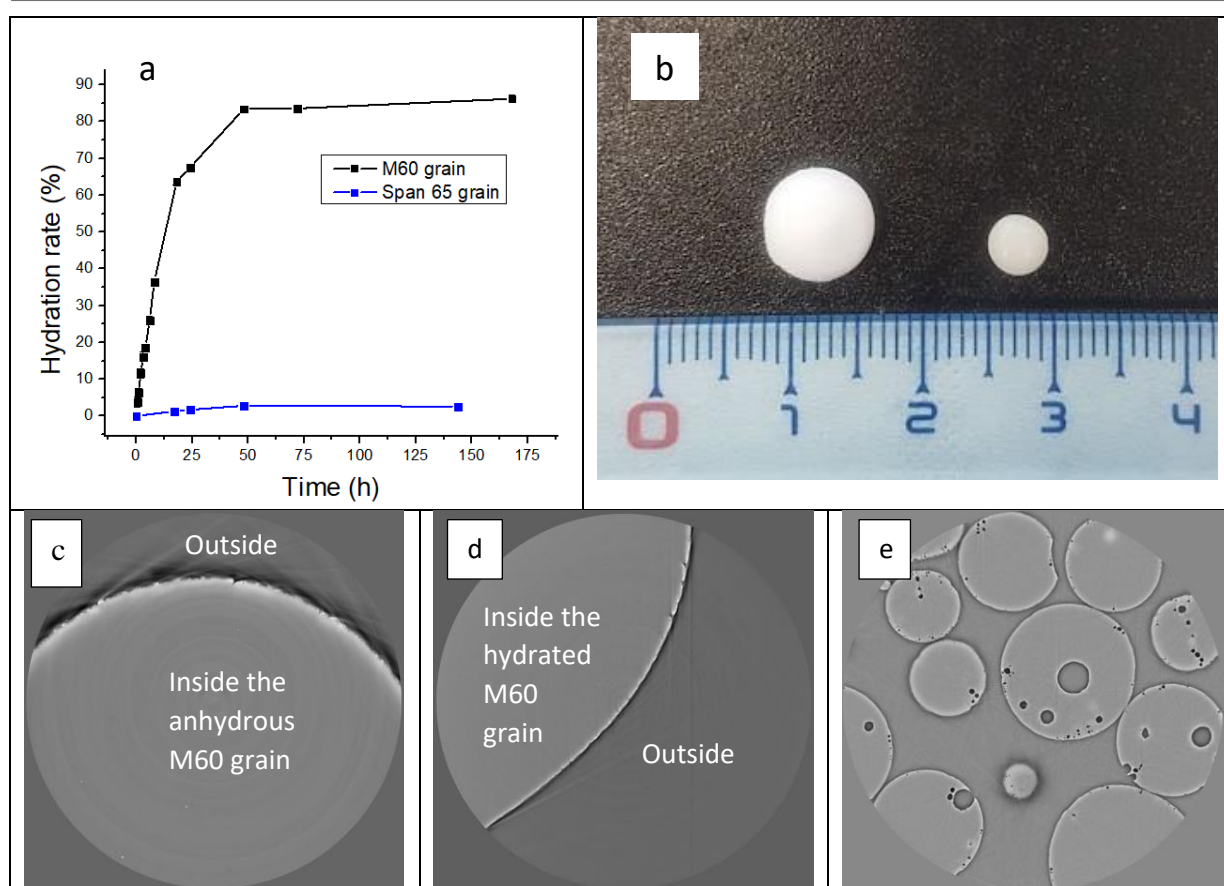


Figure 5.4. Spontaneous hydration experiment shows (a) hydration rate of M60 grain over time (the error bars of hydration rate are from 0.5% - 1%, which is too small to be seen in the graph), (b) the photo of M60 grain in DI water after 3 days (left) and anhydrous M60 grain (right), (c) the SR μ CT photo of anhydrous M60 grain, (d) the SR μ CT photo of hydrated M60 grain, (e) the SR μ CT photo of lipid microsphere containing water domains as a comparison reference. The width of each view of SR μ CT photos is 1843 μ m

Figure 5.5 shows the S-WAXS spectra of anhydrous M60 grain and hydrated M60 grains that present the microscopic lipid structure of swollen M60 grain. In the SAXS region, the arrow showed the peak of the hydrated structure, confirming that water entered the lamellar structure and extended the lamellar distance. In the WAXS region, we can see that the hydrated M60 grain still has the H- α structure, indicating the solid lamellar lipid layers (peak at 15.12 nm^{-1}) [8]. From these observations, we can confirm that due to the higher content of monoester, M60 hydrated more and faster than Span 65. For the application of loading drugs having opposite solubility, M60 would be a more suitable material due to the high hydration rate. In addition, we can see that the M60 grain shape and structure remained stable and solid in water, meaning that in excess water conditions, M60 molecules are not dispersed. We hypothesized that this structure would remain the same when we reduce the size of the M60 grain to micro- and nano-size. The structure and swelling behavior of M60 are interesting and the details are investigated and discussed in the section below.

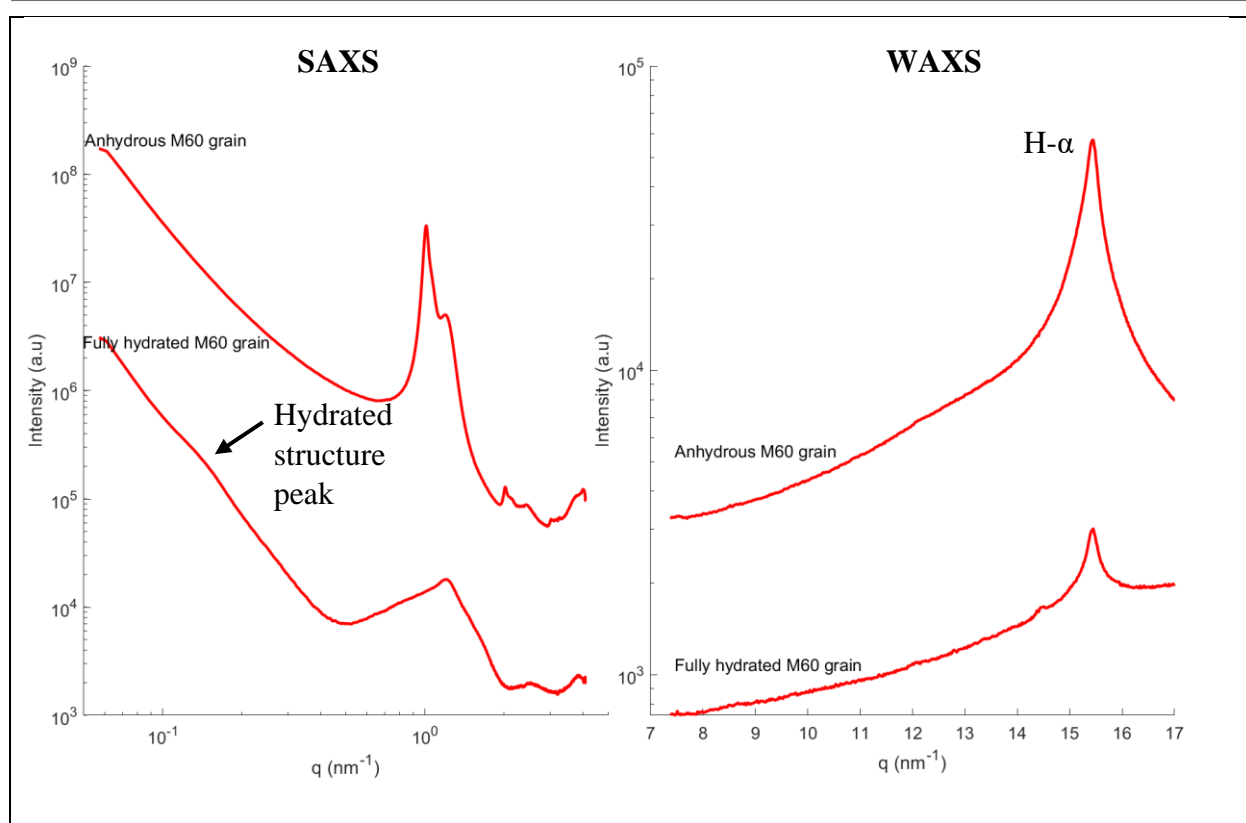


Figure 5.5. Structure of a fully hydrated M60 grain in comparison with an anhydrous M60 grain, the arrow shows the hydrated structure peak.

3.3. Crystal structure and lyotropic behavior of Montane 60 studied by hot hydration method

3.3.1. The structure of hydrated M60 at ambient temperature

To demonstrate the data analysis method, the SAXS spectrum of 20% hydrated Montane 60 is shown in Figure 5.6 as an example. We can clearly identify a series of lamellar structure peaks from the SAXS spectrum. The S-WAXS spectra at room temperature of hydrated Montane 60 are shown in Figure 5.7a. Our results partially agree with previously published results of anhydrous sorbitan monostearate [7]. In the WAXS region, regardless of the hydration rate, Montane 60 exhibits an H- α form (the only peak at $q = 15.12 \text{ nm}^{-1}$), meaning that lipid chains are arranged in the hexagonal configuration [7,8]. In contrast to the lamellar distance of 5.45 nm reported by Vang Sparso and Krog [7], in anhydrous Montane 60, we detected a water-sensitive lamellar structure (with a lamellar distance of 6.23 nm at $q = 1 \text{ nm}^{-1}$) and a hydrophobic lamellar structure (with a lamellar distance of 4.96 nm at $q = 1.27 \text{ nm}^{-1}$) in SAXS region. The water-sensitive lamellar structure distance increases when the hydration rate increases, while the lamellar distance of the hydrophobic structure stays constant. The water-sensitive lamellar structure may come from amphiphilic molecules, i.e., sorbitan monostearate or monopalmitate, while the hydrophobic one may come from lipophilic molecules, such as triesters or tetraesters of sorbitan. The lamellar distance of the

water-sensitive structure can be up to 42.5 nm at 90% hydration rate. Besides the 2 main lamellar structures mentioned above, another lamellar structure (with a distance of 5.94 nm at $q = 1.06 \text{ nm}^{-1}$) was also detected from a series of low-intensity peaks. However, this minor structure cannot be found anymore when the hydration rate is higher than 60%, showing that this structure has a low concentration and/or low degree of crystallinity in the hydrated sample. After 2 months of aging in the ambient condition, there are no changes in the structure of anhydrous and all hydrated Montane 60 samples.

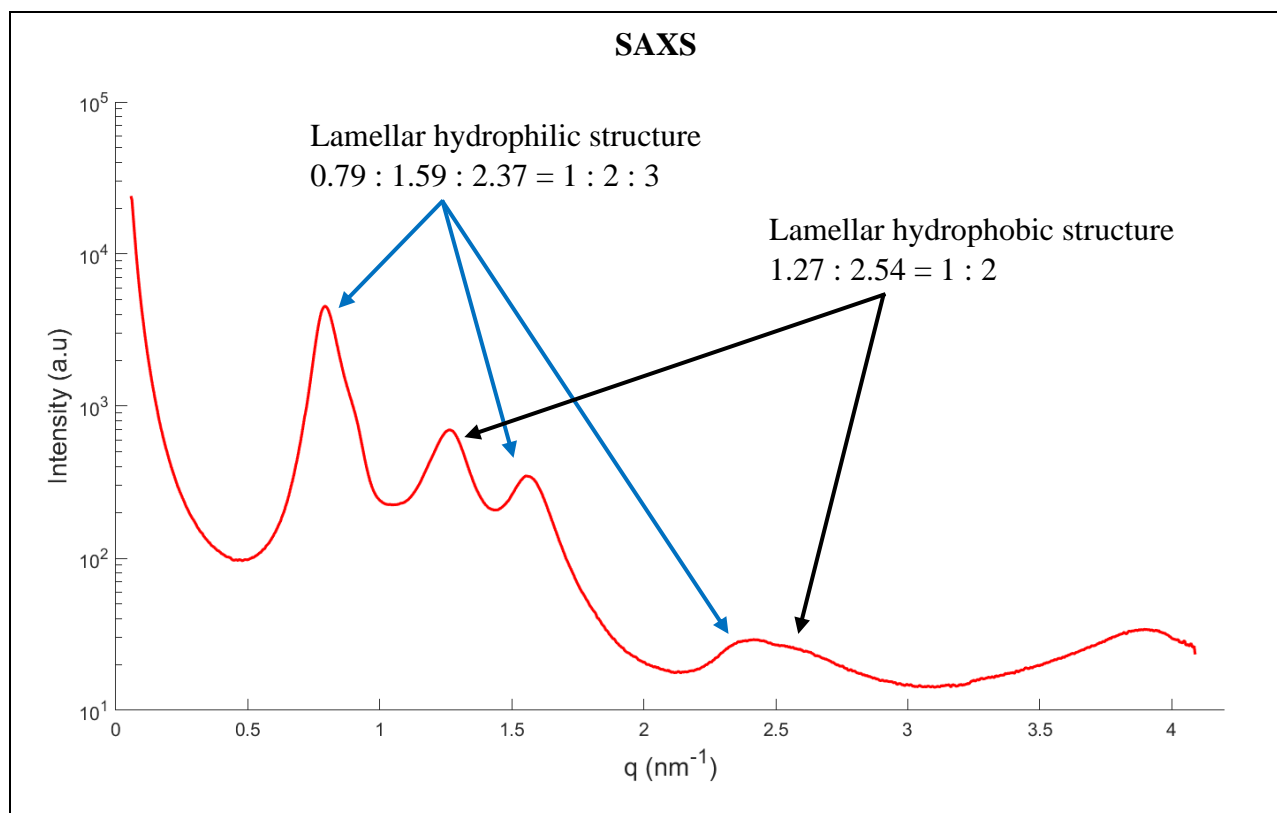


Figure 5.6. SAXS spectrum of 20% hydrated Montane 60 as an example of peak identification

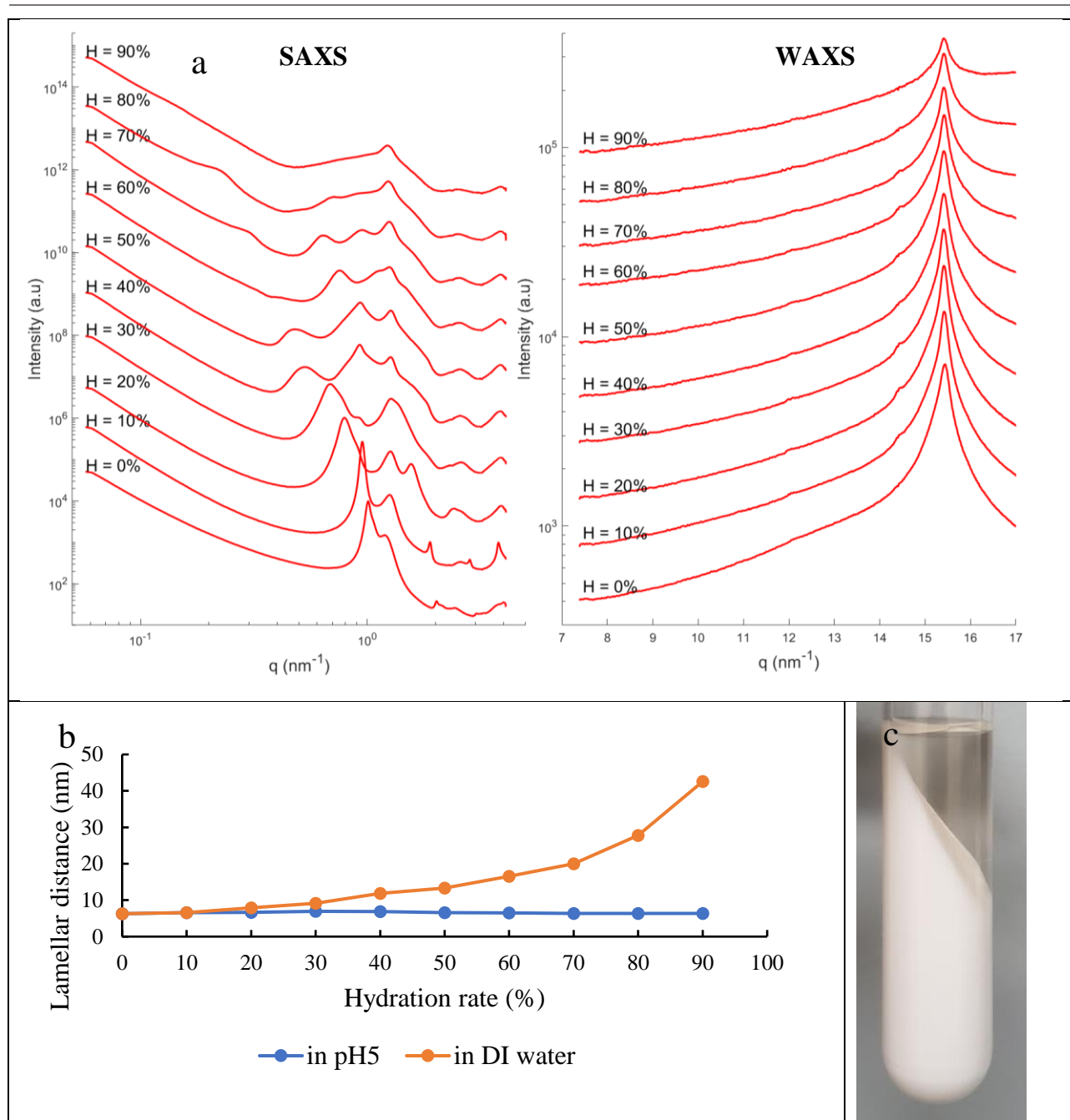


Figure 5.7. (a) S- and WAXS spectra at room temperature of anhydrous and Montane 60 hydrated by hot hydration method in DI water, (b) the evolution of the lamellar distance of Montane 60 with the hydration rate in DI water and in buffer pH5, (c) 80% hydrated M60 sample after ultra-centrifugation.

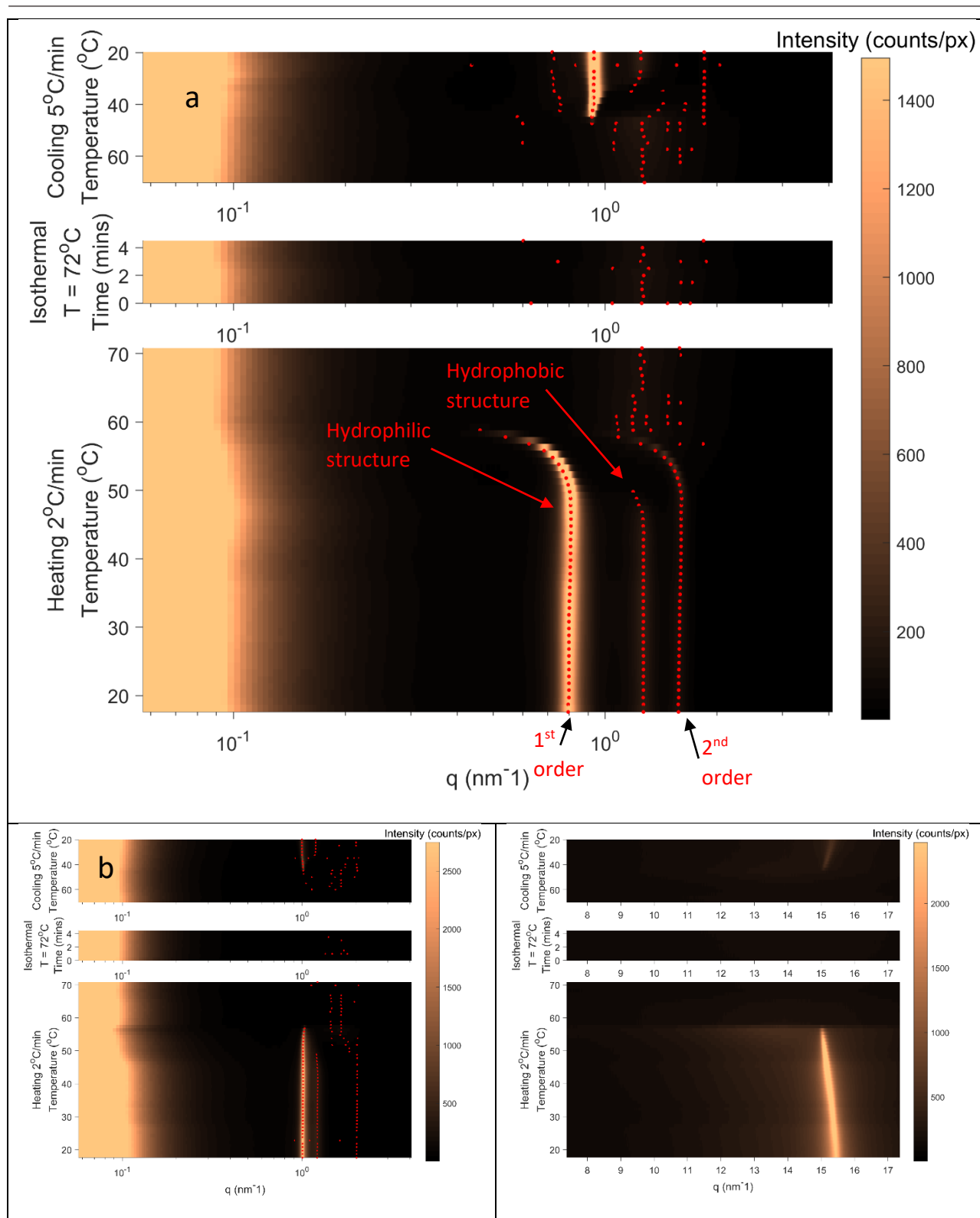
The effect of continuous swelling of M60 up to 90% hydration rate was also observed and reported in the α -gel phase of other materials such as monoglycerides or fatty alcohols [21]. This swelling effect is so important that it was reported to be infinite by some authors [21,22]. Interestingly, the cause of this effect is charged groups on the surface of the lipid bilayer [21–23]. For example, the continuous swelling observed in an industrial monostearin was caused by residual fatty acid [23]. In M60, as shown in Figure 5.7b, in pH 5 (the point that most -COOH groups are not ionized), the lamellar

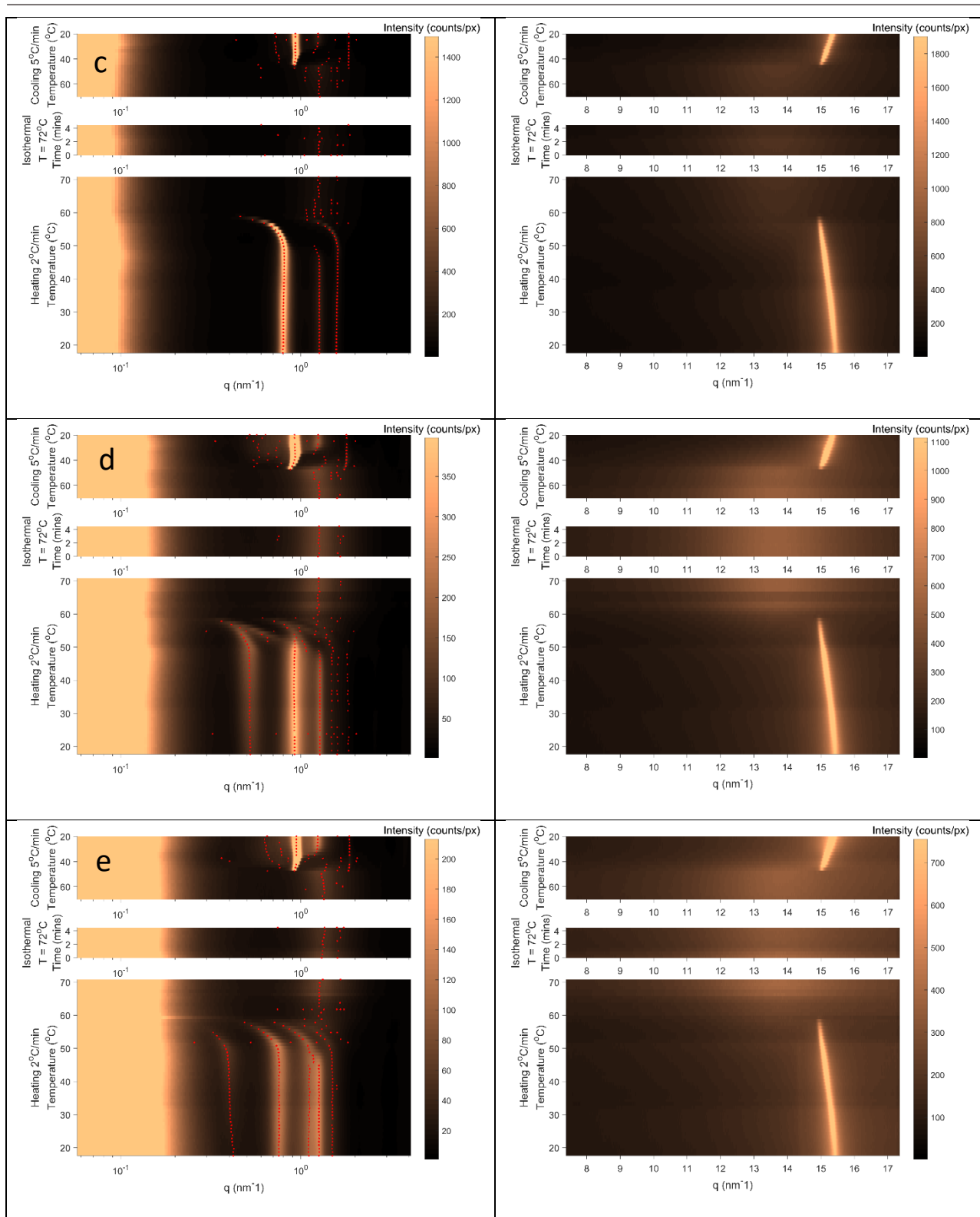
distance of 90% hydrated M60 is only 6.38 nm, indicating that the continuous swelling behavior of M60 also comes from the effect of ionized residual fatty acid. From the acid value provided by the supplier, the quantity of fatty acid (hypothesized to be 50 wt% stearic acid and 50 wt% palmitic acid) was calculated to be around 2.4 wt%.

Results from the hot hydration method are comparable to the spontaneous hydration method. The process of mixing melted M60 with water at 85°C, then cooling to room temperature did not separate the hydrophilic monoester and the hydrophobic triester part. By ultra-centrifuging 80% hydrated M60 sample, we confirm that there was not any lipid phase separation after the hot hydration method (Figure 5.7c). Since the density of sorbitan monostearate is larger than 1 g/mL and the density of sorbitan tristearate is smaller than 1 g/mL [24], if there had been a lipid phases separation after the hot hydration method, it would have been 3 layers (sorbitan tristearate on top, water in the middle and sorbitan monoester on the bottom of the centrifugation tube, as we observed with cocoa butter in the previous chapter). The supernatant is unbound water, indicating that not all water stays inside M60. Bound water stabilized inside the lipid matrix still stayed in the lamellar structure, even after being centrifuged, suggesting a strong interaction between bound water and the hydrophilic structure of M60.

3.3.2. The evolution of the structure of hydrated M60 during the hot hydration process

We investigated the structure of hydrated M60 at different temperatures to observe the evolution of the lipid structure during the hot hydration process. Figure 5.8 shows the evolution of S-WAXS spectra of anhydrous and hydrated Montane 60 in a heating-cooling cycle. An example of SAXS spectra of 20% hydrated Montane 60 at different temperatures is shown in Figure 5.8a. The x-axis is the wavevector value and the colored z-axis is the scattering X-ray intensity. The y-axis indicates the temperature, so one horizontal line is one SAXS spectrum at a given temperature. Going up the y-axis from the origin of the graph, the temperature increases from room temperature, reaches a plateau at 72°C and then decreases to room temperature. We can identify peaks by following the dark-light-dark pattern horizontally. To facilitate the peaks recognition, which is quite difficult in this type of graph, especially for low-intensity or shoulder peaks, each peak is marked with one red dot.





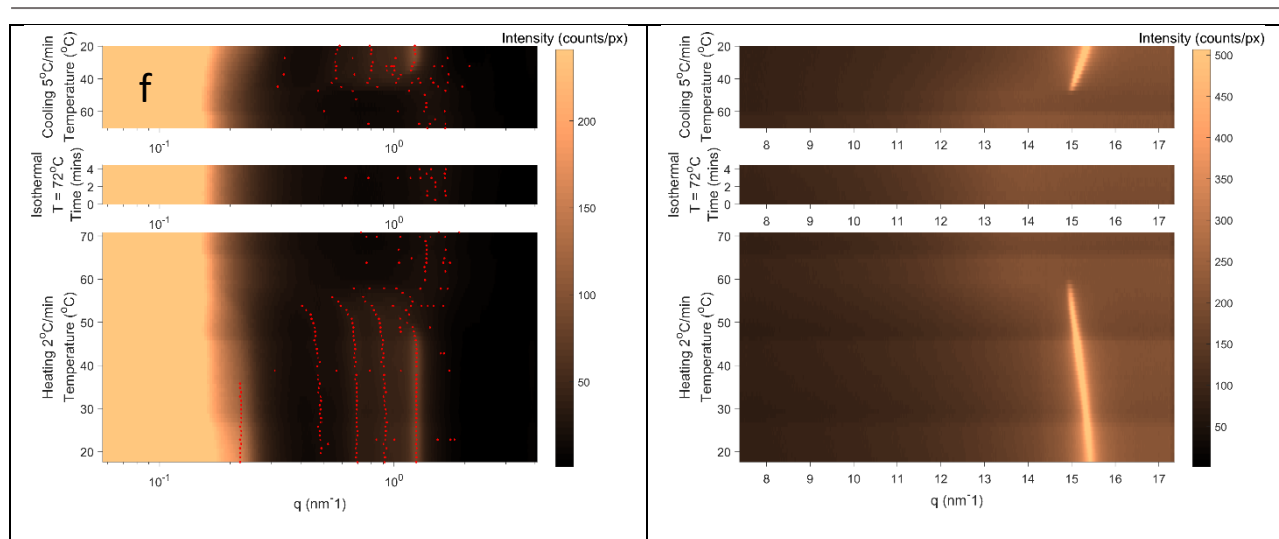


Figure 5.8. (a) SAXS spectra at different temperature of 20% hydrated Montane 60 as an example of the visualization, and S-WAXS spectra at different temperature of anhydrous and hydrated Montane 60 (b) $H = 0\%$, (c) $H = 20\%$, (d) $H = 40\%$, (e) $H = 60\%$, (f) $H = 80\%$

In all samples, when being heated, the hydrophobic lamellar structure of Montane 60 melted first at 47.8°C , while the water-sensitive structure melted later. In hydrated samples, regardless of the hydration rate, when the temperature was higher than 49°C , the lamellar distance of the water-sensitive structure increased until it was fully melted. Interestingly, in 40% hydrated Montane 60, besides the water-sensitive and hydrophobic lamellar structures, another structure, which may be cubic at room temperature and then change to lamellar structure from 53.8°C , has been detected. Upon heating, this potentially cubic structure changed to a lamellar structure at 53.8°C , then melted at 56.8°C , right before the melt of the water-sensitive structure at 60.8°C . This structure was not found in other hydration rate samples.

The extension of lamellar distance upon hydration and heating of Montane 60 is interesting and we would like to discuss and hypothesize the cause of this phenomenon by analyzing the literature. The change of lamellar distance with temperature was not observed in the anhydrous Montane 60 sample. To confirm if the effect comes from the melt of the hydrophobic structure or only from the temperature, Montane 60 hydrated at 60% was kept at 49°C (the point that the hydrophobic structure is melted) and its structure was monitored for 20 minutes. There were no changes in the lamellar distance, indicating that the increase in the lamellar distance when heating depended only on the temperature. However, the fact that the lamellar layers only expand after the melting of the hydrophobic structure suggests an increase in the mobility and flexibility of lipid chains. The rise in the temperature causes the increase in the distance between lipid chains (as observed in WAXS) due to their higher flexibility, hence leading to the increase in the surface area of the lipid bilayer membrane. The high surface area allows the adhesion of more water molecules, holding more water inside the structure. In addition, the separation of lipid chains reduces the interaction between the $-\text{COOH}$ head of fatty acids with other $-\text{COOH}$ or hydrophilic groups in the vicinity. It has been

demonstrated that the packing state and the interaction between -COOH groups highly influence the pKa of fatty acids [25]. So, when the lipid chains are less packed at high temperatures, the pKa of the fatty acids on the lamellar surface would decrease, leading to the rise in their hydrophilicity due to the increase in the ionization of -COOH groups, helping to stabilize more water in the lamellar structure.

In monoglycerides containing fatty acids as impurities, the surface area and the hydrophilicity of the lipid bilayer membrane also increase when heated [23]. The transition from the α -gel phase (lipid chains in solid state) to lamellar phase (lipid chains in molten state) of 70% hydrated monostearin (by increasing the temperature from 25°C to 60°C) decreases the lamellar distance from 19.12 nm to 12.81 nm [23]. It seems contrary to our observation with Montane 60. However, the difference lies in the hydration behavior and the nature of the two materials. In the α -gel phase of monoglycerides, it was considered that most of the water is in the lamellar structure. Hence, when the phase changes from α -gel to lamellar phase, while the volume of water inside the lamellar structure does not change, the increase in the surface area leads to the decrease in the water layer thickness. In Montane 60, as we observed, water can be found outside of the M60 lipid matrix, probably because besides the main component sorbitan monostearate, there is a significant amount of triester and tetraester of sorbitan. When the temperature increases, free water outside can come inside the lamellar structure and increase the lamellar distance. After being cooled down, while the lamellar distance of the hydrophobic structure stays the same as before heating, that of the water-sensitive structure decreases, indicating the phase separation, i.e., the escape of water from hydrated M60 to outside.

The lamellar distance of hydrated Montane 60 at different hydration rates as a function of temperature is summarized in Figure 5.9a. From the hydration rate and lamellar distance, we tried to find the percentage of hydrophilic and hydrophobic fractions in M60. Figure 5.9b shows the measured lamellar distance in comparison to the theoretical lamellar distance. The theoretical lamellar distance (also called ideal swelling distance) is calculated from the assumption that M60 contains only a hydrophilic structure and all water is bound in the lamellar structure. Our hypothesis is that the increase in lamellar distance of hydrated M60 when heated is because water enters lamellar layers. The highest lamellar distance of heated hydrated M60 is hypothesized to be the point that all water has entered the lamellar structure. Using the highest lamellar distance at high temperatures, we calculate the corrected hydration rate (H_{corr}), which is the hydration rate of hydrophilic structure in M60 (because the hydrophobic structure cannot be hydrated). From H_{corr} and experimental hydration rate H calculated from the mass of water and M60, we can find the mass percentage of hydrophilic structure in M60.

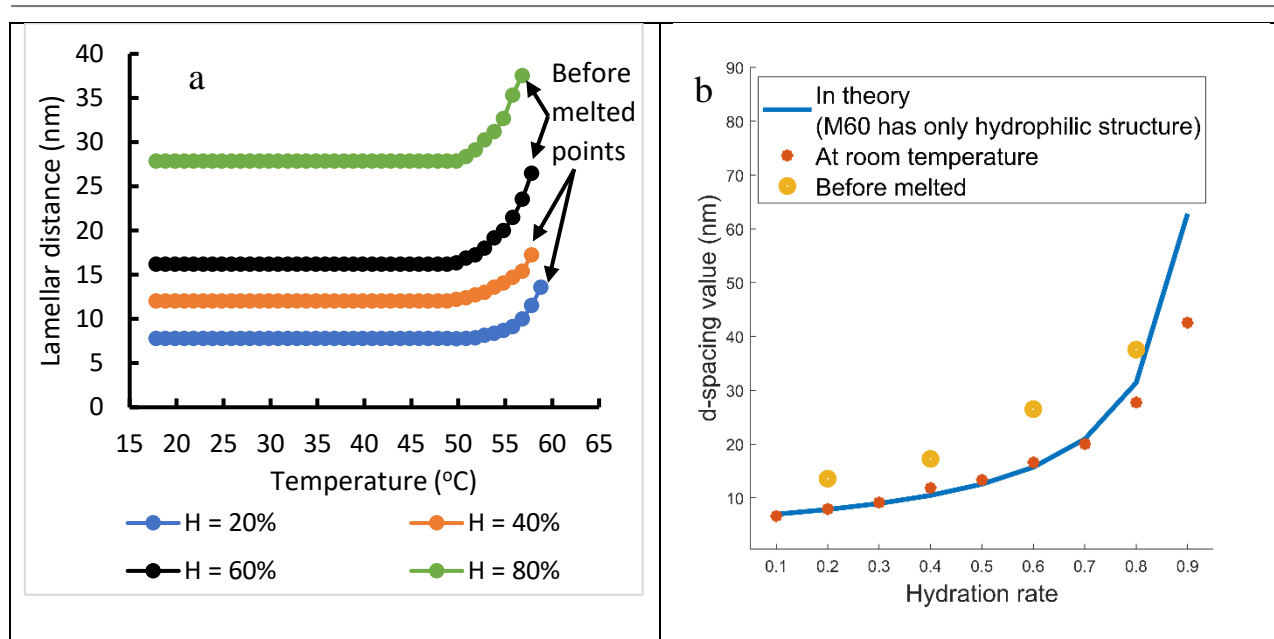


Figure 5.9. (a) Lamellar distance of hydrated Montane 60 as the function of temperature and (b) the lamellar distance of hydrated Montane 60 at room temperature, before melted in comparison with the theoretical case, in which Montane 60 contains only hydrophilic structure. The lamellar distance of the theoretical case is the maximum lamellar distance that Montane 60 may have due to the hydration effect (i.e. the expansion due to water getting into the lamellar structure). Note: In figure b, the fit relation between the lamellar distance at room temperature (orange point) and the curve in theory (blue) is purely coincidental.

Firstly we plot the blue curve of theoretical lamellar distance in Figure 5.9b. This theoretical lamellar distance is the maximum lamellar distance that we can have at a certain hydration rate, because the assumptions are that M60 contains only the hydrophilic structure and all water is bound inside the M60 lamellar structure.

$$d_{theory} = \frac{2 \cdot l_{hydrophobic\ chain}}{1-H} \quad (\text{Equation 5.3})$$

with $l_{hydrophobic\ chain}$ is the length of the hydrophobic chain of sorbitan monostearate, which we estimate to be the length of sorbitan monostearate molecule. So $2 \cdot l_{hydrophobic\ chain} \sim 6.23$ nm, which is the hydrophilic structure lamellar distance in the anhydrous state. H in the equation is the water fraction, or the experimental hydration rate. This curve seems to fit the d-spacing values at room temperature which is purely coincidental. Indeed, this would mean that M60 contains 100% of hydrophilic structures which is not the case.

From Equation 5.3, the corrected hydration rate is :

$$H_{corr} = 1 - \frac{2 \cdot l_{hydrophobic\ chain}}{d_{max}} \quad (\text{Equation 5.4})$$

with d_{max} being the maximum lamellar distance at high temperatures.

For example, at the experimental hydration rate of 20%, the maximum lamellar distance at high temperature is 13.6 nm, then $H_{\text{corr}} = 54\%$. It means that because only the hydrophilic structure can be hydrated, when taking into account only the hydrophilic structure fraction, the corrected hydration rate is higher than the experimental hydration rate.

The corrected hydration rate can also be present as:

$$H_{\text{corr}} = \frac{m_{\text{water}}}{m_{\text{water}} + k \cdot m_{\text{M60}}} \quad (\text{Equation 5.5})$$

with m_{water} being the mass of water in the sample, m_{M60} being the mass of M60 in the sample, and k being the mass percentage of hydrophilic structure in M60 (condition $k < 1$). The ratio $m_{\text{water}}/m_{\text{M60}}$ can be calculated from the experimental hydration rate:

$$H = \frac{m_{\text{water}}}{m_{\text{water}} + m_{\text{M60}}} \quad (\text{Equation 5.6}).$$

From Equation 5.4, Equation 5.5, and Equation 5.6, we can obtain the value k (mass percentage of hydrophilic structure in M60). For example, at the experimental hydration rate of 20%, $k = 0.21$. This value increases with hydration rate and reaches 0.38, 0.47 and 0.81 at 40%, 60% and 80% respectively. These results call for several comments. First, the k value changes with conditions, which sounds wrong as the hydrophilic structure fraction is constant. This means probably that during the heating of the mixtures in capillaries, water diffusion is more difficult at small hydration rates and increases with this rate. From our calculation, for the fully hydrated sample, at 80%, the fraction of hydrophilic structures is around 0.81 which is similar to the contents of sorbitan monoester and diester estimated with the LC-MS results. At a low hydration rate (for example, $H = 20\%$), the mass percentage of the hydrophilic fraction k of M60, which contains both sorbitan monoester and diester, should be much higher than 0.21, as discussed in the LC-MS experiments. When k is higher than 0.21 (more hydrophilic structure), water will have to expand more lamellar layers, decreasing the thickness of the water layer and then decreasing the theoretical lamellar distance. In this case, the highest measured lamellar distance at high temperatures will be higher than the theoretical lamellar distance. However, it is not possible for the lamellar structure to expand larger than the theoretical lamellar distance only by swelling with water. It means there is another factor that contributes to the increase in the lamellar distance upon heating the sample.

We proposed that Helfrich's undulation of lipid bilayers contributes to the swelling effect. The Helfrich's undulation comes from the thermal fluctuation of lipid bilayers. In multilamellar systems, the difference between the entropy between free membranes and bound membranes generates a repulsion [26,27]. This undulation force is dependent on the temperature and the rigidity of the lipid membrane. The more rigid the membrane, the smaller the undulation force. It may be that after the melting of the

hydrophobic structure, the hydrophilic lamellar layers are softened and mobile, increasing the undulation repulsion. As discussed in a report, the “indefinitely far” lamellar distance cannot be explained solely based on Van der Waals attraction and electrostatic repulsion [28]. Peliti introduced the term effective steric interaction resulting from thermally excited undulations [28]. This repulsion interaction is dominant at long distances, where direct forces (Van de Waals, hydration, and electrostatic forces) are negligible. Abillon and Perez stated that the stability of swollen lamellar phases, which have lamellar distances up to several hundred of nm, results from the undulation force [29]. Moreover, similar to our results, deviation from the ideal swelling of the slightly charged lamellar system was also observed and explained by undulation repulsion [30].

From the obtained results, the structure of M60 can be demonstrated in Figure 5.10. The hydrophilic structure is made of sorbitan monoester and sorbitan diester molecules. In pure sorbitan monostearate, the lamellar configuration is 1L, however in Montane 60, due to the presence of diester molecules, the lamellar structure is 2L [7]. Residual fatty acids are found in the hydrophilic lamellar layer. They help to stabilize water and contribute to the high water holding capacity of M60. The hydrophobic structure is made of sorbitan triester and sorbitan tetraester molecules. It also has a 2L configuration; however, due to the chain arrangement, its lamellar distance is smaller than that of the hydrophilic structure. M60 has a stable lamellar structure in H- α configuration, regardless of the hydration state. Due to this monomorphic property, the hydrated state of M60 can be stable for a long time [15]. Indeed, the structure of hydrated M60 samples did not change after 2 months at room condition. M60 can hold a lot of water, which stays between the hydrophilic lamellar layers and expands them. A lamellar distance as large as 42.5 nm can be achieved when Montane 60 is hydrated at 90%, while it is only 6.23 nm in the anhydrous state. The hydrophilic lamellar structure of Montane 60 also expands upon heating. The cause may be the increase in the hydrophilicity of fatty acids, penetration of water into the structure or the undulation effect, or the combination of them. However, these explanations stay as hypothesis without experimental data. Further investigation is required to understand this interesting behavior of Montane 60.

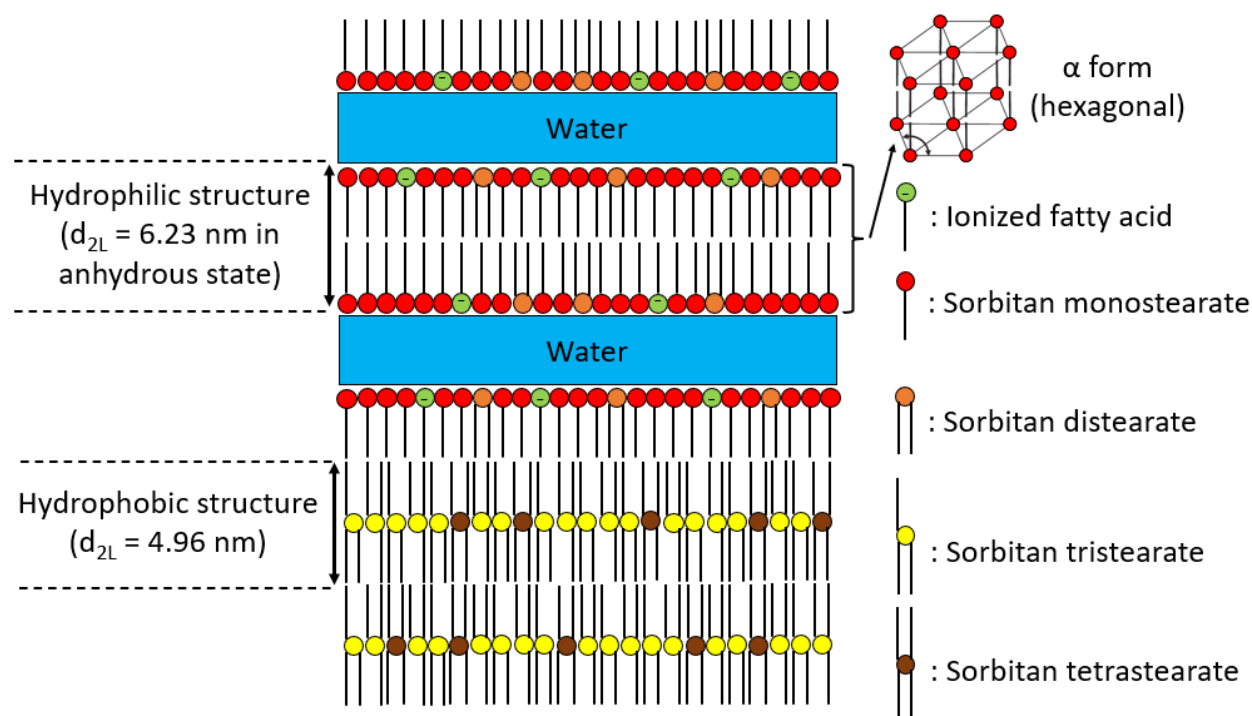


Figure 5.10. Illustration of Montane 60 structure

3.4. Formation of Montane 60 α -gel suspension

M60 solid lipid suspension is fabricated by top-down method and using SDS as the hydrophilic surfactant. The energy of the fabrication instrument decides the size of the lipid particles. When the suspension is agitated by the ultra-turrax, the obtained lipid particles are in micro-scale (around 200-700 nm, Figure 5.11), with a very high Polydispersity Index – PDI value (from 0.6-1, Figure 5.11). We called them Montane 60 microparticles (M60 MPs). When the M60 MPs were broken further down by using a high-pressure homogenizer, whose energy is much higher than the energy of the ultra-turrax, we obtained quite homogenous lipid particles in the nanoscale (around 150 nm, with PDI = 0.2). We called these nanoscale lipid particles M60 nanoparticles (NPs). Due to the negative charge of SDS, in NaCl 3mM, both M60 MPs and NPs are charged negatively, with a zeta potential of around -60 mV. Interestingly, both M60 MPs and NPs can be stabilized even with only 0.1 wt% of SDS in the formulation (while the percentage of M60 is 20 wt% of the formulation).

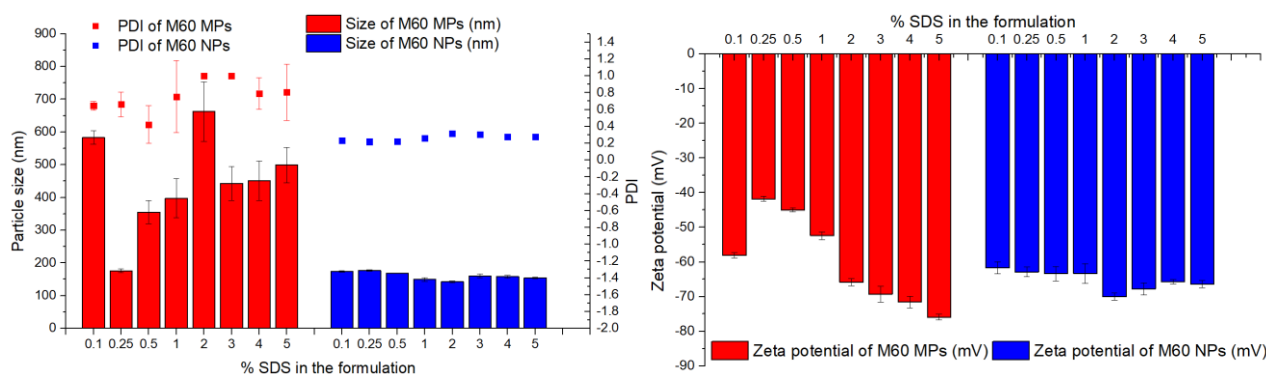


Figure 5.11. Size distribution and zeta potential of M60 microparticles (MPs) and nanoparticles (NPs), the sample dilution for DLS and zeta potential measurement reduces the SDS concentration to below its critical micelle concentration (CMC) point.

The structure of M60 MPs and M60 NPs was investigated using S-WAXS. Since we want to investigate the influence of SDS on the structure of lipid particles, particles stabilized by different SDS concentrations were studied. At first glance, both M60 MPs and M60 NPs have a similar structure to M60 in the bulk state (Figure 5.12a and Figure 5.12b). A wide-distance lamellar structure was detected for all samples. The lipid chains are in the H- α arrangement, meaning that SDS had been integrated into the lipid layer of M60. While the hydrophobic structure is found in M60 MPs, it cannot be detected in M60 NPs. The explanation may be the low periodicity of lipid structure at the nanoscale, which leads to the low-intensity signal in SAXS. For instance, with a lamellar distance of about 24 nm for M60 NPs stabilized by 1% SDS, there are only about 6 lamellar layers in 150 nm nanoparticles.

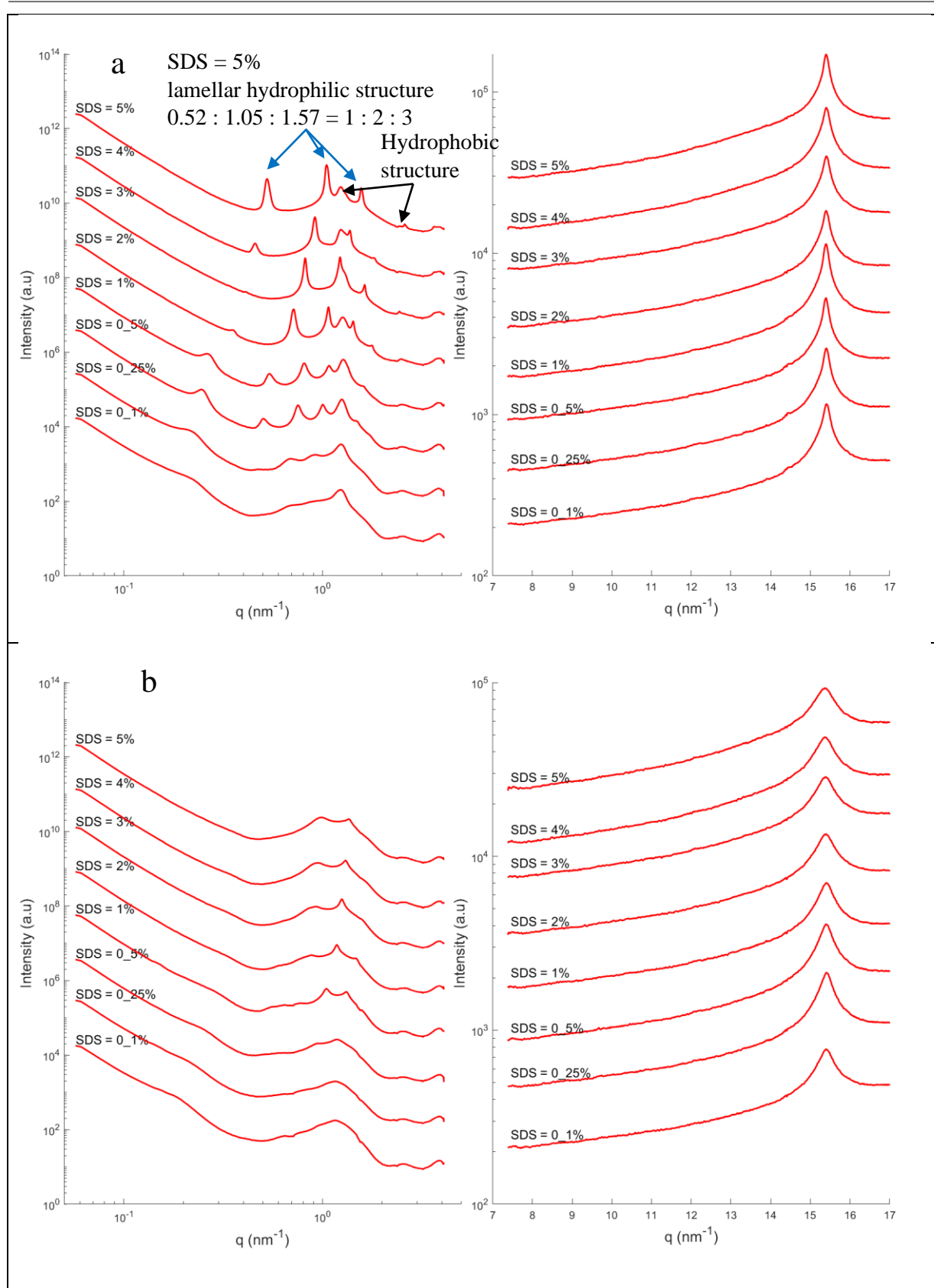


Figure 5.12. The S-WAXS spectra of (a) M60 MPs and (b) M60 NPs

Figure 5.13a shows the effect of SDS on the lamellar distance of M60. As shown above, in pH5 buffer, the swelling capacity of M60 is limited due to the deionization of fatty

acids. The addition of SDS introduces hydrophilic ionic heads on the lipid bilayer surface, hence restores the swelling capacity of M60 in pH5 buffer. This effect of ionic surfactant has also been reported in monoglycerides [7,22]. Interestingly, in water, the addition of SDS to M60 does not increase further the lamellar distance. Instead, when the concentration of SDS increases, the lamellar distance decreases, due to the rise in the concentration of Na^+ ions. Na^+ is reported to reduce the lamellar distance of α -gel structure, because it can bind to anionic groups on the surface of the lipid bilayer [21,23]. On the other hand, von Berlepsch and de Vries suggested that the reduction in the lamellar distance when SDS concentration increases is because of the decrease of the undulation repulsion when the electrostatic repulsion increases [30]. However, it is hard to conclude which effect, undulation or electrostatic repulsion, is dominant in our system. M60 composition is complex, with hydrophilic lamellar structure in a mixture with hydrophobic structure. Both the rigidity of the lipid bilayers and the charge distribution are hard to calculate.

In the case of M60 hydrated in NaCl solution, the higher the concentration of Na^+ , the more ionic groups are neutralized, hence reducing the lamellar distance (Figure 5.13b). In contrast, in the system slightly charged C_{10}E_3 of von Berlepsch and de Vries [30], when the NaCl concentration increased, the lamellar distance increased because the charges were neutralized. This difference may be due to the main repulsion effect of each material. C_{10}E_3 has shorter hydrophobic chains, leading to soft lipid bilayers and the domination of undulation force. Meanwhile, in our M60 system, the lipid chain is C_{18} and solid, reducing the undulation effect and making the electrostatic repulsion dominant. Figure 5.13b presents the effect of NaCl and offers another view of the effect of SDS on M60. When the SDS is added to the formulation, besides the introduction of anionic charges on the lipid bilayer surface, there are also Na^+ ions in the aqueous phase. While the anionic charges from dodecyl sulfate anion (DS^-) and fatty acids maintain the lamellar layers and expand the lamellar distance, Na^+ ion neutralizes anionic charges and shrinks the hydrated α -gel structure. Moreover, not all SDS molecules locate in the lipid phase. SDS is soluble in water and known to form micelles in water when the concentration reaches about 0.2 wt% [31] (the CMC of SDS in our project is 0.13 wt% - chapter 4). Only a fraction of SDS is incorporated inside the lipid bilayer; the rest solubilizes in the solution to form micelles in equilibrium with free SDS molecules. The peak at 1% SDS of M60 MPs fabricated in buffer pH5 in Figure 5.13a may indicate the fact that above CMC, the addition of SDS will stay mainly in water and not enter the lipid matrix anymore. Therefore, when the quantity of SDS increases, the concentration of Na^+ increases, while there is an equilibrium of the amount of SDS in the lipid phase and in the aqueous phase.

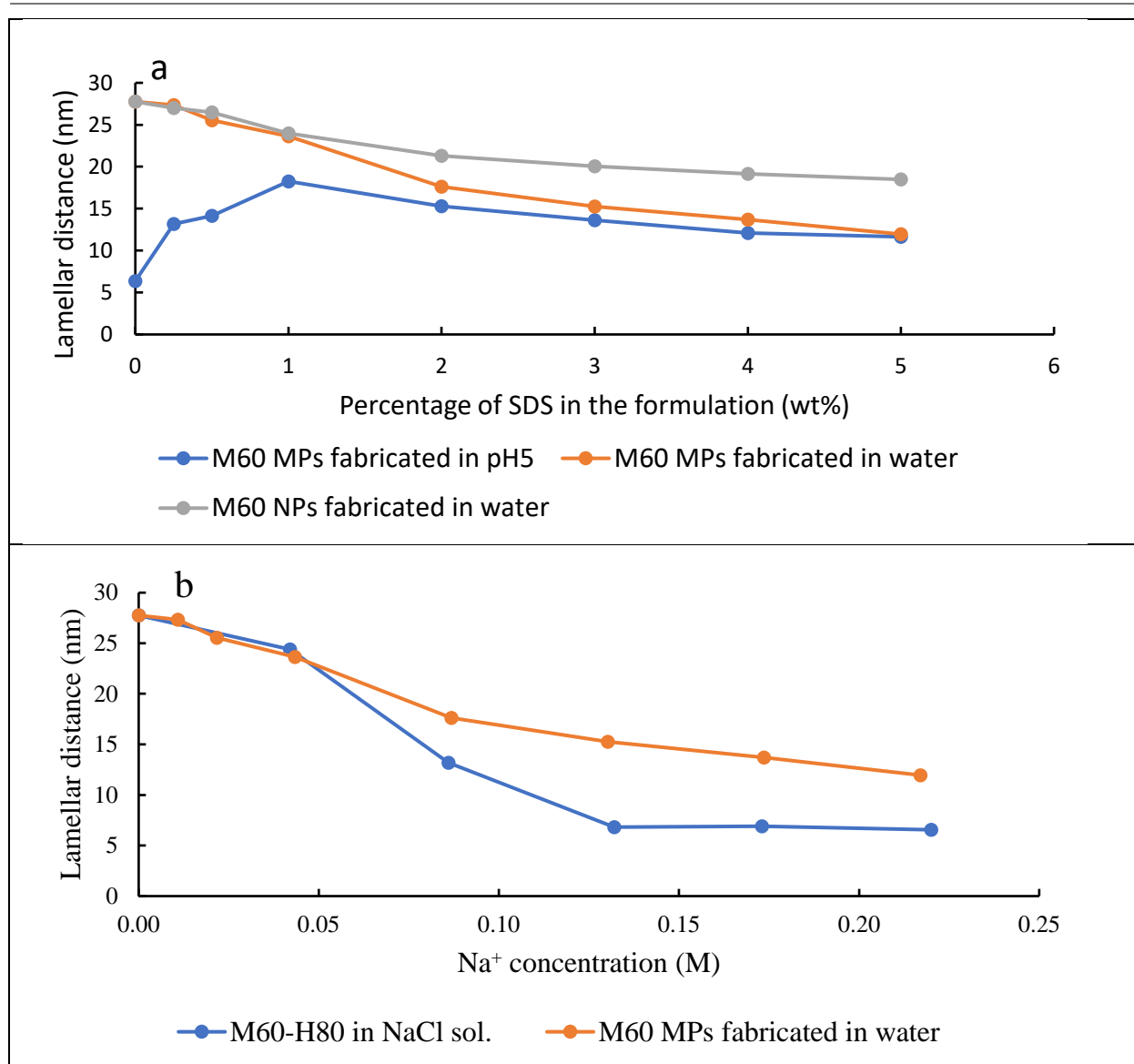


Figure 5.13. (a) The change in the lamellar distances with different concentrations of SDS in M60 MPs and M60 NPs in different media; (b) the lamellar distance of 80% hydrated M60 in NaCl solution in comparison with the lamellar distance of M60 MPs in water. Note: the percentage of M60 is 20 wt% of the formulation.

The combination of the shrinking effect from pH or Na^+ , the swelling effect of anionic charges from DS^- , the distribution of DS^- in the lipid and aqueous phase determine the lamellar distance of M60 MPs and NPs. This hypothesis can explain that at the same percentage of SDS, the lamellar distance of M60 NPs is higher than that of M60 MPs (Figure 5.13a). M60 NPs have a higher specific surface area than M60 MPs due to their smaller size. While the lamellar surface area would stay similar, the surface area of the hydrophobic structure of M60 particles increases as the particle size decreases. So, in the case of M60 NPs, there is more DS^- on the surface of particles than in the case of MPs. Na^+ ions will be attracted by negative charges both on the surface of particles and on the surface of lamellar layers. When more Na^+ ions locate on the surface of particles,

there are fewer Na^+ ions on the surface of lamellar layers, hence reducing the neutralization of the charge's effect on lipid bilayers, leading to higher lamellar distance.

To understand the structure of M60 particles and the formation mechanism, the structure of M60 MPs stabilized by 0.1wt%, 0.5wt%, and 2wt% of SDS was investigated at different temperatures (Figure 5.14). Similar to the case of M60, when the temperature increased, the hydrophobic structure melted first. However, for MPs stabilized by 0.5wt% (Figure 5.14b) and 2%wt (Figure 5.14c) of SDS, above the melting temperature of M60, although the lipid chains have melted (no peaks in WAXS regions), the water-sensitive structure was still detected in lamellar structure, indicating a liquid crystal state. The lamellar liquid crystal structure was stable during the isothermal process at 72°C, then returned to a solid lamellar structure (α -gel) when the temperature decreased below the melting temperature. Since the lamellar structure stayed unbroken during the heating and after the cooling process, water was kept inside all the time, unlike the case of hydrated M60 samples mentioned above, where we observed a phase separation after the cooling process. Therefore, we postulate that SDS can integrate into the lamellar structure and stabilize water on the lipid bilayer surface, even at high temperatures, when lipid chains have been melted. SDS may have stabilized and rigidified the M60 lamellar structure. It is very interesting that although having a packing parameter of around 0.3, SDS still can integrate well inside lamellar layers of M60, whose packing parameter is 0.5 – 1 [32–34].

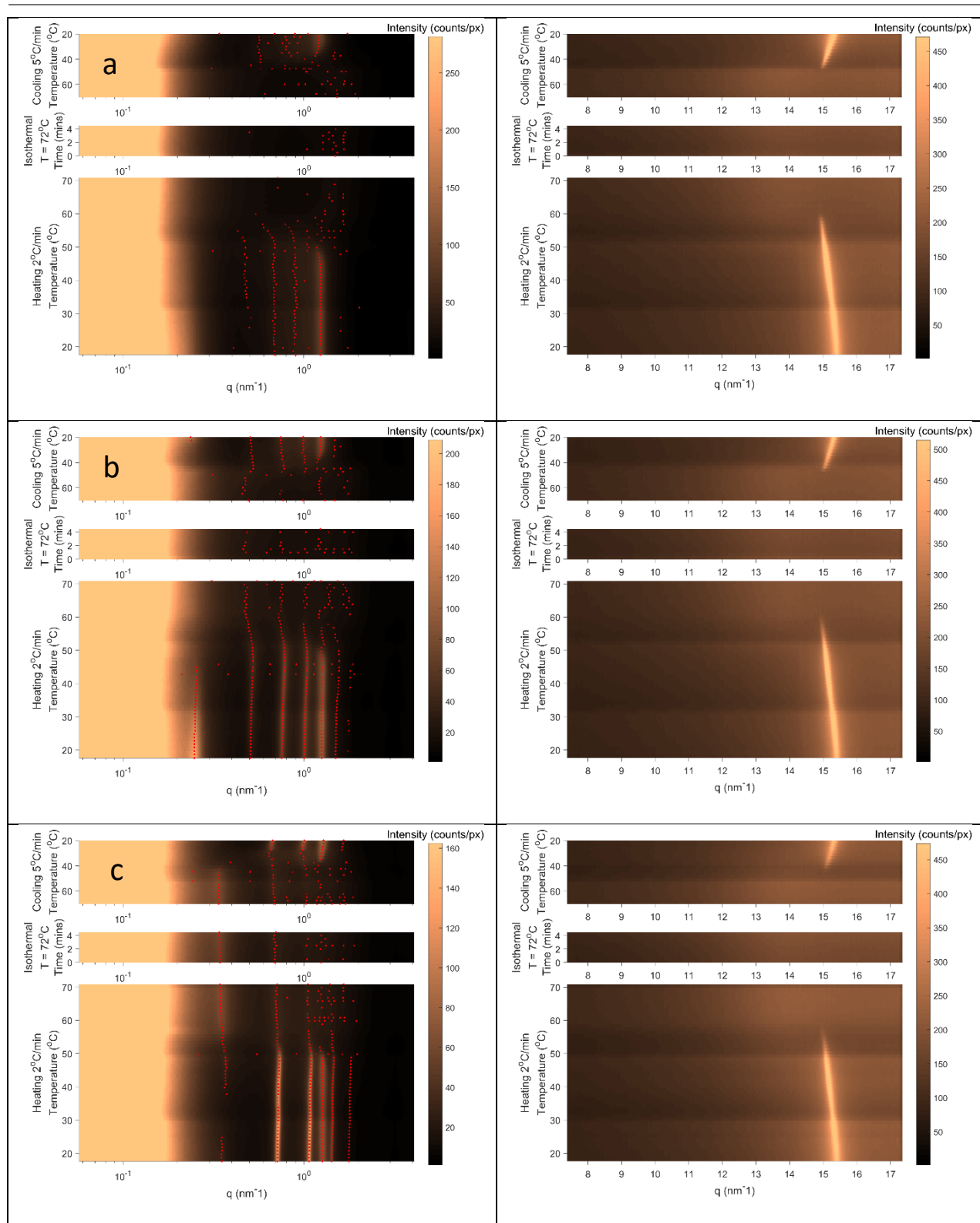


Figure 5.14. Structure of M60 MPs stabilized by (a) 0.1% SDS, (b) 0.5% SDS, (c) 2% SDS at different temperatures

The swelling of the lamellar structure at high temperatures of M60 particles is limited due to the competition between electrostatic and undulation repulsion. As shown in Figure 5.15, when the SDS content in M60 MPs increases, the maximum lamellar

distance at high temperatures decreases. We mentioned above that when the hydrophobic structure melted, the undulation effect started taking place due to the increase in the temperature and in the softness of the lipid bilayers. However, as the SDS concentration increased, the undulation effect decreased due to the rise of electrostatic repulsion [26,30]. Therefore, the undulation effect observed in the 2% SDS sample is small, while it is significant in the 0.1% SDS sample.

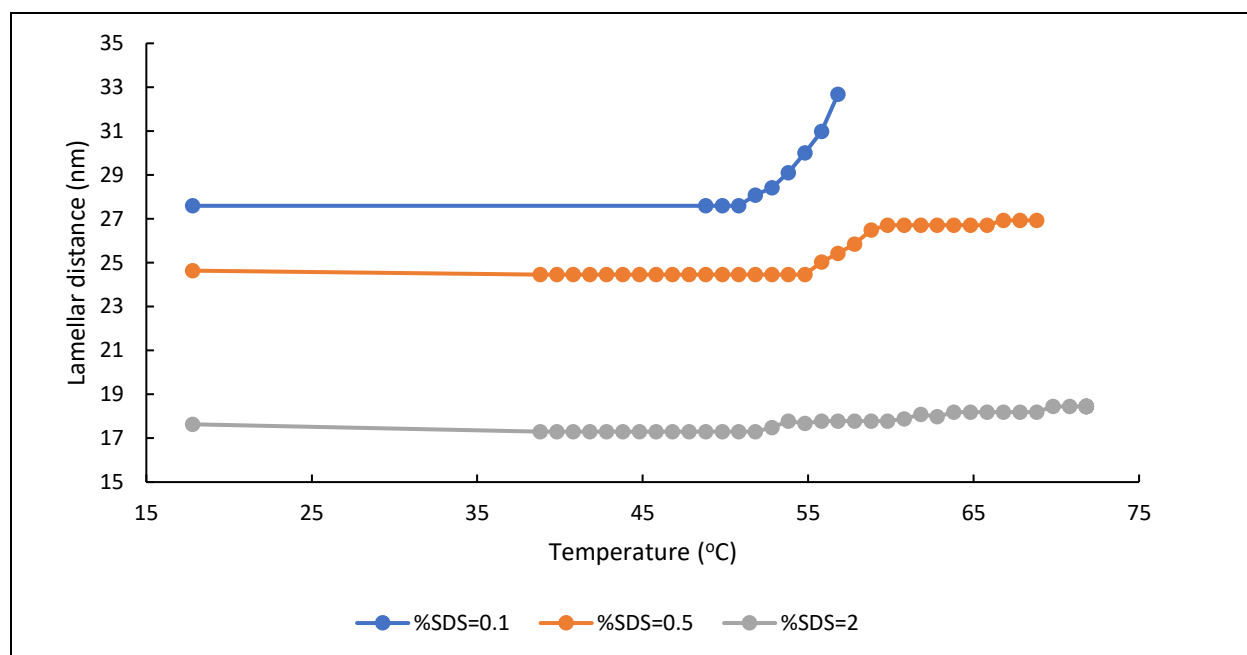


Figure 5.15. The increase in the lamellar distance versus temperature of M60 MPs stabilized by different SDS concentration

To see if another hydrophilic surfactant can reproduce the M60 lamellar layer stabilization effect, we fabricated M60 α -gel particles using lecithin P90G, whose packing parameter ranges from 0.7 – 1 [35]. It favors the formation of lamellar structure and may blend well in the lamellar layer of M60. The results show that P90G does not change the lipid structure of M60 (Figure 5.16). From 2%-5% of P90G, we observed another lamellar structure in SAXS, possibly from P90G at 1 nm^{-1} . When M60-2% P90G MPs were heated, both water-sensitive and hydrophobic structures behaved similarly to those of M60. After M60 had been melted, the lamellar structure of P90G appeared more clearly. Its peaks in SAXS stay stable during the isothermal and cooling process. This observation is logical, since the melting temperature of P90G (about 200°C [36]) is much higher than that of M60 (about 58°C). So, it is reasonable to hypothesize that P90G did not blend inside the M60 lamellar structure. A portion of P90G covers the surface of the lipid particles, while the rest is separated from the M60 lipid matrix and may stay in the suspension in the form of multilamellar vesicles. So, we can conclude that not all hydrophilic surfactants can integrate inside the lipid matrix of M60, even having a packing parameter that favors lamellar structure.

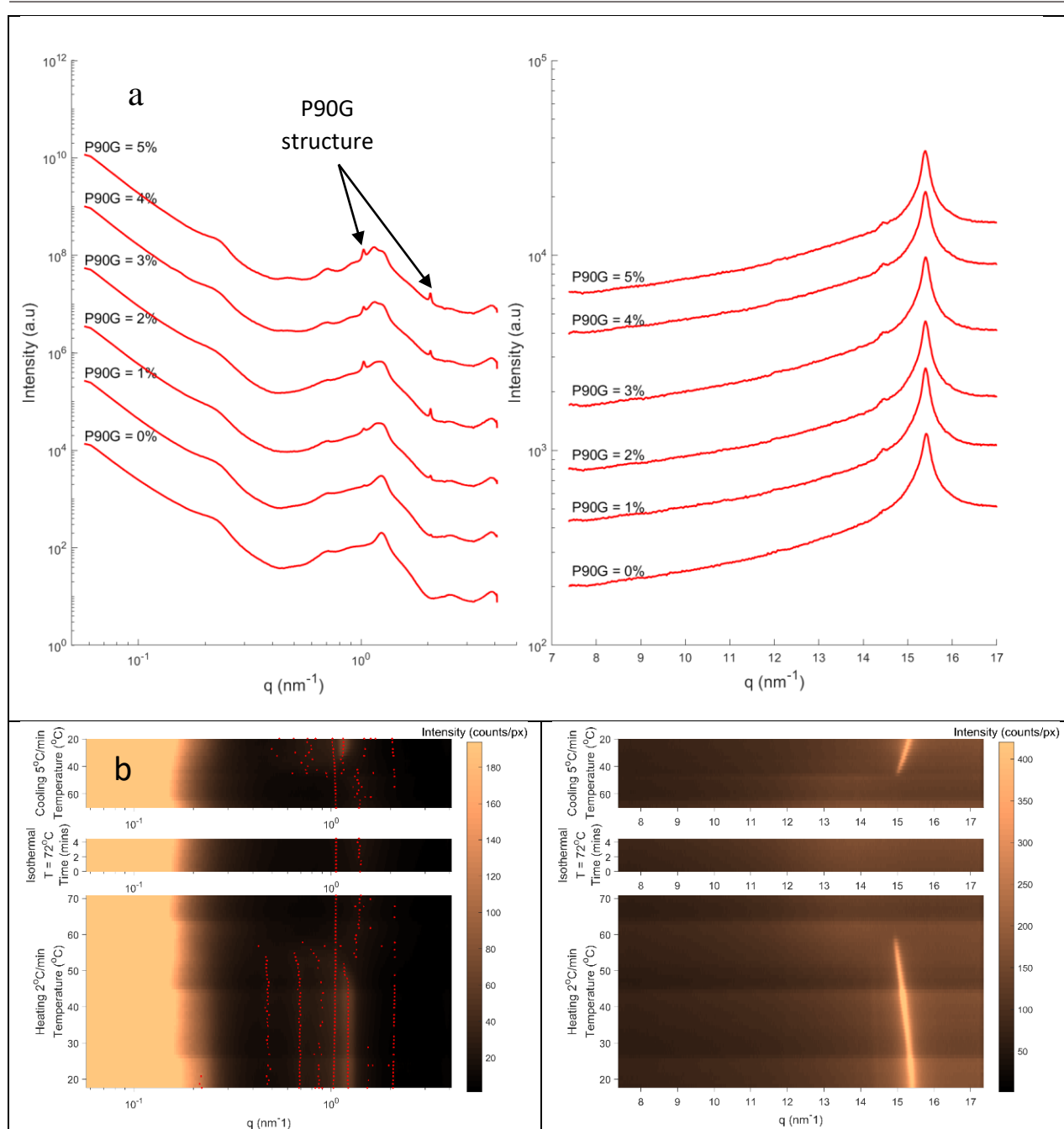


Figure 5.16. S-WAXS spectra of (a) M60 α -gel MPs stabilized by P90G at different concentrations, and (b) the structure of M60–2% P90G α -gel MPs at different temperatures.

4. Conclusion

Taking advantage of the α -gel phase of Montane 60, we have fabricated α -gel particles with tunable sizes from microscale to nanoscale. The suspension can have a very high lipid content (20 wt% in our case). The fabrication process is simple and scalable. Due to the monomorphism of M60, the α -gel structure is stable for a long time. In addition, having both lipophilic and hydrophilic parts in one particle, substances having opposite solubilities can be loaded inside α -gel particles at the same time. The swelling effect of M60 is very important, leading to a potential for a high drug loading rate. The swollen

lamellar structure is stabilized by the combination of electrostatic and undulation force. So, the hydration behavior of M60 particles can be controlled by changing pH, ion concentration and adding suitable surfactants. This sensibility to environmental conditions of α -gel structure can be used to control the release rate of substances from the formulation in different biological media, opening many potential applications in the pharmaceutical field.

From chapter 4, we have identified the input materials and their interactions. We also fixed process fabrication parameters. In this chapter, we understand the structure and hydration behavior of the main materials. We conclude that the proposal of making a w/o/w emulsion cannot be done, due to the crystallization behavior of lipids and the nanoscale size of lipid particles. Because Montane 60 can be hydrated under heating and shearing, the hot high-pressure homogenization method is robust, scalable and suitable for our lipid particles. The lipid mixture can be hydrated, loaded with drugs and cut down to nanosize at the same time in 1 process without losing its properties. After fabrication, the structure of the particles stays stable for a long period of time. In the last chapter of the thesis, we report the fabrication of the final product, including the polymer coating step and its antimicrobial activity *in vitro*.

References

- [1] C.-M.J. Hu, L. Zhang, Nanoparticle-based combination therapy toward overcoming drug resistance in cancer, *Biochem. Pharmacol.* 83 (2012) 1104–1111. <https://doi.org/10.1016/j.bcp.2012.01.008>.
- [2] P. Parhi, C. Mohanty, S.K. Sahoo, Nanotechnology-based combinational drug delivery: an emerging approach for cancer therapy, *Drug Discov. Today.* 17 (2012) 1044–1052. <https://doi.org/10.1016/j.drudis.2012.05.010>.
- [3] L.-T.-C. Tran, S. Lesieur, V. Faivre, *Janus* nanoparticles: materials, preparation and recent advances in drug delivery, *Expert Opin. Drug Deliv.* 11 (2014) 1061–1074. <https://doi.org/10.1517/17425247.2014.915806>.
- [4] J. Huang, Y. Guo, S. Gu, G. Han, W. Duan, C. Gao, W. Zhang, Multicompartment block copolymer nanoparticles: recent advances and future perspectives, *Polym. Chem.* 10 (2019) 3426–3435. <https://doi.org/10.1039/C9PY00452A>.
- [5] T. Suzuki, Liquid Crystal and α -gel-Based Emulsion and Soft Gel formulations, *Acc. Mater. Surf. Res.* (2017), Vol.2, No.1, 21-40
- [6] T. Iwata, Chapter 25 - Lamellar Gel Network, (n.d.) 33.
- [7] F. Vang Sparso, N. Krog, Food Emulsifiers: Their Chemical And Physical Properties, in: S. Friberg, K. Larsson, J. Sjöblom (Eds.), *Food Emuls.*, CRC Press, 2003. <https://doi.org/10.1201/9780203913222.ch2>.

- [8] C. Himawan, V.M. Starov, A.G.F. Stapley, Thermodynamic and kinetic aspects of fat crystallization, *Adv. Colloid Interface Sci.* 122 (2006) 3–33.
<https://doi.org/10.1016/j.cis.2006.06.016>.
- [9] F.C. Wang, A.G. Marangoni, Advances in the application of food emulsifier α -gel phases: Saturated monoglycerides, polyglycerol fatty acid esters, and their derivatives, *J. Colloid Interface Sci.* 483 (2016) 394–403.
<https://doi.org/10.1016/j.jcis.2016.08.012>.
- [10] M.V. González-Rodríguez, M.S. Dopico-García, R. Noguerol-Cal, T. Carballeira-Amarelo, J.M. López-Vilariño, G. Fernández-Martínez, Application of liquid chromatography in polymer non-ionic antistatic additives analysis, *J. Sep. Sci.* 33 (2010) 3595–3603. <https://doi.org/10.1002/jssc.201000460>.
- [11] C. Baiocchi, M. Magni, F. Romaniello, E. Forte, M. Fontana, Chemical Characterization of Sorbitan Tri-Stearate Commercial Samples and Their Determination in Confectionery Fats by HPLC HIGH -Resolution Mass Spectrometry, *J. Am. Oil Chem. Soc.* 97 (2020) 1057–1069. <https://doi.org/10.1002/aocs.12392>.
- [12] Z. Wang, M. Fingas, Analysis of sorbitan ester surfactants. Part I: High performance liquid chromatography, *J. High Resolut. Chromatogr.* 17 (1994) 15–19.
<https://doi.org/10.1002/jhrc.1240170104>.
- [13] N. Garti, E. Wellner, A. Aserin, S. Sarig, Analysis of sorbitan fatty acid esters by HPLC, *J. Am. Oil Chem. Soc.* 60 (1983) 1151–1154.
<https://doi.org/10.1007/BF02671346>.
- [14] A. Nava, P. Mahoney, L. Bondioli, A. Coppa, E. Cristiani, L. Fattore, G. McFarlane, D. Dreossi, L. Mancini, Virtual histology of archaeological human deciduous prenatal enamel through synchrotron X-ray computed microtomography images, *J. Synchrotron Radiat.* 29 (2022) 247–253.
<https://doi.org/10.1107/S160057752101208X>.
- [15] T. Cottrell, J.V. Peij, Sorbitan Esters and Polysorbates, in: R.J. Whitehurst (Ed.), *Emuls. Food Technol.*, Blackwell Publishing Ltd, Oxford, UK, 2004: pp. 162–185.
<https://doi.org/10.1002/9780470995747.ch7>.
- [16] EFSA Panel on Food Additives and Nutrient Sources added to Food (ANS), A. Mortensen, F. Aguilar, R. Crebelli, A. Di Domenico, B. Dusemund, M.J. Frutos, P. Galtier, D. Gott, U. Gundert-Remy, J. Leblanc, O. Lindtner, P. Moldeus, P. Mosesso, D. Parent-Massin, A. Oskarsson, I. Stankovic, I. Waalkens-Berendsen, R.A. Woutersen, M. Wright, M. Younes, P. Boon, D. Chrysafidis, R. Gürtler, P. Tobback, A. Altieri, A.M. Rincon, C. Lambré, Re-evaluation of sorbitan monostearate (E 491), sorbitan tristearate (E 492), sorbitan monolaurate (E 493), sorbitan monooleate

(E 494) and sorbitan monopalmitate (E 495) when used as food additives, EFSA J. 15 (2017). <https://doi.org/10.2903/j.efsa.2017.4788>.

- [17] J.L. Humphrey, The separation and characterisation of sorbitan esters using gas and liquid chromatographic techniques, Department of Chemistry, The University of Hull, 2007. <https://hydra.hull.ac.uk/resources/hull:1600> (accessed January 12, 2022).
- [18] J. Li, A. Spina, J.A. Moulijn, M. Makkee, Sorbitol dehydration into isosorbide in a molten salt hydrate medium, *Catal. Sci. Technol.* 3 (2013) 1540–1546. <https://doi.org/10.1039/C3CY20809E>.
- [19] I. Bonnin, R. Mereau, T. Tassaing, K.D.O. Vigier, One-pot synthesis of isosorbide from cellulose or lignocellulosic biomass: a challenge?, *Beilstein J. Org. Chem.* 16 (2020) 1713–1721. <https://doi.org/10.3762/bjoc.16.143>.
- [20] J. Hermans, S. Ongay, V. Markov, R. Bischoff, Physicochemical Parameters Affecting the Electrospray Ionization Efficiency of Amino Acids after Acylation, *Anal. Chem.* 89 (2017) 9159–9166. <https://doi.org/10.1021/acs.analchem.7b01899>.
- [21] G. Eccleston, Multiple-phase oil-in-water emulsion, *J Soc Cosmet Chem.* 41 (1990).
- [22] K. Larsson, N. Krog, Structural properties of the lipid—water gel phase, *Chem. Phys. Lipids.* 10 (1973) 177–180. [https://doi.org/10.1016/0009-3084\(73\)90014-5](https://doi.org/10.1016/0009-3084(73)90014-5).
- [23] N. Krog, A.P. Borup, Swelling behaviour of lamellar phases of saturated monoglycerides in aqueous systems, *J. Sci. Food Agric.* 24 (1973) 691–701. <https://doi.org/10.1002/jsfa.2740240609>.
- [24] G.G. Hawley, R.J. Lewis, *Hawley's condensed chemical dictionary*, 13th ed., Van Nostrand Reinhold, New York, 1997.
- [25] J.R. Kanicky, D.O. Shah, Effect of Degree, Type, and Position of Unsaturation on the pKa of Long-Chain Fatty Acids, *J. Colloid Interface Sci.* 256 (2002) 201–207. <https://doi.org/10.1006/jcis.2001.8009>.
- [26] D. Roux, C.R. Safinya, A synchrotron X-ray study of competing undulation and electrostatic interlayer interactions in fluid multimembrane lyotropic phases, *J. Phys.* 49 (1988) 307–318. <https://doi.org/10.1051/jphys:01988004902030700>.
- [27] J. Lemmich, J.H. Ipsen, T. Hønger, K. Jørgensen, O.G. Mouritsen, K. Mortensen, R. Bauer, SOFT AND REPULSIVE: RELATIONSHIP BETWEEN LIPID MEMBRANE IN-PLANE FLUCTUATIONS, BENDING RIGIDITY, AND REPULSIVE UNDULATION

FORCES, Mod. Phys. Lett. B. 08 (1994) 1803–1814.

<https://doi.org/10.1142/S0217984994001710>.

- [28] L. Peliti, EFFECTIVE RIGIDITY OF MEMBRANES, (n.d.) 9.
- [29] O. Abillon, E. Perez, Swollen lamellar phases between two solid walls : undulation forces and generation of defects, J. Phys. 51 (1990) 2543–2556. <https://doi.org/10.1051/jphys:0199000510220254300>.
- [30] H. von Berlepsch, R. de Vries, Weakly charged lamellar bilayer system: Interplay between thermal undulations and electrostatic repulsion, Eur. Phys. J. E. 1 (2000) 141–152. <https://doi.org/10.1007/PL00014594>.
- [31] A. Chatterjee, S.P. Moulik, S.K. Sanyal, B.K. Mishra, P.M. Puri, Thermodynamics of Micelle Formation of Ionic Surfactants: A Critical Assessment for Sodium Dodecyl Sulfate, Cetyl Pyridinium Chloride and Dioctyl Sulfosuccinate (Na Salt) by Microcalorimetric, Conductometric, and Tensiometric Measurements, J. Phys. Chem. B. 105 (2001) 12823–12831. <https://doi.org/10.1021/jp0123029>.
- [32] G. Basu Ray, I. Chakraborty, S. Ghosh, S.P. Moulik, A critical and comprehensive assessment of interfacial and bulk properties of aqueous binary mixtures of anionic surfactants, sodium dodecylsulfate, and sodium dodecylbenzenesulfonate, Colloid Polym. Sci. 285 (2006) 457–469. <https://doi.org/10.1007/s00396-006-1589-1>.
- [33] K.M. Sachin, S.A. Karpe, M. Singh, A. Bhattarai, Self-assembly of sodium dodecylsulfate and dodecyltrimethylammonium bromide mixed surfactants with dyes in aqueous mixtures, R. Soc. Open Sci. 6 (2019) 181979. <https://doi.org/10.1098/rsos.181979>.
- [34] M.I. Khan, A. Madni, S. Ahmad, M.A. Mahmood, M. Rehman, M. Ashfaq, Formulation design and characterization of a non-ionic surfactant based vesicular system for the sustained delivery of a new chondroprotective agent, Braz. J. Pharm. Sci. 51 (2015) 607–615. <https://doi.org/10.1590/S1984-82502015000300012>.
- [35] T. Onadeko, Preparation and Characterization Of Oil-in-water Nano-emulsions Of Trifluoperazine For Parenteral Drug Delivery, (n.d.) 113.
- [36] F.C. Kenechukwu, M.A. Momoh, P.O. Nnamani, A.A. Attama, Solid lipid micro-dispersions (SLMs) based on PEGylated solidified reverse micellar solutions (SRMS): a novel carrier system for gentamicin, Drug Deliv. 22 (2015) 710–722. <https://doi.org/10.3109/10717544.2014.900152>.

Chapter 6. Solid lipid particles - chitosan nanocomposite for chemoattraction and elimination of *Helicobacter pylori*

Hung V. Nguyen¹, Christophe Burucoa^{2,3}, Vincent Faivre¹

¹Université Paris-Saclay, CNRS, Institut Galien Paris-Saclay, 5 rue JB Clément, 92296 Châtenay-Malabry, France.

²Université de Poitiers, Faculté de Médecine et de Pharmacie, Inserm U1070, 86022 Poitiers, France.

³University Hospital of Poitiers, Infectious Agents Department, Bacteriology and Infection Control Laboratory, 86021 Poitiers, France

Abstract

Helicobacter pylori (*H. pylori*) is a bacterium that lives inside the human stomach. It infects more than 50% of the world's population. The infection of *H. pylori* may lead to gastric cancer. While living in the stomach, *H. pylori* cannot live in acids. It runs away from acid and follows the urea gradient to find gastric epithelium. It then makes niches in the gastric glands, below the mucus layer, where the pH is neutral. The treatment of *H. pylori* is difficult due to the low activity of antibiotics in gastric acid. In this report, we fabricated a lipid nanoparticle–chitosan (LNP-C) nanocomposite, which co-loads erythromycin, a hydrophobic antibiotic, and urea, a hydrophilic compound. The lipid nanoparticles have α -gel structure, which has both hydrophilic and lipophilic domains to load compounds having opposite solubilities. The LNP-C nanocomposite shows high urea and erythromycin loading capacity, with a sustainable *in vitro* release rate for 4 hours. The nanocomposite shows antimicrobial activity *in vitro* against *H. pylori*, thanks to the encapsulated erythromycin. Taking advantage of the chemotactic movement toward the urea of *H. pylori*, the urea released from the nanocomposite may attract the bacteria. Upon contact, the chitosan may stick to the bacteria due to the interaction with bacterial adhesins, while erythromycin will be released to eliminate the bacteria in its neutral environment. The chitosan also has the mucoadhesive property, increasing the retention time of the nanocomposite in the stomach. However, experiments on the chemoattraction property of the nanocomposite are still ongoing.

1. Introduction

Helicobacter pylori (*H. pylori*) is a spiral-shaped, gram-negative bacterium colonizing the human stomach. More than 50% of the human population is infected with *H. pylori* [1]. The high prevalence is generally related to the low hygienic living condition, explaining the high prevalence in developing regions [2]. *H. pylori* stay in the human stomach by lying around a few hundred microns away from the low-pH lumen and making niches in the stomach mucosa [3]. *H. pylori* is responsible for about 89% of gastric cancer cases worldwide and since 1994, International Agency for Research on Cancer (IARC) has

categorized *H. pylori* as carcinogen class 1 [2,4]. The World Health Organization (WHO) has classified *H. pylori* as high priority for the research and development of antibiotics in 2017 [5]. Besides, it is also a casual cause of peptic, gastritis, duodenal ulcers, and mucosal-associated lymphoid tissue lymphoma [6,7]. *H. pylori* adapts to the high-acid environment in the stomach by regulating the activity of urease, an enzyme that catalyzes the degradation of urea into NH_3 and CO_2 [6]. Because of the activity of urease, a buffer environment having lower acidity than the stomach lumen is created in the cytoplasm and periplasm of the bacterium. Since urea is very important for them to survive in the acid environment, they have the ability to sense urea and then swim to the high urea concentration region, thanks to the presence of the TlpB receptor [8]. *H. pylori* simultaneously senses and destroys urea, helping it to neutralize acid while finding the way to the urea source, which is the gastric epithelial layer [8]. Due to the high acidity of the stomach, the treatment of *H. pylori* includes the using a combination of antibiotics with a proton-pump inhibitor (PPI) and/or with bismuth salt [9]. The eradication rate of *H. pylori* is decreasing every year, with an average value of only around 75% [10]. The persistence of *H. pylori* may associate with its deep location in the gastric gland [11]. Therefore, new treatments for *H. pylori* eradication are necessary.

We propose a new strategy to treat *H. pylori* using solid lipid particles administrated orally. The solid lipid particles contain an antibiotic in the lipid matrix to eliminate the bacteria. In our work, we use erythromycin as a model antibiotic to investigate the interaction between the lipid particles and the acid environment, as erythromycin degrades in acid. Inside the lipid particles, we use a lipophilic surfactant to stabilize the urea solution inside the lipid matrix. Upon administration, urea will be released and create an urea gradient, attracting *H. pylori* toward the particles via chemotactic attraction, and facilitating the meeting between the bacteria and the lipid particles. The use of natural taxes to design drug delivery systems has been analyzed and may improve the targeting property of the system [12]. Chitosan will encapsulate the lipid particles via electrostatic interaction to form a nanocomposite of lipid particles – chitosan. Thanks to the positive charge in the acid environment, chitosan will stick to the stomach lining, where the *H. pylori* hide. In addition, chitosan also adheres to the *H. pylori* membrane, anchors the lipid particles to the bacteria once they have made the contact [13]. Therefore, unlike the traditional drug administration, where antibiotics go into the blood circulation and diffuse to the bacteria, our site of action of antibiotics is in the stomach, where *H. pylori* live. This strategy targets the bacteria directly and reduces the quantity of antibiotics needed.

2. Materials and methods

2.1. Materials

Cocoa butter is provided by Edna Group. Sorbitan monostearate was provided by Seppic under the trade name of Montane 60 (M60). Sodium dodecyl sulfate (SDS, GPR Retapur®) was purchased from VWR chemical. Na_2HPO_4 , NaH_2PO_4 , K_2HPO_4 , KH_2PO_4 , NaCl were purchased from Carlo Erba. Glacial acetic acid (CH_3COOH) was purchased

from Sigma-Aldrich. Urea (Molecular Biology grade, Ultrapure, Batch 200927) was purchased from Thermo Scientific. Erythromycin was purchased from Cooper. Chitosan (30 – 100 cps, degree of deacetylation of 92.11%) was purchased from Glentham Life Sciences. Defibrinated horse blood was purchased from Thermo Scientific.

2.2. Fabrication of lipid nanoparticles suspension

The lipid nanoparticle suspension was fabricated using the high-pressure homogenizer method. The lipid particles had a solid lipid core of cocoa butter and Montane 60, which was stabilized by SDS on the particle's surface. Generally, 2.8g of cocoa butter, 11.2g of Montane 60, 0.7g of SDS, and 0.7g of erythromycin were heated together in a beaker at 85°C. The melted lipid mixture was agitated until erythromycin was totally dissolved. 85°C preheated 54.6g of buffered urea solution 32.85 wt% (eutectic point with water [14]) was added to the lipid mixture. The use of urea solution at the eutectic point maximizes the urea loading capacity. The urea solution was buffered by Na₂HPO₄ (83.5 mM) and NaH₂PO₄ (27.8 mM). The pH was adjusted to 7.4. The neutral pH buffer is to neutralize the acid acetic (in chitosan solution) added in the next step (below), protecting erythromycin and urea from degradation during the fabrication process. We avoided using potassium salts to prevent the precipitation of potassium dodecyl sulfate [15,16]. The lipid-buffered urea solution mixture was then mixed by the ultra-turrax® mixer (IKA T18 basic) at speed level 5 (no-load speed of 20000 rpm) for 5 minutes to obtain the coarse suspension. The coarse suspension was rapidly poured into the preheated high-pressure homogenizer (HPH, APV-2000 SPXFLOW) and homogenized for 5 minutes at 600 bars, 85°C. The obtained suspension was cooled down in an ice bath until the temperature reached room temperature. The product was then called lipid nanoparticles (LNP) suspension.

2.3. Physico-chemical characterization of LNP suspension

2.3.1. Lipid structure characterization

The lipid structure was determined by the small- and wide-angle X-ray scattering technique (S-WAXS) using the Bruker MicroCalix machine. The S-WAXS patterns were acquired at the laboratory using a microfocus X-ray tube (I μ S, Incoatec), selecting the Cu K α radiation. It was used with an intensity of 1000 μ A and a voltage of 50 kV. The incident beam was focused at the detector with multilayer Montel optics and 2D Kratky block collimator. Small-angle (SAXS) and wide-angle (WAXS) X-ray scattering analyses were performed simultaneously using two position-sensitive linear detectors (Vantec-1, Bruker) set perpendicular to the incident beam direction, up to 7° (2 θ) and at 19° to 28° (2 θ) from it, respectively. The direct beam was stopped with a W-filter. The temperature of the samples was controlled by a Microcalix calorimeter cell (Bruker). Silver behenate and tristearin (β form) were used as standards to calibrate SAXS and WAXS detectors, respectively.

The scattered intensity was reported as a function of the scattering vector:

$$q=4\pi \sin \theta/\lambda \quad (\text{Equation 6.1})$$

where θ is half the scattering angle and λ is the wavelength of the radiation. The d-spacing can be calculated from the scattering vectors:

$$d = 2\pi/q \quad (\text{Equation 6.2})$$

where q is the scattering vector.

Samples for X-ray experiments were contained inside quartz glass capillary tubes (1.5 mm inner diameter) purchased from Glas Müller, Germany. All samples were measured 3 times to ensure repeatability.

2.3.2. Particle size and zeta potential characterization

The particle size and zeta potential at room temperature were determined using Zetasizer Nano ZS90 (Malvern Panalytical Ltd.). LNP suspension was diluted 30 times in NaCl 3 mM solution for measurement. The diluted particle concentration was calculated to be 7 mg/mL. All measurements were repeated 3 times.

2.3.3. Erythromycin and urea dosage by HPLC, encapsulation efficiency and drug loading calculation

To find erythromycin crystals in the LNP suspension, Nikon Eclipse E600 dark-field light microscope was used. A Mightex USB camera attached to the microscope was used to take photos.

The loading and encapsulation efficiency of erythromycin and urea were found using high-performance liquid chromatography (HPLC, Thermo UltiMate 3000 UHPLC system, Thermo Scientific™). The liquid chromatographic conditions for the dosage of erythromycin and urea are described in the paragraph below. The LNP suspension is centrifuged at 40000 rpm, 4°C for 16 hours using an ultracentrifuge (Optima L-90K, Beckman Coulter), with the rotor 70.1 Ti to separate the liquid part (supernatant) and the solid part (precipitate). The quantity of erythromycin and urea in the supernatant is considered non-encapsulated, while the quantity of erythromycin and urea in the precipitate is considered encapsulated. To prepare the sample for HPLC, the supernatant was diluted by 2 in acetonitrile (ACN) and filtered through a 200 nm syringe filter. The precipitate was mixed with the solution ACN : H₂O (1:1), heated at 60°C to melt the lipid, agitated for 5 minutes and then cooled down at room temperature. The cooled solution was then filtered through the 200 nm syringe filter. The percentage of erythromycin inside lipid particles, drug loading, encapsulation efficiency were calculated as below:

$$\text{Percentage of drug inside particles} = \frac{\text{Quantity API}_{\text{precipitate}}}{\text{Quantity API}_{\text{precipitate}} + \text{Quantity API}_{\text{supernatant}}} \quad (\text{Equation 6.3})$$

$$\text{Encapsulation efficiency (EE)} = \frac{\text{Quantity API}_{\text{precipitate}}}{\text{Quantity API}_{\text{Input}}} \quad (\text{Equation 6.4})$$

$$\text{Drug loading (mg API per gram of lipid)} = \frac{\text{Quantity API}_{\text{precipitate}}}{\text{Mass of lipid}} \quad (\text{Equation 6.5})$$

The dosage of erythromycin was adapted from the literature with some modifications [17]. We used a 150 x 4.6 mm I.D YMC-Triart C18 column (particle size of 3 μm and pore size of 12 nm). The mobile phase was acetonitrile (ACN) : 8 mM K_2HPO_4 solution in water at pH 9 (1:1) and flowed at 1 mL/min in the isocratic condition. The temperature of the column was kept at 50°C. The detection wavelength was 210 nm. The injection volume of samples was 20 μL . In running conditions, the stable pressure was 147 bar. Erythromycin retention time was 14 minutes. The running time was 30 minutes to be able to detect degraded products of erythromycin. The limit of detection (LOD) and limit of quantification (LOQ) of erythromycin were 4.1 $\mu\text{g}/\text{mL}$ and 12.3 $\mu\text{g}/\text{mL}$, respectively. After each analytical sequence, the column was rinsed with ACN : H_2O (1:1) for 30 minutes, followed by ACN 100% for 30 minutes and stored in ACN.

The dosage of urea was adapted from the technical note of the column supplier. We used a 250 x 4.6 mm I.D Synergi™ Polar-RP column (particle size of 4 μm and pore size of 8 nm). The mobile phase was 2% ethanol (EtOH) in H_2O and flowed at 0.8 mL/min in the isocratic condition. The temperature of the column was kept at 22°C. The detection wavelength was 202 nm. The injection volume of samples was 20 μL . In running conditions, the stable pressure was 124 bar. The urea retention time was 3.86 minutes. The running time was 10 minutes, to get rid of any contamination that may have in the sample. The LOD and LOQ were 3.4 $\mu\text{g}/\text{mL}$ and 10.4 $\mu\text{g}/\text{mL}$, respectively. The column was rinsed for 30 minutes and stored in ACN : H_2O (65:35). In the case of samples having both erythromycin and urea, to avoid the possible accumulation of erythromycin in the column after each injection, we used a gradient flow condition to flush erythromycin out after each injection. The condition was 0-10 minute: 2% EtOH in H_2O , 0.8 mL/min; 10-24 minutes: 100% ACN, 1 mL/min; 24-30 minutes: 2% EtOH in H_2O , 0.8 mL/min. The first step is to dose urea. The second step is to flush out erythromycin, which is highly soluble in ACN. The last step is to recondition the column for the next injection.

2.3.4. Cryogenic transmission electron microscopy (Cryo-TEM) imaging

The dispersions were diluted in water in order to reach a lipid concentration of around 5 mg/mL. 4 μL were deposited on a 200-mesh holey carbon-coated grid. After blotting with filter paper, the grid was frozen by fast plunging in liquid ethane and was inserted in the microscope using a nitrogen-cooled side entry Gatan 626 cryo-holder at a temperature of -178 °C. Observations were carried out in a Thermo Fisher Titan Themis 300 transmission electron microscope using an accelerating voltage of 300 kV.

2.4. Fabrication process of lipid nanoparticles – chitosan (LNP-C) nanocomposite

The obtained LNP after the HPH process was centrifuged at 40000 rpm, 4°C for 16 hours using an ultracentrifuge (Optima L-100K, Beckman Coulter), with the rotor 70.1 Ti to collect the lipid particles in the precipitate and eliminate non-encapsulated drugs in the aqueous phase (supernatant). The collected precipitate pellet of lipid particles was then redispersed in chitosan solution (0.05 wt% in acid acetic 0.1% v/v). The pH after the addition of chitosan solution was 7, thanks to the presence of buffer solution added during the LNP fabrication described above. The neutral pH prevented the degradation

of erythromycin during the redispersion step. The interaction between chitosan and negative charges of particles jellified the suspension, creating a composite between lipid particles and chitosan. The mixture was frozen and lyophilized at 94 mTorr, the condenser temperature was -90.6°C (freeze drier Cryotec Cosmos-80) to obtain the lipid particles - chitosan nanocomposite.

2.5. Physico-chemical characterization of LNP-C nanocomposite

2.5.1. Lipid structure characterization

The crystal structure of the LNP-C nanocomposite was determined by the small- and wide-angle X-ray scattering technique (S-WAXS) using the Bruker MicroCalix machine. To study the hydration behavior of the nanocomposite, it was mixed with water at different hydration rate. The structure of the hydrated nanocomposite sample was measured by S-WAXS using the Bruker MicroCalix machine. The details about the machine have been explained above.

2.5.2. Urea and erythromycin loading determination

The urea and erythromycin loading of the LNP-C nanocomposite was determined by HPLC. The liquid chromatography condition was described above. To prepare the sample for HPLC, in general, 60 mg of the LNP-C nanocomposite powder was dispersed in 5 mL of ACN : H₂O (1:1). The suspension was heated at 60°C for 5 minutes to ensure the melting of the lipid powder. The suspension was then filtered through a 200 nm syringe filter. The drug loading is calculated as Equation 6.4.

2.5.3 Acquisition of the synchrotron radiation computed microtomography (SR μ CT) dataset

SR μ CT measurements were conducted at the SYRMEP beamline of Elettra using a multi-scale approach [18]. At SYRMEP the X-ray beam is delivered by a bending magnet source and experiments were performed in a filtered white-beam configuration (filters: 1.5 mm Si + 0.025 mm Mo) with a mean energy of ~27 keV (estimated entrance dose of the order of kiloGray). Projections were recorded with a microscope camera based on a 16-bit, water-cooled sCMOS detector (2048 × 2048 pixels) coupled to a 15 μ m-thick LSO:Tb scintillator screen. Using the optical zoom of the detecting system, the effective pixel size of 0.9 μ m was set corresponding to a field of view of about 1.8 × 1.8 mm.

For each scan, we acquired 1800 projections over a 180° rotation with an exposure time/projection of 500 ms. The experiment was conducted in propagation-based phase-contrast mode with the sample-to-detector distance set to 150 mm for all measurements. The slice reconstruction was carried out using the custom-developed SYRMEP Tomo Project (STP) software. Before reconstruction, a ring-removal algorithm was applied. Then, projections were processed by a single-distance phase-retrieval algorithm with a δ/β parameter (ratio between the real and imaginary parts of the refraction index of the material $n = 1 - \delta - i\beta$) chosen on an ad hoc basis for a good

visualization of fine details in the tooth enamel balancing between contrast and spatial resolution. In our case, the δ/β ratio was set to 100.

2.6. *In vitro* release studies of LNP-C nanocomposite

The release of erythromycin and urea from the LNP-C nanocomposite in simulated gastric fluid (SGF) pH5 was determined. The recipe of the medium was adapted with some modifications from the literature [19]. The SGF pH5 medium simulates the state of the stomach in the middle-fed state [19]. We however removed milk from the SGF pH5 recipe, since we wanted to investigate the effect of pH on the release properties of LNP-C nanocomposite. The SGF pH5 medium contained CH_3COOH (17.12 mM), CH_3COONa (29.75 mM) and NaCl (237.02 mM). The pH was adjusted to be 5.

To study the release of urea and erythromycin from the nanocomposite, in general, about 200 mg of LNP-C composite powder was redispersed in 10 mL SGF pH5. The quantity of composite powder was calculated to make sure the maximum concentration of erythromycin released to the medium was 0.4 mg/mL (much lower than the saturation concentration of erythromycin in water of 2 mg/mL). The flask was agitated at 75 rpm, 37°C. At each time point, 100 μL of the solution was taken, rapidly neutralized by 100 μL of phosphate buffer pH 7.2 (containing 50 mM K_2HPO_4 and 50 mM KH_2PO_4). The use of potassium salt was to precipitate SDS [16], hence promoting the aggregation of lipid nanoparticles and free SDS. Without the step of precipitation of nanoparticles, the amount of erythromycin and urea may be overestimated due to the presence of nanoparticles in the solution. The neutralized solution was then filtered through a syringe 200 nm filter to eliminate all precipitated particles. We mixed 100 μL of filtered neutralized solution with 100 μL of ACN, and filtered the mixture through a 200 nm syringe filter to get rid of any precipitation that may occur. This dilution in ACN step was to ensure that there would not be any precipitation in the column after the injection of samples.

To study the release of particles from the LNP-C nanocomposite to the medium, in general, about 300 mg of LNP-C composite powder was redispersed in 15 mL SGF pH5. The flask was agitated at 75 rpm, 37°C. At each time point, 1 mL of sample was taken and filtered through a 5 μm syringe filter to get rid of big pieces of powder that may have in the solution. The filtered suspension was inserted in the Zetasizer Nano ZS90 (Malvern Panalytical Ltd.) to measure the derived count rate, which was the scattered light intensity and proportional to the number of particles and the hydrodynamic size of particles.

To see the morphology of nanoparticles released from the nanocomposite in SGF pH5, we dispersed the nanocomposite without chitosan (named PEU-C0) in SGF pH5 at 37°C, 75 rpm. After 30 minutes, 2 mL of the solution was taken and filtered through a 5 μm syringe filter. The filtered sample was then deposited on a 200-mesh holey carbon-coated grid for Cryo-TEM. The grid was frozen by fast plunging in liquid ethane and was inserted in the microscope using a nitrogen-cooled side entry Gatan 626 cryo-holder at

a temperature of $-178\text{ }^{\circ}\text{C}$. Observations were carried out in a Thermo Fisher Titan Themis 300 transmission electron microscope using an accelerating voltage of 300 kV.

2.7. Antimicrobial and chemoattraction property studies of LNP-C nanocomposite

The minimum inhibitory concentration required to inhibit the growth of *H. pylori* (MIC) of LNP-C nanocomposite was determined by the agar dilution method, which is recommended for the MIC test of *Helicobacter* species [20]. In general, 80 mg of LNP-C nanocomposite powder was resuspended in 3 mL of DI water and used as the mother solution for the dilution. A desired volume of the suspension was then mixed with Mueller Hinton agar and defibrinated horse blood at 40°C . The mixture was then poured and let solidify in a Petri dish. The final agar concentration and defibrinated horse blood were 8 wt% and 10 % v/v respectively. The range of erythromycin concentration in agar gel used for the MIC test was from $8\text{ }\mu\text{g/mL}$ to $0.06\text{ }\mu\text{g/mL}$. $5\text{ }\mu\text{L}$ of microbial suspension (3-4 McFarland, measured by a nephelometer ATP 1550 API, BioMerieux) was inoculated on the surface of the prepared agar plates. The plates were then incubated in an airtight container containing gas packs (BD GasPak™ EZ Campy Container System) at 35°C . The results were read after 5 days to ensure the growth of bacteria. 9 *H. pylori* strains were used for the MIC test. We used 8 strains obtained from patients in Poitiers University Hospital and the wild-type J99 strain as the reference. Among 8 strains from patients, we had 4 strains resistant to erythromycin and 4 strains sensible to erythromycin.

3. Results and discussion

3.1. Physico-chemical properties and structure of lipid nanoparticles suspension (LNP) and lipid nanoparticles - chitosan nanocomposite (LNP-C)

3.1.1. Structure of LNP

The structure of LNP after each step of fabrication is shown in Figure 6.1. The LNP suspension has a hydrated lamellar structure, whose distance is 12.5 nm. The percentage of cocoa butter was optimized to be fully integrated inside the Montane 60 matrix, so we could not detect any structure of cocoa butter [chapter 4]. Because of the hydrated lamellar distance, urea solution can be loaded inside lipid particles. The lamellar distance of the hydrated lamellar structure of LNP is higher than that of the coarse suspension obtained after ultra-turrax ($d = 11\text{ nm}$, Figure 6.1). The difference in the lamellar distance of hydrated structure before and after HPH is due to the size of the lipid particles. The nanoscale size of LNP allows more positive ions to be adsorbed on the particles' surface, reducing the neutralization effect of positive ions. This effect has been found and discussed in detail in our previous work [Chapter 5]. In both cases, the hydrophobic lamellar structure of Montane 60 at around 1.2 nm^{-1} was still found [Chapter 5]. The WAXS region shows that LNP suspension has hexagonal alpha ($\text{H-}\alpha$) arrangement of lipid chains, similar to Montane 60 (single peak at 15.1 nm^{-1}) [Chapter 5], indicating that the lipid particles are indeed solid. The solid, hydrated lamellar structure of LNP is called the α -gel structure [21]. After the ultra-centrifugation to

eliminate non-encapsulated drugs, the obtained LNP pellet still had a hydrated lamellar structure, with a distance of 10.8 nm. Although the reduction of the lamellar distance of LNP after centrifugation signifies the loss of water, the dehydration effect is small. There is still a significant amount of bound urea solution inside lipid particles.

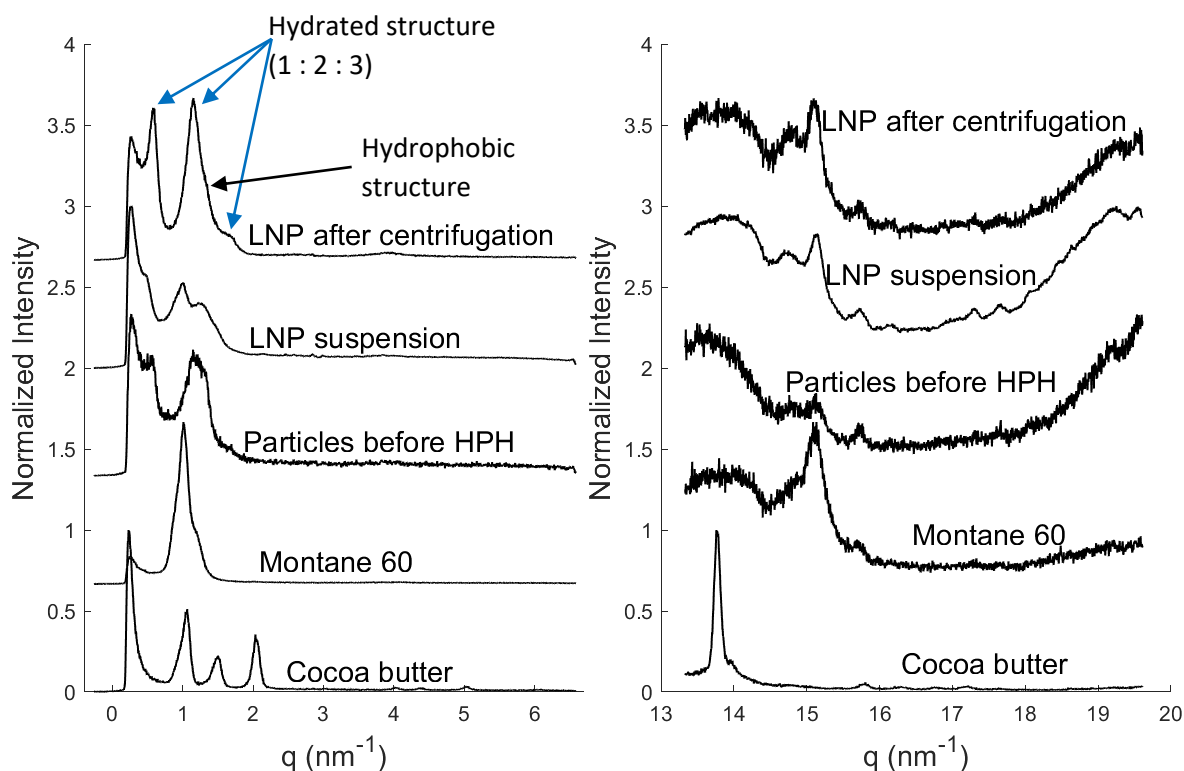


Figure 6.1. The change in the structure of LNP during the fabrication process examined by S-WAXS

Table 6.1 clearly shows the effect of HPH on the size of lipid particles. While the coarse suspension has a size in microscale, the LNP suspension has a size of around 485 nm. We observed that the encapsulation of erythromycin made the zeta potential less negative. In pH7, erythromycin is charged positively due to its pKa value from 8.6 – 8.9 [22]. The protonated erythromycin interacts with the negative charges of LNP, making the particles less negative. The small negative charges of LNP-E1% cannot stabilize well the suspension like in the case of blank LNP-E0%, probably leading to the aggregation of 485 nm. The electrostatic interaction between erythromycin and negatively charged lipid may indicate that erythromycin molecules are located on the lamellar surface of LNP.

Formulation	Zeta potential (mV)	Size (nm)	PDI
LNP-E1% before HPH	-21	2300	1
LNP-E1%	-22	485	0.28
LNP-E0%	-70	125	0.26

Table 6.1. Size and zeta potential of LNP in suspension (having 1 wt% erythromycin, in comparison to blank particles having 0 wt% erythromycin)

We used cryo-TEM to observe the nanoparticles in the dilution condition, which is close to the state of particles after administration in the stomach. Cryo-TEM image has low contrast, thin, disk-like particles, with a size smaller than 100 nm. We can see different orientations of nanodisks in Figure 6.2, from the round faces to thin edges. These disks may be one lamellar layer from the lamellar structure particles. With the high lamellar distance of particles shown in Figure 6.1, the attraction force between 2 lamellar layers (mainly hydrophilic interaction) is reduced significantly. Under dilution and agitation effects, these layers can easily fall out of the lamellar structure and become single-layer disks. In dilution with water for cryo-TEM, the effect of salts and pH in the stomach is however not the same. The presence of salt and acidic pH in the stomach may limit the expansion of the lamellar structure.

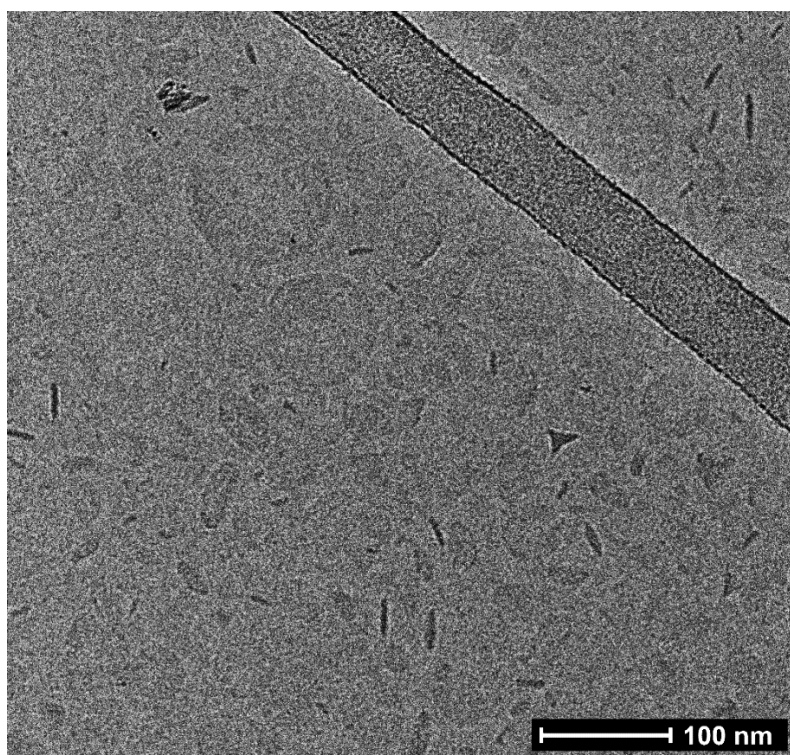


Figure 6.2. Cryo-TEM image of LNP-E1% in dilution condition. The nanoparticles do not contain chitosan.

3.1.2. Erythromycin loading optimization in LNP

While urea is soluble in the water phase between lamellar layers of LNP, the loading of erythromycin is more complicated. We may check the solubility of erythromycin in the melted lipid phase; however, it would change when the lipid particles solidify at room temperature. Erythromycin was loaded inside the particles by simply solubilizing it in the melted lipid phase during the suspension fabrication process. Even if erythromycin was totally soluble in the melted lipid phase (determined by optical microscopy, described in chapter 4), the recrystallization of erythromycin might occur when the lipid particles crystallize. To find the drug loading and encapsulation efficiency value, we used ultra-centrifugation methods to separate the solid particles and the aqueous phase. We had to make sure that there was no drug crystal in the suspension, since it

may be in the pellet part after centrifugation, along with lipid particles. So, we tried to find erythromycin crystals by observing LNP loaded with erythromycin under a dark field microscope. The samples were not diluted, because the dilution might solubilize erythromycin crystals, or create more crystals due to the decrease in the concentration of SDS in the solution. Because of the nano-size, the nanoparticles cannot be observed by a normal light microscope. In the dark field, we can observe scattered light from nanoparticles, which appear as blinking light dots. Without cocoa butter, the erythromycin-loaded suspension was jellified, which appeared to be solid pieces of amorphous materials under polarized light microscopy and S-WAXS. We believe there is an electrostatic interaction between positively charged erythromycin and negatively charged fatty acid or SDS. This interaction connects particles, SDS in the solution, and free erythromycin together, forming a gel network. The addition of cocoa butter helps to prevent the gelation of the suspension, by increasing the hydrophobicity of the lamellar structure and reducing the charged area of particles. Figure 6.3 shows the saturation point of erythromycin in lipid particles. From 2 wt% of erythromycin in the formulation, erythromycin crystals in platelet shape started to form. Therefore, we chose the percentage of erythromycin in the formulation to be 1 wt%.

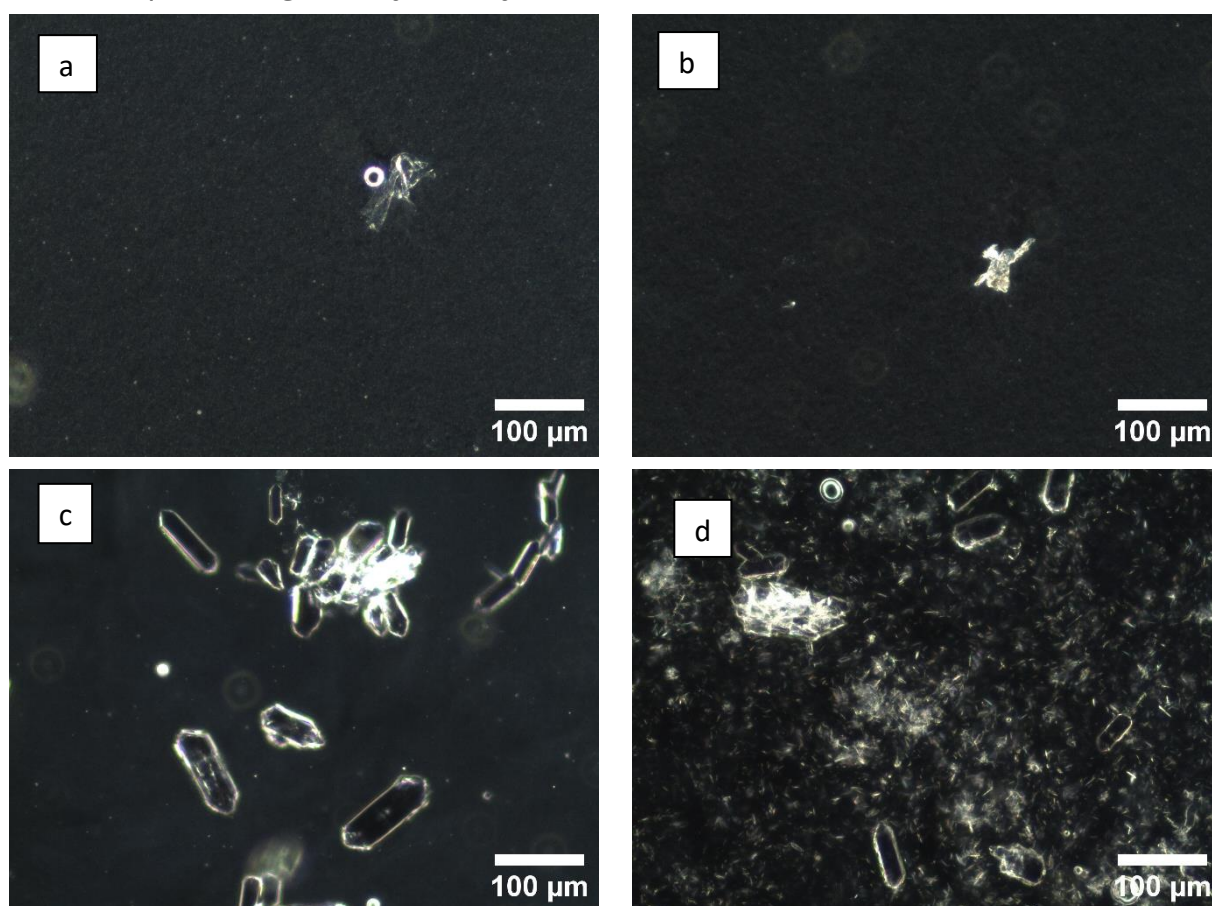


Figure 6.3. LNP loaded with erythromycin under a dark field optical microscope, the percentage of erythromycin in the formulation is (a) 0.5 wt%, (b) 1 wt%, (c) 2 wt% and (d) 4 wt%. The percentage of lipid in the formulation is 20%, the samples were not diluted. The large particles in figures a and b are dust.

Because there are not any chemical bonds between erythromycin and lipid particles, erythromycin can diffuse to the aqueous phase due to its slight solubility in water (approximately 2 mg/mL, determined by HPLC, agreed with the literature [23]). Under the presence of surfactant, the solubility of erythromycin in water increases significantly [24]. In the fabrication process, SDS was used as the surfactant to stabilize lipid particles. SDS is an amphiphilic molecule and can solubilize in both lipid and aqueous phases. Since there is an amount of SDS in water, it may facilitate the solubilization of erythromycin in the water phase, reducing the amount of drug loaded in lipid particles. Therefore, it is important to separate the aqueous phase and lipid particles by ultra-centrifugation to dose separately the amount of erythromycin in each phase. From the dosage, drug loading and encapsulation efficiency can be obtained. We have found that after mixing the lipid phase with the water phase by ultra-turrax to obtain the coarse suspension, the concentration of erythromycin in the aqueous phase was very high (around 7.6 mg/mL, Table 6.2). It may be due to the formation of SDS micelle in the aqueous phase [24]. The use of HPH reduced the size of lipid particles to the nanoscale, leading to an increase in the specific surface area. The high surface area made more room for the adsorption of SDS onto the surface of lipid particles, reducing the amount of SDS in the aqueous phase. The lower concentration of SDS in the aqueous phase reduced the solubility of erythromycin in the aqueous phase to around 2.4 mg/mL (Table 6.2). From the amount of erythromycin in the aqueous phase and in the lipid phase, we can calculate the percentage of erythromycin inside lipid particles, which is 24.2% for lipid particles before HPH and 73.4% for LNP. So, HPH plays an important role in the incorporation of erythromycin inside lipid particles. After HPH, the drug loading capacity increased from 10.5 to 28.2 mg erythromycin/g lipid (Table 6.2). The drug encapsulation efficiency is calculated from the amount of erythromycin inside lipid particles in comparison with the amount of erythromycin input. The encapsulation efficiency of lipid particles before HPH and LNP are 21.2% and 56.4%, respectively. The encapsulation efficiencies are smaller than the values of the percentage of erythromycin inside particles, indicating a quantity of erythromycin has been lost during the fabrication process. While erythromycin was not degraded due to heat, an amount of erythromycin (around 10% – 20%, determined from different batches of LNP) may be retained on the shaft of the ultra-turrax and inside the HPH machine.

Formulation	ERY concentration in aqueous phase (mg/mL)	% ERY inside particles (%)	Drug loading (mg/g lipid)	Encapsulation efficiency (%)
LNP – E1% before HPH	7.6 ± 0.05	24.2 ± 3.3	10.5 ± 0.8	21.2 ± 2.8
LNP – E1%	2.4 ± 0.02	73.4 ± 2.1	28.2 ± 0.3	56.4 ± 1.4

Table 6.2. Dosage of erythromycin inside and outside lipid particles, drug loading and encapsulation efficiency of LNP-E1% (LNP suspension having 1 wt% of erythromycin) before and after HPH, the errors are the standard deviation of measurements from 3 samples.

To summarize the loading behavior of erythromycin in the lipid particle suspension during the fabrication, we propose that there is an equilibrium of SDS and erythromycin in the lipid suspension (Figure 6.4). While SDS can integrate inside and on the surface of the lipid particles, SDS also forms micelles in the solution when the SDS concentration reaches the CMC. For erythromycin, while the amount of free erythromycin in solution is small (saturated at around 2 mg/mL), the amount of erythromycin in SDS micelles can be very high, depending on the SDS concentration [24]. When the SDS concentration in solution increases above the CMC, micelles are created, facilitating the solubility of erythromycin in solution and reducing the amount of erythromycin in lipid particles. By using HPH, the size of lipid particles decreases, and the specific surface area of the lipid particles increase, providing more area for the adsorption of SDS molecules. The increase in the adsorption of SDS on lipid particles reduces the concentration of SDS in the solution, hence reducing the amount of erythromycin in the solution. Therefore, by reducing the size of the particles, we reduced the concentration of SDS and erythromycin in the solution and increased the amount of erythromycin loaded inside lipid particles.

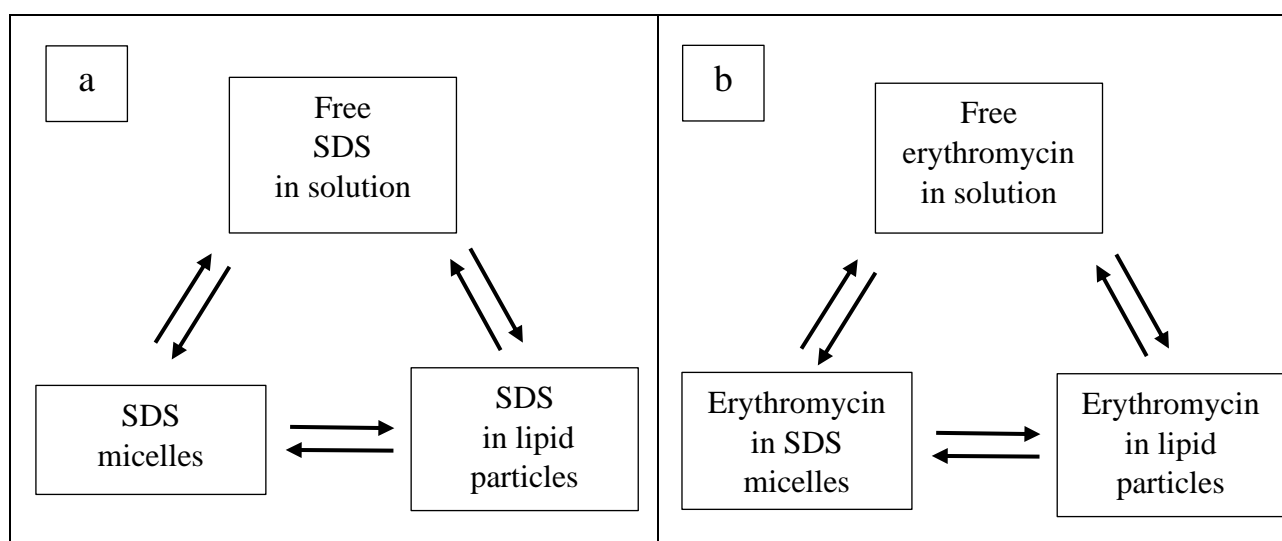


Figure 6.4. Equilibrium of (a) SDS and (b) erythromycin in lipid particle suspension during the fabrication, when lipid mixture is in liquid form.

3.1.3. Structure and properties of LNP-C

The structure of the lipid nanoparticles – chitosan (LNP-C) nanocomposite powder containing both erythromycin and urea (PEU-C5 in short) can be analyzed in Figure 6.5. In the SAXS region, PEU-C5 has a lamellar structure. Interestingly, the lamellar distance of PEU-C5 (5.7 nm) is slightly smaller than that of Montane 60 (6.3 nm). This effect was also observed in the mixture of Montane 60 and SDS without water. The introduction of SDS induces stress on the lamellar structure of Montane 60 due to the difference in the packing parameter between SDS and sorbitan monostearate molecules. The stress in the structure may cause the tilt of lipid chains, leading to a tilt angle of about 25° (calculated from the lamellar distance in Figure 6.5) and decreasing the lamellar distance. The spectra in the WAXS region show that PEU-C5 has hexagonal alpha (H- α) arrangement of lipid chain, similar to Montane 60. We also detected two peaks of urea, indicating that we have urea crystal outside of the lipid powder. After 1 month, the structure of PEU-C5 was still unchanged, indicating the high stability of the structure. In addition, it shows that cocoa butter was well integrated inside the Montane 60 lipid matrix; otherwise, we should have a beta peak of cocoa butter stable form in WAXS [25].

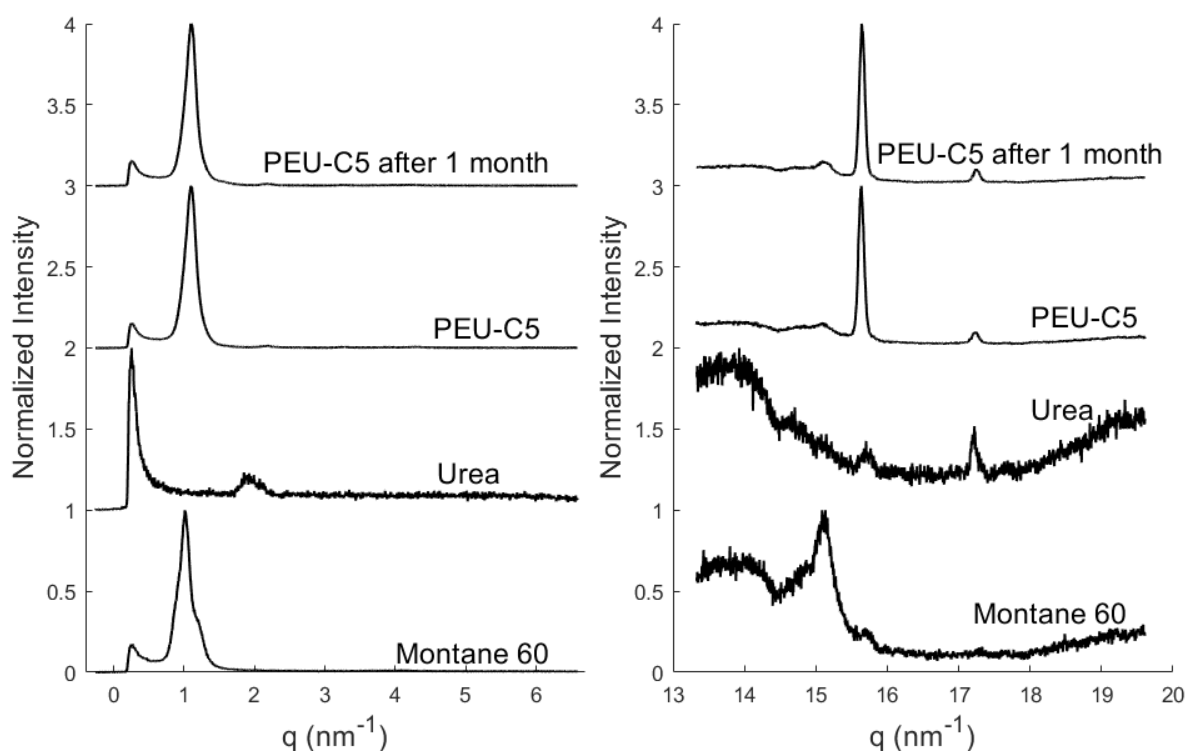


Figure 6.5. S-WAXS spectra of lyophilized powder of solid lipid particles - chitosan nanocomposite containing both erythromycin and urea (PEU-C5)

The morphology of LNP-C was examined using SR μ CT. The technique gave us images of the internal structure of the lyophilized powder. By examining several slices of the sample, we discovered that the LNP-C lyophilized powder is highly porous, with different pore sizes in the micrometers range (Figure 6.6). The formation of the porous

structure may be similar to the mechanism of fabrication of cryogel by lyophilization described in the literature [26]. The sublimation of water crystals has left pores with irregular size. The high porosity of the powder may increase the rehydration of the powder and facilitate the drug release

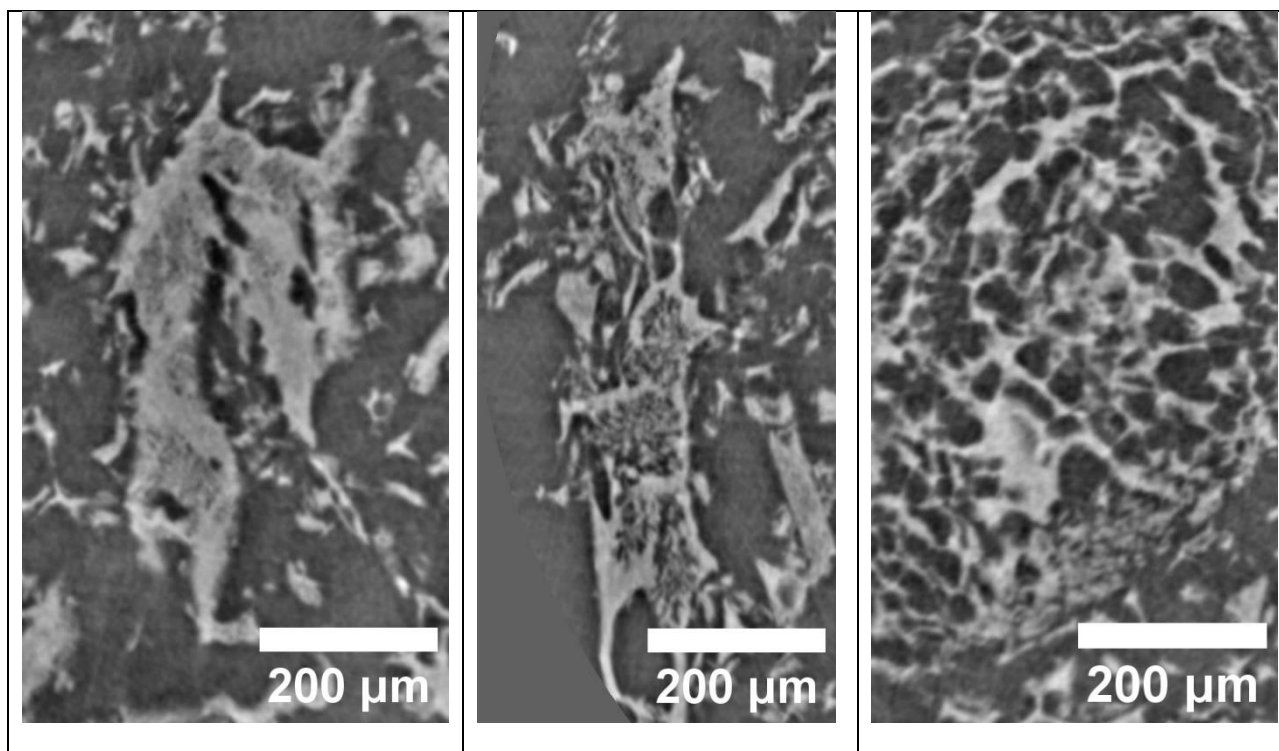


Figure 6.6. The SRμCT images of LNP-C powder show the high porosity with different pore sizes.

3.2. Drugs and particles release profile of LNP-C nanocomposite *in vitro*

To test the release behavior of the LNP-C nanocomposite PEU-C5 *in vitro*, we used SGF pH5 as a simulation of the middle-fed state of the stomach [19]. The release of small particles was followed by the derived count rate from the DLS experiment (Figure 6.7). The particle size in the graphs is only the average value calculated from the raw correlation function. From the increase in derived count rate over time, we can see that the particles were released over time from the powder. In addition, the overall size of particles found in the solution increased over time. In fact, the phenomenon is complicated and may include the release of particles of different sizes and the aggregation of particles. Moreover, the powder may release large aggregation particles (> 5 microns in diameter), which are eliminated by the filter when the samples are taken for measurement. After 4 hours, we still had the release of particles, indicating that the release was sustainable for a very long time. The slow release of particles and aggregation of particles is favorable for our application. In the stomach, the powder will be attached to the mucus layer thanks to chitosan. Then, lipid particles will be released slowly to the mucus layer, stick there and continue to release drugs to attract and eliminate the bacteria.

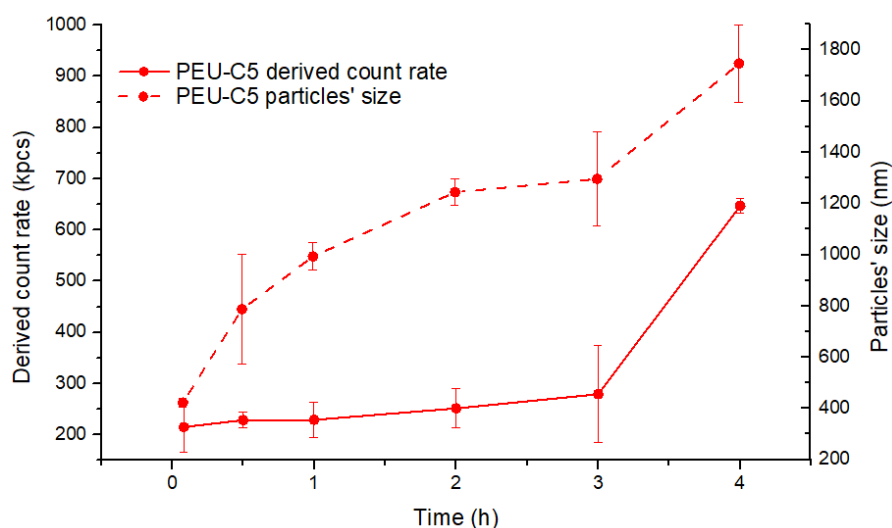


Figure 6.7. The release of particles from lipid nanoparticles - chitosan nanocomposite PEU-C5 in SGF pH5

Lipid nanoparticles are released slowly over time because the PEU-C5 powder is in the form of dry particle aggregation. The particles' size released from the powder was still in the range of the particles' size before lyophilization. In addition, the lipid crystalline structure was still preserved after lyophilization (Figure 6.5). It may be due to the cryoprotectant effect of urea loaded inside lipid particles and chitosan [27–29]. As discussed by Pham et al. [27], urea may have an interaction with the hydrophilic head groups and replaces water under dehydration conditions. The strategy of using urea as a cryoprotectant is in fact applied in nature by some animals, helping them to hibernate through freezing winter [30]. Chitosan can also be used as a cryo-protectant for protein during frozen storage [29].

To see the morphology of nanoparticles released from the lyophilized formulation in SGF pH5, we dispersed the nanocomposite without chitosan (PEU-C0) in the same condition. The cryo-TEM image of the released nanoparticles is in Figure 6.8. Since this formulation does not contain chitosan, all the observed particles are from the lipid formulation. In Figure 6.8a, we can see that the nanoparticles have a size of around 50 – 100 nm and they indeed tend to aggregate as proposed above. Figure 6.8b shows that the particles have porous matrices, with water inside the lipid structure, however, without any clear orders. The porous structure of lipid nanoparticles may contain urea solution and regulate the release of urea solution. The shape of the particles is similar to the shape of the reported emulsified microemulsion in the literature [31,32]. However, in the literature, emulsified microemulsion has a disordered structure and is made from lipids in the liquid state, such as monoolein.

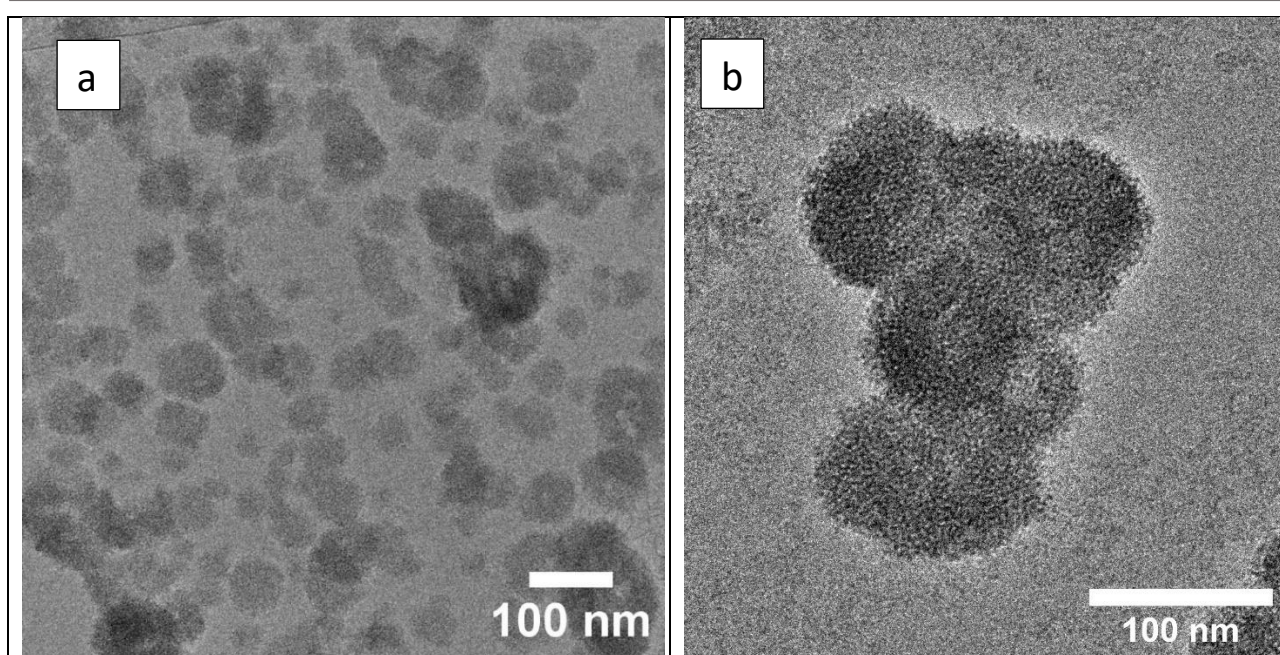


Figure 6.8. (a) Cryo-TEM image of nanoparticles released from nanocomposite without chitosan (PEU-C0) after 30 minutes in SGF pH5 and (b) the internal structure of an aggregation of nanoparticles

In Figure 6.9, we hydrated the nanocomposite PEU-C0 in SGF pH5 to investigate its hydrated structure in SGF pH5. In the SAXS region, the hydrophilic structure peak of PEU-C0 shifted to the left when the nanocomposite was hydrated, indicating that water entered the lamellar structure. Interestingly, this behavior is similar to the swelling properties we observed at the macroscale with the Montane 60 grains (chapter 5). The lamellar distance at 30%, 60% and 80% hydration rates were however similar, indicating that above a threshold, the dilution does not have any effects on the water incorporation into the lamellar structure. This strongly suggests that the structure observed with cryo-TEM is not altered by the high dilution we made. Unfortunately, we could not confirm that with our lab SAXS-WAXS apparatus as the signal is too low. In the WAXS region, all samples, regardless of the hydration rate, has the H- α structure. In the anhydrous sample, there are 2 peaks of urea crystals in WAXS, which were dissolved in water in hydrated samples. Therefore, we may conclude that the nanoparticles released to the SGF pH5 medium were α -gel nanoparticles, which had water inside the structure.

While we obtained nanoparticles from LNP-C formulation (PEU-C5) in a similar experiment, the concentration of nanoparticles after 30 minutes was not enough for cryo-TEM. We did not observe anything in cryo-TEM.

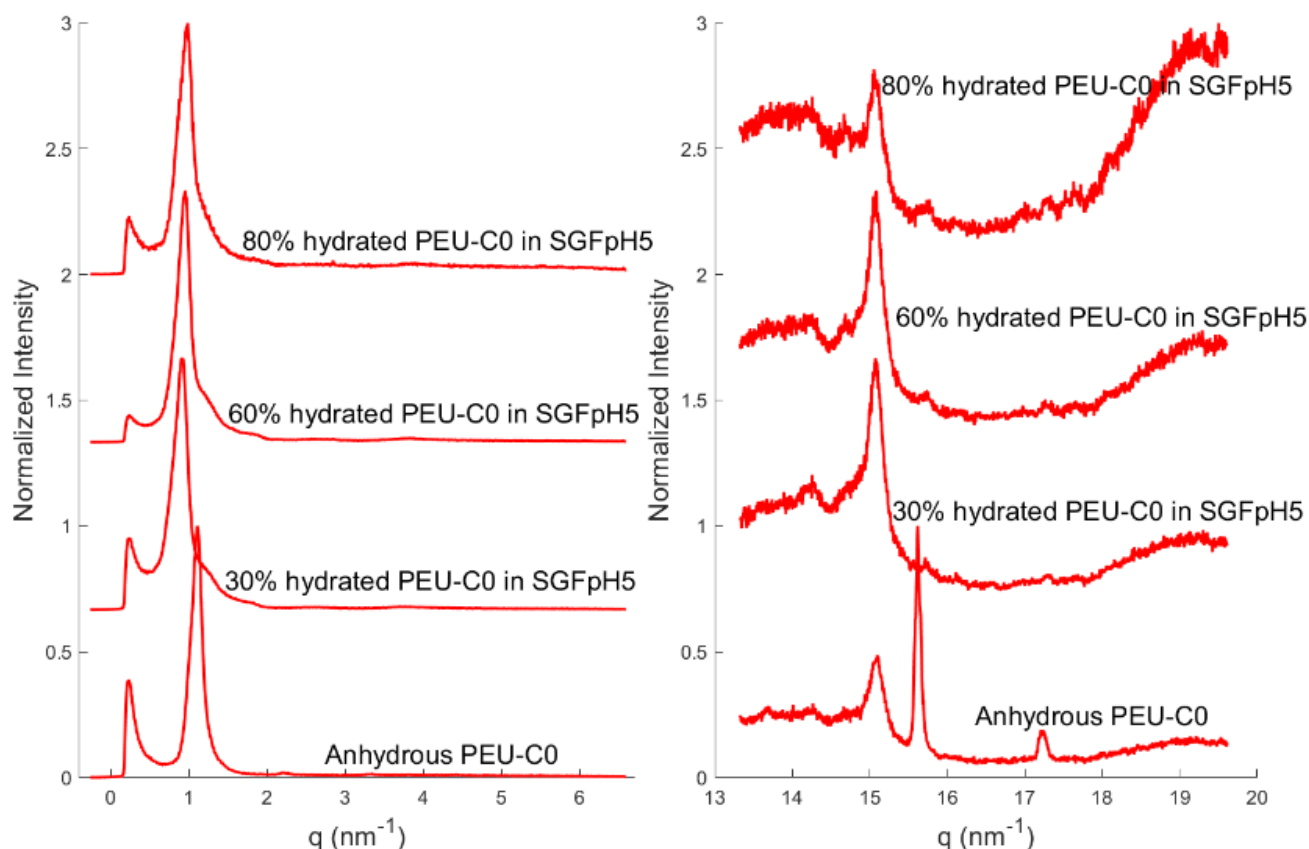


Figure 6.9. The hydration behavior of PEU-C0 in SGF pH5

After dosing the concentration of urea and erythromycin in the SGF pH5 solution over time, we obtained the drug release curve (Figure 6.10). For the release of erythromycin, an erythromycin solution was used as a control. We can see that in SGF pH5 at 37°C, erythromycin was degraded slowly over time because of its instability in acid (blue curve) [31–33]. About the release of erythromycin from PEU-C5 (black curve), initially, there was a burst release of 20% erythromycin after 5 minutes. The release of erythromycin peaked after 15 – 30 minutes, then decreased slowly over time. This behavior is from the combination of the release rate and the degradation rate of erythromycin. At the time point 4h, we dosed the total amount of erythromycin released into the solution and left inside PEU-C5. We detected the same amount of erythromycin as in the case of control (erythromycin from erythromycin solution) after 4h. It means that the powder formulation could not protect the erythromycin from acid. It is reasonable since the LNP-C nanocomposite has a lamellar structure and can swell into the α -gel structure, which allows water and H^+ to penetrate rapidly. In addition, erythromycin may locate on the surface of each lamellar layer, facilitating its interaction with acid. However, after 4h, there was 12% of erythromycin left inside PEU-C5, indicating the role of an erythromycin reservoir of PEU-C5. PEU-C5 may stay locally in the stomach due to the mucoadhesive property of chitosan and continue to release erythromycin for more than 4h.

For the release of urea, using urea solutions as the control for the release of urea (green curve), 100% of the urea solution was in the solution after 5 minutes. We did not detect the degradation of urea in SGF pH5. From the powder PEU-C5, 60% of urea was released immediately after 5 minutes (red curve). This amount of urea may come from unbound urea crystals detected in Figure 6.5. Urea was then released sustainably over time for up to 3-4 hours.

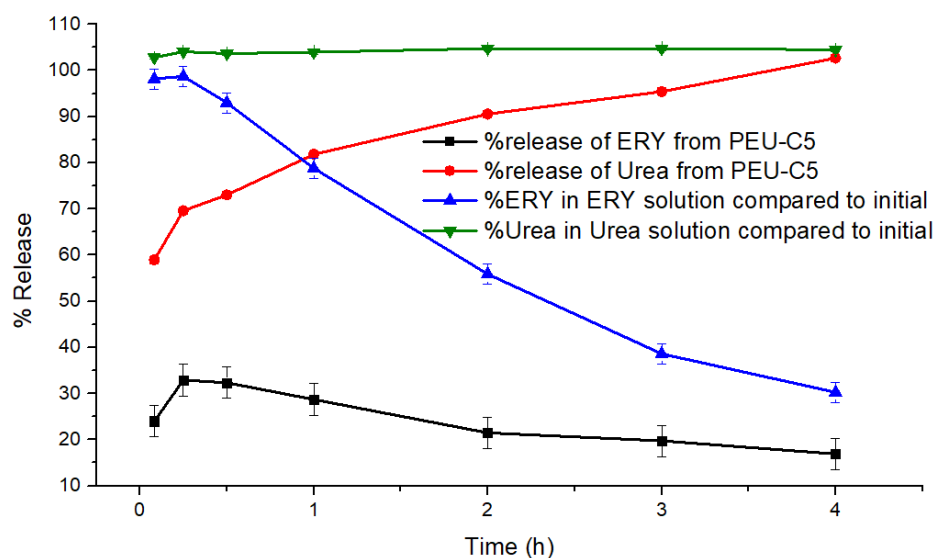


Figure 6.10. The release of erythromycin and urea from lipid particles - chitosan nanocomposite PEU-C5 in SGF pH5

It is very interesting that while water could access rapidly into the lamellar structure to degrade erythromycin, the urea release rate was not very rapid, despite urea's high solubility in water. This fact suggests an interaction between urea and the hydrophilic head of lipids, which hinders the release of urea into the solution. The replacement of water by urea on the hydrophilic head of lipid during dehydration as discussed by Pham et al. [27] may contribute to the formation of interaction between urea and lipid after the lyophilization step. The reduction in lipid swelling capacity due to the effect of salt concentration and pH may also contribute to the sustainable release rate of erythromycin and urea. As discussed in our previous work [Chapter 5], the presence of salts and acid may neutralize electrostatic charges in Montane 60, leading to a low hydration rate. In SGF pH5, the lipid particles may become more compact, reducing the diffusion rate of erythromycin and urea from the particles to the solution. Lastly, we also examined the release rate in the absence of chitosan coating, which did not affect the release rate of erythromycin and urea. Probably because the content of chitosan in the formulation is too small.

3.3. Antimicrobial and chemoattraction properties of LNP-C

We examined the antimicrobial properties of 6 LNP-C nanocomposite formulations to control the effect of chitosan, urea, and erythromycin. The loading value of erythromycin and urea was found using HPLC. The loading value of chitosan was calculated from the volume of chitosan added to the lipid particle pellet before

lyophilization. We used 9 *H. pylori* strains, which were the wild-type strain J99 and 8 others obtained from patients in Poitiers University Hospital (Table 6.3). Among 8 strains obtained from patients, we picked 4 strains resistant to clarithromycin, meaning that they are also resistant to erythromycin. From Table 6.4, we can see that the chitosan coating did not influence the antimicrobial effect. Samples having chitosan have the same MIC value as the samples without chitosan. Blank LNP-C nanocomposite (PB-C0, PB-C5) and LNP-C nanocomposite containing only urea (PU-C0, PU-C5) did not show any antimicrobial activity. In addition, all formulations, even those containing erythromycin, were not effective against the erythromycin-resistant strains. So, the antimicrobial effect of the LNP-C nanocomposite came only from erythromycin. We can conclude that our LNP-C nanocomposite formulation PEU-C5 does have an antimicrobial effect against *H. pylori*, thanks to the encapsulated erythromycin.

From the MIC value of erythromycin in LNP-C, the volume of the stomach, the release rate of LNP-C powder and the hypothesis that all LNP-C powder stays in the stomach during 4h, we can estimate the amount of LNP-C powder needed to maintain the MIC of erythromycin in the stomach for 4h. We use the MIC of erythromycin as 0.06 µg/mL, with the percentage of erythromycin in LNP-C nanocomposite is 1.2 wt%, so the MIC of the LNP-C powder is 0.005 mg/mL. In the release study in SGF pH5, the concentration of erythromycin in the solution was kept at around 20-30% for 4h, so the amount of LNP-C powder needed to maintain the erythromycin concentration in the stomach higher than MIC is $0.005/0.2 = 0.025$ mg/mL. The average volume of the stomach is 25 – 50 mL when empty and 1 – 1.5 L after a meal [34]. Taking the value 1L for the stomach volume, the weight of the LNP-C nanocomposite is $0.025 \times 1000 = 25$ mg. Therefore, with only 25 mg of LNP-C powder, the concentration of erythromycin in the stomach (in fed state pH 5) can be kept above the MIC for 4h, indicating the potential treatment efficiency of the formulation.

Strain	MIC of clarithromycin ($\mu\text{g}/\text{mL}$)	Clarithromycin resistance mutation	Note
2206-131806	<0.016		Sensible to clarithromycin
2206-081192	0.016		Sensible to clarithromycin
2206-220738	<0.016		Sensible to clarithromycin
2206-271989	0.016		Sensible to clarithromycin
J99	<0.016		Wild type, sensible to clarithromycin
2204-130972	>256	A2143G	Resistant to clarithromycin
2203-281091	12	A2143G	Resistant to clarithromycin
2204-130766	16	A2143G	Resistant to clarithromycin
2206-030753	>256	A2142G	Resistant to clarithromycin

Table 6.3. *H. pylori* strains description with data from Poitiers University Hospital

Sample	%Chitosan (wt%)	%Urea (wt%)	%ERY (wt%)	MIC of Erythromycin ($\mu\text{g}/\text{mL}$)								
				2206-131806	2206-081192	2206-220738	2206-271989	J99	2204-130972	2203-281091	2204-130766	2206-030753
PB-C0	0	0	0	Did not show antimicrobial activity								
PB-C5	0.12	0	0									
PU-C0	0	24	0									
PU-C5	0.12	24.7	0									
PEU-C0	0	27.9	1.2	<0.06	<0.06	<0.06	<0.06	<0.06	>8	>8	>8	>8
PEU-C5	0.12	27.4	1.2	<0.06	<0.06	<0.06	<0.06	<0.06	>8	>8	>8	>8

Table 6.4. MIC value of erythromycin in different nanocomposite formulations tested on 9 *H. pylori* strains

4. Conclusion

We have successfully fabricated an LNP-C nanocomposite having an antimicrobial property against *H. pylori in vitro* thanks to the encapsulated erythromycin. The fabrication process is robust with the use of industrial excipients, showing the potential for large-scale production. The LNP-C nanocomposite is lipid nanoparticles incorporated inside a chitosan matrix, giving the formulation the mucoadhesive property. Upon administration, the *in vitro* release study showed the release of lipid nanoparticles, erythromycin, and urea at the same time. The lipid nanoparticles can penetrate the gastric mucus layer, where *H. pylori* hides, and release erythromycin to eliminate them. From our theoretical calculation, the concentration of erythromycin in the stomach can be kept above the MIC for 4 hours by using only 25 mg of LNP-C nanocomposite. Urea loaded inside the LNP-C nanocomposite can be released slowly for 3-4 hours, enabling the ability to chemotactically attract *H. pylori* toward the formulation. However, the experiments on the chemoattraction activity of the formulation are still ongoing.

References

- [1] D.M. Parkin, International variation, *Oncogene*. 23 (2004) 6329–6340.
<https://doi.org/10.1038/sj.onc.1207726>.
- [2] J.K.Y. Hooi, W.Y. Lai, W.K. Ng, M.M.Y. Suen, F.E. Underwood, D. Tanyingoh, P. Malfertheiner, D.Y. Graham, V.W.S. Wong, J.C.Y. Wu, F.K.L. Chan, J.J.Y. Sung, G.G. Kaplan, S.C. Ng, Global Prevalence of *Helicobacter pylori* Infection: Systematic Review and Meta-Analysis, *Gastroenterology*. 153 (2017) 420–429.
<https://doi.org/10.1053/j.gastro.2017.04.022>.
- [3] A. Debraekeleer, H. Remaut, Future perspective for potential *Helicobacter pylori* eradication therapies, *Future Microbiol.* 13 (2018) 671–687.
<https://doi.org/10.2217/fmb-2017-0115>.
- [4] I.F.N. Hung, B.C.Y. Wong, Assessing the risks and benefits of treating *Helicobacter pylori* infection, *Ther. Adv. Gastroenterol.* 2 (2009) 141–147.
<https://doi.org/10.1177/1756283X08100279>.
- [5] WHO publishes list of bacteria for which new antibiotics are urgently needed, (n.d.). <https://www.who.int/news/item/27-02-2017-who-publishes-list-of-bacteria-for-which-new-antibiotics-are-urgently-needed> (accessed September 30, 2022).
- [6] C.-Y. Kao, B.-S. Sheu, J.-J. Wu, *Helicobacter pylori* infection: An overview of bacterial virulence factors and pathogenesis, *Biomed. J.* 39 (2016) 14–23.
<https://doi.org/10.1016/j.bj.2015.06.002>.

- [7] J. Calam, J.H. Baron, ABC of the upper gastrointestinal tract: Pathophysiology of duodenal and gastric ulcer and gastric cancer, *BMJ*. 323 (2001) 980–982. <https://doi.org/10.1136/bmj.323.7319.980>.
- [8] J.Y. Huang, E.G. Sweeney, M. Sigal, H.C. Zhang, S.J. Remington, M.A. Cantrell, C.J. Kuo, K. Guillemin, M.R. Amieva, Chemodetection and Destruction of Host Urea Allows *Helicobacter pylori* to Locate the Epithelium, *Cell Host Microbe*. 18 (2015) 147–156. <https://doi.org/10.1016/j.chom.2015.07.002>.
- [9] E. Garza-González, A review of *Helicobacter pylori* diagnosis, treatment, and methods to detect eradication, *World J. Gastroenterol*. 20 (2014) 1438. <https://doi.org/10.3748/wjg.v20.i6.1438>.
- [10] Y. Tang, G. Tang, L. Pan, H. Zhu, S. Zhou, Z. Wei, Clinical factors associated with initial *Helicobacter pylori* eradication therapy: a retrospective study in China, *Sci. Rep*. 10 (2020) 15403. <https://doi.org/10.1038/s41598-020-72400-0>.
- [11] C. Fung, S. Tan, M. Nakajima, E.C. Skoog, L.F. Camarillo-Guerrero, J.A. Klein, T.D. Lawley, J.V. Solnick, T. Fukami, M.R. Amieva, High-resolution mapping reveals that microniches in the gastric glands control *Helicobacter pylori* colonization of the stomach, *PLOS Biol*. 17 (2019) e3000231. <https://doi.org/10.1371/journal.pbio.3000231>.
- [12] H.V. Nguyen, V. Faivre, Targeted drug delivery therapies inspired by natural taxes, *J. Controlled Release*. 322 (2020) 439–456. <https://doi.org/10.1016/j.jconrel.2020.04.005>.
- [13] I.C. Gonçalves, A. Magalhães, M. Fernandes, I.V. Rodrigues, C.A. Reis, M.C.L. Martins, Bacterial-binding chitosan microspheres for gastric infection treatment and prevention, *Acta Biomater*. 9 (2013) 9370–9378. <https://doi.org/10.1016/j.actbio.2013.07.034>.
- [14] L. Yuan, S. Clevers, N. Couvrat, Y. Cartigny, V. Dupray, G. Coquerel, Precise Urea/Water Eutectic Composition by Temperature-Resolved Second Harmonic Generation, *Chem. Eng. Technol*. 39 (2016) 1326–1332. <https://doi.org/10.1002/ceat.201600032>.
- [15] H. Suzuki, T. Terada, Removal of dodecyl sulfate from protein solution, *Anal. Biochem*. 172 (1988) 259–263. [https://doi.org/10.1016/0003-2697\(88\)90440-X](https://doi.org/10.1016/0003-2697(88)90440-X).
- [16] A. Žilionis, Removal of sodium dodecyl sulfate from protein samples, *Chemija*. 29 (2018). <https://doi.org/10.6001/chemija.v29i4.3835>.
- [17] L.T.C. Tran, Development of nanodispersions based on polyoxylglycerides to protect unstable molecules : Application to *Helicobacter pylori* treatment, These de

doctorat, Paris 11, 2014. <http://www.theses.fr/2014PA114836> (accessed July 15, 2022).

- [18] A. Nava, P. Mahoney, L. Bondioli, A. Coppa, E. Cristiani, L. Fattore, G. McFarlane, D. Dreossi, L. Mancini, Virtual histology of archaeological human deciduous prenatal enamel through synchrotron X-ray computed microtomography images, *J. Synchrotron Radiat.* 29 (2022) 247–253. <https://doi.org/10.1107/S160057752101208X>.
- [19] N. Fotaki, M. Vertzoni, Biorelevant Dissolution Methods and Their Applications in *In vitro- In vivo* Correlations for Oral Formulations~!2009-09-14~!2009-11-02~!2010-04-29~!, *Open Drug Deliv. J.* 4 (2010) 2–13. <https://doi.org/10.2174/1874126601004020002>.
- [20] M. Balouiri, M. Sadiki, S.K. Ibnsouda, Methods for *in vitro* evaluating antimicrobial activity: A review, *J. Pharm. Anal.* 6 (2016) 71–79. <https://doi.org/10.1016/j.jpha.2015.11.005>.
- [21] T. Suzuki, Liquid Crystal and α -gel-Based Emulsion and Soft Gel formulations, *Acc. Mater. Surf. Res.* (2017), Vol.2, No.1, 21-40
- [22] R.C. Goldman, S.W. Fesik, C.C. Doran, Role of protonated and neutral forms of macrolides in binding to ribosomes from gram-positive and gram-negative bacteria, *Antimicrob. Agents Chemother.* 34 (1990) 426–431. <https://doi.org/10.1128/AAC.34.3.426>.
- [23] Z. Wang, J. Wang, M. Zhang, L. Dang, Solubility of Erythromycin A Dihydrate in Different Pure Solvents and Acetone + Water Binary Mixtures between 293 K and 323 K, *J. Chem. Eng. Data.* 51 (2006) 1062–1065. <https://doi.org/10.1021/je0505265>.
- [24] P.A. Bhat, A.A. Dar, G.M. Rather, Solubilization Capabilities of Some Cationic, Anionic, and Nonionic Surfactants toward the Poorly Water-Soluble Antibiotic Drug Erythromycin, *J. Chem. Eng. Data.* 53 (2008) 1271–1277. <https://doi.org/10.1021/je700659g>.
- [25] C. Himawan, V.M. Starov, A.G.F. Stapley, Thermodynamic and kinetic aspects of fat crystallization, *Adv. Colloid Interface Sci.* 122 (2006) 3–33. <https://doi.org/10.1016/j.cis.2006.06.016>.
- [26] I.V. Tyshkunova, D.N. Poshina, Y.A. Skorik, Cellulose Cryogels as Promising Materials for Biomedical Applications, *Int. J. Mol. Sci.* 23 (2022) 2037. <https://doi.org/10.3390/ijms23042037>.

- [27] Q.D. Pham, A. Wolde-Kidan, A. Gupta, A. Schlaich, E. Schneck, R.R. Netz, E. Sparr, Effects of Urea and TMAO on Lipid Self-Assembly under Osmotic Stress Conditions, *J. Phys. Chem. B.* 122 (2018) 6471–6482. <https://doi.org/10.1021/acs.jpcc.8b02159>.
- [28] A. Nowacka, S. Douezan, L. Wadsö, D. Topgaard, E. Sparr, Small polar molecules like glycerol and urea can preserve the fluidity of lipid bilayers under dry conditions, *Soft Matter.* 8 (2012) 1482–1491. <https://doi.org/10.1039/C1SM06273E>.
- [29] S.S. Dey, K.C. Dora, Suitability of chitosan as cryoprotectant on croaker fish (*Johnius gangeticus*) surimi during frozen storage, *J. Food Sci. Technol.* 48 (2011) 699–705. <https://doi.org/10.1007/s13197-010-0197-8>.
- [30] J.P. Costanzo, R.E. Lee Jr, Cryoprotection by urea in a terrestrially hibernating frog, *J. Exp. Biol.* 208 (2005) 4079–4089. <https://doi.org/10.1242/jeb.01859>.
- [31] A. Hassanzadeh, J. Barber, G.A. Morris, P.A. Gorry, Mechanism for the Degradation of Erythromycin A and Erythromycin A 2'-Ethyl Succinate in Acidic Aqueous Solution, *J. Phys. Chem. A.* 111 (2007) 10098–10104. <https://doi.org/10.1021/jp073030y>.
- [32] D.A. Volmer, J.P.M. Hui, Study of erythromycin A decomposition products in aqueous solution by solid-phase microextraction/liquid chromatography/tandem mass spectrometry, *Rapid Commun. Mass Spectrom.* 12 (1998) 123–129. [https://doi.org/10.1002/\(SICI\)1097-0231\(19980214\)12:3<123::AID-RCM126>3.0.CO;2-4](https://doi.org/10.1002/(SICI)1097-0231(19980214)12:3<123::AID-RCM126>3.0.CO;2-4).
- [33] Y. Nakagawa, S. Itai, T. Yoshida, T. Nagai, Physicochemical Properties and Stability in the Acidic Solution of a New Macrolide Antibiotic, Clarithromycin, in Comparison with Erythromycin, *Chem. Pharm. Bull. (Tokyo).* 40 (1992) 725–728. <https://doi.org/10.1248/cpb.40.725>.
- [34] I. Sensoy, A review on the food digestion in the digestive tract and the used *in vitro* models, *Curr. Res. Food Sci.* 4 (2021) 308–319. <https://doi.org/10.1016/j.crfs.2021.04.004>.

IV. GENERAL DISCUSSION AND CONCLUSION

In this section, we will discuss the main points of the project, the milestones that we have finished, and the work that may be interesting to do in the future.

1. About the formulation

Our initial idea of using 2-step emulsification to create w/o/w solid lipid nanoemulsion has been rejected. The important criterion of the method is making a w/o emulsion, in which the water droplet is in nano-size. When using Montane 60 as the lipophilic surfactant, instead of being in nano-size droplets form, water is stabilized in the lamellar structure of Montane 60. In other words, in hydrated Montane 60, water exists in the form of nano-sheets rather than nano-droplets. Taking advantage of the hydration behavior of Montane 60, we change the formulation strategy from w/o/w solid lipid nanoemulsion to α -gel nanoparticles. The fabrication procedure can be simplified to one step of hot HPH, while the formulation still can co-load both hydrophilic and lipophilic drugs.

The chitosan coating step in our project is simple and is not fully developed. We can ensure the interaction between chitosan and lipid particles due to the electrostatic interaction between positively charged chitosan and negatively charged SDS. This interaction acts as a cross-linking method, which may strengthen the stability of chitosan gel in gastric acid. However, the optimization of the amount of chitosan, stability of the chitosan coating in acid, and the mucoadhesive effect of chitosan have not been investigated. Since chitosan hydrogel is commonly used to control the release of urea in agricultural applications [2], we may optimize the percentage of chitosan in the formulation, the molecular weight and the cross-linking method for our application. On the other hand, controlling the jellification behavior of chitosan is difficult in our formulation. Chitosan is only soluble in an acidic solution, in which erythromycin is degraded. So, the pH during the fabrication process must be neutral. Upon the addition of chitosan to the lipid nanoparticles suspension, chitosan is precipitated immediately due to the neutral pH and the electrostatic interaction with SDS.

Montane 60 (M60, sorbitan monostearate) is a very interesting lipid mixture. Firstly, sorbitan monostearate has been widely used in several industries, has high availability and is safe for human health. The monomorphism of components of Montane 60 makes its hydrated structure stable over time, which ensures the stability of encapsulated compounds in the Montane 60. The hydrated α -gel structure can expand very large, increasing the hydrophilic molecules loading capacity. While we can detect the large lamellar distance by SAXS, we lack a visualization characterization result. Freeze-fracture electron microscopy can visualize the extended α -gel lamellar structure (Figure IV.1) [3]. However, the lamellar distance of α -gel structure is sensitive to the

environment, such as ionic strength and pH. So, the fabrication process and the application environments need to be well-defined and studied.

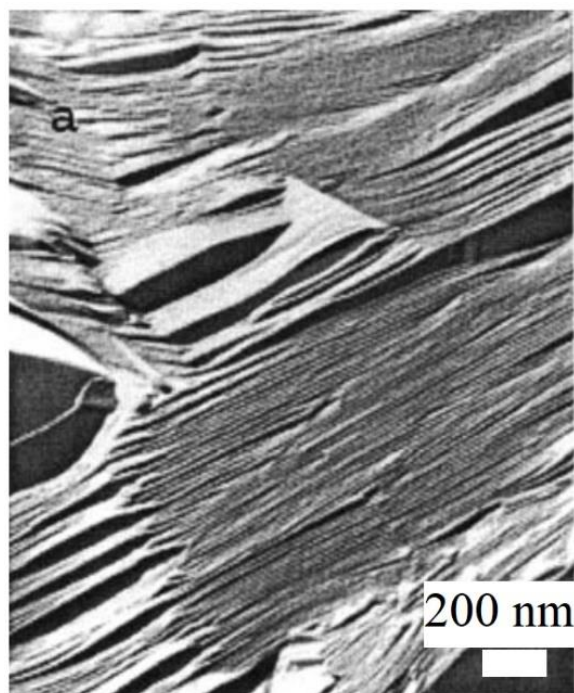


Figure IV.1. Freeze-fracture transmission electron microscopy image of the α -gel structure of distilled saturated monoglycerides in water (25 : 75); figure adapted from ref. [3]

While hydrated Montane 60 lamellar distance is sensitive to ionic strength and pH as shown in chapter 5, urea did not affect the lamellar structure of hydrated Montane 60. We hydrated Montane 60 with eutectic urea solution and compared the lamellar distance with the lamellar distance of Montane 60 hydrated with distilled water. The S-WAXS of Montane 60 hydrated with eutectic urea solution shows the lamellar structure in SAXS, with a hydrophilic lamellar structure and a hydrophobic lamellar structure (Figure IV.2a). The lipid chains arrangement is H- α , as shown in WAXS (Figure IV.2a). The lamellar distance of Montane 60 hydrated with eutectic urea solution is similar to the lamellar distance of Montane 60 hydrated with water when the hydration rate is the same (Figure IV.2b). Therefore, urea does not affect the lamellar structure of Montane 60.

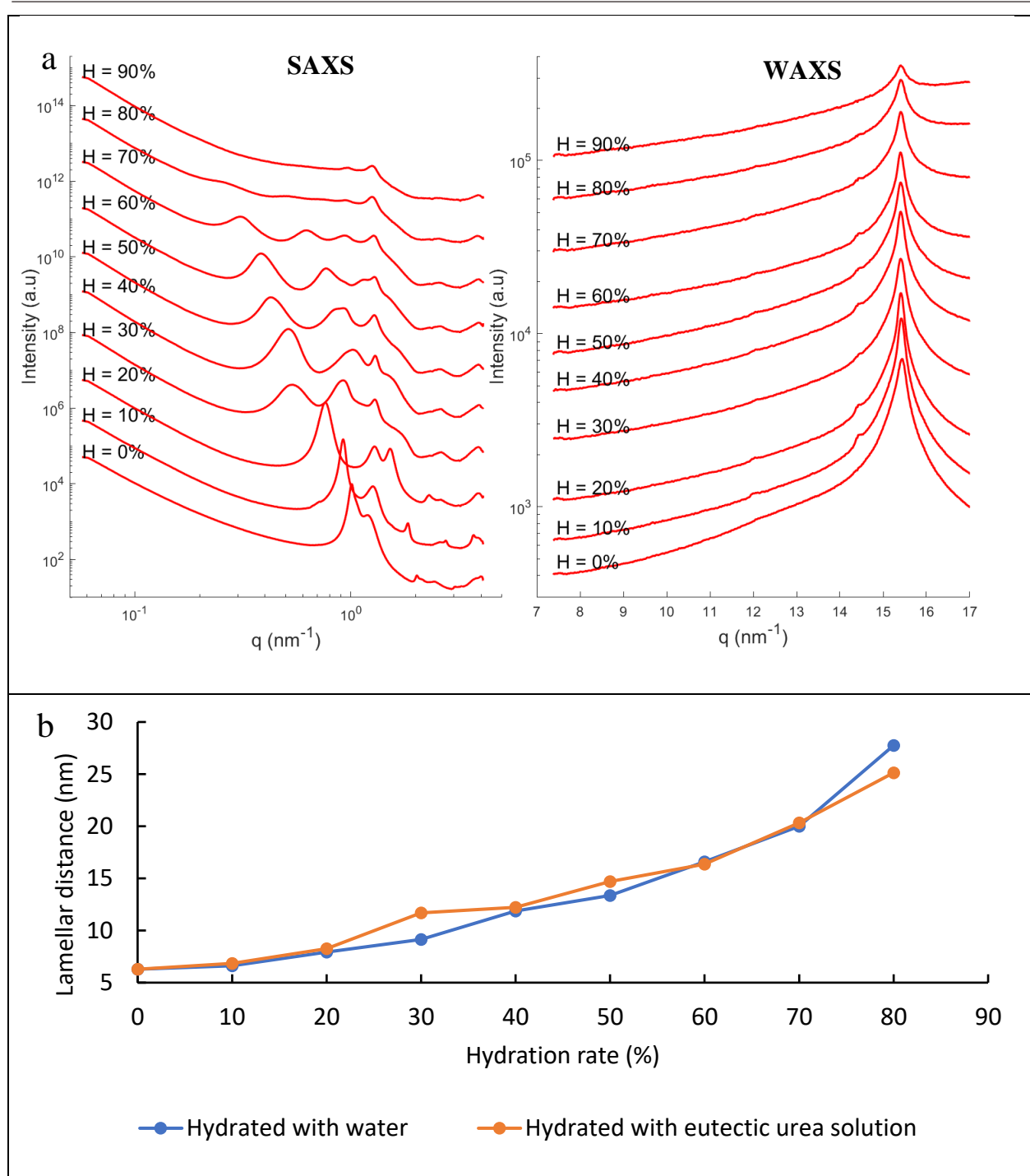


Figure IV.2. (a) S-WAXS spectra of M60 hydrated with eutectic urea solution and (b) the lamellar distance in comparison with M60 hydrated with water

The fine entanglement between water and lipid layers allows us to incorporate a large amount of urea in the formulation. However, it facilitates the exposure of erythromycin to low pH when the environment is acidic. As explained in this manuscript, w/o/w solid lipid dispersions having the nano-size are difficult to produce. For that reason, we are developing solid lipid microspheres using the prilling technique, which can co-encapsulate urea and erythromycin. A microsphere is a w/o solid lipid emulsion, which has water droplets stabilized inside a solid lipid matrix. The microsphere can be

fabricated from long-chain triglycerides as the lipid matrix, and Montane 60 as the lipophilic surfactant. Figure IV.3 demonstrates a SR μ CT photo of solid lipid microspheres fabricated from Precirol (glyceryl distearate, provided by Gattefosse) and Montane 60. We can see in the photo solid lipid microspheres, in which we have 2 domains, gray domain and black domain. The gray domain may be the hydrated Montane 60, while the black domain may be water droplets. The co-encapsulation of urea and erythromycin has been done successfully, showing potential for this doctoral project. Details about materials, fabrication methods and characterization of the solid lipid microspheres are out of the scope of this thesis, but they will be reported in another project by our colleague (Claire DELMAS) in the near future.

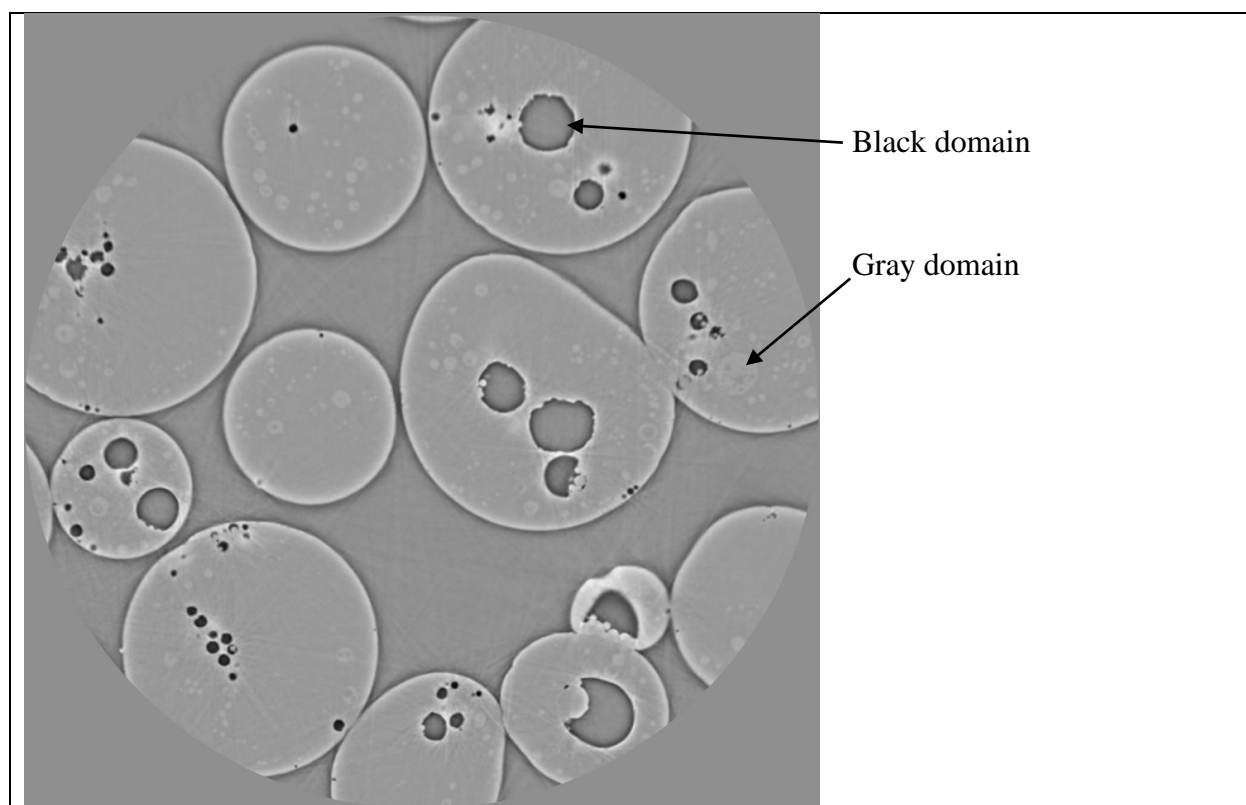


Figure IV.3. SR μ CT photo of solid lipid microsphere fabricated from Precirol and Montane 60 by the prilling method. The width of the view is 1843 μ m.

2. About the *in vitro* drug delivery and anti-microbial activity tests

Because our formulation could not protect erythromycin from gastric acid, pH 1.2 of the fasted state simulated gastric fluid (SGF) degraded the antibiotic rapidly. So, the *in vitro* release study test was done in SGF pH5, which mimics the gastric environment in the fed state [4]. In the fed state, there should be food in the stomach. Food can be solid or liquid. They may be carbohydrates, fibers, protein, lipids etc., which will interact with the formulation, depending on which type of foods. Our formulation may adhere to food particles instead of the gastric mucus layer. The stability of the lipid structure may be changed due to lipids from food, leading to a change in the drug release rate. In a simple case, homogenized long-life milk (3.5% fat) or liquid meals were used to

mimic the food content in the stomach in several reports [4]. In our case, to simplify the experiment, we did not use any food and considered only the effect of pH and NaCl in SGF on the formulation. The pH value around 5 could be also obtained by using proton pump inhibitors which are used during *H. pylori* treatment; this would reduce the food effect. We used erythromycin as a model molecule to investigate the protective property of the lipid matrix. An alternate strategy could be to incorporate clarithromycin as this antimicrobial agent has similar activity to erythromycin but is more stable in acidic conditions.

The *in vitro* antimicrobial activity of the formulation has been confirmed. Our urea and erythromycin co-encapsulated sample show the antimicrobial activity against clinical *H. pylori* strains isolated from patients, indicating the potential in clinical treatment. The activity of the formulation has been confirmed to be from encapsulated erythromycin, while the formulation did not show any effects.

3. About *in vitro* chemotactic experiments

3.1. Video-microscope experiment

While the antimicrobial activity has been confirmed, the chemotactic activity experiment is still in progress. We planned to use the video-microscopy technique to visualize the chemotactic movement of *H. pylori*. The technique was used to observe the chemotactic movement of *H. pylori* towards urea and away from acid [5]. In general, an Eppendorf Femtotip II was used to inject a solution into the bacterial culture medium. Using the camera, we can observe and record the movement of bacteria toward or away from the injected substances. The configuration of the experiment is in Figure IV.4. After recording the video, certain frames (15 in the cited article) were taken to determine the mobility trace of bacteria. The number of black pixels from the trace of bacteria was used as the indication for the number of bacteria. By comparing the number of bacteria before and after the injection of urea, we can confirm the chemotactic behavior of bacteria.

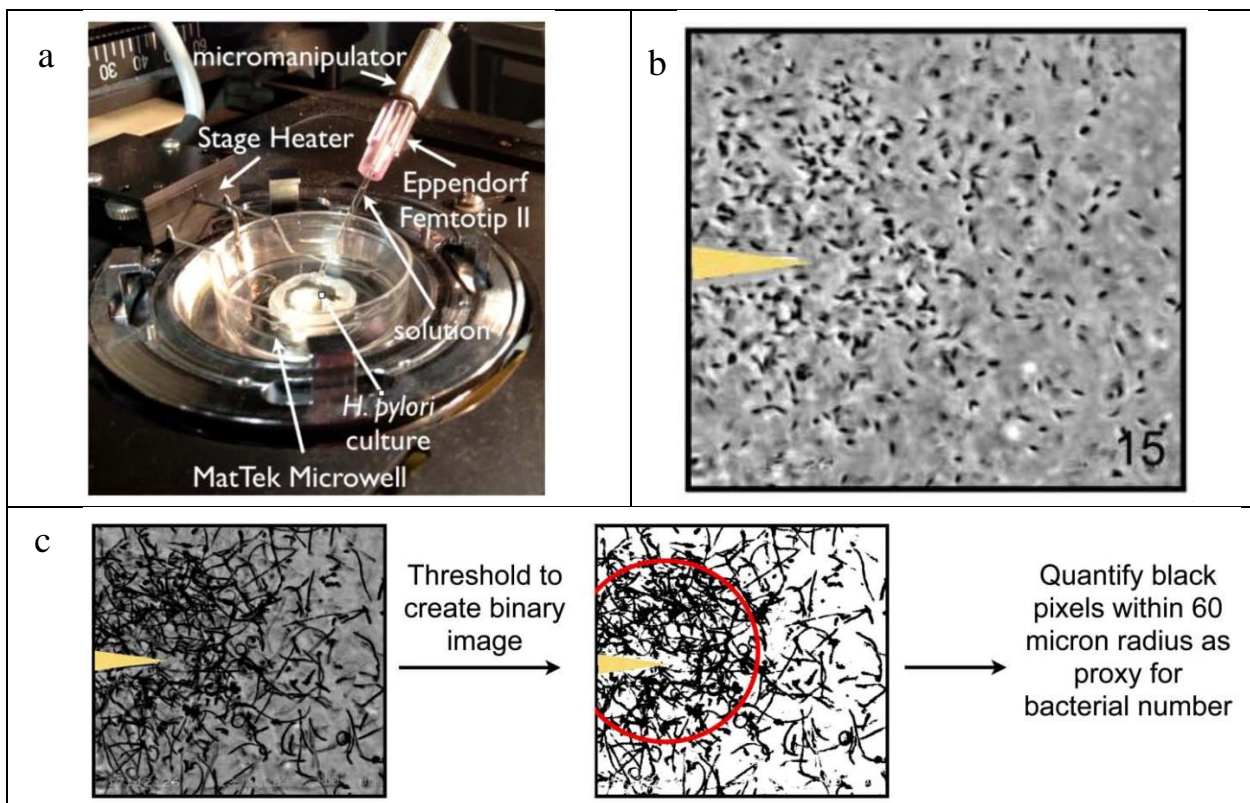


Figure IV.4. (a) Configuration of the video-microscopy experiment, (b) the view of the microscope, the yellow arrow indicates the pipette tip, black spots are *H. pylori*, and (c) the image treatment method for quantification, figure adapted from ref. [5].

In the first attempt to set up the experiment, we tested the mobility of *H. pylori* toward the formulation loaded with urea only (without erythromycin, without chitosan) named PU-C0 in Table IV.1. Since the formulation is in powder form, which would not be suitable to put in the pipette micro-size tip. We melted briefly the powder on the glass substrate to stick the powder to the substrate and injected *H. pylori* (strain PMSS1), grown in Brucella Broth, 10% Fetal Bovine Serum (FBS) to the chamber. The bacteria were filmed using a phase-contrast microscope. To determine the chemoattraction effect of the formulation, we compared the number of bacteria near the particles after injection of bacteria and after 10s by tracing swimming bacteria for 2 seconds. Figure IV.5a shows the view of the microscope. In the view, the formulation powder particles are white, marked by orange stars. To determine the number of bacteria in the view around these particles initially, we traced the bacteria in the view from $t=0s$ to $t=2s$. The trace of bacteria from $t=0$ to $t=2s$ is shown in Figure IV.5b in the form of black lines. The area of the black pixels (px) in Figure IV.5b is 218217 px. Similarly, after 10s, we determined the number of bacteria in the view around the particles to see if the number of bacteria increased. Figure IV.5c shows the trace of bacteria in the view from $t=8s$ to $t=10s$, with the area of black pixels being 255251 px (increased by 1.17 times). So, from 0s to 10s, we have seen a very slight increase in the number of bacteria in the view. In addition, we seem to have more bacteria swimming around the particles after 10s.

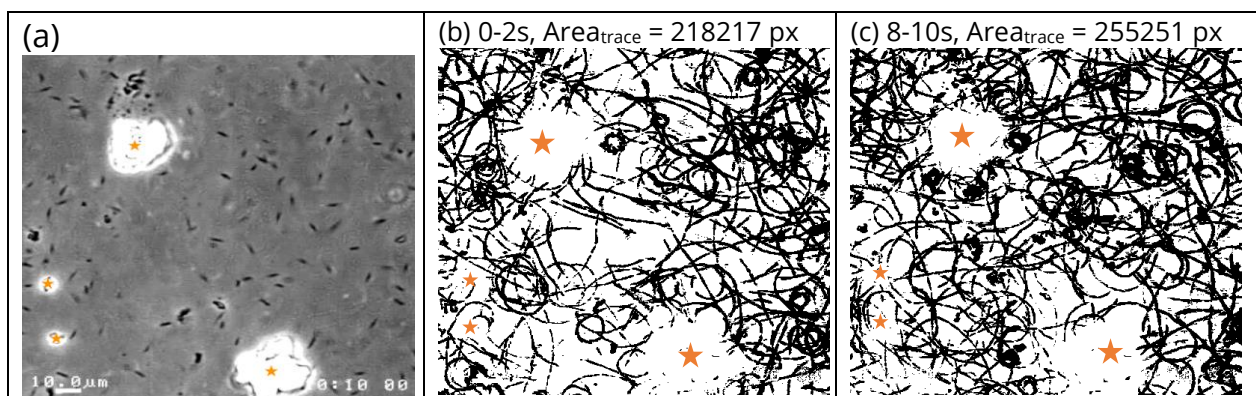
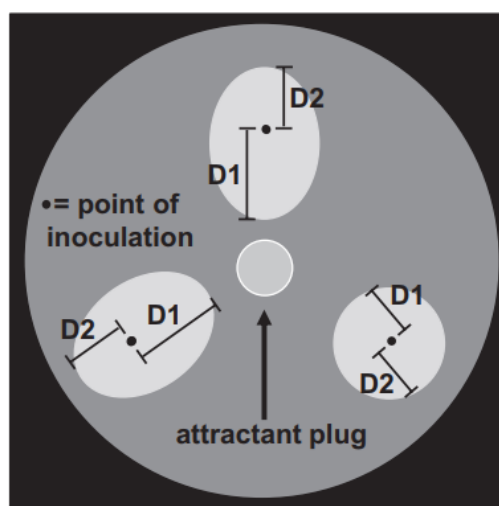


Figure IV.5. Photo from video-microscopy of *H. pylori* in interaction with the formulation containing only urea (PU-C0), (a) phase-contrast image at $t=0$, (b) the trace of bacteria in the view from 0 to 2s, (c) trace of bacteria in the view from 8 to 10s. The orange stars indicate the position of lipid particles.

The setup of the experiment is not ideal, since we have several sources of urea from different particles. It is then difficult to optimize the view of the microscope. In addition, the mass of the particles on the substrate is hard to measure, leading to a possibly too large dilution factor. The dilution may decrease the urea concentration and reduce the chemotactic activity of bacteria. We did a similar experiment with urea and erythromycin-containing formulation (PEU-C0 in Table IV.1). The bacteria were not inactivated around the erythromycin-containing particles, even after 83 minutes, indicating the possibility that the concentration of erythromycin was too low. Another factor is the homogeneity of the lyophilized powder. We have checked and confirmed the homogeneity in the urea and erythromycin loading in the powder at the scale of 20 mg. However, the mass of particles on the substrate in the video-microscopy experiment may be too small to ensure the homogeneity of drug loading. There may not be enough urea or erythromycin in the particles in the experiments.

3.2. Gradient soft agar swim plate assay

On the other hand, we tried to investigate the chemotactic activity via the swarming behavior of bacteria on the agar gel surface. While the swarming movement is not the same as the swimming movement of bacteria, we may see the attraction effect of the formulation. There are several types of chemotactic movement tests, which have been reviewed in detail in ref. [6]. Based on the availability of equipment, we choose gel-based tests. Since the chemical-in-plug test for *H. pylori* may have false-positive results [7], we choose to use the gradient soft agar swim plate assay (Figure IV.6). In this assay, a chemoattractant containing plug is put in the middle of the petri dish. The bacteria are inoculated on the surface of the gel, at a distance of around 2 cm, as suggested in ref. [6]. If the chemoattractant plug induces a bacterial chemotactic movement, the shape of the bacteria after incubation will be oval, indicating the growing direction toward the chemoattractant source; otherwise, the shape of the bacteria colony is round.



$$\text{Response index (RI)} = \frac{(D1)}{(D1 + D2)}$$

Figure IV.6. Gradient soft agar swim plate assay configuration, oval shape colony indicates the response of bacteria to the plug, while round shape indicates that the bacteria are not sensitive to the chemoattractant.

In our project, the gradient soft agar swim plate assay has been done using 4 wt% Mueller Hilton agar gel containing 10% v/v defibrinated horse blood. We tested 7 gel plug buttons, described in Table IV.1. The blank gel button composition is the same as the cultural environment and is used as the control for the effect of lipids. PB-C0 and PB-C5 are blank formulations without urea nor erythromycin, used as the control for the effect of urea, and there is chitosan in PB-C5. PU-C0 and PU-C5 are formulations that have only urea (without erythromycin), and there is chitosan in PU-C5. PEU-C0 and PEU-C5 are formulations that have both urea and erythromycin, and there is chitosan in PEU-C5. To prepare the button plug, an amount of formulation is added to a volume of 8% agar gel to have the desired concentration of urea and/or erythromycin in the plug button. The concentration of urea and erythromycin in the buttons is in Table IV.1. The concentration of urea if 100% of urea is released to the gel Petri disk is still much higher than the minimum urea detection concentration of *H. pylori* (50 nM [5]). The concentration of erythromycin if 100% erythromycin is released to the gel Petri disk is larger than the MIC of erythromycin (<0.06 µg/mL). After the preparation of the plug button, it was plugged into the middle of the petri dish. 10µL of bacterial suspension (3-4 McFarland) was inoculated on the surface of the petri dish. The *H. pylori* strains used for the experiment are listed in Table IV.2. The plates were then incubated in an airtight container containing gas packs (BD GasPak™ EZ Campy Container System) at 35°C. The results were read after 5 days to ensure the growth of bacteria.

Sample	%Chitosan (wt%)	%Urea (wt%)	%ERY (wt%)	Conc. Urea in the button (mM)	Conc. Urea after 100% release (mM)	Conc. ERY in the button ($\mu\text{g}/\text{mL}$)	Conc. ERY after 100% release ($\mu\text{g}/\text{mL}$)
Blank gel button	0	0	0	0	0	0	0
PB-C0	0	0	0	0	0	0	0
PB-C5	0.12	0	0	0	0	0	0
PU-C0	0	24	0	2.67	0.029	0	0
PU-C5	0.12	24.7	0	2.74	0.03	0	0
PEU-C0	0	27.9	1.2	3.1	0.034	8	0.09
PEU-C5	0.12	27.4	1.2	3.05	0.034	8	0.09

Table IV.1. Sample description of formulations used in chemotactic swarming experiments

No.	Strain	MIC of clarithromycin ($\mu\text{g}/\text{mL}$)	Note
1	2206_220738	<0.016	Sensible to clarithromycin
2	2206_271989	0.016	Sensible to clarithromycin
3	J99	<0.016	Sensible to clarithromycin
4	2203_281091	12	Resistant to clarithromycin
5	2204_130766	16	Resistant to clarithromycin

Table IV.2. *H. pylori* strains used for chemotactic swarming experiments with data from Poitiers University Hospital

The chemotactic swarming behavior of *H. pylori* is shown in Figure IV.7. Most of the bacterial colony spots are round, indicating that they did not respond to the formulation. The swarming behavior is agar gel concentration-dependent [8]. While the agar concentration recommended for the swarming experiment is 1.5 wt% [8], we could not have a solid gel agar below 4 wt%. Maybe that is one reason why the bacteria did not respond in the experiment. The video-microscopy technique may be more suitable to observe the chemotactic response of bacteria.

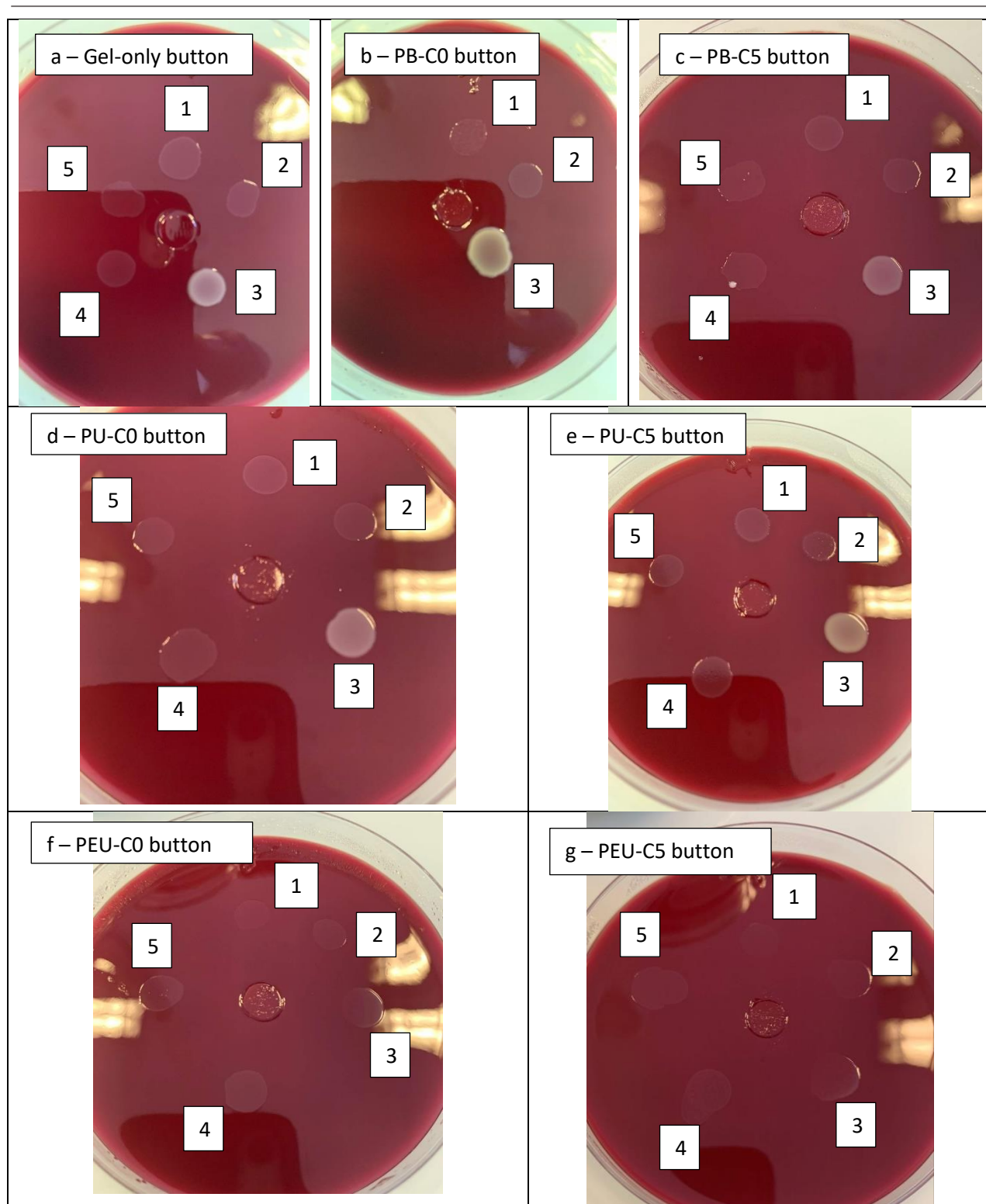


Figure IV.7. Chemotactic swarming experiments of *H. pylori* on agar gel, induced by (a) a blank gel plug button acting as a reference, (b) PB-C0 button, (c) PB-C5 button, (d) PU-C0 button, (e) PU-C5 button, (f) PEU-C0 button and (g) PEU-C5 button.

The use of natural taxis to attract the target toward the drug carrier is an interesting approach, which has been reviewed in chapter 2. It would increase the targeting efficiency, facilitating the meeting between the target and the drug carrier. Not only on

bacteria, but this strategy may also apply to any other moving targets, for example, metastasis cancer cells or immune cells. Our project aims to be a proof-of-concept work, which may demonstrate the use of chemotaxis to attract a moving target toward the drug carrier. However, we still need more experimental data to definitely support our proposal.

4. Perspective

Because the project focuses on the pre-formulation and formulation aspect, it lacks the data of the biological test aspect. To complete the *in vitro* dataset, the project will be complete with the chemotactic behavior of *H. pylori*. The mucoadhesive property of the formulation needs to be investigated via the interaction with mucin. The adhesion of the formulation to *H. pylori* can also be done by fluorescence labeling. After that, the *in vivo* experiments are also interesting to find the treatment efficiency of the formulation, in comparison to treatment in the clinic. The process of the formulation in the stomach and going through the gastrointestinal tract *in vivo* would also be interesting to study.

References

- [1] for the Taiwan Gastrointestinal Disease and Helicobacter Consortium, J.-M. Liou, P.-Y. Chen, Y.-T. Kuo, M.-S. Wu, Toward population specific and personalized treatment of *Helicobacter pylori* infection, *J. Biomed. Sci.* 25 (2018) 70. <https://doi.org/10.1186/s12929-018-0471-z>.
- [2] R. Michalik, I. Wandzik, A Mini-Review on Chitosan-Based Hydrogels with Potential for Sustainable Agricultural Applications, *Polymers.* 12 (2020) 2425. <https://doi.org/10.3390/polym12102425>.
- [3] F. Vang Sparso, N. Krog, Food Emulsifiers: Their Chemical And Physical Properties, in: S. Friberg, K. Larsson, J. Sjöblom (Eds.), *Food Emuls.*, CRC Press, 2003. <https://doi.org/10.1201/9780203913222.ch2>.
- [4] N. Fotaki, M. Vertzoni, Biorelevant Dissolution Methods and Their Applications in *In vitro- In vivo* Correlations for Oral Formulations~!2009-09-14~!2009-11-02~!2010-04-29~!, *Open Drug Deliv. J.* 4 (2010) 2–13. <https://doi.org/10.2174/1874126601004020002>.
- [5] J.Y. Huang, E.G. Sweeney, M. Sigal, H.C. Zhang, S.J. Remington, M.A. Cantrell, C.J. Kuo, K. Guillemin, M.R. Amieva, Chemodetection and Destruction of Host Urea Allows *Helicobacter pylori* to Locate the Epithelium, *Cell Host Microbe.* 18 (2015) 147–156. <https://doi.org/10.1016/j.chom.2015.07.002>.
- [6] R.E. Parales, J.L. Ditty, Chemotaxis to Atypical Chemoattractants by Soil Bacteria, in: M.D. Manson (Ed.), *Bact. Chemosensing*, Springer New York, New York, NY, 2018: pp. 255–280. https://doi.org/10.1007/978-1-4939-7577-8_21.

- [7] J. Li, A.C. Go, M.J. Ward, K.M. Ottemann, The chemical-in-plug bacterial chemotaxis assay is prone to false positive responses, *BMC Res. Notes.* 3 (2010) 77. <https://doi.org/10.1186/1756-0500-3-77>.
- [8] D.B. Kearns, A field guide to bacterial swarming motility, *Nat. Rev. Microbiol.* 8 (2010) 634–644. <https://doi.org/10.1038/nrmicro2405>.

V. CURRICULUM VITAE

Hung V. NGUYEN

- Location: Île-de-France
- Email: Hungnv241@gmail.com

- Languages:
- English: Fluent
 - French: Fluent
 - Vietnamese: Native



Education

- **10/2019 – 12/2022** - PhD in Pharmaceutics and Biopharmaceutics
Faculty of Pharmacy, Université Paris-Saclay, Châtenay-Malabry
- **09/2017 – 09/2019** - Master in Nanoscale Engineering
INSA de Lyon, Villeurbanne (GPA: 16.34/20), IDEX Scholarship of Excellence (2017)
- **09/2014 – 08/2017** - Bachelor in Materials Science and Nanotechnology
University of Science and Technology of Hanoi (USTH), Vietnam (GPA: 16.28/20)

Working experience

- **10/2019 – 12/2022** – PhD Candidate
Institute Galien Paris-Saclay, CNRS, Châtenay-Malabry
 - Developed lipid formulation for oral delivery of poorly soluble drugs
 - Handled formulation development from pre-formulation to drug release testing
 - Characterized physical-chemical properties of industrial lipid excipients
- **03/2019 – 09/2019** – Master 2 Research Intern
Institute Néel, CNRS, Grenoble
 - Synthesized degradable silica nanoparticles acting as nanocarrier targeting tumors
 - Gained knowledge about sol-gel chemistry and organosilica particles.
- **01/2018 – 03/2018 & 06/2018 – 08/2018** – Master 1 Research Intern
INSA Lyon and Université de Lyon 1, Villeurbanne
 - Characterized carbon nanotube yarns and silica gels for energy application
- **07/2016 – 07/2017** – Bachelor Research Intern

Institute of Materials Science, Vietnam

- Fabricated nanocarbon aerogel for environmental and energy application

Technical skills

- Materials and nanomaterials characterization methods (SAXS, EM, AFM, FTIR, DSC, TGA v.v..)
- Analytical chemistry techniques (HPLC, LC-MS)
- Colloidal stability characterization (DLS, Zeta potential)
- Formulation manufacturing and quality control (design of experiments, homogenization, lyophilization, drug loading test)
- Dissolution and drug release tests in biological media
- Data analysis and presentation (OriginLab, Matlab, ImageJ, Excel)

Publications

- Cassandre Miralaei et al., Effect of extreme mechanical densification on the electrical properties of carbon nanotube micro-yarns, *Nanotechnology* 33 (2022) 275708; DOI: 10.1088/1361-6528/ac6039
- Mustapha El Hadri et al., Structural and Vibrational Investigations of Mixtures of Cocoa Butter (CB), Cocoa Butter Equivalent (CBE) and Anhydrous Milk Fat (AMF) to Understand Fat Bloom Process, *Applied Science* (2022), 12(13), 6594; DOI: 10.3390/app12136594
- Hung V. Nguyen et al., Synthesis and properties of porous ester-silica nanoparticles, *Microporous and Mesoporous Materials*, 317 (2021), 110991; DOI: 10.1016/j.micromeso.2021.110991
- Hung V. Nguyen, Vincent Faivre, Targeted drug delivery therapies inspired by natural taxes, *Journal of Controlled Release*. 322 (2020) 439–456. DOI: 10.1016/j.jconrel.2020.04.005